# Tandem Reactions of Carbon Dioxide Reduction and Hydrocarbon Transformation

Elaine Gomez

Submitted in partial fulfillment of the
requirements for the degree of
Doctor of Philosophy
in the Graduate School of Arts and Sciences

COLUMBIA UNIVERSITY

2019

Abstract

Tandem Reactions of Carbon Dioxide Reduction and Hydrocarbon Transformation

Elaine Gomez

High atmospheric concentrations of $CO_2$ contribute to adverse effects that impact human health and the climate. The need to reduce $CO_2$ is evident, and climate stabilization will require a combination of mitigation, utilization, and even negative emission technologies. Thus, one key approach will be to transform abundant $CO_2$ into a useful feedstock for processes that not only produce value-added products but also match the scale necessary to impact anthropogenic emissions. The tandem $CO_2$ reduction and light alkane transformation reactions over specialized bifunctional catalysts have the potential to produce olefins or synthesis gas by efficiently utilizing the $C_2$-$C_4$ components in shale gas while reducing a greenhouse gas.

The reactions of $CO_2$ with light alkanes may occur through two distinct pathways, oxidative dehydrogenation ($CO_2 + C_nH_{2n+2} \rightarrow C_nH_{2n} + CO + H_2O$, $CO_2$-ODH) and dry reforming ($nCO_2 + C_nH_{2n+2} \rightarrow 2nCO + (n+1)H_2$, DR). The two reactions can occur simultaneously at temperatures ≥823 K with considerable conversions. Until recently, there has been little understanding regarding the identification of bimetallic catalytic systems that either selectively cleave the C-H bonds to produce olefins or effectively break all the C-C and C-H bonds to produce dry reforming products. In this work, we discuss a combined approach of flow reactor experiments, in situ characterization, and density functional theory (DFT) calculations to help create a design platform for catalysts that are inherently active and selective for the reactions of $CO_2$ and light alkanes.

Particularly, it was of interest to use propane as $CO_2$ reduction feedstock due to its increasing abundance and highly marketable respective olefin. Through the combined approach,

non-precious $Fe_3Ni_1$ and precious $Ni_3Pt_1$ supported on $CeO_2$ were identified as promising catalysts for the $CO_2$-ODH and DR of propane, respectively. In situ X-ray absorption spectroscopy measurements revealed the oxidation states of metals under reaction conditions and DFT calculations were utilized to identify the most favorable reaction pathways over the two types of catalysts. While both the $CO_2$-ODH and DR reactions of alkanes produce valuable molecules, the separation of gas phase products is challenging. Therefore, it was highly desirable to develop a tandem reaction scheme in which the reaction of $CO_2$ and alkanes can produce liquid products.

Another potential chemistry with increased similarity to the operating conditions of $CO_2$-ODH, is the tandem reactions of $CO_2$-assisted oxidative dehydrogenation and aromatization of light alkanes ($CO_2$-ODA). In this process, alkanes are transformed directly into aromatics without the need for expensive naphtha while increasing the consumption of $CO_2$ per mol of value-added product and facilitating downstream separation because of the production of liquid aromatics. One critical change upon the introduction of $CO_2$ to the dehydrogenation/aromatization pathway is the formation of water. The presence of water under reaction conditions has been shown to be problematic for zeolites as it causes changes in the framework. Phosphorous modification at an optimal loading improved the hydrothermal stability of Ga/ZSM-5, reduced coke formation on the catalyst surface, and allowed for the formation of more liquid aromatics through the $CO_2$-ODAE reaction pathway compared to the direct dehydrogenation and aromatization reaction. With the aid of DFT calculations, the mechanisms for the production of aromatics from ethane were identified, providing insight on the effect of Ga modification on ethylene formation over ZSM-5 as well as the role of $CO_2$ on the aromatization of ethylene. Future efforts should be geared toward enhancing aromatics yield through the design of hydrothermal stable zeolite-based materials with bimetallic active centers that are capable of activating $CO_2$.

## Table of Contents

## List of Figures

## List of Tables

## Commonly used abbreviations

| Abbreviation | Full Name | Abbreviation | Full Name |
|---|---|---|---|
| $CO_2$-ODH | $CO_2$-oxidative dehydrogenation | $C_3$ | Propane |
| DR | Dry reforming | $C_4$ | Butane |
| DD | Direct dehydrogenation | | |
| $CO_2$-ODA | $CO_2$- assisted dehydrogenation & aromatization | | |
| DDA | Direct dehydrogenation & aromatization | | |
| RWGS | Reverse water-gas shift | | |
| DFT | Density functional theory | | |
| XAFS | X-ray absorption fine structure | | |
| EXAFS | Extended X-ray absorption fine structure | | |
| XANES | X-ray absorption near edge spectroscopy | | |
| XRD | X-ray diffraction | | |
| TGA | Thermogravimetric analysis | | |
| Synthesis/Syngas | $CO + H_2$ | | |
| TOF | Turnover frequency | | |
| GC | Gas chromatograph | | |
| *O | Adsorbed oxygen | | |
| $C_2$ | Ethane | | |

## Acknowledgements

I would like to thank my advisor, Dr. Jingguang G. Chen, for his guidance, support, and encouragement. I feel very fortunate to have been able to contribute to research projects that align with my interests and to have had the opportunity to publish the work in a format that will allow our findings to make an impact. Dr. Chen, thank you for investing your time on me and my thesis work.

I also would like to thank my committee, Professors Daniel Esposito, Ah-Hyung (Alissa) Park, Robert Farrauto, and Robert B. Barat. Dr. Esposito and Dr. Park have participated in every stage of this thesis work, from qualifier to defense, and their input elevated the quality of discussions provided. Dr. Farrauto provided insightful discussions and posed compelling questions that helped me widen my perspective on the work. Dr. Barat has been an encouraging mentor since my very first undergraduate research experience at NJIT and his advice has been invaluable during my Ph.D. candidacy.

All current and past Chen group members have been very helpful, and I particularly would like to thank Lea Winter, Brian Tackett, Zhexi Lin, and Marc Porosoff. I would also like to thank my co-authors, Dr. Binhang Yan, Dr. Shyam Kattel, Dr. Zhenhua Xie, and Dr. Siyu Yao.

Lastly, I would like to thank my family. My parents, Juan and Gloria Gomez, and sister, Janice Gomez, are my inspiration and have encouraged me throughout my studies. I am thankful for the support of my loving husband, Luis J. Mendez, who has spent countless of hours entertaining my discussions on the fields of chemical engineering and catalysis.

# Chapter 1: Introduction

## 1.1 Tandem reactions of $CO_2$ reduction and dehydrogenation of light alkanes

The abundant availability of shale gas has increased the interest in utilizing all its components as raw materials for producing value-added chemicals and fuels. Ethane, propane, and butane can comprise up to 15% v/v of shale gas depending on the source, with the most abundant fraction belonging to ethane.[1] Unlike methane[2], these light alkanes contain C-C bonds that can be used to produce olefins. The demand for olefins is high since they are important petrochemical building blocks, but the conventional routes of production from thermal steam cracking and direct dehydrogenation (DD) processes require high operating temperatures and suffer from severe coking problems due to over-oxidation and cracking.[3,4] The tandem reactions of $CO_2$ reduction and $CO_2$-assisted oxidative dehydrogenation ($CO_2$-ODH) of light alkanes combined as one process over a bifunctional catalyst presents opportunities to more efficiently utilize the $C_2$-$C_4$ components in shale gas while also reducing a greenhouse gas. If all ethylene, propylene, and butylene/butadiene demand (5.2E+12 $mol \cdot yr^{-1}$)[5] is satisfied with $CO_2$-ODH, with the assumption that 1 mol of olefin produced equals 1 mol of $CO_2$ consumed, then the process would consume 14.6% of total global chemical industry $CO_2$ emissions per year with the current global emission value (5.34E+13 $mol \cdot yr^{-1}$)[6] as a reference. Replacing only ethylene demand with the $CO_2$-ODHE reaction would consume 9.8% of total global chemical industry $CO_2$ emissions per year and would require the consumption of only 0.026% of total global natural gas reserves[7] assuming that ethane fraction is at least 1% v/v.[1] For context, the available ethane produced from shale gas (which is nearly consumed by current demand) would only satisfy 62% of olefin production in 2018.

In the $CO_2$-ODH reaction, $CO_2$ is a soft oxidant that prevents over-oxidation and does not form an explosive reactive mixture, unlike $O_2$-ODH. In principle, the introduction of $CO_2$ alters the dehydrogenation pathway by providing oxygen (via direct C=O dissociation) and oxidizing the abstracted hydrogen from the alkane, producing water and consequently reducing both the Gibbs free energy of the reaction and the operating temperature. $CO_2$ as a soft oxidant can also lead to modifications of a catalyst surface or bulk composition, which in turn affects the redox, adsorption, and electronic properties that are known to influence activity and selectivity.[8,9]

The $CO_2$-ODH reaction requires a bifunctional catalyst that would allow $CO_2$ to dissociate to produce CO and reactive oxygen species (*O).[8,10] The resulting *O would then assist the dehydrogenation of the adsorbed alkane to produce the corresponding olefin and water. Reducibility and abundant lattice oxygen are key features that allow the described process to turn over efficiently and for that reason reducible oxide-supported metal (Cr, Fe, V, Mo) catalysts have received much attention for $CO_2$-ODH reactions.[11] While Cr-oxides show high initial conversion and selectivity due to a $Cr^{6+}$ active center generated from a redox cycle with $Cr^{3+}$, their implementation is undesirable due to short life cycles and high toxicity. Other non-reducible $CO_2$-ODH catalysts such as Ga-based catalysts are proposed to follow a two-step oxidative dehydrogenation mechanism, where the catalyst first dehydrogenates the alkane to the olefin and $H_2$, then the $H_2$ reduces $CO_2$ to CO via the reverse water gas shift reaction (RWGS, $CO_2 + H_2 \rightarrow CO + H_2O$). Ga-based catalysts are effective for $CO_2$ activation but have been shown to displace the adsorbed alkane to undesired sites in which cracking is favorable[12], increasing coke formation and leading to quick deactivation.[13] Thus, there is a need for the discovery of active and more stable bifunctional $CO_2$-ODH catalysts.

Wang and Zhu were among the first to summarize the progress on the development of catalysts for the $CO_2$-ODH of light alkanes, which at the time consisted of activity trends and ex situ characterization, but lacked detailed information on the type of active sites and mechanisms on Cr, Mn, Fe, and $Mo_2C$ catalysts.[14] Some of the reviews in the literature on the ODH of light alkanes use $O_2$ as the oxidant and only briefly mention the use of $CO_2$ as a mild oxidant.[15,16,17,18] Other prominent reviews on the subject discussed at length the influence of $CO_2$ as a soft oxidant and specific requirements for $CO_2$ activation with smaller sections summarizing the catalysts (mainly Cr-oxides) used for the $CO_2$-ODH reactions of ethane, propane, and butane.[19,8] The latest review by Atanga et al. focuses on the $CO_2$-ODH of propane over zeolites and metal oxide-based catalysts (Cr, V, Ga, and In). Their review recognizes that at high temperatures where thermodynamics favors alkane conversion, the scission of the C-C bond becomes increasingly favorable compared to the cleavage of the C-H bond of alkanes and the selectivity to the desired olefin decreases significantly.[20,21] Thus, another important characteristic of a $CO_2$-ODH catalyst is that it must selectively break C-H bonds while preserving C-C bonds in order to avoid promoting the dry reforming (DR) reaction.

This Chapter will focus on how to properly address the temperature challenge and asses inherent activity for the selective oxidative C-H bond scission versus the competing C-C bond cleavage pathways. The chapter will include, for the first time in literature, stable bimetallic and metal-modified carbide catalysts and contribute to the understanding of the active sites of these two types of promising catalysts for the $CO_2$-ODH of light alkanes. There will be an emphasis on the importance of catalytic measurements, in situ characterization, and density functional theory (DFT) calculations in identifying reaction mechanisms and key descriptors for designing improved catalysts.

### 1.1.1 Relevant reactions and thermodynamic analysis

Thermodynamic analyses of the $CO_2$-ODH of alkanes following a one-step mechanism (e.g., $C_2H_6 + CO_2 \rightarrow C_2H_4 + CO + H_2O$) and a two-step mechanism (DD, e.g., $C_2H_6 \rightarrow C_2H_4 + H_2$ followed by RWGS, i.e., $CO_2 + H_2 \rightarrow CO + H_2O$) at atmospheric pressure for various temperatures were performed with the assistance of HSC Chemistry Outotec v8 software, which utilizes a Gibbs free energy minimization algorithm. **Figure 1-1** shows that the addition of $CO_2$ to the feed of the reaction for the two-step mechanism can effectively increase the equilibrium conversion of the alkane ($C_2$-$C_4$), and therefore the olefin yield, by consuming $H_2$ (from DD) through the RWGS reaction. Other thermodynamic studies in the literature also report that equilibrium conversions of the alkane in the presence of $CO_2$ are higher than in the presence of inert gas with the two-step pathway illustrating higher equilibrium conversions than the one-step $CO_2$-ODH pathway.[22,14] Thermodynamic studies have also shown that changes in the Gibbs free energy of the $CO_2$-ODH reactions of alkanes become increasingly favorable with higher alkanes: (i-$C_4$>$C_3$>n-$C_4$>$C_2$).[20]

Decomposition or cracking reactions can occur throughout the entire range of temperatures that $CO_2$-ODH reaction may occur and the propensity of olefin cracking ($C_2^=$, $C_3^=$, $C_4^=$) is greater than alkane cracking. However, $CO_2$ can consume the resulting coke via the reverse Boudouard reaction ($CO_2 + C \rightarrow 2CO$). High reaction temperatures also favor the production of CO and $H_2$ via the DR pathway, and therefore promising catalysts should kinetically control the extent of dry reforming. However, equilibrium calculations have demonstrated that the yield of olefin and synthesis gas composition can be varied by altering the temperature and molar ratio of $CO_2$: alkane.[23]

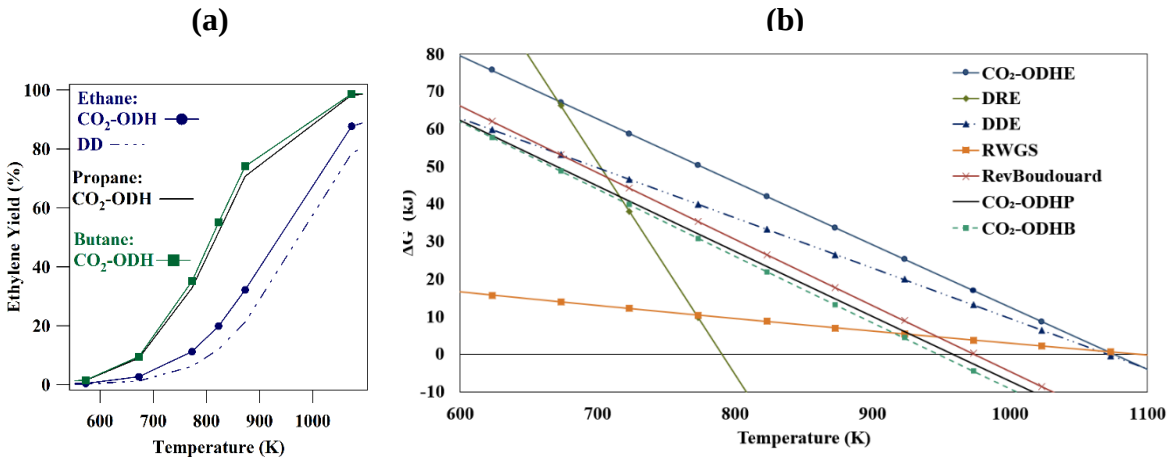


**Figure 1-1.** Thermodynamic analysis of $CO_2$-assisted alkane dehydrogenation and direct dehydrogenation. **(a)** Ethylene yield as a function of reaction temperature.$CO_2$-ODH process assumes a two-step mechanism with RWGS and a $CO_2$/alkane molar ratio of 1/1. The DD reactions are presented with an Ar/alkane molar ratio of 1/1. **(b)** ΔG as a function of temperature for the $CO_2$-assistied oxidative dehydrogenation ($CO_2$-ODHE), dry reforming (DRE), and direct dehydrogenation (DDE) of ethane as well as the RWGS, reverse Boudouard reaction and the $CO_2$-ODH of propane and butane.

### 1.1.2 $CO_2$-ODH of light alkanes over oxide catalysts

Efforts for the $CO_2$-ODH of light alkanes prevalent in the literature have focused on metal oxide-based catalysts[3,20,24] composed of Cr[25,26,27], V[28,29,30], Ga[31,32], and to a lesser extent In[33,34] and Co[35,36,37]. Other less examined catalytic systems include Ca-doped $ThO_2$[38] and a nanostructured $CeO_2$ catalyst doped with CaO[39]. Commonalities among these materials include redox properties (with the exception of Ga) and choice of high surface area mixed oxides[40,41,42], mesoporous silica[43], or zeolites as the support.[44] Reducibility helps promote redox type mechanisms (i.e., Mars-van-Krevelen) where $CO_2$ reoxidizes the metal-oxide that provides lattice oxygen to assist in the hydrogen abstraction from the alkane (**Figure 1-2**).[45] The choice of support can shift catalytic

activity since it influences the acid-base properties and the distribution of the surface metal-oxide species.[46,47] In addition, the preparation methods can have a significant impact on performance due to correlations to dispersion and location (deposited on or in the framework) with metal-support interactions.

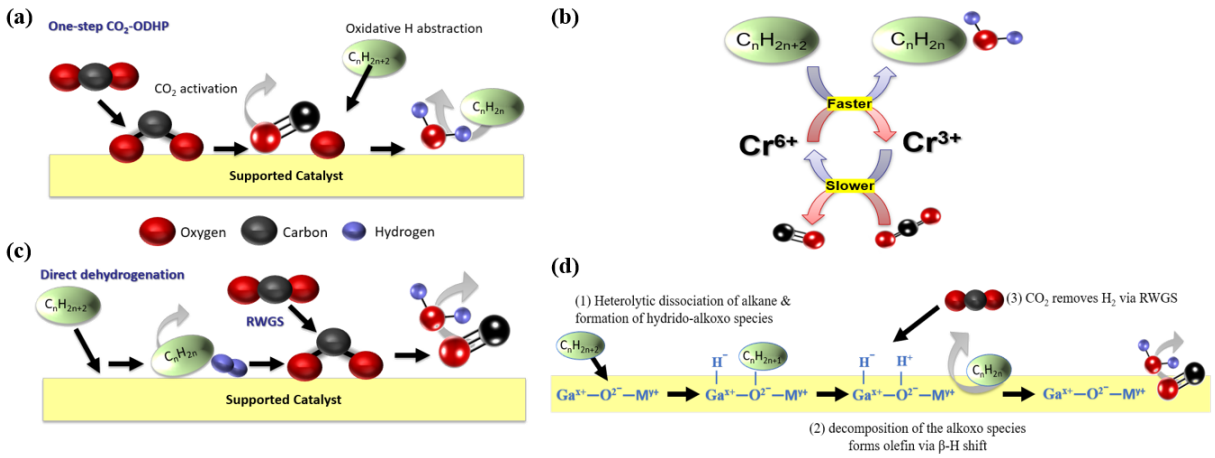


**Figure 1-2.** Graphical literature summary. **(a)** schematic of one-step $CO_2$-ODHP occurring over a catalytic system with strong reducibility, **(b)** typical one-step mechanism with understood kinetic overview of the $CO_2$-ODH reactions over Cr catalysts[23], **(c)** schematic of two-step mechanism with RWGS, and **(d)** two-step mechanism of $CO_2$-ODH over gallium oxide.[94]

### 1.1.2.a Cr-oxide based catalyst

Chromium catalysts achieve high ethane conversions at early reaction times, but overall $CO_2$ conversion is low and the catalysts are unstable, exhibiting short lifecycles due to coke formation from the interaction with allylic hydrogen from the alkanes.[48] Supports of choice that have shown good activity and selectivity for the chromium $CO_2$-ODH catalysts include $SiO_2$, siliceous MCM-41, and high silica H-ZSM-5.[49,23] While Cr species can also be incorporated into mesoporous structures, it has been shown that the increased activity is also accompanied by increased selectivity to undesired products due to a high ratio of inactive polychromate species.[50]

Various studies have attributed the activation of $CO_2$ over chromium-based catalysts to a $Cr^{6+}$ active center generated from a redox cycle with $Cr^{3+}$.[51,52,53,54,55] High $Cr^{6+}/Cr^{3+}$ ratios result in increased alkane conversion, but upon reaching a maximum threshold of Cr loading, no further improvement is observed.[56,57] Increased loading of Cr can result in larger particle sizes, uneven distributions, and a tendency to agglomerate leading to inactive polychromate species.[58,52,54] In addition, it has been suggested that there is a kinetic hindrance that prevents the efficacy even of highly dispersed chromia species.[45] Mimura et al. discovered that $Cr^{6+}$=O species dehydrogenate the alkane to the respective olefin at a rate that is faster compared to the re-oxidation of the resulting $Cr^{3+}$ via the reduction of $CO_2$ to CO.[26] Thus, even highly dispersed Cr catalysts with an appropriate metal loading deactivate due to the reduction of active chromium sites and eventual coke formation.[54] For instance, Asghari et al. evaluated Cr/MCM-41 nanocatalysts for the $CO_2$-ODH of ethane at 823 K and while the initial selectivity towards ethylene was 90%, the maximum conversion of ethane achieved was less than 8%.[57] After 12 hours on stream, the catalyst deactivated and only maintained 30% selectivity toward the olefin. Doping the catalyst with small amounts of Fe, Co, and Mn can improve ethylene selectivity since their presence contributes to a higher concentration of weak acid sites that facilitate ethane activation and lowers strong acid-base sites that favor reforming and cracking.[59] Similarly, to improve the low conversion of $CO_2$ over Cr-based $CO_2$-ODH catalysts, it was found that the addition of Ni to the $CrOx/SiO_2$ catalyst lowered the activation energy for the dissociation of $CO_2$. This is due to the strong chemisorption of $CO_2$ on Ni, leading to a bent configuration of the $CO_2$ molecule producing CO and activated atomic oxygen.[60] Despite these advances, Cr catalysts are not often implemented due to their short life cycles and high toxicity –which requires meticulous attention during the preparation, use, and disposal of the catalytic material.

### 1.1.2.b V-oxide based catalyst

Similar to Cr-based catalysts for $CO_2$-ODH, the activity of vanadium-based catalysts also largely depends on the support due to the correlations with reducibility, acid-base properties, and dispersion.[20,61] The $CO_2$-ODH of alkanes over vanadium-based catalysts was shown to be able to proceed via both a one-step oxidative dehydrogenation pathway and or through a two-step pathway with RWGS according to DFT calculations and isotopic experiments performed over a partially reduced vanadia dimer and a $WO_x$-$VO_x/SiO_2$ catalyst, respectively.[62,63] Since the majority of vanadium-based catalysts proceed via a Mars-van-Krevelen mechanism[64], increased participation of lattice oxygen from the support can improve olefin selectivity, such as in the case of $V_2O_5$ supported on $CeO_2$-$ZrO_2$ which was examined for the $CO_2$-ODH of butane.[65] The inclusion of $CeO_2$ as part of the mixed-oxide support increased oxygen mobility and oxygen vacancies while allowing the formation of $CeVO_4$. In general, mixed-oxide supports were shown to improve activity compared to single oxides due to increased acid-base bifunctionality.[66] In addition, it has been suggested that acidic $V_2O_5$ species interact weakly with acidic supports, leading to poorly dispersed $V_2O_5$ crystallites.[8] Several studies show that polymeric vanadium species lead to low olefin yield, again indicating that dispersion is a key factor in selectivity.[67,68,69] However, a DFT study performed for the various possible supported vanadia species (monomeric, dimeric, polymeric, compared to bulk) identified that the exact optimal size of vanadia differs with choice of support ($SiO_2$ vs. $CeO_2$). In addition, while there is no energetic preference for larger or smaller species, there is a kinetic preference for dimer species as they can perform hydrogen abstraction (the rate-determining step) faster.[70] Informed by these calculations, Xue et al. dispersed vanadium onto three-dimensional mesoporous silica nanospheres and achieved 90% propylene selectivity during 8 hour-cycles in which the conversion decreased from 60 to 20 %.[71] Up to eight

regeneration cycles were performed successfully while keeping the framework intact. The progress on vanadia catalysts is promising, but the presence of acidic sites that promote the cracking of olefins remains a challenge, and there are also health concerns regarding vanadium pentoxide dust.

### 1.1.2.c In- and Ga- based catalysts

Other studies for the $CO_2$-ODH of light alkanes mainly investigate the use of $In_2O_3$ and $Ga_2O_3$. Indium-based catalysts exhibit good redox characteristics ($In^{3+}$ to $In^0$), but cannot be re-oxidized by $CO_2$ under reaction conditions and therefore typically proceed via a two-step $CO_2$-ODH pathway.[33,34,72] Among $In_2O_3$-$MO_x$ binary mixed oxide catalysts (M: Al, Zn, Zr, Ti, Fe, Mg, Si, and Ce)[73], the $In_2O_3$-$Al_2O_3$ was found to have the highest propylene formation with good stability due to high indium dispersion. The combination with $CeO_2$ showed the lowest activity despite that the $In_2O_3$-$CeO_2$ catalyst has been shown to help promote the RWGS reaction.[74] Chen et al. discovered that an induction period of three hours is required to obtain considerable activity over an $In_2O_3$-$Al_2O_3$ catalyst, the increased activity was attributed to the formation of metallic indium active sites with increasing time on stream. Thus, like Cr- and V- catalysts, the support plays a crucial role in the dispersion of $In_2O_3$ and acid-base properties.

Unlike the catalysts mentioned above, gallium-based catalysts for $CO_2$-ODH do not exhibit strong redox properties because $Ga^{3+}$ is considerably stable. Ga is believed to promote the heterolytic dissociation of the alkane and efficiently activate $CO_2$.[45,75,76] Unsupported $Ga_2O_3$ was reported to have high initial propylene selectivity (30%), but after 10 minutes the selectivity decreased to less than 10% due to deactivation from coke formation.[77] Among a series of $Ga_2O_3$ supported $TiO_2$, $ZrO_2$, $\gamma$-$Al_2O_3$, $SiO_2$, and MgO it was found that only over $TiO_2$ did the presence of $CO_2$ enhance the activity and selectivity due to its unique ability to promote the reverse water

gas shift reaction.[12] While neither the activity nor selectivity of the $Ga_2O_3/ZrO_2$ catalyst was enhanced with $CO_2$, the stability did improve, and this was attributed to the ability to promote coke removal via the reverse Boudouard reaction. The suppressed activity of $Ga_2O_3$ supported on $ZrO_2$ and $Al_2O_3$ was a result of a competitive interaction between $CO_2$/alkane on Ga which displaces the alkane to unfavorable sites. Thus, the role of $CO_2$ over gallium-based catalysts is largely dependent on the support. Ga-oxide catalysts outperform Cr- and V-based catalysts, but still exhibit high susceptibility to coke, competitive interactions with $CO_2$, and low stability.

### 1.1.3 $CO_2$-ODH of light alkanes over bimetallic and carbide catalysts

Bimetallic systems often illustrate properties that are distinct from their parent metals, presenting an opportunity to design new catalysts with enhanced selectivity and stability.[78] Studies performed on $CO_2$ reduction with $H_2$[79] showed that reducible $CeO_2$ is a suitable support because it can store/release oxygen[80] and induce the direct C=O bond scission of $CO_2$[81], while also providing available lattice oxygen for coke suppression.[82,83] The combination of supported metals on $CeO_2$ should promote the effective activation of $CO_2$, while the choice of the bimetallic system should influence the selectivity.[39,84,85]

#### 1.1.3.a Case study: Reactions of $CO_2$ and ethane over $Fe_xNi_y$ catalysts

Myint et al. evaluated $CeO_2$ supported bimetallic $Co_3Pt_1$, $Co_3Mo_1$, $Ni_3Mo_1$, and $Fe_3Ni_1$ catalysts at 600°C, a temperature at which both the $CO_2$-ODHE and DRE pathways may occur, in order to identify which systems could selectively break the C-H bonds of ethane to produce ethylene.[86] Flow reactor experiments identified that $Fe_3Ni_1/CeO_2$ (1.4 wt.% Fe and 0.5 wt.% Ni) had promising selectivity to ethylene via oxidative C-H bond cleavage with improved stability compared to the monometallic catalysts. The DFT calculations were performed on mixed

FeNi(111) and Ni-terminated FeNi(111) surfaces to compare the thermodynamics of C-H and C-C bond cleavage pathways. On the mixed surface FeNi(111) surface, oxidative C-H bond cleavage was energetically more favorable than oxidative C-C bond cleavage, leading to higher production of $CH_2CH_2$*. On the Ni-terminated FeNi(111) surface, the oxidative C-C bond cleavage was more energetically favorable resulting in the production of CO*, $H_2O$, and $CH_3^*$. These DFT calculations were the first to suggest that the activity of the Fe-Ni system is influenced by structural variation and that in-depth verification using a combined approach of techniques was necessary. Subsequently, Yan et al. investigated the nature of the Fe-Ni active sites for the reactions of $CO_2$ and ethane to determine how to selectively control the scission of C-H bonds and therefore increase ethylene selectivity.[87] The following sections describe the combined approach of flow reactor experiments, in situ characterization, and DFT calculations that were used to identify and understand the inherent activity differences between the $Fe_xNi_y$ catalysts for the reactions of $CO_2$ and ethane.

### 1.1.3.b Flow reactor studies on the reactions of $CO_2$ and ethane over $Fe_xNi_y$ catalysts

Flow reactor studies of the $CO_2$-assisted oxidative dehydrogenation of ethane over a series of $CeO_2$-supported Fe-Ni catalysts with different Fe/Ni ratios were performed in a packed bed reactor at atmospheric pressure. The selectivity of $C_2H_4$ (via the $CO_2$-ODH pathway: selectively cleave the C-H bonds while preserving the C-C bond) varied from 1% to 78% by changing the Fe/Ni ratio, with the $Fe_3Ni_1/CeO_2$ catalyst showing the highest $C_2H_4$ selectivity. As a comparison, $Fe_1Ni_3/CeO_2$ showed the highest yield of CO (via the dry reforming pathway: efficiently break all the C-H and C-C bonds) with a selectivity of 99%. The selectivity of $C_2H_4$ for $Fe_3Ni_1/CeO_2$ and the selectivity of CO for $Fe_1Ni_3/CeO_2$ are almost unchanged at comparable $C_2H_6$ conversion under reaction-limited conditions, suggesting that the difference comes from the intrinsic kinetics

without the effect of the heat/mass transport. In order to make this conclusion more convincing, the selectivity vs. conversion plots for both catalysts was examined. For a given conversion with a given feed, the selectivity of $C_2H_4$ for $Fe_3Ni_1/CeO_2$ and the selectivity of CO for $Fe_1Ni_3/CeO_2$ remained stable at around 70% and 95%, respectively. All these results unequivocally illustrate that ethylene is the primary reaction product from the reaction of ethane with $CO_2$ over $Fe_3Ni_1/CeO_2$. Therefore, $Fe_3Ni_1/CeO_2$ was identified to be a promising catalyst for $CO_2$-ODHE, and $Fe_1Ni_3/CeO_2$ a reforming catalyst.

Additionally, the $Ni/CeO_2$ was an excellent DR catalyst while $Fe/CeO_2$ was a poor catalyst for both reactions; thus the distinct performance of $Fe_3Ni_1/CeO_2$ was inferred to be due to the formation of new active sites that originated from interactions between Fe and Ni. To verify this, control experiments using $Fe_3Ni_1/CeO_2$ and the physically-mixed sample ($Ni/CeO_2$ + $Fe/CeO_2$) were performed. The results confirmed that the interaction between Fe and Ni results in a structural variation of active sites, leading to significant differences in the reaction mechanism and product selectivity.

### 1.1.3.c In situ and ex situ characterization of $Fe_xNi_y$ catalysts

The structural information of $Fe_3Ni_1/CeO_2$ and $Fe_1Ni_3/CeO_2$ under reaction conditions can be revealed by in situ X-ray diffraction (XRD) experiments. Under reaction conditions, metallic Ni or FeNi alloy with face-centered cubic (FCC) structure was observed on both catalysts. To confirm whether it was metallic Ni or FeNi alloy, in situ XRD analysis for $Ni_3/CeO_2$ and $Fe_3/CeO_2$ was also performed. For $Ni_3/CeO_2$, the FCC structural metallic Ni with a lattice constant of 3.558 Å was observed. The corresponding lattice constants were calculated to be 3.575 ($Fe_3Ni_1/CeO_2$) and 3.570 Å ($Fe_1Ni_3/CeO_2$), indicating the formation of Ni-rich FeNi alloy with FCC structure.

In situ X-ray absorption near edge structure (XANES) spectra was collected to further determine the valence state of Ni and Fe on $Fe_3Ni_1/CeO_2$ and $Fe_1Ni_3/CeO_2$. The oxidation state of Ni in both catalysts was metallic Ni, while the Fe species in both catalysts exhibit similar near edge features between FeO and $Fe_3O_4$ (closer to $Fe_3O_4$) under reaction conditions. The detailed extended X-ray absorption fine structure (EXAFS) fitting results revealed that the coordination numbers (C.N.) of Ni-Ni(Fe) on $Fe_3Ni_1/CeO_2$ and $Fe_1Ni_3/CeO_2$ are 10.4 and 11.3, indicating metallic FeNi alloy resided in the form of particles with diameters of 2.5-4.0 nm (based on hemisphere FCC models). Fe-Ce bonding at 3.6-3.7 Å was observed on both $Fe_3Ni_1/CeO_2$ and $Fe_1Ni_3/CeO_2$, indicating a strong interaction between Fe and the $CeO_2$ support. Combined with the small coordination numbers for the Fe-O bonding, the existence of Fe-Ce bonding suggested that the oxidized Fe species tend to form thin layers on $CeO_2$.

To confirm the formation of amorphous $FeO_x$ thin layers on $CeO_2$, ex situ scanning transmission electron microscopy with electron energy loss spectroscopy (STEM-EELS) analysis was conducted on the spent $Fe_3Ni_1/CeO_2$ and $Fe_1Ni_3/CeO_2$ catalysts. The presence of a $FeO_x$ layer was confirmed by the high-resolution STEM imaging, which showed that a layer of 2 nm amorphous $FeO_x$ formed on the $CeO_2$ particles of $Fe_3Ni_1/CeO_2$. To further verify this conclusion, EELS line scan analysis of Fe species was conducted on the two samples. The EELS line scan profiles of Fe species showed the presence of a thin layer of $FeO_x$ on $CeO_2$ particles in $Fe_3Ni_1/CeO_2$ while this layer was absent in $Fe_1Ni_3/CeO_2$. Combined with the results revealed by the in situ characterization, it can be concluded that Fe (in the form of amorphous $FeO_x$) is preferred to exist between metal particles and the $CeO_2$ support (as the Fe-Ce bonding was found on both catalysts) under reaction conditions.

For $CeO_2$-supported Ni catalysts, the reducible oxide, $CeO_2$, helps enable facile $CO_2$ dissociation and the production of *O species on the surface. The produced *O species reacts with carbon originated from the ethane decomposition on the metallic Ni particles at the metal-support interfaces. When a small amount of Fe is added to $Ni_3/CeO_2$ (i.e., $Fe_1Ni_3/CeO_2$), although $FeO_x$ is preferred to exist underneath the predominantly Ni particles, the Ni-$CeO_x$ interfacial sites still dominate the conversion of ethane with $CO_2$, maintaining the CO selectivity at a high level (over 95%). The Ni-$CeO_x$ interfaces (**Figure 1-3**) are identified as the most likely active sites for dry reforming of ethane with $CO_2$ (effective C-H and C-C bonds scission of $C_2H_6$ to produce synthesis gas) due to the highest activity observed in $Fe_1Ni_3/CeO_2$. When a large amount of Fe is introduced (i.e., $Fe_3Ni_1/CeO_2$), the amorphous $FeO_x$ spreads far enough to form the Ni-$FeO_x$ interfacial sites on the perimeter of Ni particles, likely replacing the Ni-$CeO_x$ interfacial sites. The Ni-$FeO_x$ interfaces are identified as the most likely active sites for $CO_2$-assisted dehydrogenation of ethane (selective C-H bond cleavage of $C_2H_6$ to produce $C_2H_4$).

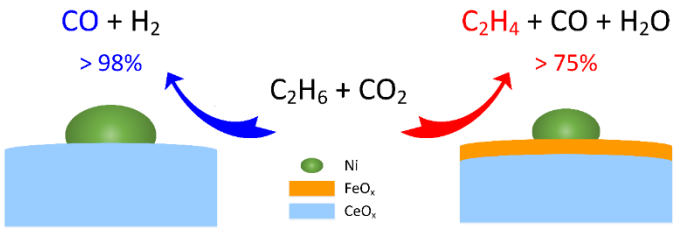


**Figure 1-3.** Schematic showing the structure of Ni-$CeO_x$ interfacial sites for dry reforming of ethane with $CO_2$ (effective C-H and C-C bonds scission of $C_2H_6$ to produce synthesis gas) and Ni-$FeO_x$ interfacial sites for $CO_2$-assisted dehydrogenation of ethane (selective C-H bond cleavage of $C_2H_6$ to produce $C_2H_4$).

### 1.1.3.d DFT calculations on the reactions of $CO_2$ and ethane over the Fe-Ni system

To gain a better understanding of the active sites for tuning the selectivity of $CO_2$ + ethane reactions on FeNi bimetallic catalysts, DFT calculations were performed on FeNi model surfaces to investigate the potential reaction pathways for the oxidative C-H bond cleavage (dehydrogenation) leading to $*CH_2CH_2 + H_2O(g)$ and C-C bond scission (reforming) leading to $*CH_3 + *CO + H_2O(g)$. The various FeNi models were considered to account for Ni/Fe segregation on the surface and the possibility of formation of oxidized Fe as observed in the experiment. Furthermore, the model surfaces were partially covered by *O due to the direct $*CO_2$ dissociation on the reduced $CeO_2$ support or the metal-oxide interfaces as observed in the $CO_2$ pulse experiments.

The DFT calculated enthalpy change in **Figure 1-4** suggests that the first step along the C-H and C-C bond cleavage pathways are thermodynamically competitive on Ni(111), Ni-terminated-$Ni_3Fe$(111) and bulk-terminated-$Ni_3Fe$(111). In contrast, the C-H bond cleavage pathway is thermodynamically more favorable than the C-C bond cleavage on $FeO_x$/Ni(111). The activation energies ($E_a$) of the elementary steps in **Figure 1-4** were calculated to further corroborate the thermodynamic preference of FeNi model surfaces for C-H and C-C bond cleavage. *O assisted first C-H bond scission of ethane is highly activated on all surfaces and is likely the most difficult step in the oxidative C-H and C-C bond cleavage of ethane. On Ni(111), the *O insertion reaction ($*CH_3CH_2 + *O \rightarrow *CH_3CH_2O + *$) along the C-C bond cleavage pathway (reaction energy ($\Delta E$) = -0.14 eV and $E_a$ = 0.44 eV) is thermodynamically and kinetically more favorable than the oxidative dehydrogenation reaction ($*CH_3CH_2 + *O \rightarrow *CH_2CH_2 + *OH$) along the C-H bond cleavage pathway ($\Delta E$ = 0.09 eV and $E_a$ = 0.97 eV). The formed $*CH_3CH_2O$ undergoes two facile dehydrogenation reactions: $*CH_3CH_2O + * \rightarrow *CH_3CHO + *H$ ($\Delta E$ = 0.29 eV and $E_a$ = 0.92 eV)

and $*CH_3CHO + * \rightarrow *CH_3CO + *H$ ($\Delta E$ = -0.48 eV and $E_a$ = 0.35 eV) to produce $*CH_3CO$, which facilitates the C-C bond cleavage to form $*CH_3 + *CO$ ($\Delta E$ = -0.48 eV and $E_a$ = 1.01 eV). The favorable C-C bond cleavage via $*CH_3CH_2O$ and $*CH_3CO$ intermediates shows that the oxidative C-C bond cleavage is preferred on Ni(111). On Ni-terminated-$Ni_3Fe$(111), the *O insertion reaction to form $*CH_3CH_2O$ is comparable with the oxidative dehydrogenation reaction to form $*CH_2CH_2$. Hence, Ni-terminated-$Ni_3Fe$(111) is expected to promote both the C-C and the C-H bond cleavage. On the other hand, on bulk-terminated-$Ni_3Fe$(111), the activation energy of oxidative dehydrogenation reaction is 0.16 eV lower in barrier than the *O insertion reaction. As a result, bulk-terminated-$Ni_3Fe$(111) is predicted to promote the C-H bond cleavage slightly more than the C-C bond cleavage, suggesting that the presence of Fe on the surface is essential to selectively facilitate the C-H bond cleavage of ethane to produce $CH_2CH_2$. Furthermore, the DFT results on $FeO_x$/Ni(111) show that the oxidative dehydrogenation reaction ($\Delta E$ = -0.13 eV and $E_a$ = 1.08 eV) is more favorable than the *O insertion reaction ($\Delta E$ = -0.04 eV and $E_a$ = 1.67 eV). Thus, in agreement with the experimental results, the DFT results predict that the Ni-$FeO_x$ interface should be active for the dehydrogenation of ethane.

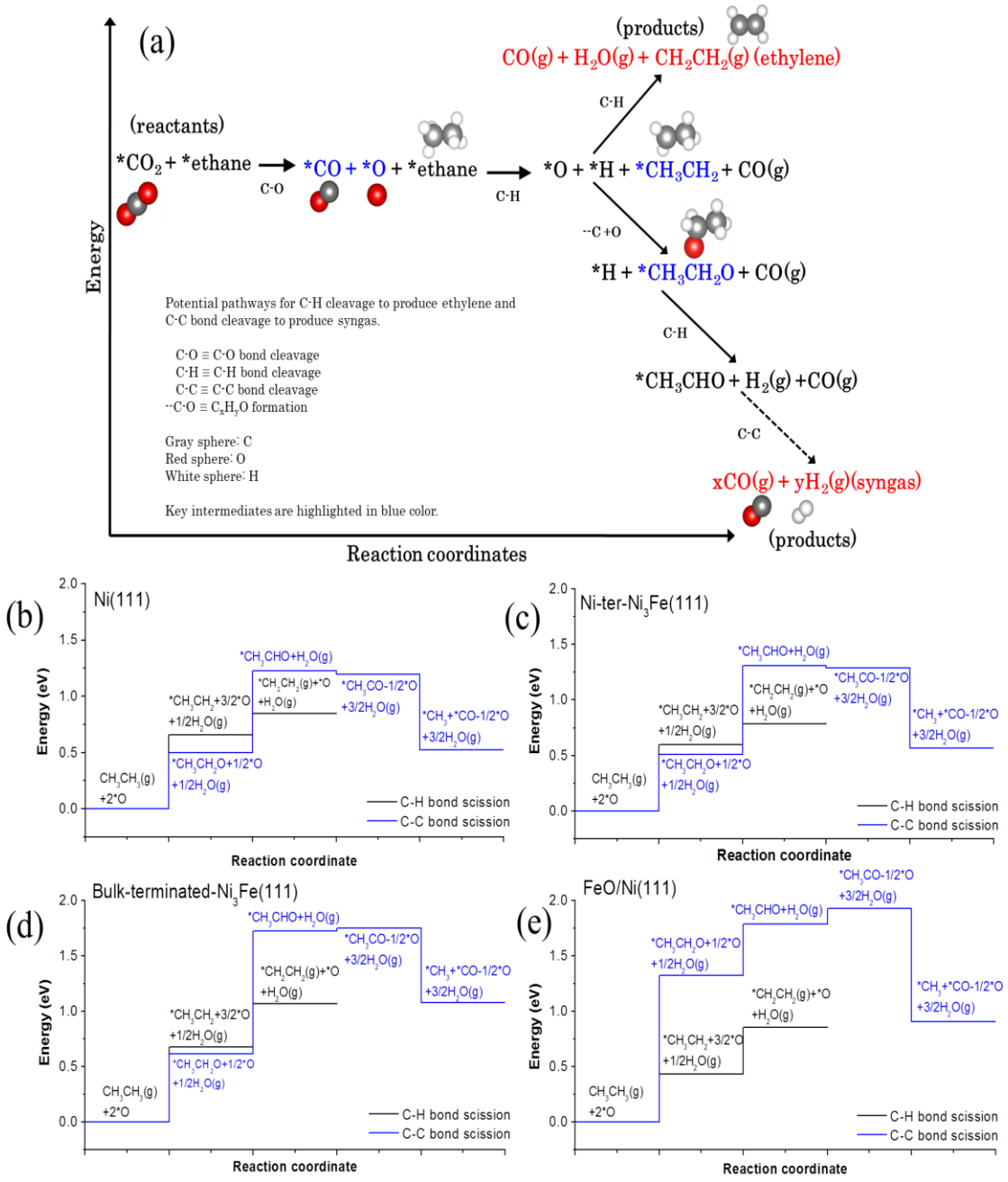


**Figure 1-4.** Potential reaction pathways for C-H and C-C bond cleavage of ethane in the presence of *O generated due to $*CO_2$ dissociation. DFT calculated energy profiles of oxidative dehydrogenation (C-H bond cleavage) and dry reforming (C-C bond scission) of ethane. **(b)** Ni(111). **(c)** Ni-terminated-$Ni_3Fe$(111). **(d)** bulk-terminated-$Ni_3Fe$(111). **(e)** $FeO_x$/Ni(111).

### 1.1.3.e $CO_2$-assisted oxidative dehydrogenation of ethane over carbide-based catalysts

$Mo_2C$ is a highly attractive choice for the $CO_2$-ODH reactions because it has shown high activity for $CO_2$ and alkane activation, oxygen mobility, and Pt-like electronic properties.[88,89,90,91,92]. Porosoff et al. identified that $Mo_2C$ and $Mo_2C$ supported on $\gamma$-$Al_2O_3$ showed enhanced selectivity toward ethylene production via the $CO_2$ oxidative dehydrogenation pathway compared to $Pt/CeO_2$ which favored the production of CO via the dry reforming pathway.[93] The DFT calculated energy profiles of reforming and oxidative dehydrogenation of ethane over a $Mo_2C(001)$ surface illustrated that oxidative C-C bond cleavage is energetically more favorable and forms $CH_2CH_2$* and $H_2$(g). The DFT calculations demonstrated that the $Mo_2C(001)$ surface has a very strong affinity to adsorb atomic oxygen. This in return makes the reaction of *O with $C_xH_y$ to form oxygenates, one of the key intermediates along C-C bond cleavage pathway, difficult. However, the strongly bound *O would promote selective C-H bond cleavage leading to ethylene as the primary product. Flow reactor experiments confirmed the predictions of the DFT calculations as the $Mo_2C$ catalyst showed inherent activity for ethylene production with 2% $C_2H_6$ conversion and 60% selectivity to $C_2H_4$. Flow reactor experiments also identified that the activity of unsupported $Mo_2C$ and supported $Mo_2C$ is different. $Mo_2C$ supported on $CeO_2$ shows lower activity than unsupported $Mo_2C$, but over the more acidic $\gamma$-$Al_2O_3$ support the activity is slightly improved. The low steady-state activity of $Mo_2C/CeO_2$ was attributed to the high initial intrinsic activity of $CeO_2$ and $Mo_2C$ toward $CO_2$ bond scission which leaves an excess of adsorbed *O on the catalyst surface causing the $Mo_2C/CeO_2$ surface to deactivate via complete oxidation. The $Mo_2C/\gamma$-$Al_2O_3$ catalyst also suffers from deactivation because the produced ethylene has high binding energy leading to coke formation through ethylene decomposition and or polymerization. In situ XANES studies showed that while $CO_2$ is necessary to form an oxycarbide phase, which

facilitates ethane dehydrogenation, excessive amounts of $CO_2$ also leads to complete deactivation. Catalyst regeneration is possible by co-feeding 5 vol% $H_2$ with the reactants or by performing a post-reaction treatment with $H_2$. Future studies are required to determine the effect of acidity on the reaction pathways of $CO_2$ and ethane over $Mo_2C/\gamma\text{-}Al_2O_3$.

Yao et al. investigated the surface properties that determine the selectivity of $Mo_2C$ catalysts for the $CO_2$-ODH of ethane.[94] Oxygen modification of the $Mo_2C$ catalyst inhibits the cleavage of the C-C bond in ethane and enhances the production of ethylene. Furthermore, the addition of Fe accelerates the formation of surface oxygen which in turn increases the ethylene yield and stability.

### 1.1.3.f Reactions of $CO_2$ with propane

A similar approach as described in the above sections was applied to the parallel investigation for the reactions of $CO_2$ with propane. The reduction of $CO_2$ with propane is a significant component of the experimental and theoretical work conducted for this dissertation; therefore, additional details are provided in **Chapter 3:** To summarize, steady-state flow reactor studies conducted at 823 K identified $Fe_3Ni_1/CeO_2$ and $Ni_3Pt_1/CeO_2$ as promising catalysts for the $CO_2$-ODH and DR of propane, respectively (**Figure 1-5**).[95] $Fe_3Ni_1/CeO_2$ was found to exhibit 58% propylene selectivity with good stability, while $Ni_3Pt/CeO_2$ was a highly active DRP catalyst with 96% selectivity toward CO. Further confirmation of selectivity profiles over the two bimetallic catalysts was provided by CO selectivity vs. conversion plots. For $Ni_3Pt_1$, the y-intercept of CO selectivity was 97%, suggesting it is a typical reforming catalyst. While for $Fe_3Ni_1$, the y-intercept of CO selectivity was found to be 22.2%. Additionally, the total amount of CO produced from $Fe_3Ni_1$ exceeded the contributions of $C_3H_6 + H_2O$ (from one-step $CO_2$-ODH pathway products and subtracting contributions from RWGS) indicating that CO was also generated via the reverse

Boudouard reaction and or some over-oxidation of olefins/lighter components. Unlike oxidation with $O_2$, which produces additional $CO_2$ upon over-oxidation, the $CO_2$-ODH reaction can achieve a net reduction of$CO_2$ and produce useful CO in the over-oxidation process.

The EXAFS fitting suggested the presence of an inserted oxygen through Fe-O-Fe bonds as well as Fe-O bonds in the $Fe_3Ni_1$ catalyst. Informed by the in situ XAS measurements, DFT calculations were performed on both the bulk $Fe_3Ni(111)$ surface and the FeO/Ni(111) interface. The DFT calculations illustrated that energetically both the $Fe_3Ni(111)$ surface and FeO/Ni(111) interface should favor C–H bond scission for the $CO_2$-ODHP pathway, whereas the Pt-terminated $Ni_3Pt(111)$ surface should favor C–C bond cleavage for the DRP pathway. This information was provided via the 'change in energy' profiles that are attained by calculating the binding energies of several possible surface intermediates. The binding energy calculations also illustrated that while the binding configuration of all intermediates was similar on both the $Fe_3Ni(111)$ and Pt-terminated $Ni_3Pt(111)$ surfaces, all the intermediates adsorbed more strongly to the $Fe_3Ni(111)$ surface. Furthermore, it was identified that one of the key differences between the two surfaces was the interaction between $*C_xH_y$ species and *O. Over the Pt-terminated $Ni_3Pt(111)$ surface the *O reacted with $*C_xH_y$ to form an oxygenated $*C_xH_yO$ intermediate, which led to the production of reforming products. Conversely, over the $Fe_3Ni(111)$ surface the more stable *O remained on the surface, facilitating selective C-H bond scission and thus the production of olefin. Overall, via a combined approach of flow reactor experiments (including kinetic measurements), in- and ex-situ characterization, and DFT calculations it was possible to identify and further understand inherent activity toward the $CO_2$-ODH pathway over DR.

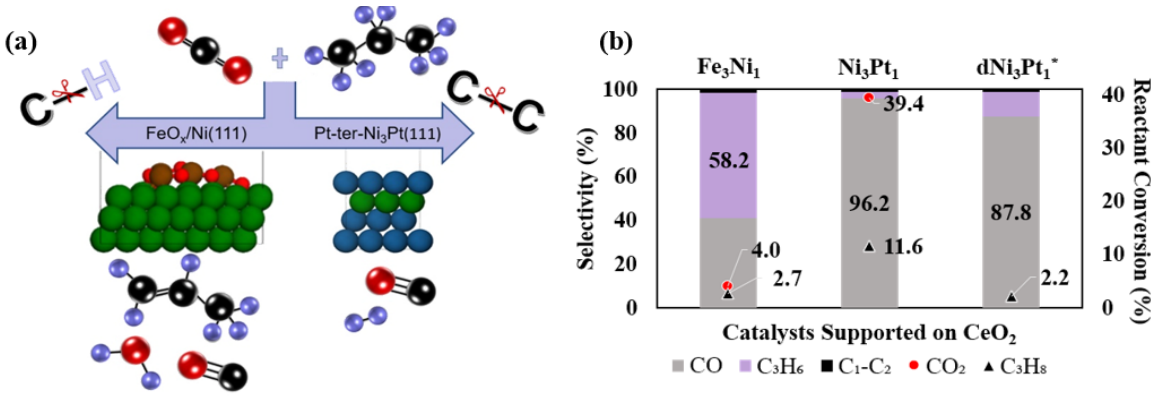


**Figure 1-5.** Reduction of $CO_2$ with propane. **(a)** Schematic with DFT constructed surfaces illustrating the preferred reaction pathway and products of $Fe_3Ni_1$ and $Ni_3Pt_1$ represented as the FeOx/Ni(111) interface and the Pt-ter-$Ni_3Pt$(111) surface, respectively. **(b)** Flow reactor results of selectivity and conversion for $Fe_3Ni_1$, $Ni_3Pt_1$, and diluted $Ni_3Pt_1$.

### 1.1.3.g Reactions of $CO_2$ with butane

The investigation for the reaction of $CO_2$ and butane at 873 K also utilized Fe-Ni/$CeO_2$ catalysts and the findings are consistent with the trend observed over $C_2$ and $C_3$.[96] Flow reactor experiments illustrated that $Fe_3Ni_1/CeO_2$ favors the production of 1,3 butadiene while the $Fe_1Ni_3/CeO_2$ catalyst favors the production of synthesis gas. The effect of oxide supports was evaluated for the $Fe_3Ni_1$ catalyst and illustrated that highly reducible supports such as $CeO_2$ and $CeO_2$-$ZrO_2$ promote the production of 1,3-butadiene, whereas $ZrO_2$ suppressed oxidative dehydrogenation activity. Deactivation patterns were investigated via TGA and in situ XRD. The findings revealed that $Fe_3Ni_1/CeO_2$ did not form a significant amount of coke or metal clusters on the surface under reaction conditions, consistent with the results obtained for the reactions of $CO_2$ + $C_3$. The $Fe_3Ni_1/ZrO_2$ catalyst showed significantly more coke production than when supported on $CeO_2$.

In situ XANES measurements for the Fe-Ni/$CeO_2$ catalysts demonstrated that the Ni species were metallic whereas the Fe mainly existed as $FeO_x$. The linear combination fitting performed for the $Fe_1Ni_3$ catalyst indicated that all Ni species were reduced to $Ni^0$, but only a third of the Fe species were reduced to $Fe^0$, and the remaining fraction was in the form of $Fe_2O_3$. For the $Fe_3Ni_1$ catalyst, 90% of the Ni species was metallic with a mixed composition of metallic Fe, FeO, $FeO_4$, and $Fe_2O_3$ in the amounts of 19, 7, 28, and 44%, respectively. DFT calculations further compared the ODH and DR pathways over Ni(111) and FeOx/Ni(111) surfaces and suggested that Ni(111) should favor C-C bond scission while FeOx/Ni(111) could promote the C-H bond cleavage. Over the Ni(111) surface, the initial step along C-C bond cleavage was more favorable than the corresponding step toward C-H bond scission. Over the FeO/Ni(111) interface, the initial steps along C-H and C-C bond cleavage were competitive, but the subsequent two steps along C-H bond scission were energetically more favorable and led to the formation of $*CH_2CHCHCH_2$. The study of Fe-Ni/$CeO_2$ catalysts for the $CO_2$-ODH of butane was able to provide insight into the effect of oxide supports through flow reactor studies. Characterization identified that two significant deactivation pathways, coking and phase transformation, did not occur when the Fe-Ni system is supported on $CeO_2$ for the $CO_2$-ODHB reaction. Finally, by integrating flow reactor and characterization to produce informative DFT surfaces/interfaces understanding of inherent activity for the C-H bond scission pathway was achieved.

### 1.1.4 Overview

The tandem reactions of $CO_2$ reduction and $CO_2$-ODH of light alkanes have the potential to influence olefin production while consuming underutilized fractions of shale gas and reducing anthropogenic $CO_2$ emissions. This reduction chemistry presents several challenges such as the need for a selective bifunctional catalytic material that can activate $CO_2$ and assist in the

transformation of the alkane to the respective olefin at a temperature range where side reactions are highly favorable. The reactions of $CO_2$ with alkanes may occur through two distinct pathways, $CO_2$-ODH or DR, simultaneously at temperatures above 823 K. Due to the toxicity and instability of previously examined catalytic systems in the literature, there is a need for the development of environmentally benign $CO_2$-ODH catalysts that are highly active, stable, and selective. In this Chapter, we discuss a combined approach of flow reactor experiments, in situ characterization, and DFT calculations to help create a design platform for catalysts that are inherently active and selective for the $CO_2$-ODH reaction of light alkanes.

## 1.2 Dissertation outline and approach

This introductory chapter describes the advantages of using light alkanes as $CO_2$ reduction feedstock. Thermodynamic calculations illustrate that at temperatures $\geq$ 823 K both the $CO_2$-assisted oxidative dehydrogenation and dry reforming reactions may occur simultaneously to produce olefins or synthesis gas. Both pathways are effective $CO_2$ reduction strategies that provide value-added products. Thus, it is highly desirable to identify catalytic systems that are inherently active and selective for each reaction pathway by utilizing the approach discussed in **Chapter 1:** of combining flow reactor experiments, in situ characterization, and DFT calculations to gain insight and understanding as to which bimetallic catalytic systems can selectively cleave C-H bonds to produce olefins or effectively break all the C-C and C-H bonds to produce reforming products. **Chapter 3:** focuses on using the combined approach for the reactions of $CO_2$ and propane and identifies non-precious $Fe_3Ni_1$ and precious $Ni_3Pt_1$ supported on $CeO_2$ as promising catalysts for the $CO_2$-ODHP and DRP reactions, respectively. **Chapter 4:** evaluates a series of bimetallic catalysts, Pt and Pd with Fe, Ni, and Co as well as non-precious combinations of Fe-

Co, Fe-Ni, and Co-Ni supported on $CeO_2$. Currently, there are no other investigations available in the literature that examines bimetallic catalysts for the reduction of $CO_2$ with propane in a temperature range at which both $CO_2$-ODHP and DRP reactions may occur or identifies catalysts that are inherently active and selective for one reaction pathway or the other. In addition to the $Ni_3Pt_1$ catalyst for DRP identified in **Chapter 3:**, the Co-Ni catalysts are shown to be a non-precious metal alternative with good activity, stability, and selectivity to producing CO. Further flow reactor studies on the $Fe_3Ni_1$ and $Ni_3Pt_1$ bimetallic systems with other oxide supports ($\gamma$-$Al_2O_3$, $ZrO_2$, $TiO_2$, and $SiO_2$) examined the effects of strong support metal interactions, surface defects, inert surfaces, and irreducibility on both the $CO_2$-ODHP and DRP pathway.

Reactants that can effectively reduce $CO_2$ are scare, but as described in **Chapters 1, 3, and 4**, $CO_2$ reduction with light alkanes is promising. However, the subsequent separation of gas phase products from the reactions of $CO_2$ and light alkanes is challenging. Commonalities from the $CO_2$-ODH of light alkanes may extend to a third route, a one-step $CO_2$-assisted oxidative dehydrogenation and aromatization reaction ($CO_2$-ODA) scheme. Expanding the library of raw materials used to produce aromatics is of significant interest, especially when using abundant and inexpensive fractions of shale gas. **Chapter 5**: evaluates the $CO_2$-assisted oxidative dehydrogenation and aromatization as well as the direct dehydrogenation and aromatization (DDA) of ethane over unmodified as well as Ga and phosphorous modified ZSM-5 catalysts in flow reactor studies at 873 K and atmospheric pressure. The incorporation of phosphorous improves the hydrothermal stability of Ga/ZSM-5, reduces coke formation, and increases the formation of liquid aromatics via the $CO_2$-assisted tandem reactions of oxidative dehydrogenation and aromatization compared to direct dehydrogenation and aromatization of ethane. DFT calculations provide fundamental insight into the mechanisms for ethane transformation to

aromatics and identify the role of $CO_2$ in promoting the production of aromatics. Finally, **Chapter 6:** offers conclusions and future recommendations to improve $CO_2$-ODH and $CO_2$-ODA catalysts.

## 1.3 Acknowledgements

E.G. acknowledges the U.S. National Science Foundation Graduate Research Fellowship Program: DGE-16-44869 and the Gates Millennium Scholarship Foundation. E.G. would like to acknowledge Dr. Binhang Yan and Dr. Shyam Kattel for their discussions and revisions during the writing of this chapter.

## 1.4 References


1. Speight JG. Liquid Fuels from Natural Gas. In: Lee S, Speight JG, Loyalka SK, eds. *Handbook of Alternative Fuel Technologies*. 2nd ed. Taylor and Francis Group; 2015:162.

2. Tang P, Zhu Q, Wu Z, Ma D. Methane activation: the past and future. *Energy Environ Sci*. 2014;7:2580-2591. doi:10.1039/C4EE00604F

3. Kawi S, Kathiraser Y. $CO_2$ as an oxidant for high-temperature reactions. *Front Energy Res*. 2015;3:1-13. doi:10.3389/fenrg.2015.00013

4. Plotkin JS. The Propylene Gap: How Can It Be Filled? ACS News Industrial Chemistry & Engineering. https://www.acs.org/content/acs/en/pressroom/cutting-edge-chemistry/the-propylene-gap-how-can-it-be-filled.html. Published September 2015.

5. IHS Markit. *Propylene, Ethylene, Butadiene- Chemical Economics Handbook*.; 2018.

6. Global Efficiency Intelligence. Chemical Industry's Energy Use and Emissions. https://www.globalefficiencyintel.com/new-blog/2018/chemical-industrys-energy-use-emissions. Published 2018.

7. U.S. Energy Information Administration. What is the volume of world natural gas reserves ? https://www.eia.gov/tools/faqs/faq.php?id=52&t=8. Published 2019.

8. Mukherjee D, Park SE, Reddy BM. $CO_2$ as a soft oxidant for oxidative dehydrogenation reaction: An eco benign process for industry. *J* $CO_2$ *Util*. 2016;16:301-312. doi:10.1016/j.jcou.2016.08.005

9. Aresta M, Dibenedetto A, Quaranta E. State of the art and perspectives in catalytic processes for $CO_2$ conversion into chemicals and fuels: The distinctive contribution of chemical catalysis and biotechnology. *J Catal*. 2016. doi:10.1016/j.jcat.2016.04.003

10. Álvarez A, Borges M, Corral-Pérez JJ, et al. $CO_2$ Activation over Catalytic Surfaces. *ChemPhysChem*. 2017;18(22):3135-3141. doi:10.1002/cphc.201700782

11. Van Santen R a., Tranca I, Hensen EJM. Theory of surface chemistry and reactivity of reducible oxides. *Catal Today*. 2015;244:63-84. doi:10.1016/j.cattod.2014.07.009

12. Xu B, Zheng B, Hua W, Yue Y, Gao Z. Support effect in dehydrogenation of propane in the presence of $CO_2$ over supported gallium oxide catalysts. *J Catal*. 2006;239(2):470-477. doi:10.1016/j.jcat.2006.02.017

13. Osaki T, Mori T. Kinetics of the reverse-Boudouard reaction over supported nickel catalysts. *React Kinet Catal Lett*. 2006;89(2):333-339. doi:10.1007/s11144-006-0145-9

14. Wang S, Zhu ZH. Catalytic Conversion of Alkanes to Olefins by Carbon Dioxide Oxidative Dehydrogenation A Review. *Energy and Fuels*. 2004;18:1126-1139. doi:10.1021/ef0340716

15. Gärtner CA, Veen AC Van, Lercher JA. Oxidative Dehydrogenation of Ethane : Common Principles and Mechanistic Aspects. *ChemCatChem*. 2013;5:3196-3217. doi:10.1002/cctc.201200966

16. Védrine JC. Heterogenous Partial (amm)Oxidation Dehydrogenation Catalysis on Mixed Metal Oxides. *Catalysts*. 2016;6(22):1-26. doi:10.3390/catal6020022

17. Grabowski R. Kinetics of Oxidative Dehydrogenation of $C_2$ - C3 Alkanes on Oxide Catalysts Kinetics of Oxidative Dehydrogenation of $C_2$ -C3 Alkanes on Oxide Catalysts. *Catal Rev*. 2006;48(02):199-268. doi:10.1080/01614940600631413

18. Cavani F, Trifirò F. The oxidative dehydrogenation of ethane and propane as an alternative way for the production of light olefins. *Catal Today*. 1995;24(3):307-313. doi:10.1016/0920-5861(95)00051-G

19. Ansari MB, Park S-E. Carbon dioxide utilization as a soft oxidant and promoter in catalysis. *Energy Environ Sci*. 2012;5(11):9419-9437. doi:10.1039/$C_2$ee22409g

20. Atanga MA, Rezaei F, Jawad A, Fitch M, Rownaghi AA. Oxidative dehydrogenation of propane to propylene with carbon dioxide. *Appl Catal B Environ*. 2018;220:429-445. doi:10.1016/j.apcatb.2017.08.052

21. Du X, Yao B, Gonzalez-Cortes S, et al. Catalytic dehydrogenation of propane by carbon dioxide: A medium-temperature thermochemical process for carbon dioxide utilisation. *Faraday Discuss*. 2015;183:161-176. doi:10.1039/c5fd00062a

22. Zangeneh FT, Taeb A, Gholivand K, Sahebdelfar S. Thermodynamic Equilibrium Analysis of Propane Dehydrogenation with Carbon Dioxide and Side Reactions. *Chem Eng Commun*. 2016;203:557-565. doi:10.1080/00986445.2015.1017638

23. Michorczyk P, Ze K, Niekurzak R, Ogonowski J. Dehydrogenation of propane with $CO_2$ – a new green process for propene and synthesis gas production. *Polish J Chem Technol*. 2012;14(4):77-82.

24. Krylov O V., Mamedov AK, Mirzabekova SR. The regularities in the interaction of alkanes with $CO_2$ on oxide catalysts. *Catal Today*. 1995;24(3):371-375. doi:10.1016/0920-5861(95)00061-J

25. Mimura N, Takahara I, Inaba M, Okamoto M, Murata K. High-performance Cr/H-ZSM-5 catalysts for oxidative dehydrogenation of ethane to ethylene with $CO_2$ as an oxidant. *Catal Commun*. 2002;3:257-262. doi:10.1016/S1566-7367(02)00117-6

26. Mimura N, Okamoto M, Yamashita H, Oyama ST, Murata K. Oxidative dehydrogenation of ethane over Cr/ZSM-5 catalysts using $CO_2$ as an oxidant. *J Phys Chem B*. 2006;110:21764-21770. doi:10.1021/jp0619661

27. Deng S, Li H, Li S, Zhang Y. Activity and characterization of modified Cr2O3/ZrO2 nano-composite catalysts for oxidative dehydrogenation of ethane to ethylene with $CO_2$. *J Mol Catal A Chem*. 2007;268:169-175. doi:10.1016/j.molcata.2006.12.033

28. Rajua G, Reddy BM, Park SE. Utilization of carbon dioxide in oxidative dehydrogenation reactions. *Indian J Chem-Sect A Inorganic, Phys Theor Anal Chem*. 2012;51(9-10):1315-1324.

29. Wei C, Xue F, Miao C, et al. Dehydrogenation of Isobutane with Carbon Dioxide over SBA-15-Supported Vanadium Oxide Catalysts. *Catalysts*. 2016;6:171. doi:10.3390/catal6110171

30. Sun G, Huang Q, Huang S, et al. Vanadium Oxide Supported on MSU-1 as a Highly Active Catalyst for Dehydrogenation of Isobutane with $CO_2$. *Catalysts*. 2016;6:41. doi:10.3390/catal6030041

31. Shen Z, Liu J, Xu H, Yue Y, Hua W, Shen W. Dehydrogenation of ethane to ethylene over a highly efficient Ga2O3/HZSM-5 catalyst in the presence of $CO_2$. *Appl Catal A Gen*. 2009;356:148-153. doi:10.1016/j.apcata.2008.12.038

32. Koirala R, Buechel R, Krumeich F, Pratsinis SE, Baiker A. Oxidative Dehydrogenation of Ethane with $CO_2$ over Flame-Made Ga-Loaded TiO2. *ACS Catal*. 2015;5:690-702. doi:10.1021/cs500685d

33. Chen M, Xu J, Cao Y, He HY, Fan KN, Zhuang JH. Dehydrogenation of propane over In2O3-Al 2O3 mixed oxide in the presence of carbon dioxide. *J Catal*. 2010;272(1):101-108. doi:10.1016/j.jcat.2010.03.007

34. Chen M, Wu JL, Liu YM, et al. Study in support effect of In2O3/MOx (M = Al, Si, Zr) catalysts for dehydrogenation of propane in the presence of CO 2. *Appl Catal A Gen*. 2011;407:20-28. doi:10.1016/j.apcata.2011.08.018

35. Zhang X, Ye Q, Xu B, He D. Oxidative dehydrogenation of ethane over Co-BaCO3 catalysts using $CO_2$ as oxidant: Effects of Co-promoter. *Catal Letters*. 2007;117:140-145. doi:10.1007/s10562-007-9122-9

36. Koirala R, Buechel R, Pratsinis SE, Baiker A. Silica is preferred over various single and mixed oxides as support for $CO_2$-assisted cobalt-catalyzed oxidative dehydrogenation of ethane. *Appl Catal A Gen*. 2016;527:96-108. doi:10.1016/j.apcata.2016.08.032

37. Zhu J, Qin S, Ren S, Peng X, Tong D, Hu C. Na2WO4/Mn/SiO2 catalyst for oxidative dehydrogenation of ethane using $CO_2$ as oxidant. *Catal Today*. 2009;148:310-315. doi:10.1016/j.cattod.2009.07.074

38. Baidya T, Vegten N Van, Baiker A. Selective conversion of ethane to ethene via oxidative dehydrogenation over Ca-doped ThO2 Using $CO_2$ as oxidant. *Top Catal*. 2011;54:881-887. doi:10.1007/s11244-011-9696-8

39. Valenzuela RX, Bueno G, Cortés Corberan V, Xu Y, Chen C. Selective oxidehydrogenation of ethane with $CO_2$ over CeO2 -based catalysts. *Catal Today*. 2000;61:43-48.

40. Talati A, Haghighi M, Rahmani F. Oxidative dehydrogenation of ethane to ethylene by carbon dioxide over Cr/TiO2–ZrO2 nanocatalyst: Effect of active phase and support composition on catalytic properties and performance. *Adv Powder Technol*. 2016;27:1195-1206. doi:10.1039/C6RA05049B

41. Thirumala Bai P, Lingaiah N, Prasad PSS, Hari Babu B, Rama Rao KS, Ramesh Y. Oxidative dehydrogenation of ethane to ethylene on Cr2O3/Al2O3–ZrO2 catalysts: the influence of oxidizing agent on ethylene selectivity. *Appl Petrochemical Res*. 2014;4:247-252. doi:10.1007/s13203-014-0043-4

42. Bugrova TA, Dutov V V., Svetlichnyi VA, Cortés Corberán V, Mamontov G V. Oxidative dehydrogenation of ethane with $CO_2$ over CrOx catalysts supported on Al2O3, ZrO2, CeO2 and CexZr1-xO2. *Catal Today*. 2018. doi:10.1016/j.cattod.2018.04.047

43. Michorczyk P, Ogonowski J, Gajek T. Dehydrogenation of light alkanes over mesoporous-siliceous supported chromium, vanadium, gallium and iron oxides in presence of carbon dioxide. *Przem Chem*. 2012;91(1).

44. Zhao X, Wang X. Oxidative dehydrogenation of ethane to ethylene by carbon dioxide over Cr/TS-1 catalysts. *Catal Commun*. 2006;7:633-638. doi:10.1016/j.catcom.2006.02.005

45. Aresta M, Dibenedetto A, Quaranta E. *Reaction Mechanisms in Carbon Dioxide Conversion*. 1st ed. Berlin: Springer-Verlag; 2016. doi:10.1007/978-3-662-46831-9

46. Kocoń M, Michorczyk P, Ogonowski J. Effect of supports on catalytic activity of chromium oxide-based catalysts in the dehydrogenation of propane with $CO_2$. *Catal Letters*. 2005;101(1-2):53-57. doi:10.1007/s10562-004-3749-6

47. Wang S, Murata K, Hayakawa T, Hamakawa S, Suzuki K. Dehydrogenation of ethane with carbon dioxide over supported chromium oxide catalysts. *Appl Catal A Gen*. 2000;196:1-8. doi:10.1016/S0926-860X(99)00450-0

48. Jin L, Reutenauer J, Opembe N, et al. Studies on dehydrogenation of ethane in the presence of $CO_2$ over octahedral molecular sieve (OMS-2) catalysts. *ChemCatChem*. 2009;1:441-444. doi:10.1002/cctc.200900149

49. Shishido T, Shimamura K, Teramura K, Tanaka T. Role of CO 2 in dehydrogenation of propane over Cr-based catalysts. *Catal Today*. 2012;185(1):151-156. doi:10.1016/j.cattod.2011.10.028

50. Liu L, Li H, Zhang Y. A comparative study on catalytic performances of chromium incorporated and supported mesoporous MSU-x catalysts for the oxidehydrogenation of ethane to ethylene with carbon dioxide. *Catal Today*. 2006;115:235-241. doi:10.1016/j.cattod.2006.02.040

51. Takehira K, Ohishi Y, Shishido T, et al. Behavior of active sites on Cr-MCM-41 catalysts during the dehydrogenation of propane with $CO_2$. *J Catal*. 2004;224(2):404-416. doi:10.1016/j.jcat.2004.03.014

52. Liu L, Li H, Zhang Y. Mesoporous silica-supported chromium catalyst: Characterization and excellent performance in dehydrogenation of propane to propylene with carbon dioxide. *Catal Commun*. 2007;8(3):565-570. doi:10.1016/j.catcom.2006.08.005

53. Takahara I, Saito M. Promoting effects of carbon dioxide on dehydrogenation of propane over a SiO2-supported Cr2O3 catalyst. *Chem Lett*. 1996;25:973. doi:0366-7022

54. Baek J, Yun HJ, Yun D, Choi Y, Yi J. Preparation of Highly Dispersed Chromium Oxide Catalysts Supported on Mesoporous Silica for the Oxidative Dehydrogenation of Propane Using CO 2 : Insight into the Nature of Catalytically Active Chromium Sites. *ACS Catal*. 2012;2(9):1893-1903. doi:10.1021/cs300198u

55. Nakagawa K, Okamura M, Ikenaga N, Suzuki T, Kobayashi T. Dehydrogenation of ethane over gallium oxide in the presence of carbon dioxide. *Chem Commun*. 1998:1025-1026. doi:10.1039/a800184g

56. Zhang F, Wu R, Yue Y, et al. Microporous and Mesoporous Materials Chromium oxide supported on ZSM-5 as a novel efficient catalyst for dehydrogenation of propane with CO 2. *Microporous Mesoporous Mater*. 2011;145(1-3):194-199. doi:10.1016/j.micromeso.2011.05.021

57. Asghari E, Haghighi M, Rahmani F. $CO_2$ Oxidative Dehydrogenation of Ethane to Ethylene over Cr/MCM-41 Nanocatalyst Synthesized via Hydrothermal/Impregnation Methods: Influence of Chromium Content on Catalytic Properties and Performance. *J Mol Catal A Chem*. 2016;418-419:115-124. doi:10.1016/j.molcata.2016.03.033

58. Botavina MA, Martra G, Agafonov YA, et al. Oxidative dehydrogenation of C3-C4 paraffins in the presence of $CO_2$ over CrOx/SiO2 catalysts. *Appl Catal A Gen*. 2008;347(2):126-132. doi:10.1016/j.apcata.2008.05.037

59. Deng S, Li S, Li H, Zhang Y. Oxidative dehydrogenation of ethane to ethylene with $CO_2$ over Fe-Cr/ZrO2 catalysts. *Ind Eng Chem Res*. 2009;48:7561-7566. doi:10.1021/ie9007387

60. Yun D, Baek J, Choi Y, Kim W, Lee HJ, Yi J. Promotional Effect of Ni on a CrO x Catalyst Supported on Silica in the Oxidative Dehydrogenation of Propane with CO 2. *ChemCatChem*. 2012;4(12):1952-1959. doi:10.1002/cctc.201200397

61. Ajayi BP, Rabindran Jermy B, Abussaud BA, Al-Khattaf S. Oxidative dehydrogenation of n-butane over bimetallic mesoporous and microporous zeolites with $CO_2$as mild oxidant. *J Porous Mater*. 2013;20(5):1257-1270. doi:10.1007/s10934-013-9710-6

62. Bliznuk V, Alexopoulos K, Reyniers M-F, et al. The role of $CO_2$ in the dehydrogenation of propane over WOx–VOx/SiO2. *J Catal*. 2016;335:1-10. doi:10.1016/j.jcat.2015.12.015

63. Cavani F, Ballarini N, Cericola A. Oxidative dehydrogenation of ethane and propane: How far from commercial implementation? *Catal Today*. 2007;127(1-4):113-131. doi:10.1016/j.cattod.2007.05.009

64. Chen K, Bell AT, Iglesia E. The relationship between the electronic and redox properties of dispersed metal oxides and their turnover rates in oxidative dehydrogenation reactions. *J Catal*. 2002;209:35-42. doi:10.1006/jcat.2002.3620

65. Raju G, Reddy BM, Park SE. $CO_2$ promoted oxidative dehydrogenation of n-butane over VOx/MO2-ZrO2 (M = Ce or Ti) catalysts. *J* $CO_2$ *Util*. 2014;5:41-46. doi:10.1016/j.jcou.2013.12.003

66. Raju G, Reddy BM, Abhishek B, Mo Y-H, Park S-E. Synthesis of C4 olefins from n-butane over a novel VOx/SnO2–ZrO2 catalyst using $CO_2$ as soft oxidant. *Appl Catal A Gen*. 2012;423-424:168-175. doi:10.1016/j.apcata.2012.02.040

67. Wang X, Ji K, Zhou G, Li Q, Zhou H, Xu C. Synthesis of V-MCM-41 Catalysts and Their Application in $CO_2$-Assisted Isobutane Dehydrogenation. *Chem Eng Technol*. 2018;41(3):563-572. doi:10.1002/ceat.201700284

68. Han ZF, Xue XL, Wu JM, Lang WZ, Guo YJ. Preparation and catalytic properties of mesoporous nV-MCM-41 for propane oxidative dehydrogenation in the presence of $CO_2$. *Chinese J Catal*. 2018;39:1099-1109. doi:10.1016/S1872-2067(18)63048-7

69. Taghavinezhad P, Haghighi M, Alizadeh R. $CO_2$/O2-oxidative dehydrogenation of ethane to ethylene over highly dispersed vanadium oxide on MgO-promoted sulfated-zirconia nanocatalyst: Effect of sulfation on catalytic properties and performance. *Korean J Chem Eng*. 2017;34(5):1346-1357. doi:10.1007/s11814-017-0026-0

70. Rozanska X, Fortrie R, Sauer J. Size-dependent catalytic activity of supported vanadium oxide species: Oxidative dehydrogenation of propane. *J Am Chem Soc*. 2014;136(21):7751-7761. doi:10.1021/ja503130z

71. Xue XL, Lang WZ, Yan X, Guo YJ. Dispersed Vanadium in Three-Dimensional Dendritic Mesoporous Silica Nanospheres: Active and Stable Catalysts for the Oxidative Dehydrogenation of Propane in the Presence of $CO_2$. *ACS Appl Mater Interfaces*. 2017;9:15408-15423. doi:10.1021/acsami.7b01498

72. Ye J, Liu C, Ge Q. DFT study of $CO_2$ adsorption and hydrogenation on the In2O3 surface. *J Phys Chem C*. 2012;116(14):7817-7825. doi:10.1021/jp3004773

73. Chen M, Xu J, Liu Y-M, Cao Y, He H-Y, Zhuang J-H. Supported indium oxide as novel efficient catalysts for dehydrogenation of propane with carbon dioxide. *Appl Catal A Gen*. 2010;377(1-2):35-41. doi:10.1016/j.apcata.2010.01.011

74. Wang W, Zhang Y, Wang Z, Yan J, Ge Q, Liu C. Reverse water gas shift over In2O3–CeO2 catalysts. *Catal Today*. June 2015. doi:10.1016/j.cattod.2015.04.032

75. Pan YX, Liu CJ, Mei D, Ge Q. Effects of hydration and oxygen vacancy on $CO_2$ Adsorption and activation on β-Ga2O3(100). *Langmuir*. 2010;26(8):5551-5558. doi:10.1021/la903836v

76. Yan Liu, Zhen Hua Li, Jing Lu, Kang-Nian Fan. Periodic Density Functional Theory Study of Propane Dehydrogenation over Perfect Ga2O3(100) Surface. *J Phys Chem C*. 2008;112(100):20382–20392. doi:10.1021/jp807864z

77. Michorczyk P, Ogonowski J. DEHYDROGENATION OF PROPANE IN THE PRESENCE OF CARBON DIOXIDE OVER OXIDE-BASED CATALYSTS. *React Kinet Catal Lett*. 2003;78(1):41-47.

78. Porosoff MD, Yu W, Chen JG. Challenges and opportunities in correlating bimetallic model surfaces and supported catalysts. *J Catal*. 2013;308:2-10. doi:10.1016/j.jcat.2013.05.009

79. Porosoff MD, Yan B, Chen JG. Catalytic reduction of $CO_2$ by H2 for synthesis of CO, methanol and hydrocarbons: challenges and opportunities. *Energy Environ Sci*. 2016;9(1):62-73. doi:10.1039/C5EE02657A

80. Trovarelli A. Catalytic Properties of Ceria and CeO2 -Containing Materials. *Catal Rev*. 1996;38(4):439-520. doi:10.1080/01614949608006464

81. Cheng Z, Sherman BJ, Lo CS. Carbon dioxide activation and dissociation on ceria ( 110 ): A density functional theory study. *J Chem Phys*. 2013;138(014702). doi:10.1063/1.4773248

82. Appel LG, Eon JG, Schmal M. The $CO_2$ – CeO2 interaction and its role in the CeO2 reactivity. *Catal Letters*. 1998;56:199-202.

83. Chueh WC, Haile SM. A thermochemical study of ceria: Exploiting an old material for new modes of energy conversion and $CO_2$ mitigation. *Philos Trans R Soc A Math Phys Eng Sci*. 2010;368(1923):3269-3294. doi:10.1098/rsta.2010.0114

84. Bueno-López A, Krishna K, Makkee M. Oxygen exchange mechanism between isotopic $CO_2$ and Pt/CeO2. *Appl Catal A Gen*. 2008;342:144-149. doi:10.1016/j.apcata.2008.03.013

85. Demoulin O, Navez M, Mugabo JL, Ruiz P. The oxidizing role of $CO_2$ at mild temperature on ceria-based catalysts. *Appl Catal B Environ*. 2007;70(1-4):284-293. doi:10.1016/j.apcatb.2005.12.024

86. Myint MNZ, Yan B, Wan J, Zhao S, Chen JG. Reforming and Oxidative Dehydrogenation of Ethane with $CO_2$ as a Soft Oxidant over Bimetallic Catalysts. *J Catal*. 2016;343:168-177. doi:10.1016/j.jcat.2016.02.004

87. Yan B, Yao S, Kattel S, et al. Active sites for tandem reactions of $CO_2$ reduction and ethane dehydrogenation. *Proc Natl Acad Sci*. 2018:2-7. doi:10.1073/pnas.1806950115

88. Solymosi F, Nemeth R. The oxidative dehydrogenation of ethane with $CO_2$ over Mo2C/SiO2 catalyst. *Catal Letters*. 1999;62:197-200.

89. Solymosi F, Németh R, Óvári L, Egri L. Reactions of Propane on Supported Mo2C Catalysts. *J Catal*. 2000;195:316-325. doi:10.1006/jcat.2000.3000

90. Neylon MK, Choi S, Kwon H, Curry KE, Thompson LT. Catalytic properties of early transition metal nitrides and carbides: n-butane Hydrogenolysis, dehydrogenation and isomerization. *Appl Catal A Gen*. 1999;183:253-263. doi:10.1016/S0926-860X(99)00053-8

91. Porosoff MD, Yang X, Boscoboinik JA, Chen JG. Molybdenum Carbide as Alternative Catalysts to Precious Metals for Highly Selective Reduction of $CO_2$ to CO. *Angew Chemie*. 2014;53:6705-6709. doi:10.1002/ange.201404109

92. Wang X, Lin L, Shi C, et al. Highly Dispersed Copper over β-Mo2C as an Efficient and Stable Catalyst for the Reverse Water Gas Shift (RWGS) Reaction. *ACS Catal*. 2016;7(1):912-918. doi:10.1021/acscatal.6b02991

93. Porosoff MD, Myint MNZ, Kattel S, et al. Identifying Different Types of Catalysts for $CO_2$ Reduction by Ethane through Dry Reforming and Oxidative Dehydrogenation. *Angew Chemie - Int Ed*. 2015;54:15501-15505. doi:10.1002/anie.201508128

94. Yao S, Yan B, Jiang Z, et al. Combining $CO_2$ Reduction with Ethane Oxidative Dehydrogenation by Oxygen-Modification of Molybdenum Carbide. *ACS Catal*. 2018;8(6):5374-5381. doi:10.1021/acscatal.8b00541

95. Gomez E, Kattel S, Yan B, Yao S, Liu P, Chen JG. Combining $CO_2$ reduction with propane oxidative dehydrogenation over bimetallic catalysts. *Nat Commun*. 2018:1-6. doi:10.1038/s41467-018-03793-w

96. Li X, Yan B, Yao S, Kattel S, Chen JG, Wang T. Oxidative dehydrogenation and dry reforming of n-butane with $CO_2$over NiFe bimetallic catalysts. *Appl Catal B Environ*. 2018;231(February):213-223. doi:10.1016/j.apcatb.2018.02.063

97. Meriaudeau P, Naccache C. The role of Ga2O3 and proton acidity on the dehydrogenating activity of Ga2O3-HZSM-5 catalysts: evidence of a bifunctional mechanism. *J Mol Catal*. 1990;59(3). doi:10.1016/0304-5102(90)85100-V

## 1.5 Highlighted references

Highlighted references are provided for the introductory chapter to facilitate access to background literature that is highly relevant and helpful in the field of $CO_2$ reduction with light alkanes.

1. Mukherjee D, Park SE, Reddy BM. $CO_2$ as a soft oxidant for oxidative dehydrogenation reaction: An eco-benign process for industry. *Journal of $CO_2$ Utilization*. 2016;16:301-312. doi:10.1016/j.jcou.2016.08.005

    - Discusses the advantages and challenges of utilizing $CO_2$ as a soft oxidant with a focus on $CO_2$ activation and favorable factors such as promoters, surface acidity/basicity, redox / lattice oxygen, and the influence of supports.

2. Ansari MB, Park S. Carbon dioxide utilization as a soft oxidant and promoter in catalysis. *Energy Environ Sci*. 2012;5(11):9419-9437. doi:10.1039/$C_2$ee22409g

    - Ansari and Park provide substantial background on $CO_2$ activation and discuss catalyst properties for the $CO_2$-ODH reaction and other chemistries for which $CO_2$ may act as a soft oxidant, including ethylbenzene to styrene.

3. Wang S, Zhu ZH. Catalytic Conversion of Alkanes to Olefins by Carbon Dioxide Oxidative Dehydrogenation A Review. *Energy and Fuels*. 2004;18:1126-1139. doi:10.1021/ef0340716

- Wang and Zhu were among the first to summarize the progress on the development of catalysts for the $CO_2$-ODH of light alkanes, $CO_2$ oxidative coupling of methane, and dehydrogenation of ethylbenzene to styrene, which at the time mainly consisted of activity trends and ex situ characterization.

4. Atanga MA, Rezaei F, Jawad A, Fitch M, Rownaghi A. A. Oxidative dehydrogenation of propane to propylene with carbon dioxide. *Appl Catal B Environ.* 2018;220:429-445. doi:10.1016/j.apcatb.2017.08.052

- Focuses on the $CO_2$-ODH of propane over zeolites and metal oxide-based catalysts and suggests that future work should be geared toward developing catalyst design platforms that take into consideration the temperature challenge of the $CO_2$-ODH reaction.

5. Kawi S, Kathiraser Y. $CO_2$ as an oxidant for high-temperature reactions. *Front Energy Res.* 2015;3:1-13. doi:10.3389/fenrg.2015.00013

- Reviews the progress on catalysts used for high-temperature $CO_2$ reactions, including $CO_2$-ODH of light alkanes, ethylbenzene to styrene, and $CO_2$ reforming of methane and alcohols.

# Chapter 2: Experimental methods

## 2.1 Catalyst synthesis

### 2.1.1 Bimetallic catalysts supported on $CeO_2$

The catalysts evaluated in Chapters **3** and **4** were synthesized through incipient wetness impregnation[1] of metals onto commercially obtained $CeO_2$ (35-45 $m^2/g$, Sigma-Aldrich) or if applicable $\gamma$-$Al_2O_3$ (80-120 $m^2/g$ Alfa-Aesar), $ZrO_2$ (90 $m^2/g$ Alfa Aesar), $SiO_2$ (168 $m^2/g$, Alfa Aesar), and $TiO_2$ (240 $m^2/g$ Alfa Aesar). The active metal precursors $Pt(NH_3)_4(NO_3)_2$, $Pd(NO_3)_2{\cdot}2H_2O$, $Fe(NO_3)_3{\cdot}9H_2O$, $Ni(NO_3)_2{\cdot}6H_2O$, and $Co(NO_3)_2{\cdot}6H_2O$ (Alfa Aesar) were dissolved in a volume of water equivalent to 90% of the pore volume of an aliquot sample of the support. The salt solutions were added dropwise to the support and subsequently mixed. The catalysts were dried at 363 K for 6 hours in order to remove water and to allow the salt to crystallize on the pore surface. Once dried, the catalysts were calcined at 563 K for 2 hours with a 0.8 K/min ramp rate.

Catalysts were synthesized by atomic ratios corresponding to a 1.67 wt.% $Pt_1$ basis for consistency with previous investigations of other bimetallic catalysts in our group and to maximize bimetallic bond formation.[2,3,4] For bimetallic synthesis, Pt (1.67 wt.%) is replaced with another metal with an equivalent atomic concentration. For example, in the $Fe_3Ni_1/CeO_2$ catalyst, $Ni_1$ replaces Pt, and then the Fe loading is calculated such that for every atom of Ni there are 3 atoms of Fe, see **Table 2-1** for metal loading wt.%.

**Table 2-1.** Equivalent atomic concentration for each metal corresponding to 1.67 wt.% Pt. The nomenclature assigned by the subscripts such as in $Co_3Pt_1$ means that there are three atoms of Co for every atom of Pt. Nomenclature for a non-precious catalyst such as in $Co_3Ni_1$ means that $Ni_1$ (0.5 wt.%) is replacing Pt in an equivalent mole amount corresponding to 1.67 wt.% $Pt_1$.

| *$Metal_x$* | *wt.%* | | *wt.%* | | *wt.%* | | *wt.%* |
|---|---|---|---|---|---|---|---|
| $Pt_1$ | 1.67 | $Fe_1$ | 0.48 | $Co_1$ | 0.5 | $Ni_1$ | 0.5 |
| $Pd_1$ | 0.91 | $Fe_3$ | 1.43 | $Co_3$ | 1.5 | $Ni_3$ | 1.5 |

Example using 1.67 wt.% Pt as a reference:

$$Weight\ \%\ of\ Ni_1 = \frac{1.67}{MW\ of\ Pt} \times MW\ of\ Ni = 0.5$$

Thus, to obtain an equivalent amount of atomic concentration corresponding to 1.67 wt.% Pt, the Ni loading is 0.5 wt.%. If the catalyst is to have 3 atoms of Fe for every atom of Ni, then the Fe wt.% loading would be 1.43 wt.% and the assigned nomenclature would be $Fe_3$. However, if Fe were to be the metal replacing $Pt_1$ then the wt.% would be 0.48% and the nomenclature would be $Fe_1$. For this investigation metal loadings, calcination, and drying treatment conditions were consistent with previous studies.[5,4,3] A summary of in situ EXAFS measurements providing structural information on Pt-Ni, Pd-Ni, and Pt-Co from previous $CO_2$ reduction studies is available in **Table 2-2** and demonstrates the presence of bimetallic bonds in these catalysts.

**Table 2-2.** In situ EXAFS of Pt-Ni, Pd-Ni, and Pt-Co from previous studies. W. Lonergan, et al., *J. Catal*., 2010, 271(2):239-250 identified that Ni-Pt bimetallic bond formation could be maximized with a Ni: Pt ratio of 3:1 when synthesized through a co-impregnation IWI method. For the sake of comparability, the atomic ratio of 3:1 and the synthesis procedure was maintained in this study.

| Pt-Pt or Pd-Pd (Å) | | | | |
|---|---|---|---|---|
| | $CO_2 + H_2$[6] | $CO_2 + CH_4$[7] | $CO_2 + C_2$[8] | $CO_2 + C_3$[5] |
| $Ni_3Pt_1$ | 2.71 ± 0.01 | | – | 2.78 ± 0.03 |
| $Ni_3Pd_1$ | 2.71 ± 0.01 | | | |
| $Co_3Pt_1$ | 2.71 ± 0.01 | – | | |
| Pt-M or Pd-M (Å) | | | | |
| $Ni_3Pt_1$ | 2.56 ± 0.001 | | 2.57 ± 0.01 | 2.56 ± 0.02 |
| $Ni_3Pd_1$ | 2.59 ± 0.01 | | | |
| $Co_3Pt_1$ | 2.6 ± 0.01 | 2.55 ± 0.06 | | |
| $\sigma^2$ (Å$^2$) | | | | |
| $Ni_3Pt_1$ | 0.008 | | 0.008 | 0.010 |
| $Ni_3Pd_1$ | 0.008 | | | |
| $Co_3Pt_1$ | 0.008 | 0.008 | | |
| M-M (Å) | | | | |
| Ni | 2.49 ± 0.01 | | 2.51 ± 0.01 | – |
| Co | 2.51 ± 0.01 | 2.44 ± 0.01 | | – |

Particle size distributions from TEM images of freshly synthesized $Ni_3Pt_1/CeO_2$, $Ni_3Pd_1/CeO_2$, and $Co_3Pt_1/CeO_2$ were previously reported by our group to be 1.7, 2.4, and 1.3 nm, respectively.[33] However, it is very challenging to obtain a reliable particle size distribution for several of the other evaluated catalysts using TEM because of the low contrast of 3d elements (Fe, Co, and Ni) over the $CeO_2$ support. From in-situ XRD measurements (**Figure 2-1**), $Fe_3Ni_1/CeO_2$ did not show any diffraction patterns from metal particles, suggesting that the particle size of $Fe_3Ni_1$ should be less than ~2nm.

Also from synchrotron XRD experiments, we have confirmed that the $CeO_2$ support is crystalline and approximately 33 nm in size.[8] In addition, under reaction conditions for the reduction of $CO_2$ with ethane the $CeO_2$ lattice has been shown to undergo abrupt expansions indicating an increase of the average Ce-O bond length due to the partial reduction of $Ce^{4+}$ to $Ce^{3+}$.[9,8] The BET surface area of the support has been reported by our group to be 49.1 $m^2 \cdot g^{-1}$ while the $Ni_3Pt_1/CeO_2$ catalyst has a surface area of 44.5 $m^2 \cdot g^{-1}$.[10]

### 2.1.2 Phosphorous and Ga modified ZSM-5 catalysts

All catalysts were synthesized with proton exchanged ZSM-5 containing a Si/Al molar ratio of 30 (sourced from Riogen Catalysis for Chemicals and Energy). Phosphorous modification, ZSM-5P(X) was achieved via a slurry technique that was mixed at 40°C for 12 hours. The calculated mixture of ethanol, water, and 85 wt.% $H_3PO_4$ was sonicated for 10 mins before combining with a paste of ZSM-5 (created with 5 ml of water). Calcination followed a program at 550°C for 6 hours (5°C/min ramp). Incorporation of 2 wt.% Ga to ZSM-5 was achieved via incipient wetness impregnation with $Ga(NO_3)_3$ salt (Sigma-Aldrich) onto ZSM-5 or ZSM-5P(X) followed by calcination at 290°C for 2 hours (0.8°C/min ramp).

## 2.2 Flow reactor studies

### 2.2.1 Reactions of $CO_2$ and propane for $CO_2$-ODHP and DRP

Flow reactor studies were conducted at 823 K and atmospheric pressure utilizing a 6.35 mm quartz U-tube shaped reactor. All catalysts were reduced at 723 K for 1 hour under 1:1 $H_2$/Ar flow (40mL/min total). After catalyst pre-treatment, the temperature was increased to (6.5 K/min) and held at 823 K in the presence of 1:1:2 $CO_2$, $C_3H_8$, and Ar (40 mL/min total) for over 12 hours.

### 2.2.2 Reactions of $CO_2$ and ethane for $CO_2$-ODAE and DDAE

Flow reactor studies were conducted at 873 K and atmospheric pressure utilizing a 6.35 mm quartz rod reactor. All catalysts were pre-treated at 873 K for 1 hour under 20 ml/min Ar flow with a 9.3 $^oC$/min ramp. After catalyst pre-treatment, reaction gasses (3, 3, and 4 ml/min of $CO_2$, $C_2H_6$, and Ar, respectively) were introduced to the reactor and allowed to stabilize for 10 minutes at 873 K before the first the GC sampled the first data point. The reaction was held for 12 hours.

### 2.2.3 Flow reactor calculations

Flow reactor effluent was analyzed on-stream by a gas chromatograph (GC) equipped with a thermal conductivity (TCD) and flame ionization detector (FID) arranged in series. An Agilent 7890 A/B series GC configured with 6-way column isolation valves were used for the experiments. For proper separation, an Agilent HP-PLOT-Q (polystyrene-divinylbenzene) column was used to separate $CO_2$, alkanes, water, and aromatics and the subsequent Molecular Sieve Packed (Mol-Sieve) column was used to separate $H_2$, Ar, $CH_4$, and CO. Helium was used as the carrier gas with flow rates of 7-11 mL/min. Adequate programming ensured (1) seamless transition of light components to the isolation valve (2) separation of heavier components through PLOT-Q and detection while Mol-Sieve was isolated, and (3) release of light components from the isolation

valve to travel through PLOT-Q and then Mol-Sieve before entering the detectors. Argon was used as the inert internal standard to calculate total flow rate and was the basis for all calculations. Blank experiments containing only quartz and treated blanks supports were conducted under steady-state conditions. These experiments showed little to no activity suggesting that the support, quartz, and gas phase reactions have no significant effect.

Conversion is defined as the rate of reactant fed initially into the reactor minus the rate of disappearance of the reactant over the initial rate multiplied by 100:

$$\text{Conversion} = \frac{\text{Rate of reactant}_{\text{fed}} - \text{Rate of reactant}_{\text{consumed}}}{\text{Rate of reactant}_{\text{fed}}} \text{ x } 100 \qquad \text{(Equation 2-1)}$$

For the reactions of $CO_2$ and $C_3H_8$, the rate of reactant consumed is defined as:

$$\text{Rate of } CO_{2\ \text{consumed}} = \frac{\text{Total CO} - H_2O}{2} + H_2O \qquad \text{(Equation 2-2)}$$

$$\text{Rate of } C_3H_{8\ \text{consumed}} = \frac{\text{Total CO} - H_2O}{6} + C_3H_6 \qquad \text{(Equation 2-3)}$$

For the reactions of $CO_2$ and $C_2H_6$, the conversion is based on the decrease in *mol·min$^{-1}$* of the reactants with time compared to the initial feed.

In order to compare catalysts according to the available active sites determined by CO chemisorption, the turnover frequency is defined as:

$$\text{TOF}_{[\text{site}^{-1}\cdot\text{min}^{-1}]} = \frac{F_{reactant}^{inlet} \times X}{U_{CO} \times W_{catalyst}} \qquad \text{(Equation 2-4)}$$

where, *F (mol·min$^{-1}$)* and *X (%/100)* are the flow and conversion of a given reactant, respectively, $U_{CO}$ is the uptake value in *mol CO·g$^{-1}$*, and *W* is the mass of catalyst used in *g*.

For Ga modified ZSM-5 catalysts, the turnover frequency is defined as:

$$\mathrm{TOF}_{[\text{mol reactant}\cdot\text{mol metal}^{-1}\cdot\text{hr}^{-1}]} = \frac{F_{reactant}^{inlet} \times \mathrm{X}}{L_{metal} \times W_{catalyst}} \quad \text{(Equation 2-5)}$$

where, $L_{metal}$ *(mol metal / catalyst sample)* is the amount of Ga in a given catalyst sample.

For catalysts with low activity, the hydrogen amount was under the detection limit of the GC; therefore, in order to maintain consistency, the selectivity is defined on an alkane basis:

$$\text{Selectivity} = \frac{\text{Amount of given carbonaceous species from } alkane}{\text{Amount of all carbonaceous species from alkane}} \text{x}100 \quad \text{(Equation 2-6)}$$

Dehydrogenation activity for $CO_2$-ODHP is based on the amount of propylene produced, dry reforming is based on the amount of CO produced from 1 mol of $C_3H_8$, and cracking is based on the sum of methane, ethane, and ethylene produced. For aromatization reactions, the sum of the selectivity toward each liquid product (i.e., benzene, toluene, ethylbenzene, o-, m-, & p- xylenes) measures the activity toward the $CO_2$-ODAE or DDAE reactions.

The CO selectivity for both $CO_2$-ODHP and $CO_2$-ODAE only accounts for CO produced only from the alkane and is defined as:

$$\text{Selectivity}_{\mathrm{CO}} = \frac{\frac{\text{Total CO} - \mathrm{H_2O}}{2}}{\text{Total Amount of all carbonaceous species from alkane}} \text{x}100 \quad \text{(Equation 2-7)}$$

Using the selectivity, the yield on an alkane basis is defined as:

$$\text{Yield}_{\text{product}} = \text{Selectivity}_{\text{product}} \times X_{alkane} \quad \text{(Equation 2-8)}$$

### 2.2.4 Kinetic measurement methods

Apparent activation energy and reaction order experiments were conducted at slightly different reaction conditions to ensure operation in an intrinsic kinetic regime and minimize transport effects. The reaction conditions for kinetic experiments adopted in the present work were

chosen based on our previous work (Xie, et al. *Appl. Catal. B: Environ.*, 245: 376-388, 2019), in which operation in a truly intrinsic kinetic regime free of heat and transport limitations was validated by both experimental approaches (*e.g.*, intra- and inter- particle dilution) and numerical criteria (*e.g.*, Weisz-Prater criterion).[10,11] Detailed kinetics experiments for catalysts that exhibit high steady-state conversions (≥10%) were performed with approximately 100 mg of diluted (1:5 $SiO_2$) and sieved catalyst (40-60 mesh) mixed with treated acid-purified granulated quartz (calcined at 1173 K, 40-60 mesh) for $CeO_2$ supported catalysts. Kinetic experiments with zeolite catalysts were performed similarly to those with $CeO_2$ supported catalysts, but with 200 mg of diluted catalyst (1:3 $SiO_2$). Catalysts with low steady-state conversion were not diluted. The amount of quartz in all experiments was adjusted in order to maintain a constant isothermal length in the reactor. Kinetics experiments began with an initial $CO_2$ + alkane treatment using the same gas flow ratios and ramp rate as in steady-state experiments, but the catalyst bed was held at constant temperature only for 10 hours for $CeO_2$ supported catalysts (5 hours for ZSM-5 catalysts). Then, the temperature or gas flow was altered depending on the experiment. Conversion values for both reactants were kept well below 10%. Deactivation extents were measured for both apparent activation energy and reaction order experiments by revisiting baseline treatment conditions after obtaining the last experimental point.

Reaction order experiments were conducted after the initial treatment by decreasing and then increasing the flow in increments of 1-2, 2-2.5 or 5-10 mL/min, depending on the catalyst. The flow was allowed to stabilize for 40 minutes before analyzing the rate. Apparent activation energy experiments were conducted upon the completion of the initial treatment. Then, the reactor temperature was cooled to the lowest temperature of interest, held for 40 mins, and then increased incrementally; this process was repeated until reaching the highest desired temperature. A second

curve can be obtained by collecting data with controlled cooling as described by Xie et al.[11] Arrhenius-type plots were constructed by using the rate of reactant consumption/product formation versus $T^{-1}$.

## 2.3 CO chemisorption

Pulse CO chemisorption was performed to quantitatively compare the number of active sites in each catalyst and for calculating the turnover frequency (TOF).[12] In addition to CO, the dissociative adsorption of $H_2$ may also be used to determine the number of active sites, with the reservation that hydrogen may desorb from some metal surfaces at room temperature. Experiments were performed using an AMI-300ip (Altamira) characterization instrument. Samples were prepared by drying 100 mg of fresh catalyst in a quartz U-tube at 393 K for half an hour with a He flow of 50 mL/min. Once dried, the catalysts were reduced in the presence of 10% $H_2$/Ar mixture (30 mL/min total) with a heating rate of 10 K/min from 323 K to 723 K and held for 40 minutes. Reduced samples were then flushed with 50 mL/min of Helium at 723 K for 20 minutes and allowed to cool to 313 K. Then, pulses of 10% CO/He (590 µL loop) were mixed with the 50 mL/min He stream and passed through the sample. A thermal conductivity detector (TCD) was used to analyze the amount of gas exiting the bed. The amount of gas adsorbed on the sample is the difference between the amount injected and the amount exiting the bed. Data collection was terminated when the peak area was constant. CO chemisorption is a crucial tool to determine the number of active metal sites on a catalyst and is required for proper activity comparison. Where applicable the activity of catalysts in this study will be normalized by the values of CO uptake assuming a stoichiometry of Metal: CO of 1 to 1. Several of the catalysts in this study are supported over $CeO_2$, which may chemisorb large amounts of CO; however, general trends may be obtained within a given set of $CeO_2$ supported catalysts.[13]

## 2.4 Thermogravimetric analysis experiments

Thermogravimetric analysis (TGA) studies are used to measure the weight loss of a spent catalyst by subjecting the sample to a controlled temperature ramp treatment in an $O_2$ or $CO_2$ rich environment. As the temperature increases, the coke on the surface of the spent catalyst is oxidized by $O_2$ or $CO_2$, and the carbon is removed in the form of $CO_2$ or CO + water, respectively. The percent decrease in mass is attributed to an equivalent amount of coke that was on the spent catalyst after the reaction. TGA experiments were conducted using a TA Instrument 8500 TGA. Approximately 15 mg of spent sample was placed onto a tared platinum weigh pan. The spent catalyst was then subjected to a drying program in which it was ramped from room temperature to 473K at 15 K/min and held at temperature for 45 minutes in the presence of Ar (40 mL/min). Then, the program ramped to 1273 K with a 10 K/min ramp rate in the presence of oxidant $O_2$ or $CO_2$ (20 mL/min). For analysis, the first derivative of the weight loss data (DTGA) is plotted against temperature. The DTGA peak is a useful indicator of the strength of interaction between surface carbon and the catalyst since higher oxidation temperatures indicate that the coke was difficult to remove. A related technique is temperature programmed oxidation (TPO), but instead of tracking weight measurements, the intensity of the oxidation products vs. temperature is obtained using a thermal conductivity detector (TCD).[14]

## 2.5 TEM with energy dispersive X-ray spectroscopy

Energy dispersive X-ray spectroscopy (EDS) can be used to map metal dispersion on catalysts that are difficult to image due to several factors such as low metal loading or high support molecular weight. Mapping a sample pre-and post-reaction can help identify whether there are any obvious metal agglomerations that may be caused by sintering. EDS operates under the principle

of X-ray fluorescence to collect compositional data in a given area of a sample. EDS mappings were conducted utilizing an FEI Talos F200X (S/TEM) with an X-FEG field emission source of brightness $1.8x10^9$ A/cm$^2$ (at 200 kV). Samples were prepared on gold grids by dropping 20 µL of the supernatant from a 7 mL acetone + 2 mg catalyst mixture that had been sonicated for 20 minutes.

## 2.6 In situ X-ray Diffraction (XRD) of $Fe_3Ni_1/CeO_2$

In situ XRD measurements have been added to investigate metal sintering. The sample underwent reduction and reaction treatment at the same temperatures and in proportional gaseous environments as in steady-state experiments. The in situ data reveal that there are no obvious metal phases, potentially a consequence of low loading. However, it is possible to infer that the metal

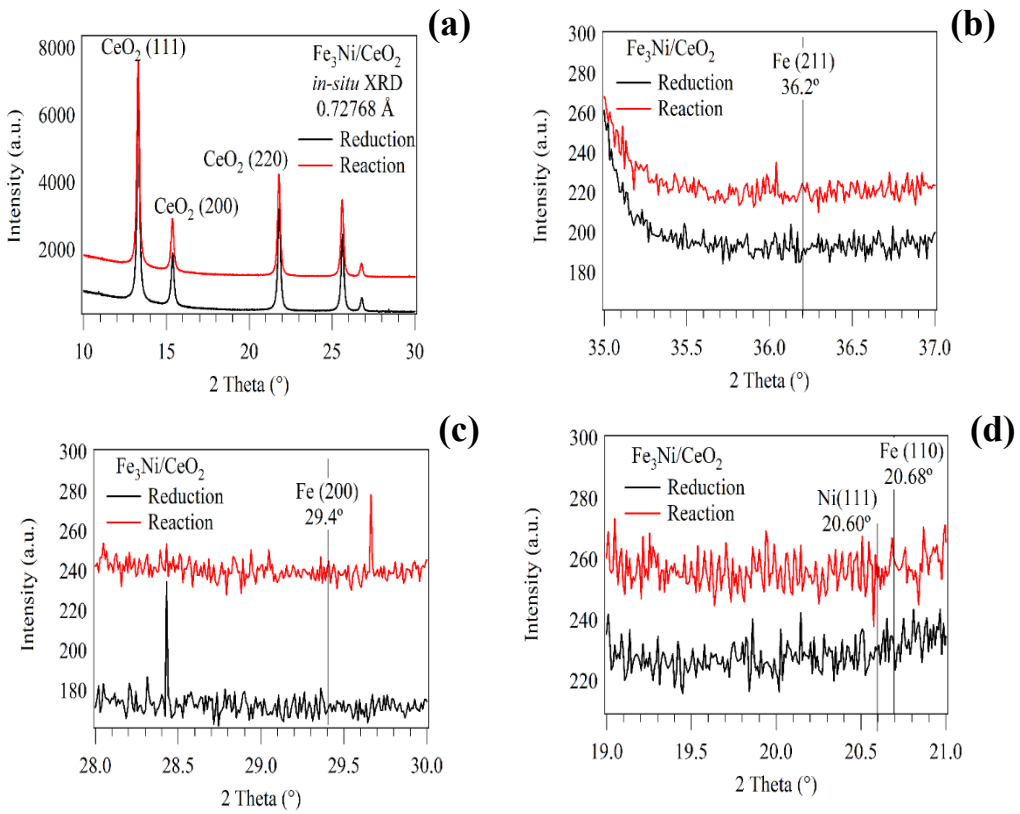


**Figure 2-1.** In-situ XRD intensity vs. 2θ for reduction and reaction treatment. **(a)** Full spectra of $Fe_3Ni_1/CeO_2$ and **(b-d)** insets for areas of interest with labeled features.

particles cannot be larger than approximately 2nm, as anything above this would be observed in XRD measurements.

## 2.7 In situ X-ray absorption near edge spectroscopy

In situ X-ray absorption near-edge spectroscopy (XANES) measurements for the Fe K edge (7112 eV), Ni K edge (8333 eV), Co K edge (7709 eV), and Pd K edge (24350 eV) were collected at the Beamline 9-BM of the Advanced Photon Source (APS) at Argonne National Laboratory. For each experiment, ~200 mg of sieved sample (60-80 mesh) was loaded into a custom Cu microchannel cell and held in place with graphite paper. Using similar procedures as with steady-state flow reactor experiments, the catalysts were first reduced in a 50/50 mixture of Ar and He at 723 K for 60 minutes. After reduction, the temperature was increased to 823 K and data collection began after the catalyst had been in contact with reaction gasses and at temperature for 10 minutes. Collecting the fluorescence or transmission signal of 3d metals, especially those of low loading (

**Table 2-1**) on a support composed by high Z element ($CeO_2$ in our system) usually results in relatively weak signals, due to the strong absorption of the oxide support as well as the relatively strong absorption of window materials at low energy edges. To improve the signal, data were collected using a vortex detector that provided higher 3d metal counts and lowered the interference from Ce. Three spectra for each edge were collected in fluorescence mode. XANES spectra were analyzed using the Athena software package with the appropriate metal foil and powder oxide as references.

## 2.8 References


1. Richardson JT. *Principles of Catalyst Development*. (Twigg MV, Spencer MS, eds.). New York: Plenum Press

2. Lonergan WW, Wang T, Vlachos DG, Chen JG. Effect of oxide support surface area on hydrogenation activity: Pt/Ni bimetallic catalysts supported on low and high surface area Al2O3 and ZrO2. *Appl Catal A Gen*. 2011;408(1-2):87-95. doi:10.1016/j.apcata.2011.09.007

3. Myint M, Yan B, Wan J, Zhao S, Chen JG. Reforming and Oxidative Dehydrogenation of Ethane with $CO_2$ as a Soft Oxidant over Bimetallic Catalysts. *J Catal*. 2016;343:168-177. doi:10.1016/j.jcat.2016.02.004

4. Porosoff MD, Myint MNZ, Kattel S, et al. Identifying Different Types of Catalysts for $CO_2$ Reduction by Ethane through Dry Reforming and Oxidative Dehydrogenation. *Angew Chemie - Int Ed*. 2015;54:15501-15505. doi:10.1002/anie.201508128

5. Gomez E, Kattel S, Yan B, Yao S, Liu P, Chen JG. Combining $CO_2$ reduction with propane oxidative dehydrogenation over bimetallic catalysts. *Nat Commun*. 2018:1-6. doi:10.1038/s41467-018-03793-w

6. Porosoff MD, Chen JG. Trends in the catalytic reduction of $CO_2$ by hydrogen over supported monometallic and bimetallic catalysts. *J Catal*. 2013;301:30-37. doi:10.1016/j.jcat.2013.01.022

7. Xie Z, Yan B, Kattel S, et al. Dry reforming of methane over $CeO_2$-supported Pt-Co catalysts with enhanced activity. *Appl Catal B Environ*. 2018;236:280-293. doi:10.1016/j.apcatb.2018.05.035

8. Yan B, Yang X, Yao S, et al. Dry Reforming of Ethane and Butane with $CO_2$ over $PtNi/CeO_2$ Bimetallic Catalysts. *ACS Catal*. 2016;6:7283-7292. doi:10.1021/acscatal.6b02176

9. Yan B, Yao S, Kattel S, et al. Active sites for tandem reactions of $CO_2$ reduction and ethane dehydrogenation. *Proc Natl Acad Sci*. 2018:2-7. doi:10.1073/pnas.1806950115

10. Xie Z, Yan B, Lee JH, et al. Effects of oxide supports on the $CO_2$ reforming of ethane over Pt-Ni bimetallic catalysts. *Appl Catal B Environ*. 2019;245:376-388. doi:10.1016/j.apcatb.2018.12.070

11. Xie Z, Yan B, Zhang L, Chen JG. Comparison of Methodologies of Activation Barrier Measurements for Reactions with Deactivation. *Ind Eng Chem Res*. 2017;56:1360-1364. doi:10.1021/acs.iecr.6b04626

12. Thomas JM, Thomas WJ. *Principles and Practice of Heterogeneous Catalysis*. 2nd ed. John Wiley & Sons, Incorporated; 2014.

13. Trovarelli A. Catalytic Properties of Ceria and $CeO_2$ -Containing Materials. *Catal Rev*. 1996;38(4):439-520. doi:10.1080/01614949608006464

14. Niemantsverdriet JW. *Spectroscopy in Catalysis: An Introduction*. 3rd ed. Weinheim: WILEY-VCH Verlag GmbH & Co. KGaA; 2007.

# Chapter 3: Combining $CO_2$ Reduction with Propane Oxidative Dehydrogenation over Bimetallic Catalysts

## 3.1 Abstract

The inherent variability and insufficiencies in the co-production of propylene from steam crackers has raised concerns regarding the global propylene production gap and has directed industry to develop more on-purpose propylene technologies. The oxidative dehydrogenation of propane by $CO_2$ ($CO_2$-ODHP) can potentially fill this gap while consuming a greenhouse gas. Non-precious FeNi and precious NiPt catalysts supported on $CeO_2$ have been identified as promising catalysts for $CO_2$-ODHP and dry reforming, respectively, in flow reactor studies conducted at 823 K. In-situ X-ray absorption spectroscopy measurements revealed the oxidation states of metals under reaction conditions and density functional theory calculations were utilized to identify the most favorable reaction pathways over the two types of catalysts.

## 3.2 Introduction

Propylene is one of the most diverse petrochemical building blocks used for the production of many chemicals (e.g. polypropylene, propylene oxide, and acrylonitrile). The co-production of propylene from steam and fluidized crackers is anticipated to be insufficient to satisfy the rapidly growing demand.[1] Consequently, there is a need for the development of economic on-purpose production techniques to produce additional propylene. The direct dehydrogenation of propane (DDP) is thermodynamically limited and is highly endothermic ($\Delta H°_r$ = 29.70 kcal/mol), requiring temperatures that may exceed 973 K for significant propylene yields.[2] In principle, the introduction of $CO_2$ as a mild oxidant into the feed alters the dehydrogenation pathway by oxidizing the

abstracted hydrogen from the alkane and consequently releasing the heat of reaction that reduces operating temperatures.[2,3] The presence of $CO_2$ can also increase the equilibrium conversion of propane by consuming $H_2$ through the reverse water gas shift reaction (RWGS), as seen in the thermodynamic calculations in **Figure 3-1a**. Additionally, unlike regular oxidative dehydrogenation with molecular oxygen, $CO_2$ as a mild oxidant suppresses over-oxidation and thus minimizes the production of carbon oxides. The reactions of propane and $CO_2$ also have the potential to employ two underutilized[4,5,6] reactants to supply propylene as well as to mitigate detrimental $CO_2$ emissions.[7,8]

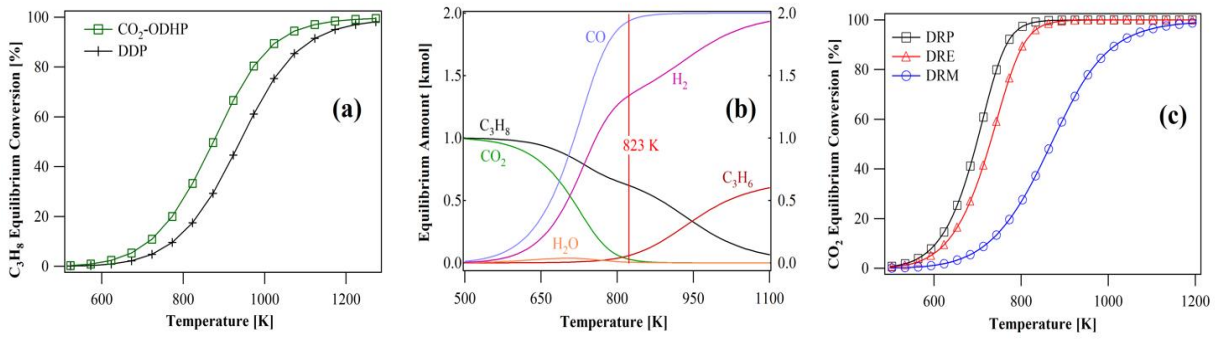


**Figure 3-1.** Thermodynamic equilibrium plots. Equilibrium calculations were performed through HSC Chemistry 8 software, which utilizes a Gibbs free energy minimization algorithm. (**a**) $C_3H_8$ equilibrium conversion for $CO_2$-ODHP and direct dehydrogenation of propane (**b**) product amounts for $CO_2$ + $C_3H_8$ system and (**c**) conversions of propane, ethane, and methane dry reforming; all vs. temperature at 1 atm.

The reactions of $CO_2$ with propane may occur through two distinct pathways, oxidative dehydrogenation ($CO_2 + C_3H_8 \rightarrow C_3H_6 + CO + H_2O$) and dry reforming ($3CO_2 + C_3H_8 \rightarrow 6CO + 4H_2$). The two reactions should occur simultaneously at temperatures around 823 K and above

with considerable conversions (**Figure 3-1b**), allowing the formation of both dehydrogenation products (propylene) and reforming products (synthesis gas). The oxidative dehydrogenation of propane by $CO_2$ ($CO_2$-ODHP) can reach an equilibrium conversion of 33% as opposed to 17% for DDP at 823 K. At that same reaction temperature, as seen in **Figure 3-1c**, $CO_2$ equilibrium conversion for the dry reforming of propane (DRP) can reach up to 98% at a temperature 150 K less than that of methane dry reforming (DRM). This in turn would reduce catalyst deactivation due to coking and phase transformations triggered by the relatively high temperatures commonly used in DRM.[9,10] Furthermore, in the $CO_2$ + $C_3H_8$ system unreacted $CO_2$ can remove surface carbon via the Boudouard reaction ($CO_2 + C_s \rightarrow 2CO$) at temperatures as low as 773 K with moderate rates.[11,12] Thus, it is of great interest to identify catalysts that can either selectively break the C-H bond to produce propylene or the C-C bonds to generate synthesis gas ($CO + H_2$).

Previous work in $CO_2$-ODH primarily focuses on supported chromium catalysts [13,14,15] as a result of their ability to exist in multiple oxidation states [16], but implementation is limited due to short lifecycles and high toxicity of chromium.[17] Ni is mainly used for dry reforming, but catalyst deactivation due to severe coking is still a problem.[18,19,20] To alleviate coke formation, precious metal catalysts (e.g. Rh, Re, Ru) have also been investigated on high surface area $Al_2O_3$.[21,22] However, large scale catalytic conversion of $CO_2$ into valuable products would require the development of cost effective, selective, and coking-resistant catalytic systems. While there are studies that examine the $CO_2$-ODHP or DRP separately, a thorough examination utilizing supported bimetallic catalysts at a temperature range that allows both pathways to occur is still lacking. Ceria ($CeO_2$) is a good choice of oxide support because it has the ability to store/release oxygen and thus may induce direct C-O bond scission of $CO_2$, while also providing available lattice oxygen for coke suppression.[23,24,25,26]

The present work will explore ceria supported bimetallic catalysts, non-precious metal $Fe_3Ni$ as well as precious metal based $Fe_3Pt$ and $Ni_3Pt$, that are active at 823 K. In summary, steady-state flow reactor studies indicate that $Fe_3Ni$ shows promising selectivity toward propylene via the $CO_2$-ODHP pathway, whereas $Ni_3Pt$ is active for the DRP with high selectivity toward CO. Density functional theory calculations on the energetics for the C-H and C-C bond scissions over the two catalysts are in agreement with experimental results.

## 3.3 Methods

### 3.3.1 Catalyst preparation and flow reactor studies

The catalysts evaluated in this study were synthesized through incipient wetness impregnation of metals onto commercially obtained $CeO_2$ (35-45 $m^2/g$, Sigma-Aldrich). Flow reactor experiments were performed under atmospheric pressure utilizing a ¼" quartz U-shaped reactor. All catalysts were reduced at 723 K for 1 hour under a 1:1 $H_2$/Ar flow (40 mL/min total). Subsequently, the temperature was increased and held at 823 K in the presence of 1:1:2 $CO_2$, $C_3H_8$, and Ar for 12 hours. Apparent activation barrier and reaction order experiments were conducted at slightly different reaction conditions to ensure operation in a true intrinsic kinetic regime and minimize transport effects. X-ray absorption near-edge spectroscopy (XANES) measurements were conducted using a custom in-situ micro-channel cell holding ~200 mg of catalyst (60-80 mesh) and a 4-channel vortex fluorescence detector.

### 3.3.2 Density functional theory (DFT) calculations

Spin polarized[31,32] density functional theory (DFT) calculations were performed as an attempt to elucidate the possible pathways of C-C and C-H bond cleavage of propane over $Fe_3Ni(111)$, $Ni_3Pt(111)$ surfaces and FeO/Ni(111) interface using the Vienna Ab-Initio Simulation

Package (VASP) code.[33,34] Projector augmented wave potentials were used to describe the core electrons with the generalized gradient approximation (GGA)[35,36] using PW91 functionals.[37] The Kohn−Sham one-electron wave functions were expanded by using a plane wave basis set with a kinetic energy cutoff of 400 eV. The Brillouin zone was sampled using a 3 × 3 × 1 k-point grid in the Monkhorst−Pack scheme.[38] Ionic positions were optimized until Hellman-Feynman force on each ion was smaller than 0.02 eV/Å. The transition state of a chemical reaction was located using the climbing image nudged elastic band (CI-NEB) method implemented in VASP.[39] The activation energy ($E_a$) of a chemical reaction is defined as the energy difference between the initial and transition states while the reaction energy ($\Delta E$) is defined as the energy difference between the initial and final states.

## 3.4 Results

### 3.4.1 Catalytic evaluation with kinetics and deactivation patterns

Flow reactor studies measuring both $CO_2$-ODHP and DRP activity simultaneously are summarized in **Table 3-1** along with CO chemisorption values. All catalysts were synthesized via incipient wetness impregnation of metals onto commercially obtained $CeO_2$ (35-45 $m^2/g$, Sigma Aldrich). Results for conversions and product selectivity following time on stream for all catalysts are shown in **Figure 3-2**.

**Table 3-1.** Catalyst flow reactor results for $CO_2$ + $C_3H_8$ reaction. 10 mL/min each reactant at 823 K with Ar diluent (20 mL/min) and 100 mg of catalyst (16-20 mesh). Catalysts marked with an asterisk indicate that the sample was diluted to achieve comparable $C_3H_8$ reactant conversion to $Fe_3Ni$. Values are obtained by averaging data from hours 10-12. Selectivity and yield are on a $C_3H_8$ basis (including only carbonaceous species). Catalysts are synthesized by atomic ratios corresponding to a 1.67 wt.% $Pt_1$ basis, thus the weight percent of $Fe_3$, $Ni_1$, and $Ni_3$ are 1.43, 0.5, and 1.5, respectively. The nomenclature assigned by subscripts such as in $Fe_3Ni$ means that there are 3 atoms of Fe for every atom of Ni.

| | | **$Fe_3Ni_1$** | **$Fe_3Pt_1$** | **$Ni_3Pt_1$** | ***$Ni_3Pt_1$** | **$Ni_1$** | **$Ni_3$** | **$Pt_1$** |
|---|---|---|---|---|---|---|---|---|
| **CO uptake (μmol·g$^{-1}$)** | | | | | | | | |
| | | 31.9 | 31.5 | 50.1 | - | 13.1 | 37.7 | 16 |
| **Conversion (%)** | | | | | | | | |
| | $CO_2$ | 4 | 2.6 | 39.4 | 7.8 | 9.3 | 32.8 | 4.2 |
| | $C_3H_8$ | 2.7 | 1.1 | 11.6 | 2.2 | 3 | 9.6 | 1.6 |
| **TOF (site$^{-1}$·min$^{-1}$)** | | | | | | | | |
| | $CO_2$ | 5.7 | 3.5 | 37.5 | - | 31.9 | 40.2 | 8.1 |
| | $C_3H_8$ | 3.4 | 1.5 | 10.5 | - | 8.9 | 11.4 | 2.8 |
| **Selectivity (%)** | | | | | | | | |
| | CO | 40.2 | 65.1 | 96.2 | 87.8 | 86.8 | 94.9 | 77 |
| | $C_3H_6$ | 58.2 | 32 | 2.8 | 11 | 12.3 | 2.9 | 21.2 |
| | $CH_4$ | 0.8 | 1.3 | 0.83 | 0.9 | 0.6 | 2.11 | 0.8 |
| | $C_2H_6$ | 0 | 0 | 0.1 | 0 | 0.24 | 0.05 | 0.9 |
| | $C_2H_4$ | 0.8 | 1.6 | 0 | 0.3 | 0 | 0.06 | 0 |
| **Yield (%)** | | | | | | | | |
| | CO | 1.1 | 0.7 | 11.1 | 2 | 2.6 | 9.1 | 1.3 |
| | $C_3H_6$ | 1.6 | 0.3 | 0.3 | 0.2 | 0.4 | 1.1 | 0.4 |

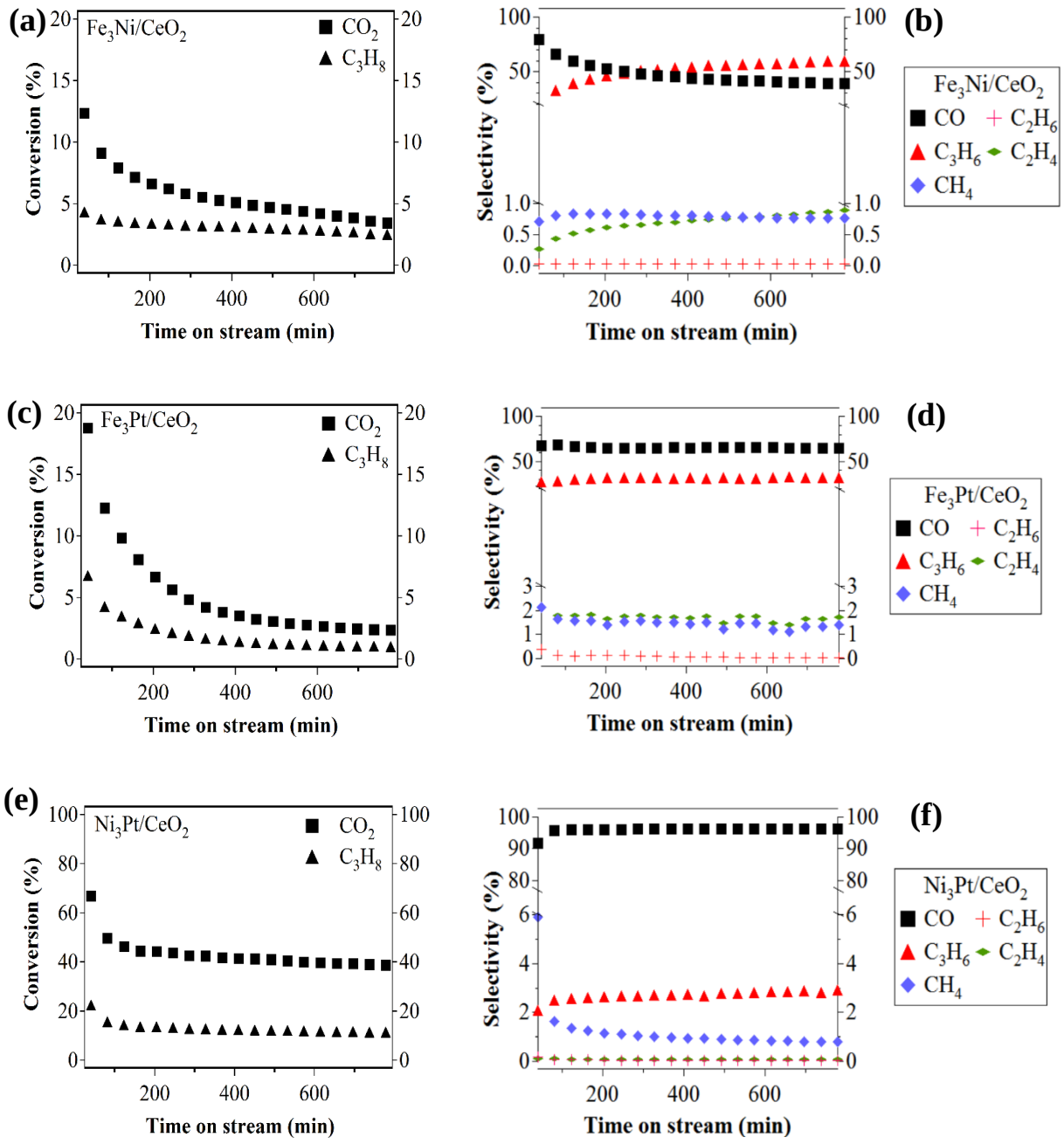


**Figure 3-2.** Steady-state flow reactor results of reactant conversion and product selectivity following time on stream. (**a, b**) $Fe_3Ni$, (**c, d**) $Fe_3Pt$, and (**e, f**) $Ni_3Pt$ for the $CO_2 + C_3H_8$ reaction (10 mL/min each) at 823 K with Ar diluent (20 mL/min) and 100 mg of catalyst.

The monometallic $Ni_1$ catalyst exhibits 12% and 87% $C_3H_6$ and reforming selectivity, respectively with minimal cracking products ($CH_4$ and $C_2$ hydrocarbons), while the $Fe_3$ monometallic catalyst is not active for either reaction. The bimetallic system, $Fe_3Ni$, however, at steady-state demonstrates propylene production from the $CO_2$-ODHP reaction, corresponding to 58.2% $C_3H_6$ selectivity. The differences among the propylene yields on a $C_3H_8$ basis provided in **Table 3-2** of $Fe_3Ni$ (1.6% $C_3H_6$ yield) and the respective monometallics ($C_3H_6$ yield of 0.4% over Ni and 0.2% over Fe) indicate that there is a synergistic effect from the formation of the bimetallic $Fe_3Ni$ catalyst. Exchanging Ni in the $Fe_3Ni$ catalyst with precious metal Pt ($Fe_3Pt$) roughly reduces the activity by half, decreases the selectivity toward $C_3H_6$ to 32%, and is unstable compared to $Fe_3Ni$ (**Figure 3-3**). The other precious metal bimetallic catalyst, $Ni_3Pt$, primarily performs the DRP reaction with 39% $CO_2$ conversion, a robust selectivity toward CO of 88% at comparable reactant conversions (**Table 3-2**) and is more stable compared to monometallic $Ni_3$ (**Figure 3-4**). Thus, when Ni is coupled with non-precious Fe at a ratio of 1:3, higher dehydrogenation activity can be achieved, and propylene is produced. In contrast, when Ni is alloyed with precious metal Pt, reforming activity is enhanced compared to monometallic $Ni_3$.

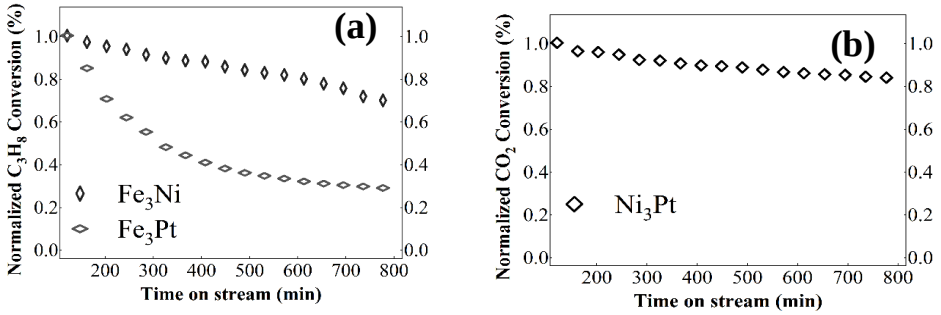


**Figure 3-3.** Normalized reactant conversion following time on stream. (**a**) $Fe_3Ni$ and $Fe_3Pt$ (**b**) $Ni_3Pt$. Normalization is performed after the initial 123 minutes on stream.

**Table 3-2.** Comparable $C_3H_8$ reactant conversion with selectivity and yield. Values are for the $CO_2 + C_3H_8$ reaction (10 mL/min each) at 823 K with Ar (20 mL/min) achieved by diluting (d) the catalyst with treated $SiO_2$ in a 1 to 5 ratio. Steady-state selectivity and yield were on a $C_3H_8$ basis (including only carbonaceous species).

| Catalyst | Conversion (%) | | Selectivity (%) | | | Yield (%) | |
|---|---|---|---|---|---|---|---|
| Supported on $CeO_2$ | $CO_2$ | $C_3H_8$ | CO | $C_3H_6$ | $C_1$-$C_2$ | CO | $C_3H_6$ |
| $Fe_3Ni$ | 4.0 | 2.7 | 40.2 | 58.2 | 1.6 | 1.1 | 1.6 |
| $Fe_3Pt$ | 2.6 | 1.1 | 65.1 | 32.0 | 2.9 | 0.7 | 0.3 |
| d-$Ni_3Pt$ | 7.8 | 2.2 | 87.8 | 11.0 | 1.2 | 2.0 | 0.2 |

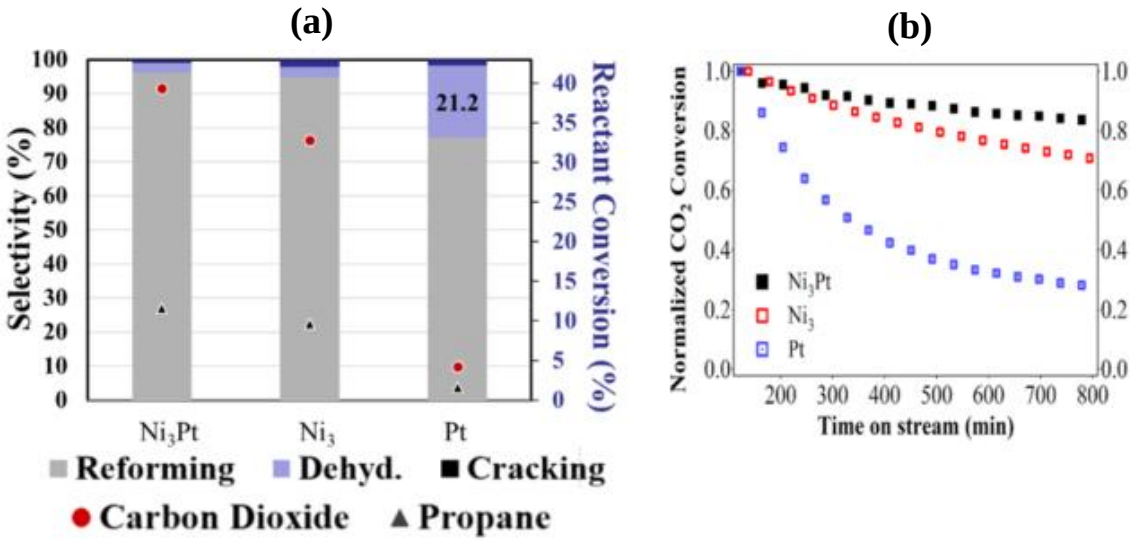


**Figure 3-4.** Comparison among $Ni_3Pt_1/CeO_2$ and the respective monometallics. Values are for the reaction of $CO_2 + C_3H_8$ (10 mL/min each) with Ar diluent (20 mL/min) at 823 K and 100 mg of catalyst. (**a**) Selectivity and conversion of $Ni_3Pt$, $Ni_3$, and $Pt_1$ (**b**) normalized $CO_2$ conversion vs. time on stream.

$CO_2$ conversion vs CO selectivity plots for $Fe_3Ni_1$ and $Ni_3Pt_1$ are depicted in **Figure 3-5** to further assess inherent activity for $CO_2$-ODHP versus DRP. For $Ni_3Pt$, the y-intercept of CO selectivity is 97%, suggesting it is a typical reforming catalyst. While for $Fe_3Ni$, the y intercept of CO selectivity is 22.2%. The primary reactions of $CO_2$ + $C_3H_8$ include the dry reforming [Rxn Equation 3-1] and $CO_2$-ODHP [Rxn Equation 3-2], which can occur simultaneously at temperatures above 823 K.

$C_3H_8 + 3CO_2 \rightarrow 6CO + 4H_2$ $\Delta H^o_R$=622 kJ mol$^{-1}$ $\Delta G^o_R$=384 kJ mol$^{-1}$ (Rxn Equation 3-1)

$C_3H_8 + CO_2 \rightarrow C_3H_6 + CO + H_2O$ $\Delta H^o_R$=166 kJ mol$^{-1}$ $\Delta G^o_R$=119 kJ mol$^{-1}$ (Rxn Equation 3-2)

Other relevant reactions for propane dry reforming include propane decomposition to carbon, $H_2$, and $CH_4$ (Rxn Equation 3-3), the reverse Boudouard reaction (Rxn Equation 3-4), the reverse water-gas shift (Rxn Equation 3-5), and direct propane dehydrogenation (Rxn Equation 3-6) as listed below.

$C_3H_8 \rightarrow CH_4 + 2C(s) + 2H_2$ $\Delta H^o_R$=30 kJ mol$^{-1}$ $\Delta G^o_R$=-26 kJ mol$^{-1}$ Rxn Equation 3-4)

$CO_2 + C(s) \rightarrow 2CO$ $\Delta H^o_R$=172 kJ mol$^{-1}$ $\Delta G^o_R$=120 kJ mol$^{-1}$ Rxn Equation 3-5)

$CO_2 + H_2 \rightarrow H_2O + CO$ $\Delta H^o_R$=41 kJ mol$^{-1}$ $\Delta G^o_R$=29 kJ mol$^{-1}$ Rxn Equation 3-6)

$C_3H_8 \rightarrow C_3H_6 + H_2$ $\Delta H^o_R$=125 kJ mol$^{-1}$ $\Delta G^o_R$=90 kJ mol$^{-1}$ Rxn Equation 3-7)

The amount of CO produced from $C_3H_8$ can be calculated via the oxygen balance (i.e., all the oxygen in CO and $H_2O$ comes from $CO_2$),

$$F^{outlet}_{CO\ originated\ from\ CO_2} = \frac{F^{outlet}_{CO} + F^{outlet}_{H_2O}}{2} \quad \text{(Equation 3-8)}$$

$$F^{outlet}_{CO\ originated\ from\ C_3H_8} = F^{outlet}_{CO} - F^{outlet}_{CO\ originated\ from\ CO_2} \quad \text{(Equation 3-9)}$$

Where *F* is the flow rate of reactant or product in mol/min. If no over-oxidation were to occur in the above reaction scheme, then the total CO produced would be equivalent to the sum of $C_3H_6$ and $H_2O$ produced. However, over the $Fe_3Ni$ catalyst there is more CO than the sum, (**Figure 3-6**), indicating that CO can also be produced via over-oxidation of olefins/lighter components and/or the reverse Boudouard reaction. It can be assumed that over-oxidation is included in reforming because all the olefins, lighter components, and C(s) are produced from $C_3H_8$ and are then oxidized by $CO_2$ to finally produce CO. Among one of the fundamental differences between $CO_2$-ODHP and conventional oxidative dehydrogenation is the net reduction of $CO_2$ and the production of CO from over-oxidation, while the latter reaction only produces more $CO_2$ upon over-oxidation.

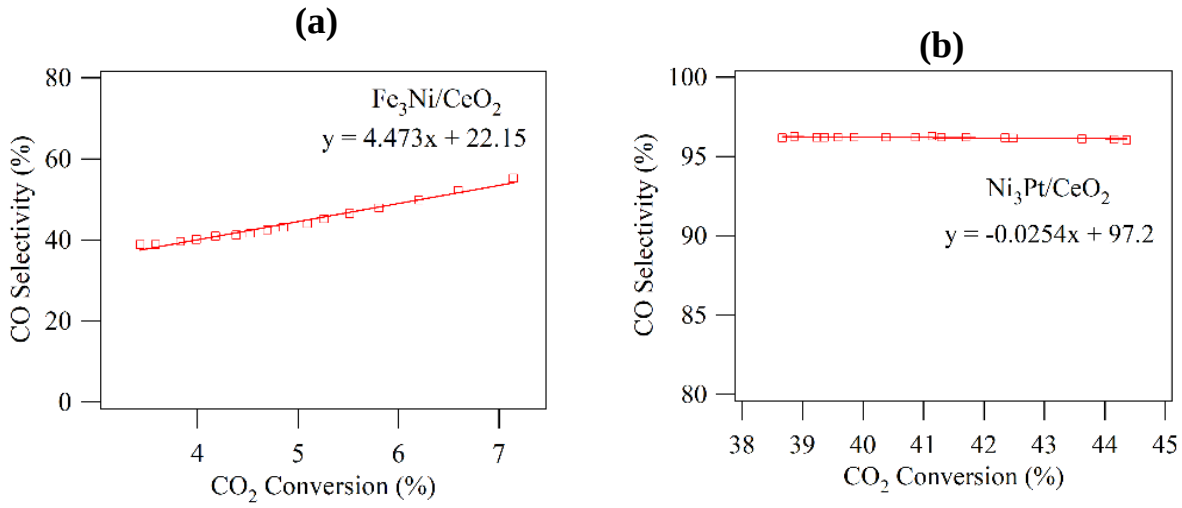


**Figure 3-5.** $CO_2$ conversion vs CO selectivity plots. (**a**) $Fe_3Ni$ and (**b**) $Ni_3Pt$ bimetallics supported on $CeO_2$.

Kinetic studies examining the influence of the reactant partial pressure and the reaction temperature on the activity of $Fe_3Ni$ and $Ni_3Pt$ were conducted to further evaluate the differences between the two types of catalysts. The apparent activation energies were derived by measuring production rates in the temperature range of 803 – 843 K. Over $Fe_3Ni$, the activation barrier for propane $CO_2$ oxidative dehydrogenation was found to be 115 $kJ \cdot mol^{-1}$, while the activation barrier for reforming over $Ni_3Pt$ was 119 $kJ \cdot mol^{-1}$. Arrhenius-type plots and additional values are available in **Figure 3-7** and **Table 3-3**, respectively.

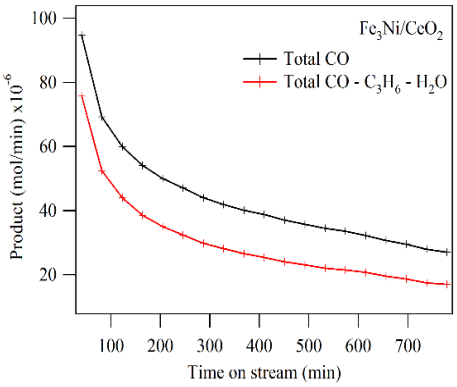


**Figure 3-6.** CO production for $Fe_3Ni$. Total CO production (top black curve) and total CO production subtracting contributions from $CO_2$-ODHP and RWGS (bottom red curve) following time on stream.

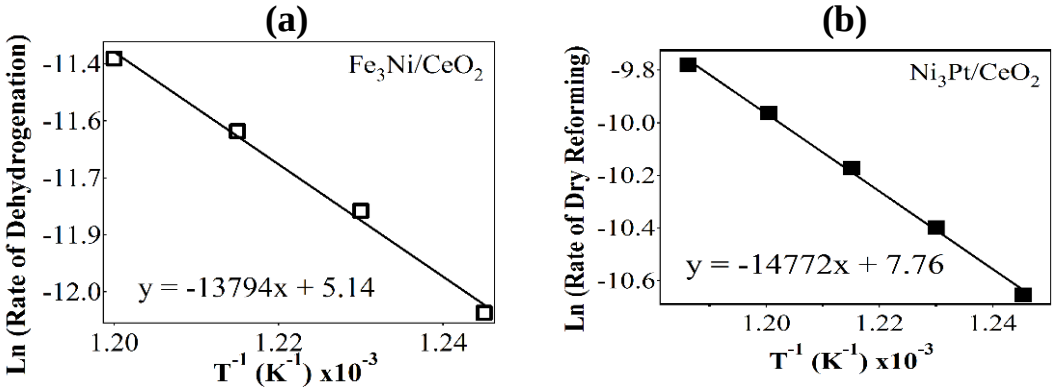


**Figure 3-7.** Apparent activation energy plots. Presented as Ln (rate) versus $T^{-1}$ for (**a**) propane $CO_2$ oxidative dehydrogenation over $Fe_3Ni$ and (**b**) reforming over $Ni_3Pt$.

**Table 3-3.** Activation barrier values for $Fe_3Ni$ and $Ni_3Pt$.

| Activation Barrier Values (kJ/mol) | | | | |
|---|---|---|---|---|
| | $C_3H_8$ | $CO_2$ | $C_3H_6$ | CO |
| $Fe_3Ni$ /$CeO_2$ | 110 | 135 | 115 | 121 |
| $Ni_3Pt$/$CeO_2$ | 109 | 123 | - | 119 |

As seen in **Figure 3-8a**, the reactant consumption rate of $C_3H_8$ for the $Fe_3Ni$ $CO_2$-ODHP catalyst was initially unaffected by increasing the partial pressure of $CO_2$ but upon reaching a $C_3H_8$: $CO_2$ ratio of 1:1, the rate started to decline. The reforming catalyst, on the other hand, was positively influenced by the partial pressure of $CO_2$ until the aforementioned ratio of 1:6. Increasing the $C_3H_8$ partial pressure produced similar trends and are shown in **Figure 3-8**. The declining rates signify that there are less catalytic sites available for one reactant when the other is in excess, indicative of competitive adsorption of adsorbates and/or surface intermediates. Particularly, the rates for both reactants decrease at high propane partial pressure, suggesting that as the reaction progresses intermediates from propane block surface sites and lead to a loss in activity.

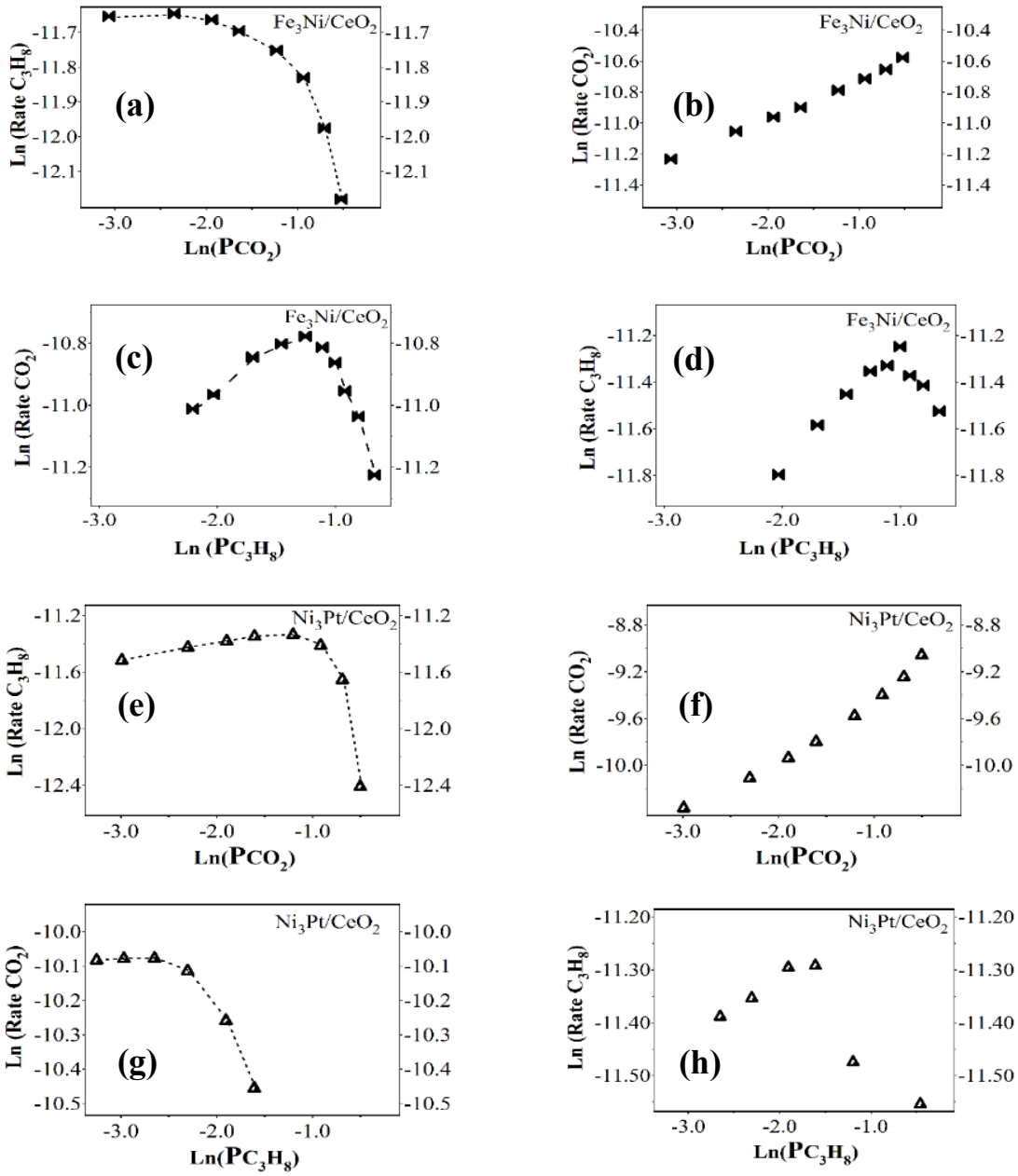


**Figure 3-8.** Effect of reactant partial pressure on reactant consumption rate. $CO_2$ partial pressure on the $C_3H_8$ and $CO_2$ consumption rate (**a, b**), (**e, f**) and the effect of $C_3H_8$ partial pressure on $CO_2$ and $C_3H_8$ consumption rate (**c, d**), (**g, h**) over $Fe_3Ni$ and $Ni_3Pt$, respectively.

To further evaluate how different reaction pathways may influence deactivation patterns, both thermogravimetric (TGA) and energy dispersive spectroscopy (EDS) experiments were conducted and results are provided in **Figure 3-9** and **Figure 3-10**, respectively. The TGA results indicate that the $Fe_3Ni$ catalyst only loses less than half a percent of its original mass, therefore, it is unlikely that the main deactivation pathway is due to coking. The EDS of the spent $Fe_3Ni$ sample shows small regions of higher Ni content, and to a lesser extent, regions with higher Fe. However, in-situ XRD measurements do not reveal obvious agglomeration formation during reaction, and the absence of metal diffraction peaks suggests that the metal particles are most likely less than 2 nm in size (**Figure 2-1**). The $Ni_3Pt$ catalyst loses about 8% of its original mass but does not illustrate signs of sintering. However, the coking over the $Ni_3Pt$ catalyst at comparable propane conversion to $Fe_3Ni$ is not significant.

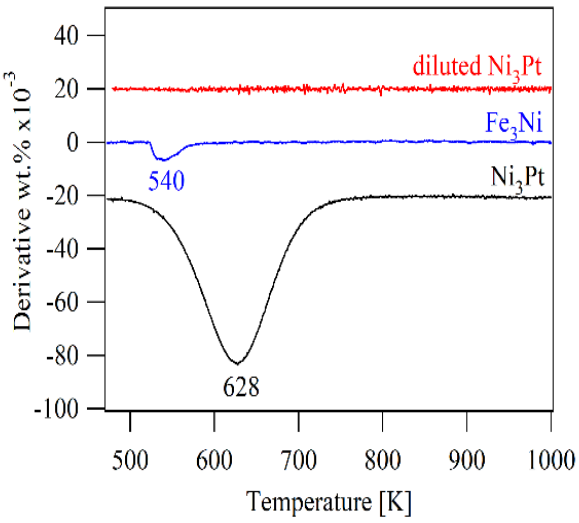


**Figure 3-9.** DTGA results. DTGA for $Fe_3Ni$, $Ni_3Pt$, and diluted $Ni_3Pt$ supported on $CeO_2$.

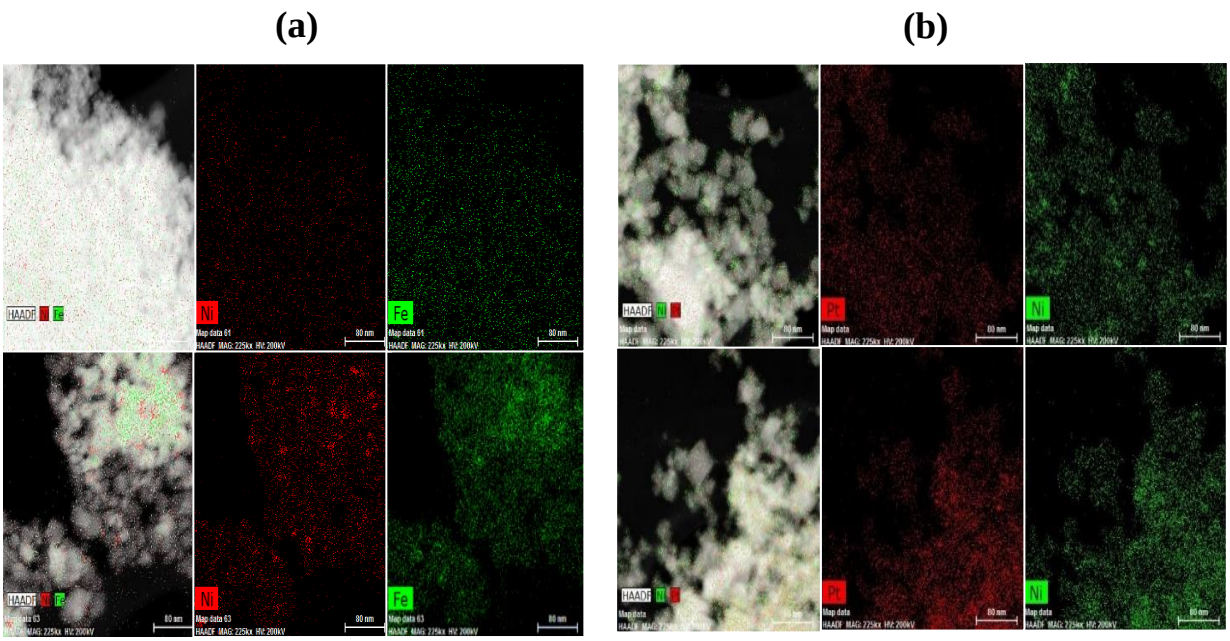


**Figure 3-10.** EDS mapping. (**a**) $Fe_3Ni_1$ and (**b**) $Ni_3Pt$. Top sets are reduced catalyst samples while the bottom set are the post reaction samples.

### 3.4.2 Oxidation states by in-situ XANES

In-situ X-ray Absorption Near Edge Spectroscopy (XANES) measurements were conducted in order to identify the local environment of the metals under reaction conditions, as shown in **Figure 3-11**. Additional details are available in section **3.5.1** which describes the rationale behind the Extended X-ray Absorption Fine Structure (EXAFS) fitting and XANES analysis.The XANES data identified that under reaction conditions the $Ni_3Pt$ catalyst consisted of metallic Pt (**Figure 3-12**) and that both the $Fe_3Ni$ and $Ni_3Pt$ catalysts consisted of metallic Ni (**Figure 3-11a**). On the other hand, the Fe in the $Fe_3Ni$ catalyst was in the oxidized form. The EXAFS fitting of $Fe_3Ni$ suggested the presence of an inserted oxygen through Fe-O-Fe as well as Fe-O bonds (**Table 3-4**). Theofanidis et al. and Kim et al. studied DRM over higher loading Ni-Fe catalysts (8 wt.% Ni-5 wt.% Fe and 8.8 wt.% Ni- 2.1 wt.% Fe, respectively) supported on magnesium aluminate and they also observed oxidized Fe under in-situ conditions but in an

oxidation state of 2+. [40,41] For the $Ni_3Pt$ catalyst, the EXAFS fitting indicates that the coordination number of the Pt-Pt and Pt-Ni bonds is 3.4 and 6.4, respectively, confirming the formation of the Pt-Ni bimetallic bond.

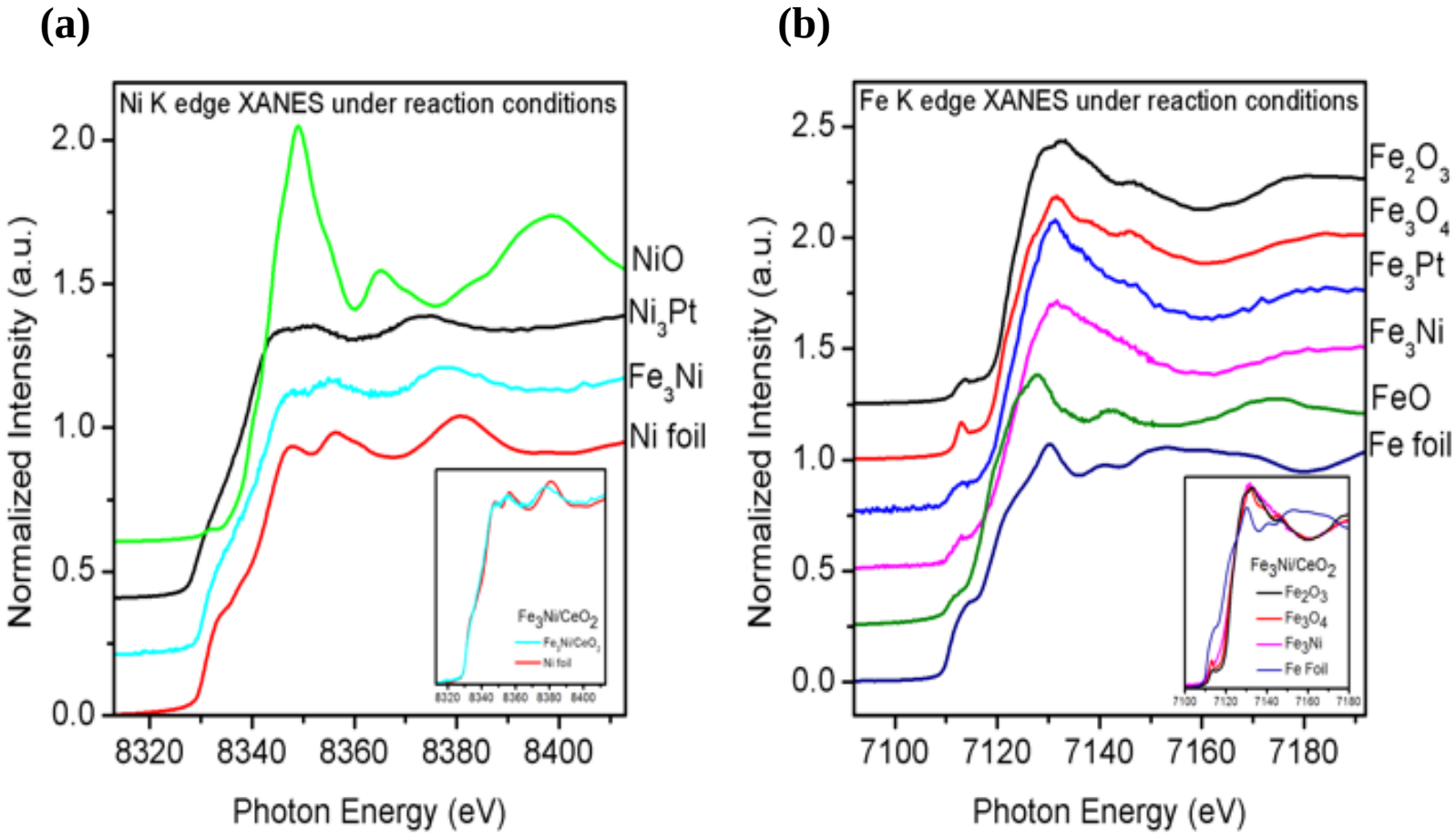


**Figure 3-11.** In-situ XANES spectra. (**a**) Ni and (**b**) Fe K edges of all the bimetallic catalysts with respective references. The insets show more detailed comparison of $Fe_3Ni$ with model compounds.

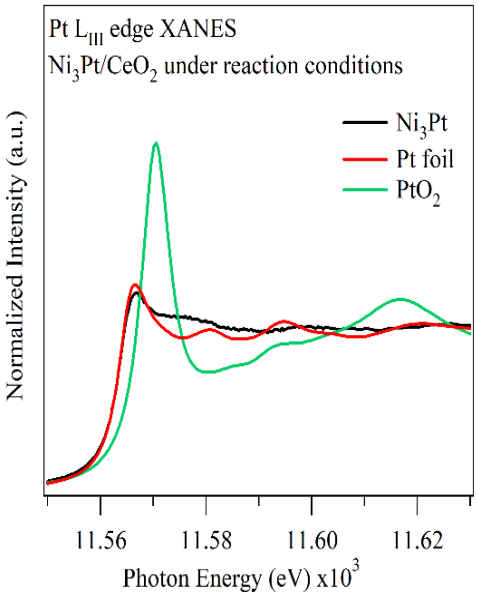


**Figure 3-12.** In-situ XANES spectra. Pt $L_{III}$ edge of $Ni_3Pt_1/CeO_2$ with respective references.

**Table 3-4.** EXAFS summary. EXAFS analysis for the reaction of $CO_2$ + $C_3H_8$ over $Fe_3Ni_1/CeO_2$ and $Ni_3Pt_1/CeO_2$.

| Sample/Reaction | K Edge | Shell | Bond length (Å) | Coordination Number | $\sigma^2$ (Å$^2$) |
|---|---|---|---|---|---|
| $Fe_3Ni/CeO_2$ $C_3$ $CO_2$-ODH | Ni | Ni-Ni/ Ni-Fe | 2.45+/-0.02 | 10.4+/-0.9 | 0.015 |
| | Fe | Fe-O | 1.88+/-0.02 | 3.9+/-1.8 | 0.012 |
| | | Fe-Fe/ Fe-Ni | 2.88+/0.02 | 1.3+/-0.5 | 0.003 |
| | | Fe-O-Fe | 3.53+/-0.03 | 0.7+/-0.4 | 0.003 |
| $Ni_3Pt/CeO_2$ $C_3$ $CO_2$-ODH | Pt $L_{III}$ | Pt-Ni | 2.56+/-0.02 | 6.4+/-1.4 | 0.010(2) |
| | | Pt-Pt | 2.78+/-0.03 | 3.4+/-0.8 | 0.010(2) |

### 3.4.3 Reaction pathways and DFT calculations

Density functional theory (DFT) calculations were performed on bulk-terminated-$Fe_3Ni(111)$ and Pt-terminated-$Ni_3Pt(111)$ surfaces (**Figure 3-13**) to further gain insight into the potential reaction pathways for the oxidative C-H and C-C bond cleavage of propane to form $*CH_3CHCH_2$ + $H_2O(g)$ and $*CH_3CH_2$ + *CO + $H_2O(g)$, respectively. In these calculations, the surfaces are first modified by *O atoms assuming that $*CO_2$ dissociates to form *CO + *O. The DFT optimized geometries in **Figure 3-14** show that the intermediates $*CH_3CH_2CH_2O$, $*CH_3CH_2CHO$ and $*H_2O$ interact with the surfaces via the oxygen atoms while other intermediates $*CH_3CH_2CH_2$, $*CH_3CHCH_2$, $*CH_3CH_2$, and *CO interact with the surfaces via the carbon atoms. It is noted that, even though the binding configurations of intermediates are similar on both surfaces, all the intermediates bind more strongly on bulk-terminated-$Fe_3Ni(111)$ than on Pt-terminated-$Ni_3Pt(111)$ (**Table 3-5** and **Table 3-6**). The DFT calculated binding energies were then used to calculate the change in energy for the oxidative C-H and C-C bond scission of propane. On bulk-terminated-$Fe_3Ni(111)$, **Figure 3-15a** shows that the pathway for the oxidative C-H bond cleavage lies lower in energy than that for the C-C bond scission. In contrast, as shown in **Figure 3-15b** on Pt-terminated-$Ni_3Pt(111)$, the pathway for the C-C bond cleavage lies lower in energy than that for the C-H bond.

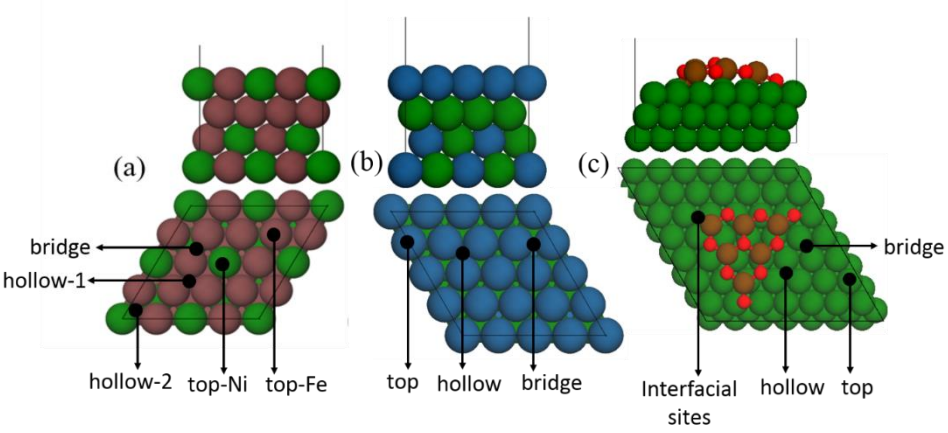


**Figure 3-13.** Optimized geometries of DFT model surfaces. Top image (side) and bottom image (top) views of (**a**) 4 × 4 bulk-terminated $Fe_3Ni(111)$, (**b**) 4 × 4 Pt-terminated-$Ni_3Pt(111)$, and (**c**) FeO/Ni(111) unit cells used in DFT calculations. Various adsorption sites are marked by black circle. Pt: blue; Ni: green; Fe: brown; O: red.

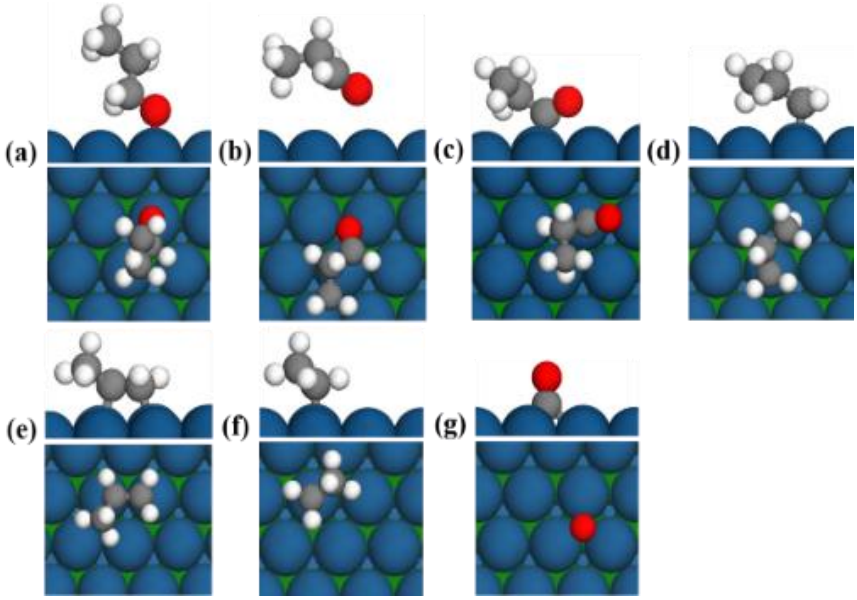


**Figure 3-14.** DFT optimized geometries on the Pt-terminated-$Ni_3Pt(111)$ surface. Top image (side) and bottom image (top) views of (**a**) $CH_3CH_2CH_2O$, (**b**) $CH_3CH_2CHO$, (**c**) $CH_3CH_2CO$, (**d**) $CH_3CH_2CH_2$, (e) $CH_3CHCH_2$, (**f**) $CH_3CH_2$, and (**g**) CO. Pt: blue, Ni: green, C: grey, O: red, and H: white.

**Table 3-5.** Binding energies. *BE* in eV of adsorbates on various sites shown in **Figure 3-13** on bulk-terminated $Fe_3Ni(111)$.

| Adsorbate | Bound via- | Site | *BE* | Comment |
|---|---|---|---|---|
| $CH_3CH_2CH_2O$ | O | top-Fe | -2.63 | |
| | | top-Ni | -- | moved to hollow |
| | | hollow-1 | -3.31 | |
| | | hollow-2 | -3.13 | |
| | | bridge | -- | moved to hollow |
| $CH_3CH_2CHO$ | C, O | top-Fe_top-Fe | -0.44 | |
| | | top-Fe_top-Ni | -0.74 | |
| | | top-Fe_hollow | -0.86 | |
| | | top-Ni_hollow | -0.78 | |
| | | bridge-bridge | -- | moved to to-hollow |
| $CH_3CH_2CO$ | C, O | top-Fe_top-Fe | -2.45 | |
| | | top-Fe_top-Ni | -2.36 | |
| | | top-Fe_hollow | -2.57 | |
| | | bridge-bridge | -2.45 | moved to top-Fe_bridge |
| $CH_3CH_2CH_2$ | C | top-Fe | -- | moved to hollow |
| | | top-Ni | -- | moved to hollow |
| | | hollow-1 | -1.80 | |
| | | hollow-2 | -1.74 | |
| | | bridge | -- | moved to hollow |
| $CH_3CHCH_2$ | C, C | top-Fe_top-Fe | -0.67 | |
| | | top-Fe_top-Ni | -- | moved to top-Fe_hollow |
| | | top-Fe_hollow | -0.77 | |
| | | bridge-bridge | -0.81 | |
| $CH_3CH_2$ | C | top-Fe | -- | moved to hollow |
| | | top-Ni | -- | moved to hollow |
| | | hollow-1 | -2.01 | |
| | | hollow-2 | -1.76 | |
| | | bridge | -- | moved to hollow |

| | | | | |
|---|---|---|---|---|
| CO | C | top-Fe | -1.90 | |
| | | top-Ni | -1.62 | |
| | | hollow-1 | -1.80 | |
| | | hollow-2 | -1.92 | |
| | | bridge | -- | moved to hollow |
| O | O | top-Fe | -- | moved to hollow |
| | | top-Ni | -- | moved to hollow |
| | | hollow-1 | -6.23 | |
| | | hollow-2 | -6.02 | |
| | | bridge | -- | moved to hollow |

**Table 3-6.** Binding energies. *BE* in eV of adsorbates on various sites shown in **Figure 3-13** on Pt-terminated-$Ni_3Pt(111)$.

| Adsorbate | Bound via- | Site | *BE* | Comment |
|---|---|---|---|---|
| $CH_3CH_2CH_2O$ | O | top | -1.38 | |
| | | hollow | -- | moved to top |
| | | bridge | -- | moved to top |
| $CH_3CH_2CHO$ | C, O | | -0.11 | physisorbed not specific to site |
| $CH_3CH_2CO$ | C | top | -2.16 | |
| | | hollow | -- | moved to top |
| | | bridge | -- | moved to top |
| $CH_3CH_2CH_2$ | C | top | -1.70 | |
| | | hollow | -- | moved to top |
| | | bridge | -- | moved to top |
| $CH_3CHCH_2$ | C, C | top-top | -0.56 | |
| | | top-hollow | -- | moved to top-top |
| | | top-bridge | -- | moved to top-top |
| $CH_3CH_2$ | C | top | -1.82 | |
| | | hollow | -1.75 | |

| | | | | |
|---|---|---|---|---|
| | | bridge | -- | moved to top |
| CO | C | top | -1.06 | |
| | | hollow | -1.30 | |
| | | bridge | -- | moved to hollow |
| O | O | top | -- | moved to hollow |
| | | hollow | -3.29 | |
| | | bridge | -- | moved to hollow |

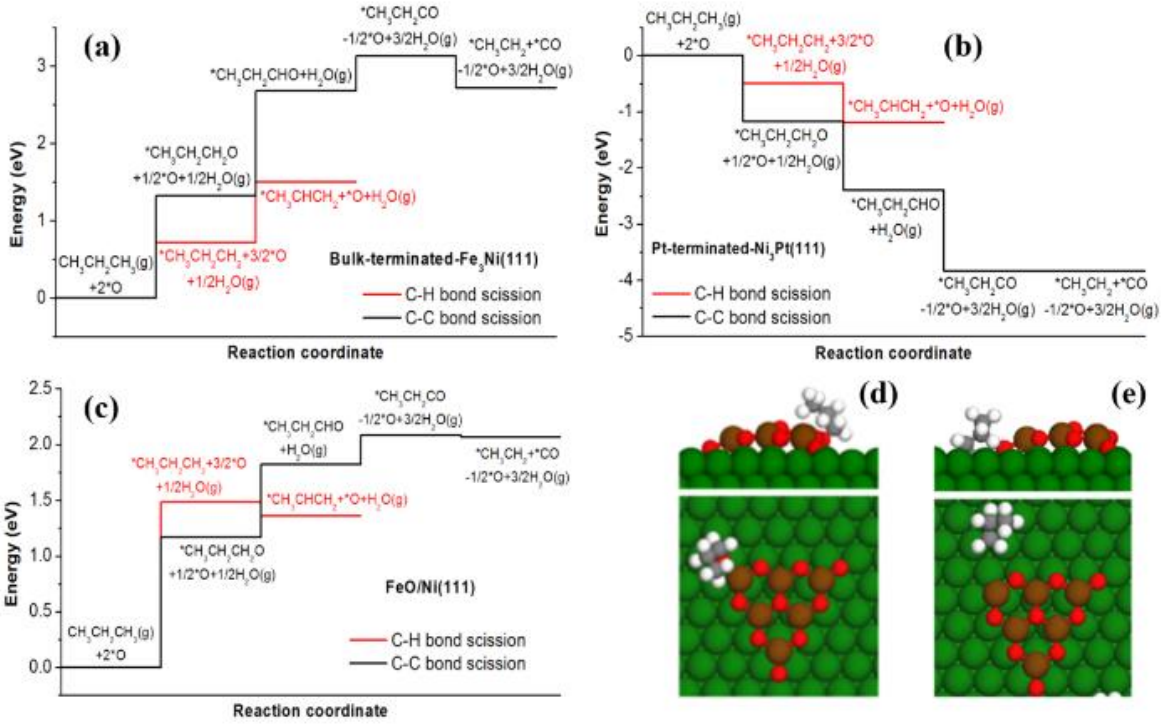


**Figure 3-15.** DFT calculated energy profiles for the oxidative C-H and C-C bond scission pathways. (**a**) bulk $Fe_3Ni(111)$ surface, (**b**) Pt-terminated $Ni_3Pt(111)$ surface, and (**c**) FeO/Ni(111) interface as well as the optimized geometries of (**d**) $CH_3CH_2CH_2O$ and (**e**) $CH_3CH_2CH_2$ on FeO/Ni(111).

Overall the DFT results reveal that the C-C bond cleavage pathway is preferred on $Ni_3Pt(111)$, while bulk-terminated-$Fe_3Ni(111)$ favors the C-H bond cleavage pathway. Kinetically, this is also the case based on the comparison of activation energies (**Table 3-7**). According to the DFT calculations, on Pt-terminated-$Ni_3Pt(111)$, the *O insertion reaction ($*CH_3CH_2CH_2 + *O \rightarrow *CH_3CH_2CH_2O + *$) along the C-C bond cleavage pathway ($\Delta E$ = -0.75 eV and $E_a$ = 1.07 eV) is thermodynamically and kinetically more favorable than the oxidative dehydrogenation reaction ($*CH_3CH_2CH_2 + *O \rightarrow *CH_3CHCH_2 + *OH$) along the C-H bond cleavage pathway ($\Delta E$ = -0.51 eV and $E_a$ = 1.33 eV). In contrast, on bulk-terminated-$Fe_3Ni(111)$, the oxidative dehydrogenation reaction ($\Delta E$ = 0.29 eV and $E_a$ = 1.02 eV) is more favorable than the *O insertion reaction ($\Delta E$ = 0.43 eV and $E_a$ = 3.30 eV). These DFT predictions are in agreement with experimental observations, suggesting that the bulk-terminated-$Fe_3Ni(111)$ surface promotes the oxidative C-H bond cleavage of propane to form $*CH_3CHCH_2$ while the Pt-terminated-$Ni_3Pt(111)$ surface promotes the C-C bond cleavage of propane to form *CO.

**Table 3-7.** DFT calculated reaction energy ($\Delta E$) and activation energy ($E_a$) in eV. Shown for selected reaction steps on Pt-ter-$Ni_3Pt(111)$, bulk-ter-$Fe_3Ni(111)$ and $Fe_3O_3$/Ni(111).

| | $*CH_3CH_2CH_3 + *O \rightarrow *CH_3CH_2CH_2 + *OH$ | | $*CH_3CH_2CH + *O \rightarrow *CH_3CH_2CH_2O + *$ | | $*CH_3CH_2CH + *O \rightarrow *CH_3CHCH_2 + *OH$ | |
|---|---|---|---|---|---|---|
| Surface | $\Delta E$ | $E_a$ | $\Delta E$ | $E_a$ | $\Delta E$ | $E_a$ |
| Pt-ter-$Ni_3Pt(111)$ | -0.49 | 1.33 | -0.75 | 1.07 | -0.51 | 1.33 |

| | | | | | | |
|---|---|---|---|---|---|---|
| Bulk-ter-$Fe_3Ni(111)$ | 0.43 | 1.61 | 0.43 | 3.30 | 0.29 | 1.02 |
| $Fe_3O_3/Ni(111)$ | 0.63 | 1.88 | 0.01 | 2.13 | -0.40 | 0.29 |

To account for the potential FeO-Ni interfacial active sites based on the in-situ experimental observation of oxidized Fe in the $Fe_3Ni$ catalyst, further DFT calculations were carried out to investigate the pathways for the oxidative C-H and C-C bond cleavage of propane on the FeO/Ni(111) interface. For the $FeO_x$ clusters supported on Ni(111), both $Fe_6O_9$ and $Fe_3O_3$ clusters on 3 layer 7 × 7 Ni(111) and 5 × 5 Ni(111) surfaces (**Figure 3-16**) were considered. The oxygenated species (*O, *CO, *$CH_3CH_2CH_2O$, *$CH_3CH_2CHO$ and *$CH_3CH_2CO$) prefer to adsorb at the interfacial sites while *$C_xH_y$ species (*$CH_3CH_2CH_2$, *$CH_3CHCH_2$ and *$CH_3CH_2$) most favourably adsorb on Ni(111) sites (**Table 3-8** and **Figure 3-17**). The energy diagram in **Figure 3-15c**, calculated based on the DFT obtained binding energies of the potential intermediates, show that the first steps in oxidative C-C and C-H bond cleavage pathways are competitive. The subsequent step to form *$CH_3CHCH_2$ is downhill in energy along the oxidative C-H bond cleavage pathway; in contrast, the subsequent steps are uphill in energy along the oxidative C-C bond cleavage pathway. Again, such thermodynamic predictions are fully supported by the calculated $E_a$, showing that the oxidative dehydrogenation reaction ($\Delta E$ = -0.40 eV and $E_a$ = 0.29 eV) is highly favorable over the *O insertion reaction ($\Delta E$ = 0.01 eV and $E_a$ = 2.13 eV) on the $Fe_3O_3/Ni(111)$ surface. This indicates that the oxidative dehydrogenation pathway should be more favorable than reforming, consistent with experimental observation.

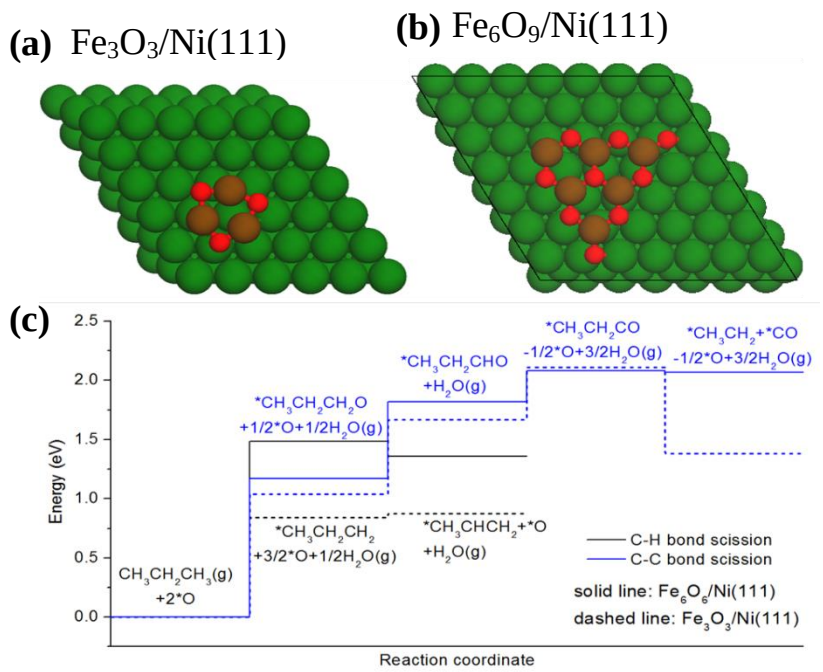


**Figure 3-16.** DFT calculations on the FeO/Ni(111) interface. (**a**) $Fe_3O_3$/Ni(111), (**b**) $Fe_6O_9$/Ni(111), and (**c**) calculated energy profiles for the oxidative C-H and C-C bond scission pathways on both model surfaces

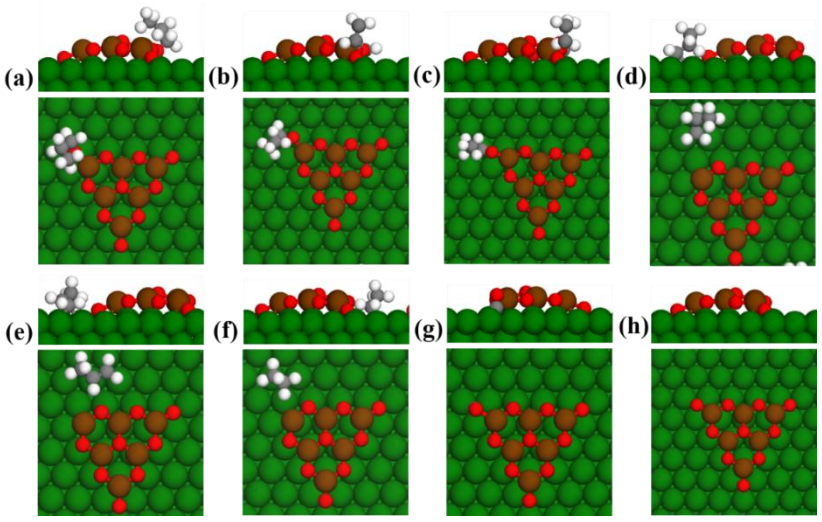


**Figure 3-17.** DFT optimized geometries on FeO/Ni(111). Top (side) and bottom (top) views of (**a**) $CH_3CH_2CH_2O$, (**b**) $CH_3CH_2CHO$, (**c**) $CH_3CH_2CO$, (**d**) $CH_3CH_2CH_2$, (**e**) $CH_3CHCH_2$, (**f**) $CH_3CH_2$, (**g**) CO and (**h**) O. Ni: green, Fe: brown, C: grey, O: red, and H: white

**Table 3-8.** Binding energies. *BE* in eV of adsorbates on various sites shown in **Figure 3-13** on $Fe_6O_9$/Ni(111). Since *O and *CO are more strongly bound at the FeO/Ni(111) interface, binding of $*C_xH_yO$ species were investigated only at the FeO/Ni(111) interface.

| Adsorbate | Bound via- | Site | *BE* | Comment |
|---|---|---|---|---|
| $CH_3CH_2CH_2O$ | O | interface | -2.77 | |
| $CH_3CH_2CHO$ | C, O | interface | -0.88 | |
| $CH_3CH_2CO$ | C, O | interface | -2.47 | |
| $CH_3CH_2CH_2$ | C | top | -- | moved to hollow |
| | | hollow | -0.96 | |
| | | bridge | -- | moved to hollow |
| | | interface | -- | moved to hollow |
| $CH_3CHCH_2$ | C, C | top-top | -- | moved to bridge-bridge |
| | | top-hollow | -- | moved to bridge-bridge |
| | | bridge-bridge | -0.50 | |
| | | interface | -- | moved to bridge-bridge |
| $CH_3CH_2$ | C | top | -- | moved to hollow |
| | | hollow | -1.40 | |
| | | bridge | -- | moved to hollow |
| | | interface | -- | moved to hollow |
| CO | C | top | -1.52 | |
| | | hollow | -1.94 | |
| | | interface | -2.04 | |
| O | O | top | | moved to hollow |
| | | hollow | -5.39 | |
| | | interface | -5.78 | |

Finally, on the three surfaces studied the desorption of *CO is expected to be a facile process due to the contribution of entropy at 823 K. *$C_2H_5$ is one of the reaction intermediates that undergoes O-insertion, C-H and C-C bond scission reactions to eventually produce CO, and $H_2$. The *O species on Pt-terminated-$Ni_3Pt$(111) react with *$C_xH_y$ to form the *$C_xH_yO$ intermediate, which promotes the C-C bond scission. In contrast, the more stable *O on bulk-terminated-$Fe_3Ni$(111) and the FeO/Ni(111) interface are expected to remain on the surface, which facilitates the selective C-H bond scission of propane to produce propylene.

## 3.5 Rationale of selected in situ XAS analysis and DFT calculations

### 3.5.1 EXAFS fitting and XANES analysis

In-situ XAS data collection began after the catalyst had been in contact with reaction gasses and at temperature for 10 minutes. Spectra were collected by alternating between edge energies, starting with the Ni K edge until there were three scans on each edge. The oxidation state of Ni was determined by merging the XANES region of the first (TOS 10-15 min), third (TOS 50-55 min), and fifth (TOS 90-95 min) scans. The XANES scans for Fe K or Pt $L_{III}$ edge were taken at TOS 30-35, 70-75, and 110-115 min. No significant spectroscopic changes were detected on a given edge within the allotted time (**Figure 3-18** and **Figure 3-19**).

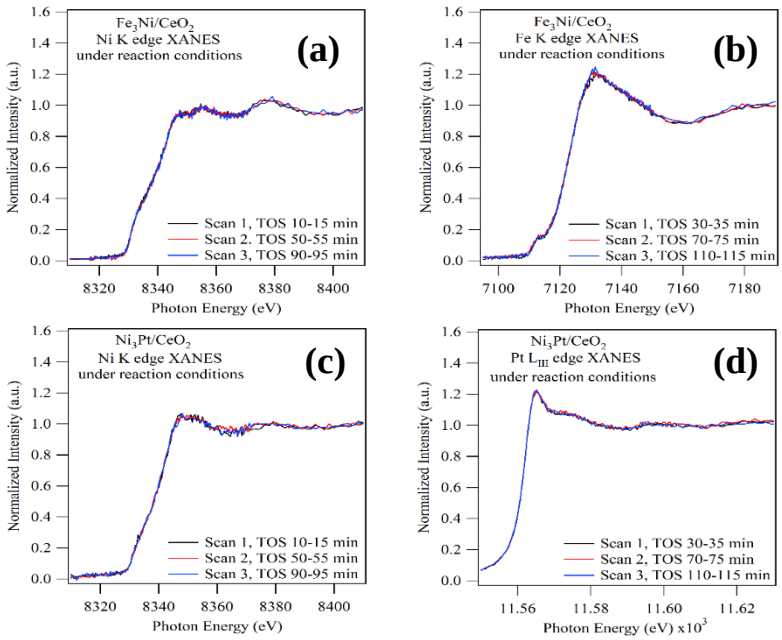


**Figure 3-18.** In-situ reaction scans with indication of time on stream (TOS). Three scans were taken at each edge energy. Ni and Fe K edges for $Fe_3Ni$ (**a**, **b**) and $Ni_3Pt$ (**c**, **d**), respectively.

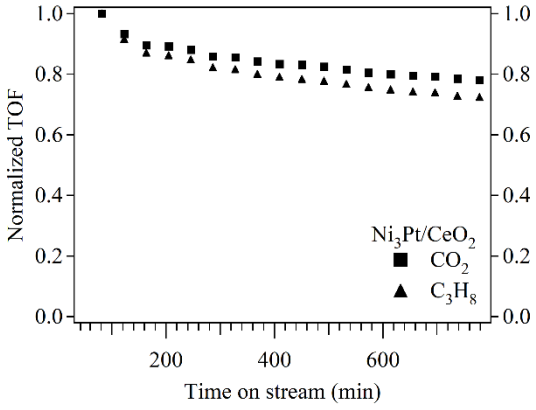


**Figure 3-19.** Normalized TOF. Reactants $CO_2$ and $C_3H_8$ over $Ni_3Pt/CeO_2$ following time on stream after 81 minutes. From the three Ni scans in Figure 3-18 it is not evident that there are any changes in oxidation that accompany the observed change in TOF.

Collecting the fluorescence signal of 3d metals on a support composed by high Z element ($CeO_2$ in our system) usually results in relatively weak signals, due to the strong absorption of the oxide support as well as the relatively strong absorption of window materials at low energy edges. For the presented catalytic systems, the Fe and Ce fluorescence signals strongly overlap. The energy range of Ni was also affected by the Cu signal (the in-situ microchannel cell used is made by Cu). In addition, the data were all collected at 873 K and at such high temperature the high thermal displacement would dump the high k data more strongly. Therefore, the data shown in **Figure 3-20a** and **Figure 3-20b** were noisy above k =10 $Å^{-1,}$ which prevent a good fitting for the relatively weak features between the distance of 2Å-3Å.

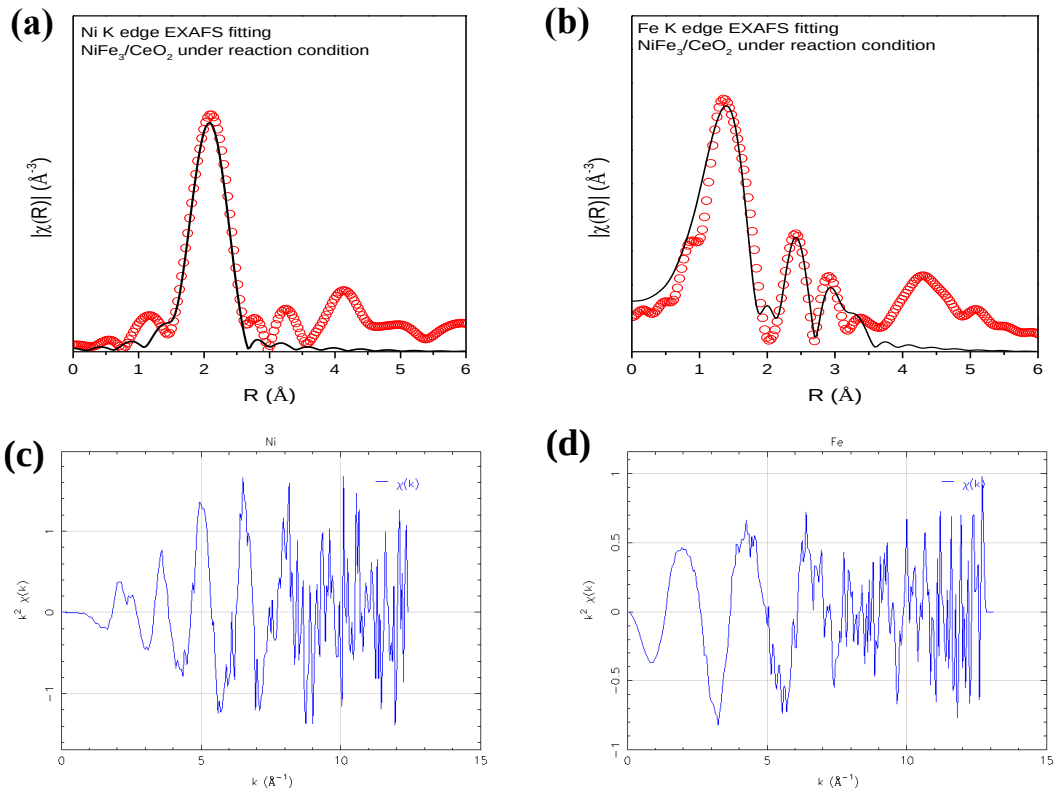


**Figure 3-20.** EXAFS fitting for $Fe_3Ni/CeO_2$. (**a**) Ni and (**b**) Fe edges. Red hollow circles indicate fitted data. (**c**) and (**d**) k space for the Ni and Fe fitting, respectively

In the presented fitting, both Ni and Fe spectra only have about 10 independent points, which could support at most 3-shell fitting (k range from 2.7 to 10.2 with an R range from 1.2 to 3.2~3.6). To reduce the correlation between parameters, constraints and restraints are required. However, since a heterogeneous catalyst is a mixture rather than a compound, there are no good constraints to make. As a result, structural hypotheses are based on the XANES in order not to introduce subjective mistakes. For Ni, metallic Ni foil is used, while for Fe, $Fe_2O_3$ and $Fe_3O_4$ are the models we used.

### 3.5.2 DFT calculations

Two models were used to describe the $Fe_3Ni$ cluster supported on $CeO_2$. One was the bulk terminated $Fe_3Ni(111)$ surface using the -L12 cubic crystal structure and a four layer 4 × 4 surface slab (**Figure 3-12a**). The other was the $FeO_x$ clusters supported on Ni(111), where both $Fe_6O_9$ and $Fe_3O_3$ clusters on 3 layer 7 × 7 Ni(111) and 5 × 5 Ni(111) surfaces (**Figure 3-13c**, **Figure 3-16a**, and **Figure 3-13b**) were considered. In agreement with our experimental observation, the DFT calculations showed that in the presence of oxygen from $*CO_2$ dissociation, Fe segregation is thermodynamically more favorable by -0.08 eV/atom than Ni segregation due to the stronger Fe-O bond than Ni-O. Such O-driven Fe segregation can result in the formation of $FeO_x$ particles over the surface, resulting in the surface and subsurface layers being Fe-deficient or Ni-rich. Therefore, the selection of FeO/Ni(111) is a reasonable model to represent the $FeO/Fe_3Ni(111)$ interface. The model of $Fe_6O_9$/Ni(111) is to describe the active interfacial sites. The choice of such small clusters is to achieve a compromise between the computational cost and a reasonable cluster size to explain the trends observed experimentally. The binding energies of intermediates vary with the size of the FeO clusters on Ni(111). However, the overall trend of selectivity may not change. To test this hypothesis, we computed energy profiles for the C-H and C-C bond cleavage using a smaller

$Fe_3O_3$/Ni(111) model. It is found that, trends observed using $Fe_3O_3$/Ni(111) are not significantly different from those obtained using $Fe_6O_9$/Ni(111) (**Figure 3-16**). Since these calculations were computationally demanding, we were unable to test this hypothesis using a FeO cluster larger than $Fe_6O_9$.

Similarly, the $Ni_3Pt$ cluster supported on $CeO_2$ was described by a $Ni_3Pt$(111) surface using the L12 cubic crystal structure and a four layer 4 × 4 surface slab (**Figure 3-13b**), where the formation of the Pt skin on the surface was included to consider the segregation of Pt according to our experimental observations.[30] In both cases, the effect of $CeO_2$ and the particle size was not taken into consideration. According to our experimental results, $CeO_2$ plays a crucial role in the initial $CO_2$ activation, while the subsequent reforming and dehydrogenation reactions take place on the surface of bimetallic particles. The different trend in the catalytic behavior between $Fe_3Ni/CeO_2$ and $Ni_3Pt/CeO_2$ observed experimentally during propane oxidative dehydrogenation is mostly associated with the surface of bimetallic alloys, which justifies our focus on the trend of different bimetallic surfaces in the DFT calculations.

The Brillouin-zone integration on bulk-terminated $Fe_3Ni$(111) and Pt-terminated-$Ni_3Pt$(111) and 5 × 5 Ni(111) surfaces was performed on a grid of 3 × 3 × 1 Monkhorst−Pack [42] special k-points while the Brillouin-zone integration was sampled at the Γ-point on FeO/Ni(111). A 14 Å thick vacuum was added along the direction perpendicular to the surface in the initial slab model to avoid the artificial interactions between the slab and its periodic images. During geometry optimization, the atoms in the top two layers were allowed to relax while the atoms in the bottom two layers were fixed. The current setup in the DFT calculations predicted the Gibbs free energy ($\Delta G$) as 1.55 eV for the reaction $CH_3CH_2CH_3(g) + CO_2(g) + * \rightarrow CH_3CHCH_2(g) + H_2O(g) + CO(g) + *$ at T = 298.15 K, which is close to the experimental value of 1.20 eV.[43]

The binding energy (*BE*) of an adsorbate is calculated as:

$$BE(adsorbate) = E(slab + adsorbate) - E(slab) - E(adsorbate), \quad \text{(Equation 3-10)}$$

where *E(slab + adsorbate)*, *E(slab)* and *E(adsorbate)* are the total energies of the slab with adsorbate, the clean slab, and the adsorbate species in gas phase, respectively.

The transition state of a chemical reaction was located using the climbing image nudged elastic band (CI-NEB) method implemented in VASP.[44] The activation energy ($E_a$) of a chemical reaction is defined as the energy difference between the initial and transition states while the reaction energy ($\Delta E$) is defined as the energy difference between the initial and final states.

## 3.6 Conclusions

Overall, the oxidative dehydrogenation of propane with $CO_2$ has the potential to combine two underutilized[4,5,6] reactants to produce propylene or syngas. Two types of bimetallic catalysts have been identified for the $CO_2$ + $C_3H_8$ system. The DFT calculation results indicate that the bulk $Fe_3Ni(111)$ surface and the FeO/Ni(111) interface should favor C-H bond scission for the $CO_2$-ODHP pathway, whereas the Pt-terminated $Ni_3Pt(111)$ surface should favor the C-C bond cleavage for the DRP pathway. Flow reactor results are consistent with the DFT calculations as it was observed that the $Fe_3Ni$ catalyst is selective for propylene production, while the $Ni_3Pt$ catalyst shows good activity and CO selectivity. The oxidation states of the different metals provided by in-situ XANES measurements reveal that $Fe_3Ni$ consists of oxidized Fe and metallic Ni. Future efforts should be geared toward enhancing propylene yield through the discovery of more stable and selective catalytic materials.

## 3.7 Acknowledgements

The work is supported by the US Department of Energy under contract number DE-SC0012704. The in-situ XAS measurements were performed at the 2-2 beamline at the Stanford Synchrotron Radiation Lightsource (SSRL) at SLAC National Accelerator Laboratory (DE-AC02-76SF00515) and the 9-BM beamline of the Advanced Photon Source (APS) at Argonne National Laboratory (DE-AC02-06CH11357). E.G. acknowledges the US National Science Foundation Graduate Research Fellowship Program: DGE-16-44869. E.G. would like to acknowledge Dr. Shyam Kattel for providing the DFT calculations and for the discussions and revisions during the writing of this chapter.

## 3.8 References


1. Plotkin, J. S. The propylene gap: how can it be filled? http://www.acs.org/content/acs/ /en/pressroom/cutting-edge-chemistry/the-propylene-gap-how-can-it-be-filled.html (2015).

2. Wang, S. & Zhu, Z. H. Catalytic conversion of alkanes to olefins by carbon dioxide oxidative dehydrogenation- a review. *Energy Fuels* **18,** 1126–1139 (2004).

3. Ansari, M. B. & Park, S.-E. Carbon dioxide utilization as a soft oxidant and promoter in catalysis. *Energy Environ. Sci.* **5,** 9419-9437 (2012).

4. G. Centi, S. Perathoner, & G. Iaquaniello. $CO_2$*: a valuable source of carbon Ch.2*. (Springer-Verlag, London, 2013).

5. Sloan, M. & Wilczewski, W. 2013 Propane market outlook. http://www.afdc.energy. gov/ uploads/publication/2016_propane_market_outlook_1_.pdf (2013).

6. Sloan, M. 2016 Propane market outlook. http://www.afdc.energy.gov/uploads/publication /2013_propane_market_outlook.pdf (2016).

7. Goddard, P. B., Yin, J., Griffies, S. M. & Zhang, S. An extreme event of sea-level rise along the Northeast coast of North America in 2009–2010. *Nat. Commun.*doi:10.1038/ncomm s7346 (2015).

8. Pachauri, R. K. *et al.* Climate change 2014: synthesis report. *Contribution of Working Groups I. II and III to the Fifth Assesment Report of the Intergovernmental Panel on Climate Change* (2014).

9. Pakhare, D. & Spivey, J. A review of dry ($CO_2$) reforming of methane over noble metal catalysts. *Chem. Soc. Rev.* **43,** 7813–7837 (2014).

10. Tang, P., Zhu, Q., Wu, Z. & Ma, D. Methane activation: the past and future. *Energy Environ. Sci.* **7,** 2580-2591 (2014).

11. Osaki, T. & Mori, T. Kinetics of the reverse-Boudouard reaction over supported nickel catalysts. *React. Kinet. Catal. Lett.* **89,** 333–339 (2006).

12. Lim, J. Y., McGregor, J., Sederman, A. J. & Dennis, J. S. The role of the Boudouard and water-gas shift reactions in the methanation of CO or $CO_2$ over Ni/g-$Al_2O_3$ catalyst. *Chem. Eng. Sci.* **152,** 754–766 (2016).

13. Baek, J., Yun, H. J., Yun, D., Choi, Y. & Yi, J. Preparation of highly dispersed chromium oxide catalysts supported on mesoporous silica for the oxidative dehydrogenation of propane using $CO_2$ : insight into the nature of catalytically active chromium sites. *ACS Catal.* **2,** 1893–1903 (2012).

14. Talati, A., Haghighi, M. & Rahmani, F. Oxidative dehydrogenation of ethane to ethylene by carbon dioxide over Cr/$TiO_2$–$ZrO_2$ nanocatalyst: effect of active phase and support composition on catalytic properties and performance. *Adv. Powder Technol.* **27,** 1195–1206 (2016).

15. Takahara, I., Chang, W.-C., Mimura, N. & Saito, M. Promoting effects of $CO_2$ on dehydrogenation of propane over a $SiO_2$ -supported $Cr_2O_3$ catalyst. *Catal. Today* **45,** 55–59 (1998).

16. Asghari, E., Haghighi, M. & Rahmani, F. $CO_2$ oxidative dehydrogenation of ethane to ethylene over Cr/MCM-41 nanocatalyst synthesized via hydrothermal/impregnation methods: influence of chromium content on catalytic properties and performance. *J. Mol. Catal. A Chem.* **418–419,** 115–124 (2016).

17. Farrauto, R. J. & Bartholomew, C. H. *Fundamentals of industrial catalytic processes*. 2nd edn (Wiley-AIChE, Hoboken, 2005).

18. Raberg, L. *et al.* Propane dry reforming to synthesis gas over Ni-based catalysts: influence of support and operating parameters on catalyst activity and stability. *J. Catal.* **249,** 250–260 (2007).

19. Siahvashi, A. & Adesina, A. A. Kinetic study of propane $CO_2$ reforming over bimetallic Mo−Ni/$Al_2O_3$ catalyst. *Ind. Eng. Chem. Res.* **52,** 15377–15386 (2013).

20. Olafsen, A. *et al.* Light alkanes $CO_2$ reforming to synthesis gas over Ni based catalysts. *Catal. Today* **115,** 179–185 (2006).

21. Solymosi, F., Tolmacsov, P. & Kedves, K. $CO_2$ reforming of propane over supported Rh. *J. Catal.* **216,** 377–385 (2003).

22. Solymosi, F., Tolmacsov, P. & Zakar, T. S. Dry reforming of propane over supported Re catalyst. *J. Catal.* **233,** 51–59 (2005).

23. Centi, G. & Perathoner, S. Opportunities and prospects in the chemical recycling of carbon dioxide to fuels. *Catal. Today* **148,** 191–205 (2009).

24. Pakhare, D. & Spivey, J. A review of dry ($CO_2$) reforming of methane over noble metal catalysts. *Chem. Soc. Rev.* **43,** (2014).

25. Valenzuela, R. X., Bueno, G., Cortés Corberan, V., Xu, Y. & Chen, C. Selective oxidehydrogenation of ethane with $CO_2$ over $CeO_2$-based catalysts. *Catal. Today* **61,** 43–48 (2000).

26. Yan, B. *et al.* Dry reforming of ethane and butane with $CO_2$ over $PtNi/CeO_2$ bimetallic catalysts. *ACS Catal.* **6,** 7283–7292 (2016).

27. Lonergan, W. W., Wang, T., Vlachos, D. G. & Chen, J. G. Effect of oxide support surface area on hydrogenation activity: Pt/Ni bimetallic catalysts supported on low and high surface area $Al_2O_3$ and $ZrO_2$. *Appl. Catal. A Gen.* **408,** 87–95 (2011).

28. Porosoff, M. D. & Chen, J. G. Trends in the catalytic reduction of $CO_2$ by hydrogen over supported monometallic and bimetallic catalysts. *J. Catal.* **301,** 30–37 (2013).

29. Myint, M., Yan, B., Wan, J., Zhao, S. & Chen, J. G. Reforming and oxidative dehydrogenation of ethane with $CO_2$ as a soft oxidant over bimetallic catalysts. *J. Catal.* **343,**168–177 (2016).

30. Lonergan, W. W., Vlachos, D. G. & Chen, J. G. Correlating extent of Pt–Ni bond formation with low-temperature hydrogenation of benzene and 1,3-butadiene over supported Pt/Ni bimetallic catalysts. *J. Catal.* **271,** 239–250 (2010).

31. Hohenberg, P. & Kohn, W. Inhomogeneous electron gas. *Phys. Rev.* **136,** B864–B871 (1964).

32. Kohn, W. & Sham, L. J. Self-consistent equations including exchange and correlation effects. *Phys. Rev.* **140,** A1133–A1138 (1965).

33. Kresse, G. & Furthmüller, J. Efficiency of ab-initio total energy calculations for metals and semiconductors using a plane-wave basis set. *Comput. Mater. Sci.* **6,** 15–50 (1996).

34. Kresse, G. & Hafner, J. Ab initio molecular dynamics for open-shell transition metals. *Phys. Rev. B* **48,** 13115–13118 (1993).

35. Kresse, G. & Joubert, D. From ultrasoft pseudopotentials to the projector augmented-wave method. *Phys.Rev. B* **59,** 1758–1775 (1999).

36. Blöchl, P. E. Projector augmented-wave method. *Phys. Rev. B* **50,** 17953–17979 (1994).

37. Perdew, J. P. & Wang, Y. Accurate and simple analytic representation of the electron-gas correlation-energy. *Phys. Rev. B* **45,** 13244–13249 (1992).

38. Pack, J. D. & Monkhorst, H. J. Special points for Brillouin-zone integrations. *Phys. Rev. B* **13,** 5188–5192 (1976).

39. Henkelman, G., Uberuaga, B. P., & Jónsson, H. A climbing image nudged elastic band method for finding saddle points and minimum energy paths. *J. Chem. Phys.* **113,** 9901–9904 (2000).

40. Theofanidis, S. A., Galvita, V. V., Poelman, H. & Marin, G. B. Enhanced carbon-resistant dry reforming Fe-Ni catalyst: role of Fe. *ACS Catal.* **5,** 3028–3039 (2015).

41. Kim, S. M. *et al.* Cooperativity and dynamics increase the performance of NiFe dry reforming catalysts. *J. Am. Chem. Soc.* **139,** 1937–1949 (2017).

42. Pack, J. D. & Monkhorst, H. J. Special points for Brillouin-zone integrations. *Phys. Rev. B* **13,** 5188–5192 (1976).

43. Dean, J. A. *Lange's Handbook of Chemistry* (McGraw-Hill, New York,1985).

44. Henkelman, G., Uberuaga, B. P. & Jónsson, H. A climbing image nudged elastic band method for finding saddle points and minimum energy paths. *J. Chem. Phys.* **113,** 9901–9904 (2000).

# Chapter 4: The effects of bimetallic interactions and the role of oxide supports for $CO_2$-assisted oxidative dehydogenation and dry reforming of propane

## 4.1 Abstract

Limited availability of $CO_2$-free $H_2$ and high operating temperatures for methane dry reforming pose challenges for current $CO_2$ reduction strategies. A viable alternative is the reduction of $CO_2$ with propane. The catalytic reduction of $CO_2$ by propane may occur via dry reforming (DRP) to produce syngas (CO + $H_2$) or oxidative dehydrogenation ($CO_2$-ODHP) to yield propylene. Utilizing propane and $CO_2$ as co-reactants presents several advantages over conventional methane dry reforming or direct propane dehydrogenation, including lower operating temperatures and less coke formation. Thus, it was of great interest to identify catalytic systems that can either effectively break the C-C bond to generate syngas or selectively break C-H bonds to produce propylene. In this study, several precious and non-precious bimetallic catalysts supported on reducible $CeO_2$ were investigated using flow reactor studies at 823 K to identify selective catalysts for the $CO_2$-ODHP and DRP reaction pathways. Of the various metal combinations, $Fe_3Ni_1$ and $Ni_3Pt_1$ on $CeO_2$ were identified as promising $CO_2$-ODHP and DRP catalysts, respectively. To explore the role of other oxide supports on the $CO_2$-ODHP and DRP reactions, flow reactor studies were performed on the two most promising bimetallic systems for each reaction pathway supported on γ-$Al_2O_3$, $ZrO_2$, $SiO_2$, and $TiO_2$. Results showed that changing the support of the $Fe_3Ni_1$ system influenced the selectivity and preferred reaction pathway. Whereas, altering the support of the $Ni_3Pt_1$ system impacted the activity but with minimal changes to selectivity, retaining preference to the DRP pathway over all examined supports.

## 4.2 Introduction

Carbon dioxide management is a prominent issue facing society that requires a diverse portfolio of innovative technologies. High atmospheric concentrations of $CO_2$ contribute to adverse effects that impact human health and the climate. The need to reduce $CO_2$ is evident, and the International Panel on Climate Change has stated that climate stabilization (no more than a 2°C rise from pre-industrial levels) will require a combination of mitigation, utilization, and even negative emission technologies.[1] Thus, one key approach will be to transform abundant $CO_2$ into a useful feedstock for processes that not only produce high value products but also match the scale necessary to impact anthropogenic emissions.

The two most relevant reactions for the catalytic conversion of $CO_2$ to CO are reverse water gas shift (RWGS) and dry reforming of methane (DRM). The CO product can be utilized as feedstock for Fischer-Tropsch reactions or methanol synthesis. These two reduction chemistries are not without obstacles, beginning with the challenge that $CO_2$ is the most thermodynamically stable carbon/oxygen-based molecule ($\Delta G_F$ = -394 kJ mol$^{-1}$).[2] Current implementation of RWGS has limited feasibility since efforts to obtain large amounts of renewable and $CO_2$-free hydrogen are still under development.[3] Furthermore, high coke deposition rates at the reaction temperatures required for DRM hinders further significant improvements in catalyst stability.[4,5]

A viable alternative is to utilize other light hydrocarbons, such as ethane or propane, as feedstock for $CO_2$ reduction. In addition to reforming, these light alkanes contain C-C bond(s) that can be advantageously utilized to build olefins.[6] Thus, the reduction of $CO_2$ via light alkanes offers two distinct reaction pathways: dry reforming and oxidative dehydrogenation. Specifically, it is of interest to explore the use of propane due to its increasing abundance, competitive pricing, and the demand for propylene, which is one of the most diverse petrochemical building blocks used in the

production of various chemicals such as fibers and textiles for a variety of applications. Currently, propylene is primarily co-produced by steam cracking of naphtha and fluidized cracking of both heavy and light oil. Recently, the cracking of lighter feeds has caused a significant gap in propylene production.[7] As the demand for propylene increases globally so does the need for more economic on-purpose propylene production processes.

The primary reactions of $CO_2$ + $C_3H_8$ include the dry reforming of propane (DRP) and $CO_2$-assisted oxidative dehydrogenation of propane ($CO_2$-ODHP), both can occur simultaneously at temperatures above 823 K, equations [1] and [2], respectively.

$$C_3H_8 + 3CO_2 \rightarrow 6CO + 4H_2 \qquad \Delta G^o_R = 384 \text{ (kJ mol}^{-1}\text{)} \qquad [1]$$

$$C_3H_8 + CO_2 \rightarrow C_3H_6 + CO + H_2O \qquad \Delta G^o_R = 119 \text{ (kJ mol}^{-1}\text{)} \qquad [2]$$

Other relevant reactions include propane decomposition (or cracking) to carbon, $H_2$, and $CH_4$ [Equation 3], the reverse Boudouard reaction [4], the RWGS reaction [Equation 5], and direct dehydrogenation of propane (DDP) [6] as listed below.

$$C_3H_8 \rightarrow CH_4 + 2C(s) + 2H_2 \qquad \Delta G^o_R = -26 \text{ (kJ mol}^{-1}\text{)} \qquad [3]$$

$$CO_2 + C(s) \rightarrow 2CO \qquad \Delta G^o_R = 120 \text{ (kJ mol}^{-1}\text{)} \qquad [4]$$

$$CO_2 + H_2 \rightarrow H_2O + CO \qquad \Delta G^o_R = 29 \text{ (kJ mol}^{-1}\text{)} \qquad [5]$$

$$C_3H_8 \rightarrow C_3H_6 + H_2 \qquad \Delta G^o_R = 90 \text{ (kJ mol}^{-1}\text{)} \qquad [6]$$

The DRP reaction reaches 50% equilibrium conversion at a temperature 150 K lower than that of DRM and results in a $H_2$:CO ratio of 2:3. The $CO_2$-ODHP has several thermodynamic advantages over DDP or even $O_2$-assisted dehydrogenation ($O_2$-ODHP).[8] The equilibrium conversion of the DDP reaction is limited by the high $H_2$ partial pressure, which shifts the reaction to the reverse direction, but $CO_2$ can help consume the produced $H_2$ via the RWGS and increase

olefin yield in $CO_2$-ODHP. The RWGS coupled with $CO_2$ assisted abstraction of H from propane should decrease the Gibbs free energy of the overall reaction and potentially allow a reduction in operating temperatures.[9] In addition, $CO_2$ is a mild oxidant and can suppress over-oxidation to increase olefin yield. Among one of the key differences between $CO_2$-ODHP and $O_2$-ODHP is the overall net reduction of $CO_2$ in the former and possible emission of anthropogenic $CO_2$ in the latter. Coke formation is expected for reactions that involve allylic hydrogens. $CO_2$ can help stabilize the catalyst by consuming coke via the reverse Boudouard reaction, which has been reported to occur at temperatures as low as 773 K.[10,11] Overall, these thermodynamic benefits allow for milder reaction conditions, thus increasing the opportunity to develop active, selective, and more stable catalytic systems.

At present the $CO_2$-ODHP efforts focus primarily on chromium-based catalysts supported on zeolites, mesoporous silica, and metal oxides.[12] The activation of $CO_2$ for chromium-based catalysts is typically attributed to a $Cr^{6+}$ active center generated from a redox cycle with $Cr^{3+}$.[13,14,15,16] Increased alkane conversion is observed with high $Cr^{6+}/Cr^{3+}$ ratios, but there is a maximum amount of $Cr^{6+}$ that can be added until no further improvement is observed. For example, on the SBA support the maximum loading is 4.3 wt.% of $Cr^{6+}$.[13,17] While Cr-based catalysts show high initial conversion and selectivity, their implementation is limited due to short lifecycles and high toxicity. Other metal modified zeolites tested for dehydrogenation include the Pt-Sn/H-ZSM-5 catalysts, which have only been shown to work in the absence of $CO_2$. For the DRP reaction, initial focus centered on precious metal catalysts[18,19,20] and later extended to Ni-based catalysts supported on $\gamma$-$Al_2O_3$ or Mg hydrotalcite-derived catalysts.[21,22,23] The Ni-based DRP catalysts exhibit instability and deactivate due to coke formation.

Due to the lack of studies investigating both reaction pathways simultaneously over bimetallic catalysts, there is little understanding regarding which catalytic systems can effectively break the C-H bond to produce propylene or break the C-C bond to produce reforming products. In the present study, we investigated bimetallic catalysts composed of precious (Pt or Pd) with non-precious metals (Fe, Co or Ni), as well as combinations of non-precious metals, all supported on $CeO_2$ for the reactions of $CO_2 + C_3H_8$ at 823 K.

Effective catalysts for $CO_2$-ODHP and DRP require the ability to activate $CO_2$ on the metal oxide support and or the interfacial sites. $CeO_2$ is a readily reducible oxide with the ability to reversibly convert between $Ce^{4+}$ and $Ce^{3+}$ and is well known for oxygen exchange properties that are critical for $CO_2$ activation.[24,25,26,27] Another remarkable feature of $CeO_2$ is the ability to accommodate high oxygen vacancy concentrations without a change in crystallographic structure even at high temperature. Ceria activates $CO_2$ via charge transfer to the lowest unoccupied molecular orbital. Effective $CO_2$ adsorption on a ceria surface is structure dependent and the adsorption configurations dictate the mechanism and energetics of $CO_2$ reduction. The adsorption process itself can weaken the C-O bond, but the vacancy geometry determines if $CO_2$ will fill the vacancy. If the split vacancy geometry is too narrow, $CO_2$ cannot heal the vacancy, but instead will provide surface oxygen. Cheng et al. performed DFT calculations regarding the adsorption of $CO_2$ on a $CeO_2$(111) surface and reported that parallel adsorption on a bridge between two Ce atoms adjacent to the vacancy provides a favorable angle that allows $CO_2$ to heal an oxygen vacancy on $CeO_2$.[28] Apart from $CO_2$ filling vacancies or providing lattice oxygen, the exchange cycle over $CeO_2$ can also provide lattice oxygen for coke suppression. Since the choice of metal oxide support can tune the selectivity profile of a catalyst, the present study also evaluated the role

of other oxide supports with the two most promising bimetallic catalytic systems identified, $Fe_3Ni_1$ and $Ni_3Pt_1$, for the reaction pathways of $CO_2$-ODHP and DRP, respectively.

## 4.3 Methods

The catalysts evaluated in this study were synthesized through incipient wetness impregnation of metals onto commercially obtained $CeO_2$ (35-45 $m^2/g$, Sigma-Aldrich), $\gamma$-$Al_2O_3$ (80-120 $m^2/g$ Alfa-Aesar), $ZrO_2$ (90 $m^2/g$ Alfa Aesar), $SiO_2$ (168 $m^2/g$, Alfa Aesar), and $TiO_2$ (240 $m^2/g$ Alfa Aesar). The active metal precursors $Pt(NH_3)_4(NO_3)_2$, $Pd(NO_3)_2{\cdot}2H_2O$, $Fe(NO_3)_3{\cdot}9H_2O$, $Ni(NO_3)_2{\cdot}6H_2O$, and $Co(NO_3)_2{\cdot}6H_2O$ (Alfa Aesar) were dissolved in a volume of water equivalent to 90% of the pore volume of an aliquot sample of the support. Flow reactor studies were conducted at 823 K and atmospheric pressure utilizing a 6.35 mm quartz U-tube shaped reactor. All catalysts were reduced at 723 K for 1 hour under 1:1 $H_2$/Ar flow (40mL/min total). After catalyst pre-treatment, the temperature was increased to (6.5 K/min) and held at 823 K in the presence of 1:1:2 $CO_2$, $C_3H_8$, and Ar (40mL/min total) for over 12 hours.

## 4.4 The effects of bimetallic interactions

### 4.4.1 Catalytic evaluation

**Table 4-1** summarizes the activity of the $CeO_2$ supported bimetallic catalysts. For comparison, the results of $Fe_3Pt_1$, $Fe_3Ni_1$, and $Ni_3Pt_1$ from the previous Chapter[30] are also provided in **Table 4-1**. Conversions following time on stream for various catalysts are available in **Figure 4-1**. The conversion and selectivity of Cu-based catalysts with $Pt_1$, $Pd_1$, $Ni_3$, and $Co_3$, as well as Ni and Co combinations with Mo, are available in **Table 4-2**.

**Table 4-1.** Catalyst flow reactor results for the $CO_2$+$C_3H_8$ reaction. 10mL/min each reactant at 823 K with Ar diluent (20 mL/min) and 100 mg of catalyst (16-20 mesh). Values are obtained by averaging data from 10-12 hr. Selectivity and yield are on a $C_3H_8$ basis (including only carbonaceous species). Cracking products ($C_1$, $C_2$, $C_2^=$) are quantified, see **Figure 4-1**.

| Catalyst /$CeO_2$ | CO uptake $\mu mol \cdot g^{-1}$ | Conversion (%) | | TOF $site^{-1} \cdot min^{-1}$ | | Selectivity (%) | | | $C_3H_8$ Yield (%) | |
|---|---|---|---|---|---|---|---|---|---|---|
| | | $CO_2$ | $C_3$ | $CO_2$ | $C_3$ | CO | $C_3H_6$ | $C_1$, $C_2$, $C_2^=$ | $C_3H_6$ | CO |
| $Pd_1$ | 14.8 | 3.2 | 0.4 | 10.5 | 1.3 | 28.3 | 44.4 | 27.4 | 0.18 | 0.11 |
| $M_3Pd_1$ | | | | | | | | | | |
| $Fe_3Pd_1$ | 23.7 | 0.1 | 0.4 | 0.2 | 0.7 | 5.6 | 57.6 | 36.8 | 0.22 | 0.02 |
| $Co_3Pd_1$ | 33.8 | 8.4 | 2.8 | 12.0 | 3.7 | 66.7 | 25.2 | 8.1 | 0.71 | 1.9 |
| $Ni_3Pd_1$ | 30.7 | 17.6 | 5.3 | 27.5 | 7.6 | 88.0 | 11.2 | 0.8 | 0.59 | 4.6 |
| $Pt_1$ | 16.0 | 4.0 | 1.6 | 11.4 | 3.9 | 76.9 | 21.4 | 1.7 | 0.34 | 1.2 |
| $M_3Pt_1$ | | | | | | | | | | |
| $Fe_3Pt_1$ | 31.5 | 2.6 | 1.1 | 3.5 | 1.5 | 65.1 | 32.0 | 2.9 | 0.3 | 0.7 |
| $Co_3Pt_1$ | 47.5 | 20.3 | 5.6 | 18.8 | 4.9 | 88.8 | 10.1 | 1.1 | 0.6 | 4.9 |
| $dCo_3Pt_1$ | | 9.5 | 3.4 | | | 71.7 | 27.3 | 1.0 | 0.93 | 2.4 |
| $Ni_3Pt_1$ | 50.1 | 39.4 | 11.6 | 37.5 | 10.5 | 96.2 | 2.8 | 0.93 | 0.33 | 11.1 |
| $Fe_xCo_y$ | | | | | | | | | | |
| $Fe_1Co_3$ | 13.4 | 1.5 | 0.9 | 5.4 | 3.0 | 42.2 | 43.8 | 14.0 | 0.39 | 0.38 |
| $Fe_3Co_1$ | 16.4 | 0.23 | 0.27 | 0.67 | 0.73 | 25.6 | 57.1 | 17.3 | 0.15 | 0.07 |
| $Fe_xNi_y$ | | | | | | | | | | |
| $Fe_3Ni_1$ | 31.9 | 4.0 | 2.7 | 5.7 | 3.4 | 40.2 | 58.2 | 1.6 | 1.6 | 1.1 |
| $Fe_1Ni_3$ | 36.0 | 26.9 | 7.4 | 34.5 | 9.2 | 96.4 | 2.9 | 0.7 | 0.22 | 7.2 |
| $Fe_3Ni_3$ | 23.5 | 16.1 | 5.0 | 29.9 | 8.6 | 76.9 | 20.4 | 2.7 | 1.0 | 3.9 |
| $Fe_9Ni_3$ | 25.0 | 10.9 | 3.4 | 18.9 | 5.4 | 73.3 | 22.5 | 4.1 | 0.83 | 2.7 |
| $Co_xNi_y$ | | | | | | | | | | |
| $Co_1Ni_3$ | 23.5 | 27.8 | 7.8 | 57.5 | 14.9 | 95.6 | 2.6 | 1.8 | 0.2 | 7.5 |
| $Co_3Ni_1$ | 16.7 | 27.1 | 7.6 | 77.4 | 19.9 | 97.5 | 2.1 | 0.5 | 0.2 | 7.4 |
| $Co_3Ni_3$ | 18.5 | 29.8 | 8.5 | 77.2 | 19.7 | 95.5 | 2.4 | 2.1 | 0.2 | 8.1 |

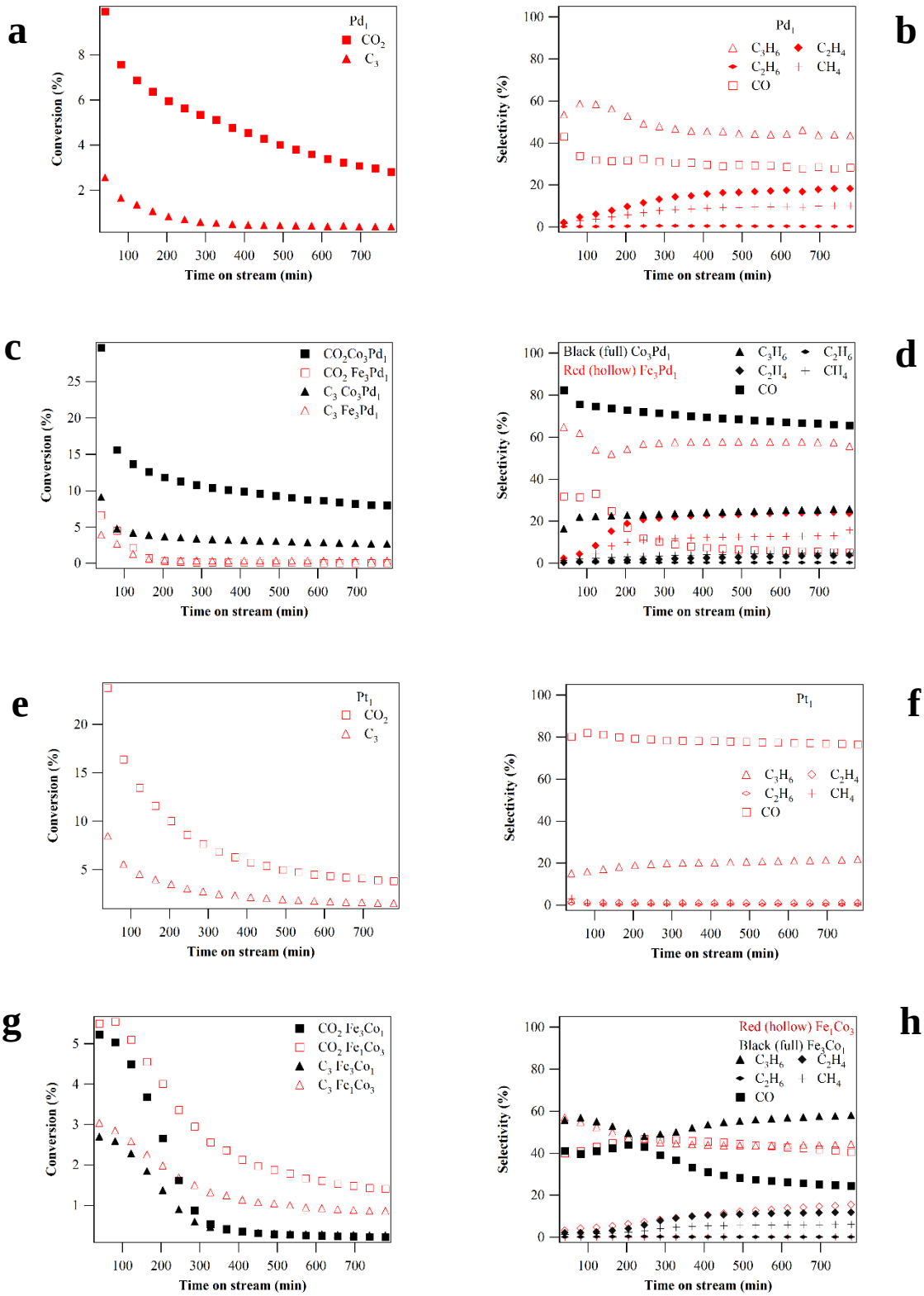
a
Pd1
CO2
C3
Conversion (%)
Time on stream (min)
b
Pd1
C3H6
C2H4
C2H6
CH4
CO
Selectivity (%)
Time on stream (min)
c
CO2Co3Pd1
CO2 Fe3Pd1
C3 Co3Pd1
C3 Fe3Pd1
Conversion (%)
Time on stream (min)
d
Black (full) Co3Pd1
Red (hollow) Fe3Pd1
C3H6
C2H4
C2H6
CH4
CO
Selectivity (%)
Time on stream (min)
e
Pt1
CO2
C3
Conversion (%)
Time on stream (min)
f
Pt1
C3H6
C2H4
C2H6
CH4
CO
Selectivity (%)
Time on stream (min)
g
CO2 Fe3Co1
CO2 Fe1Co3
C3 Fe3Co1
C3 Fe1Co3
Conversion (%)
Time on stream (min)
h
Red (hollow) Fe1Co3
Black (full) Fe3Co1
C3H6
C2H4
C2H6
CH4
CO
Selectivity (%)
Time on stream (min)

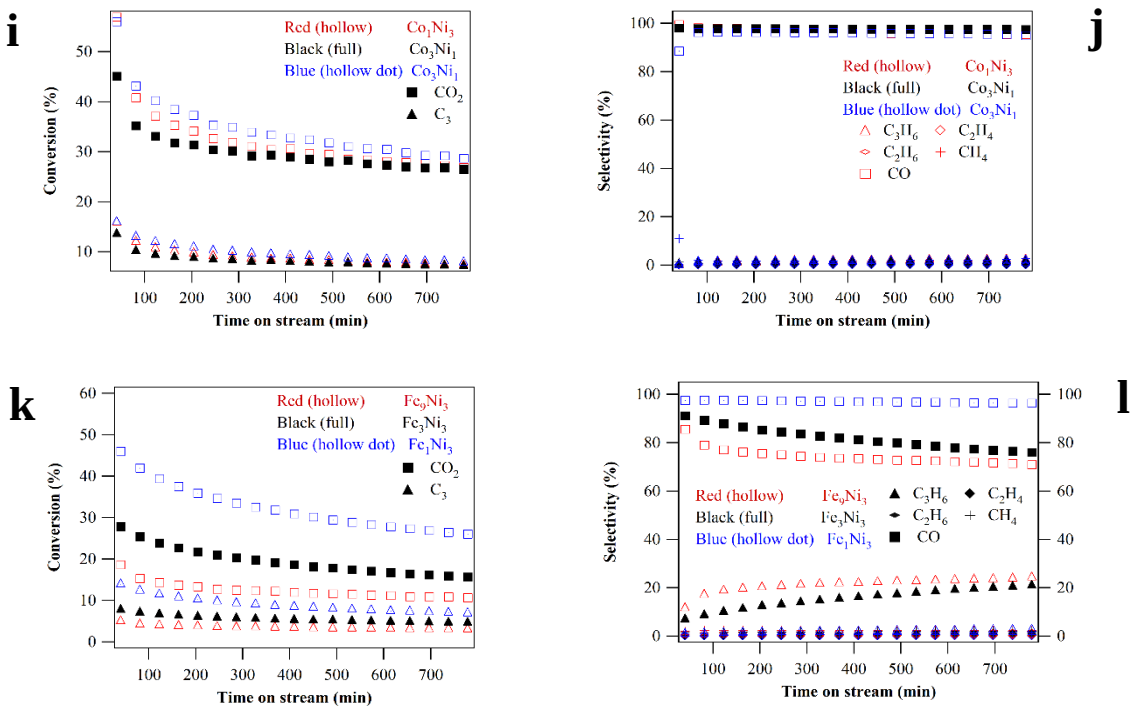


**Figure 4-1.** Conversion and selectivity following time on stream. Shown here for (**a-b)** $Pd_1$, (**c-d)** $Fe_3Pd_1$ and $Co_3Pd_1$, (**e-f)** $Pt_1$, **g-h** $Fe_xCo_y$, (**i-j)** $Co_xNi_y$, and (**k-l)** $Fe_xNi_y$. Conversion and selectivity plots for $Fe_3Pt_1$ and $Fe_3Ni_1$ can be found in the previous Chapter.[30]

**Table 4-2.** Flow reactor results for additional catalysts. Cu and Mo based catalysts were examined. The asterisk symbol indicates that the catalyst was diluted to achieve comparable $C_3$ conversion as with $Fe_3Ni_1$.[30]

| Catalyst /$CeO_2$ | Conversion (%) | | Selectivity (%) | | | $C_3H_8$ Yield (%) | |
|---|---|---|---|---|---|---|---|
| | $CO_2$ | $C_3$ | CO | $C_3H_6$ | $C_1$, $C_2$, $C_2^=$ | $C_3H_6$ | CO |
| $Cu_3$ | 0.05 | 0.15 | 73.0 | 8.9 | 18.1 | 0.01 | 0.1 |
| $Cu_3Pd_1$ | 0.11 | 0.24 | 13.5 | 62.4 | 24.1 | 0.15 | 0.03 |
| $Cu_3Pt_1$ | 0.4 | 0.7 | 13.2 | 53.0 | 33.8 | 0.37 | 0.1 |
| $Cu_3Co_3$ | 9.9 | 2.7 | 90.0 | 8.8 | 1.3 | 0.24 | 2.4 |
| $Cu_3Ni_3$ | 13.6 | 3.8 | 85.5 | 11.8 | 2.7 | 0.45 | 3.3 |
| $Mo_1$ | | | | | | | |
| $Mo_1Co_3$ | 9.1 | 2.8 | 94.5 | 4.9 | 0.6 | 0.14 | 2.6 |
| $Mo_1Ni_3$ | 17.6 | 5.2 | 93.4 | 4.8 | 1.8 | 0.25 | 4.9 |
| Diluted $Fe_1Ni_3^*$ | 7.9 | 2.1 | 90.6 | 8.2 | 1.2 | 0.2 | 1.9 |

### 4.4.2 Bimetallic catalyst of precious (Pt and Pd) and non-precious (Fe, Co, and Ni) metals

Bimetallic catalysts often show distinct electronic and chemical properties compared to their parent metals, providing an opportunity to design catalysts with improved activity, selectivity, and stability.[37] Among the Pt and Pd based catalysts with $Fe_3$, $Co_3$, and $Ni_3$ an improvement in both conversion and stability compared to the respective parent monometallics was observed for $Co_3Pd_1$, $Co_3Pt_1$, and $Ni_3Pt_1$, shown in **Figure 4-2**. Among the bimetallic catalysts, lower overall activity (conversion and TOF) was observed over Pd-based bimetallics compared to the Pt-based counterparts (**Figure 4-3**). Therefore, further bimetallic effect studies were performed with $Co_3Pt_1$ and $Ni_3Pt_1$. As shown in **Figure 4-4**, bimetallic $Co_3Pt_1$ and $Ni_3Pt_1$ showed higher conversion and stability compared to physical mixtures of the respective monometallics ($Co_3 + Pt_1$ and $Ni_3 + Pt_1$), indicating that there was a synergistic interaction between Co-Pt and Ni-Pt when combined.

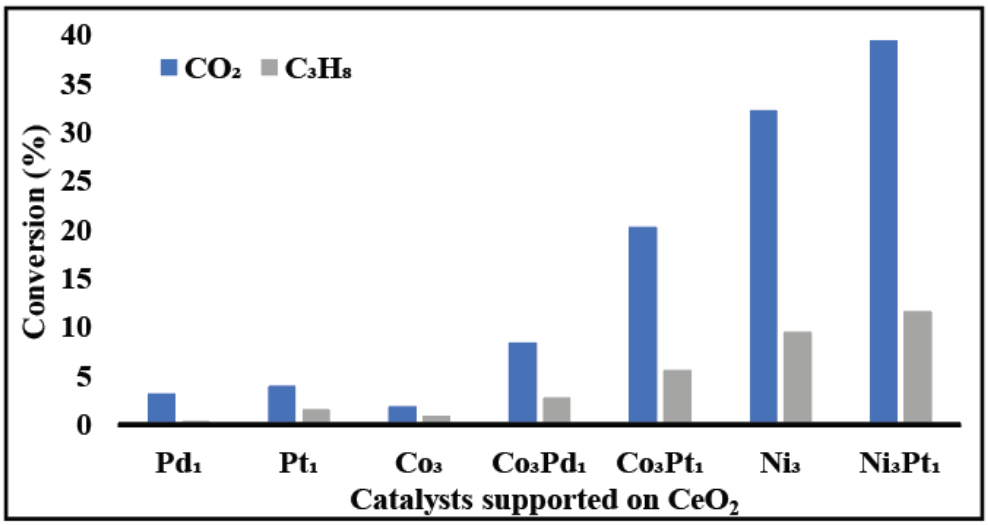


**Figure 4-2.** Reactant conversion. Shown for precious metal-based bimetallic catalysts with respective monometallic catalysts that illustrate a synergistic interaction with parent metals (bimetallic effect).

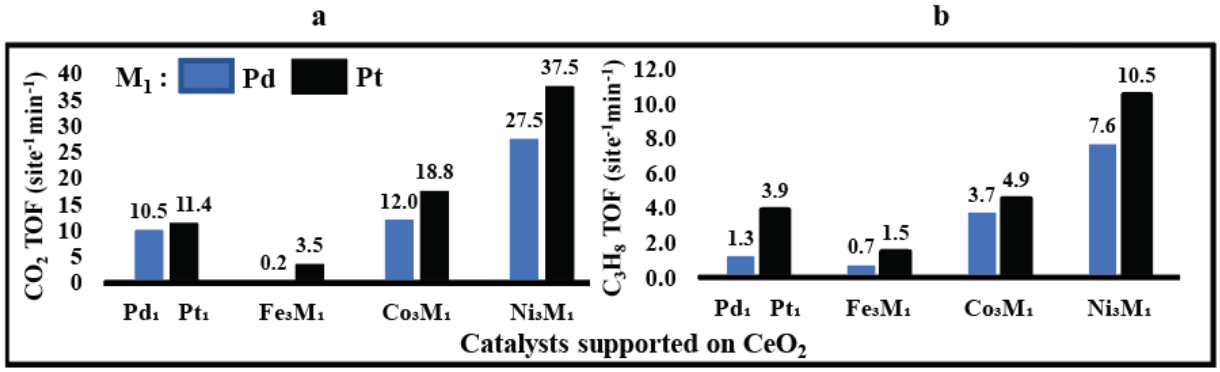


**Figure 4-3**. TOF values. **(a)** $CO_2$ TOF values and **(b)** $C_3H_8$ TOF values for monometallic Pd and Pt and bimetallic $Fe_3M_1$, $Co_3M_1$, and $Ni_3M_1$ catalysts.

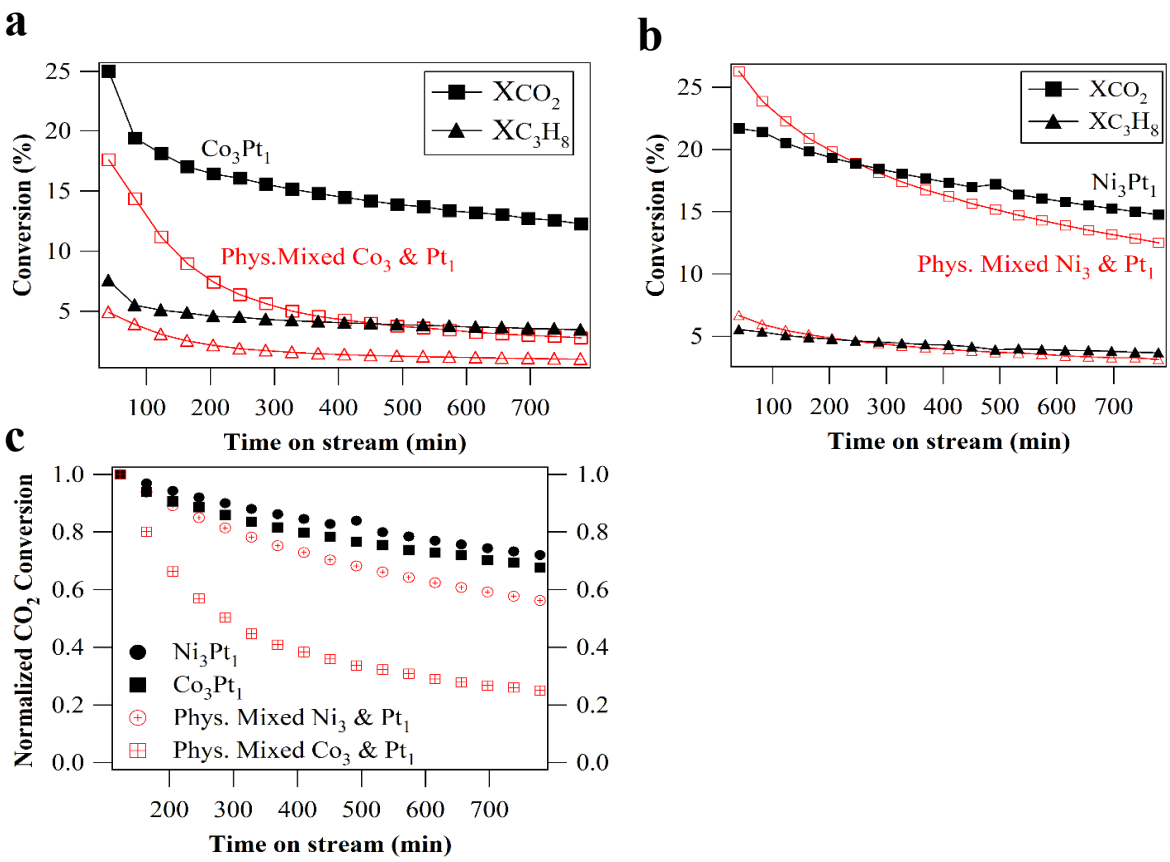


**Figure 4-4.** Bimetallic effect. Conversion following time on stream shown for **(a)** $Co_3Pt_1$, **(b)** $Ni_3Pt_1$, and **(c)** illustrates the stability profiles of the bimetallics with their respective physical mixture. Lower catalyst loading was used compared to steady state experiments and the physical mixtures were made with an equivalent amount of metal as in the bimetallic experiments for accurate comparison.

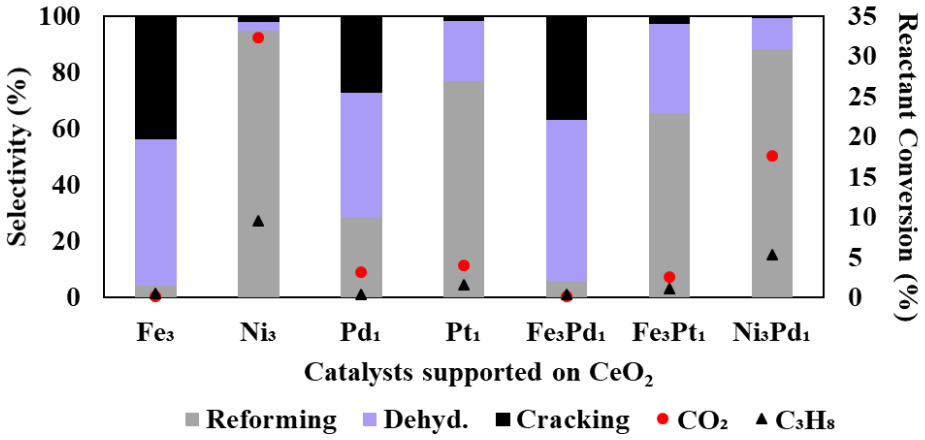


**Figure 4-5.** Parent metals with bimetallics. Shown for $Fe_3Pd_1$, $Fe_3Pt_1$, and $Ni_3Pd_1$.

Additional comparison is shown in **Figure 4-5** for the evaluation of $Fe_3Pt_1$, $Fe_3Pd_1$, and $Ni_3Pd_1$ with their respective monometallics. The $Fe_3$ monometallic was inactive at the tested conditions. Compared to $Pt_1$, $Fe_3Pt_1$ showed lower steady-state conversion and stability but higher propylene selectivity. The $Fe_3Pd_1$ catalyst was less active than $Pd_1$, and no improvements in stability were observed. The $Ni_3Pd_1$ bimetallic only showed higher conversion and stability when compared to $Pd_1$ but not $Ni_3$.

The Fe-containing catalysts with $Pt_1$ and $Pd_1$ were $CO_2$-ODHP catalysts due to their ability to produce propylene, but these combinations exhibited the lowest conversion. The $Fe_3Pt_1$ catalyst was active and at steady-state illustrated 2.6% and 1.1% $CO_2$ and $C_3H_8$ conversion, respectively, with 32% and 65% $C_3H_6$ and CO selectivity, respectively.[30] In comparison, the $Fe_3Pd_1$ catalyst quickly deactivated within the first 2 hours on stream while exhibiting $C_3H_6$ selectivity greater than 50%. Changing $Fe_3$ to $Co_3$ with $Pt_1$ ($Co_3Pt_1$) not only increased the conversion to 20.3% $CO_2$ and 5.6% $C_3H_8$ conversion but also enhanced the dry reforming pathway with 88.8% CO selectivity. Compared to the $Co_3Pt_1$ catalyst, the conversion of $CO_2$ over the $Co_3Pd_1$ catalyst was 2.5 times lower. A diluted $Co_3Pt_1$ sample ($dCo_3Pt_1$), which showed similar reactant conversion to

$Co_3Pd_1$, is listed in **Table 4-1** to examine the selectivity accurately but at comparable conversions. While the $Co_3Pd_1$ catalyst was only slightly less selective to CO (66.7% $Co_3Pd_1$ vs. 71.7% $dCo_3Pt_1$), the selectivity to cracking products ($C_1$, $C_2$, $C_2^=$) increased by a factor of 8 compared to the $dCo_3Pt_1$ sample. On the other hand, both $Ni_3Pt_1$ and $Ni_3Pd_1$ were DRP catalysts and demonstrated higher activity and stability than the Pt and Pd counterparts with $Fe_3$ and $Co_3$. A twofold increase in conversion was observed over the $Ni_3Pd_1$ and $Ni_3Pt_1$ catalysts compared to $Co_3Pd_1$ and $Co_3Pt_1$ (**Figure 4-6a**), respectively.

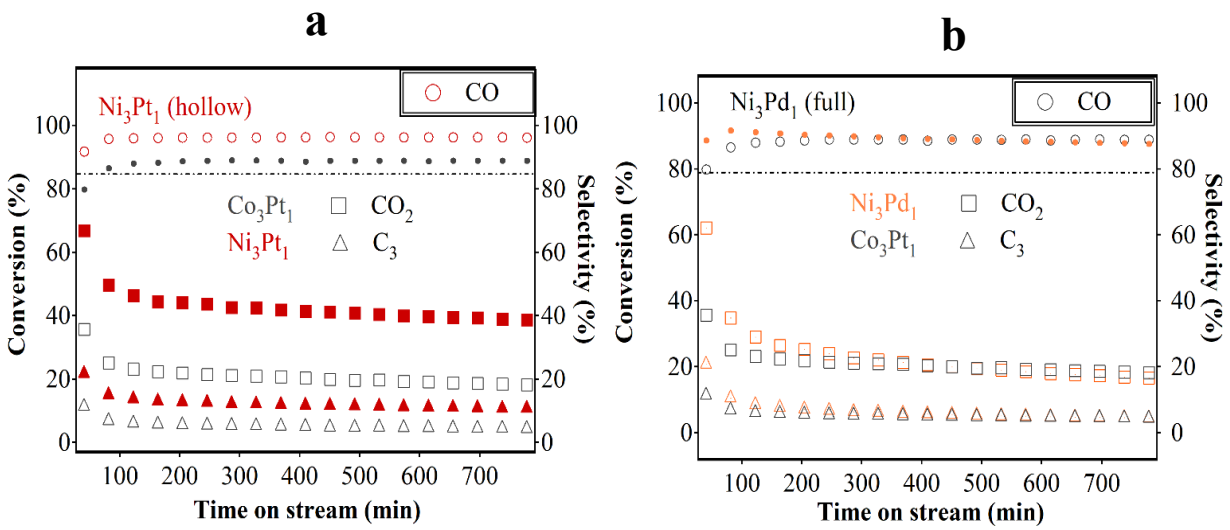


**Figure 4-6.** Conversion and selectivity versus time on stream. **(a)** $Co_3Pt_1$ and $Ni_3Pt_1$ and **(b)** $Co_3Pt_1$ and $Ni_3Pd_1$.

Detailed kinetic measurements comparing the two most promising Pt-based bimetallic catalysts, $Ni_3Pt_1$ and $Co_3Pt_1$, are shown in **Figure 4-7**. When examining the effect of increasing $CO_2$ partial pressure with the $CO_2$ consumption rate, it was evident that $Ni_3Pt_1$ consumes $CO_2$ at a faster rate than $Co_3Pt_1$. Upon reaching a $C_3H_8/CO_2$ ratio of 0.42 the rate began to plateau and then eventually declined over the $Co_3Pt_1$ catalyst, indicative of competitive adsorption. Additionally, the kinetic study demonstrated that the $Co_3Pt_1$ catalyst exhibited higher $C_3H_8$ consumption rates with increasing $C_3H_8$ partial pressure compared to $Ni_3Pt_1$. However, the transformation of propane

into products over the $Co_3Pt_1$ catalyst, which mainly produced CO, occurred at a lower rate compared to $Fe_3Ni_1$, which primarily produced $C_3H_6$. Additionally, in a previous investigation for the reduction of $CO_2$ with propane, it was observed that the rate of reactant consumption decreased at high propane partial pressures for both $CO_2$-ODHP and DRP catalysts.[30] This suggested that as the reaction progressed intermediates from propane may have blocked surface sites, which led to a loss in $CO_2$-ODHP and DRP activity and consequently increased the cracking products.

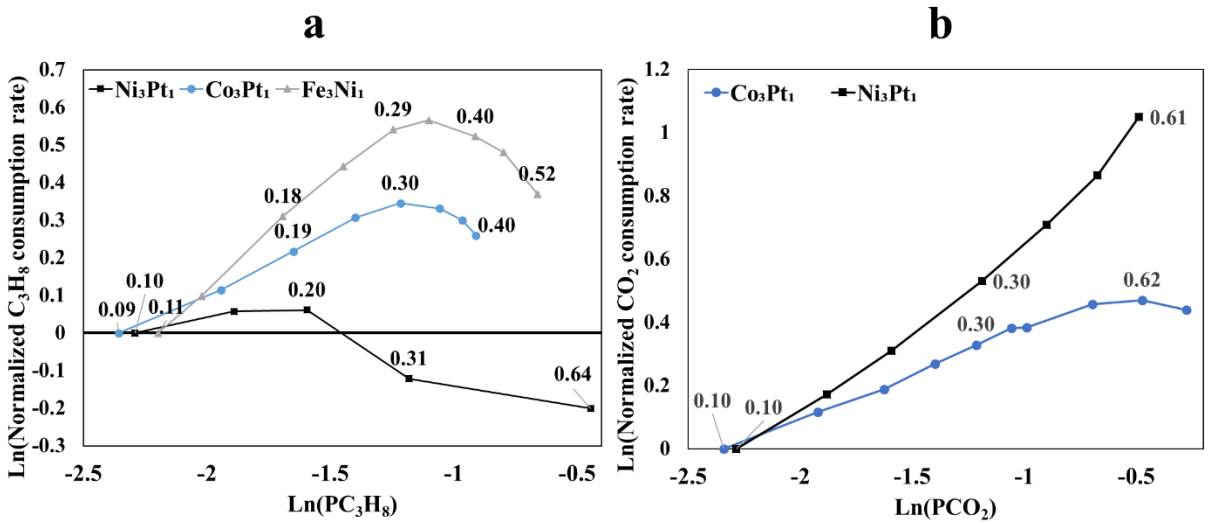


**Figure 4-7.** Effect of reactant A/B consumption rate vs. reactant A/B partial pressure. **(a)** Consumption rate of $C_3H_8$ vs $C_3H_8$ partial pressure for $Ni_3Pt_1$, $Co_3Pt_1$, and $Fe_3Ni_1$. **(b)** Consumption rate of $CO_2$ vs $CO_2$ partial pressure for $Ni_3Pt_1$ and $Co_3Pt_1$. The data labels with values represent the partial pressure of the varying reactant, the reactant held constant has a partial pressure of 0.125, and the total system pressure is 1 atm.

To further assess the potential differences and similarities among the $Co_3Pt_1$ and $Ni_3Pt_1$ catalysts, apparent activation barriers and thermogravimetric values are provided. The apparent activation barrier of the reforming route over the $Co_3Pt_1$ catalyst was 126 $kJ \cdot mol^{-1}$, and the previously reported value for $Ni_3Pt_1$ was 119 $kJ \cdot mol^{-1}$, refer to **Figure 4-8** for the Arrhenius-type

plot. These similar apparent activation energies signified that both catalysts potentially undergo similar oxidative reaction routes. Based on previous density functional theory (DFT) calculations, the ODH pathway requires the adsorbed oxygen species (produced from the dissociation of $CO_2$) to interact with adsorbed $C_xH_y$ fragments to form an oxygenated intermediate before further C-C bond cleavage to form CO.[29] Furthermore, if the reaction pathways were similar over both catalysts then the mechanism for deactivation would also be consistent with coking. The previously reported TGA weight loss of $Ni_3Pt_1$ is 8%, and the $Co_3Pt_1$ catalyst in this study lost 4%, see **Figure 4-9**. The extent of coking was similar after considering the different $C_3H_8$ conversions over the two catalysts.

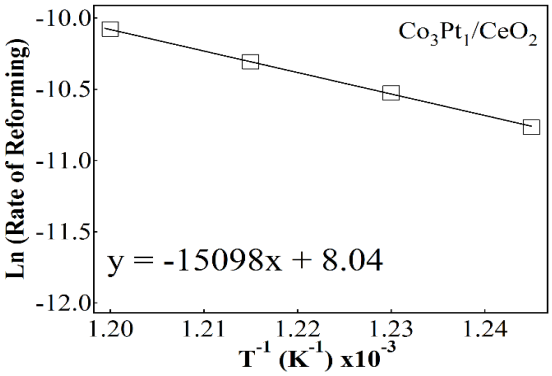


**Figure 4-8.** Arrhenius-type plot. Shown for $Co_3Pt_1$.

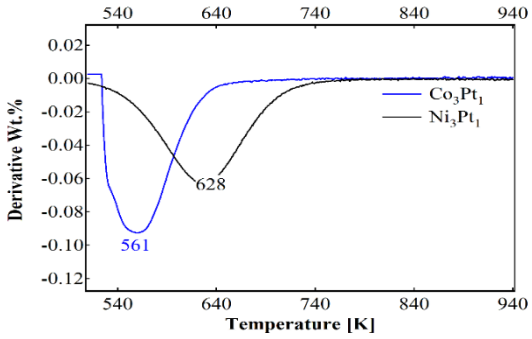


**Figure 4-9.** Thermogravimetric analysis. First derivative of weight loss plotted against temperature. The coke on the $Co_3Pt_1$ catalyst can burn off at 561 K and corresponds to a 4% weight loss.

### 4.4.3 Non-precious bimetallic catalysts composed of Fe, Co, and Ni

Flow reactor studies were performed on the $Fe_xNi_y$, $Co_xNi_y$, and $Fe_xCo_y$ bimetallic systems to assess which non-precious catalysts exhibited inherent activity for $CO_2$-ODHP or DRP. **Figure 4-10** illustrates the conversion and selectivity of the parent metals for the $Fe_xNi_y$, $Co_xNi_y$, and $Fe_xCo_y$ catalysts. Monometallic $Fe_1$, $Fe_3$, and $Co_1$ were all inactive at steady-state and the $Co_3$ monometallic, as stated in the last section, exhibited low conversion. Both $Ni_3$ and $Ni_1$ were active dry reforming catalysts. The various Fe-Ni catalysts showed different conversion and selectivity profiles than their parent monometallics, illustrating that there was a unique interaction between Fe and Ni on $CeO_2$ see **Figure 4-11**. Of all the Fe-Ni catalysts examined, only $Fe_3Ni_1$ was selected for further bimetallic effect experiments. A physical mixture of $Fe_3$ and $Ni_1$ illustrated less than 14% propylene selectivity at 4% $C_3H_8$ conversion whereas the bimetallic $Fe_3Ni_1$ exhibited 58% propylene selectivity at 2.7% $C_3H_8$ conversion, see **Figure 4-12**.

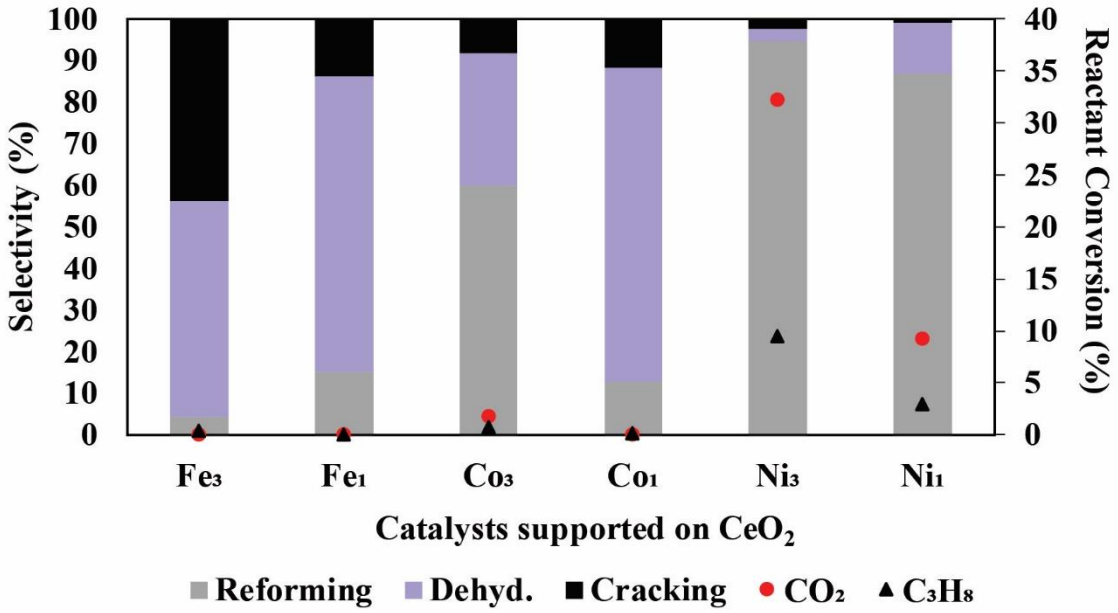


**Figure 4-10.** Selectivity and reactant conversion. Shown for monometallic Fe, Co, and Ni for the $Fe_xCo_y$, $Fe_xNi_y$, and $Co_xNi_y$ systems.

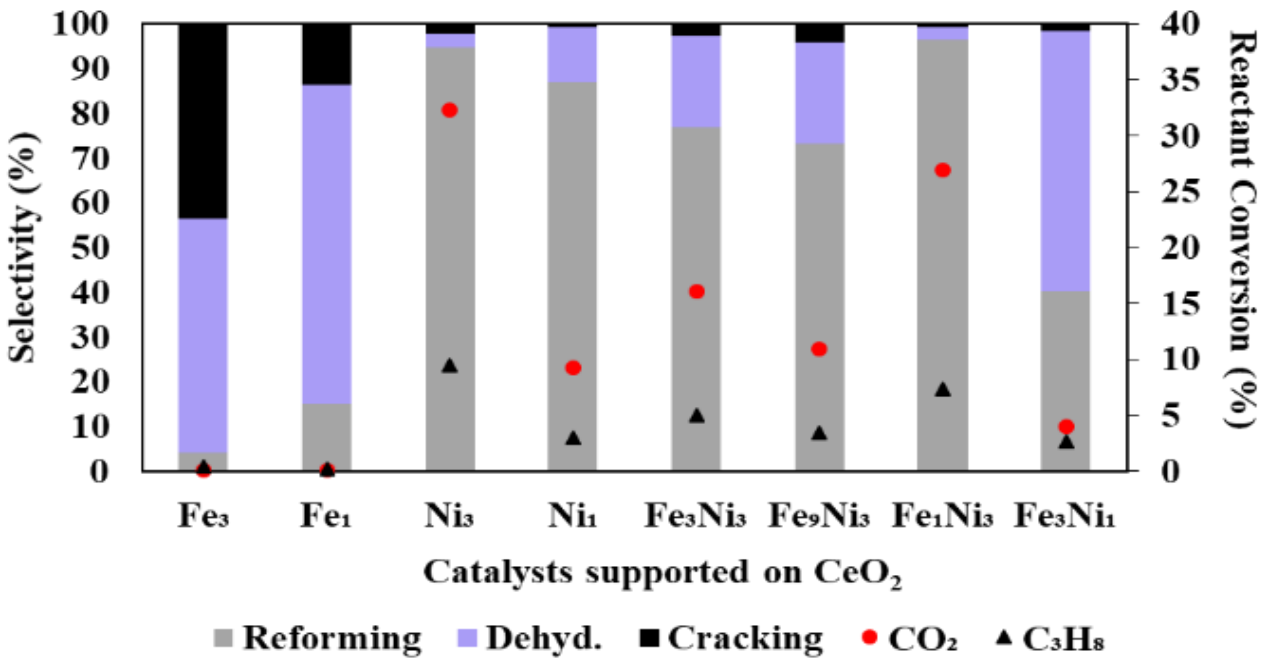


**Figure 4-11.** Parent metals with bimetallics. Shown for the $Fe_xNi_y$ system

Both $Fe_1Co_3$ and $Fe_3Co_1$ only exhibited higher $CO_2$ and $C_3H_8$ conversions compared to their respective monometallics during the first 5 hours on stream. The stability of $Fe_1Co_3$ was greater than $Fe_1$ but less than $Co_3$, whereas for the $Fe_3Co_1$ catalyst the stability was less than both monometallics. The $Co_3Ni_1$ catalyst showed higher steady-state conversion over both reactants and improved stability compared to $Ni_1$ and $Co_3$, while keeping high CO selectivity that was comparable to $Ni_1$ (but higher than $Co_3$). $Co_1Ni_3$ and $Co_3Ni_3$ both showed comparable reactant conversion and stability profiles compared to their respective monometallic counterparts. The stability profiles can be found in **Figure 4-13**.

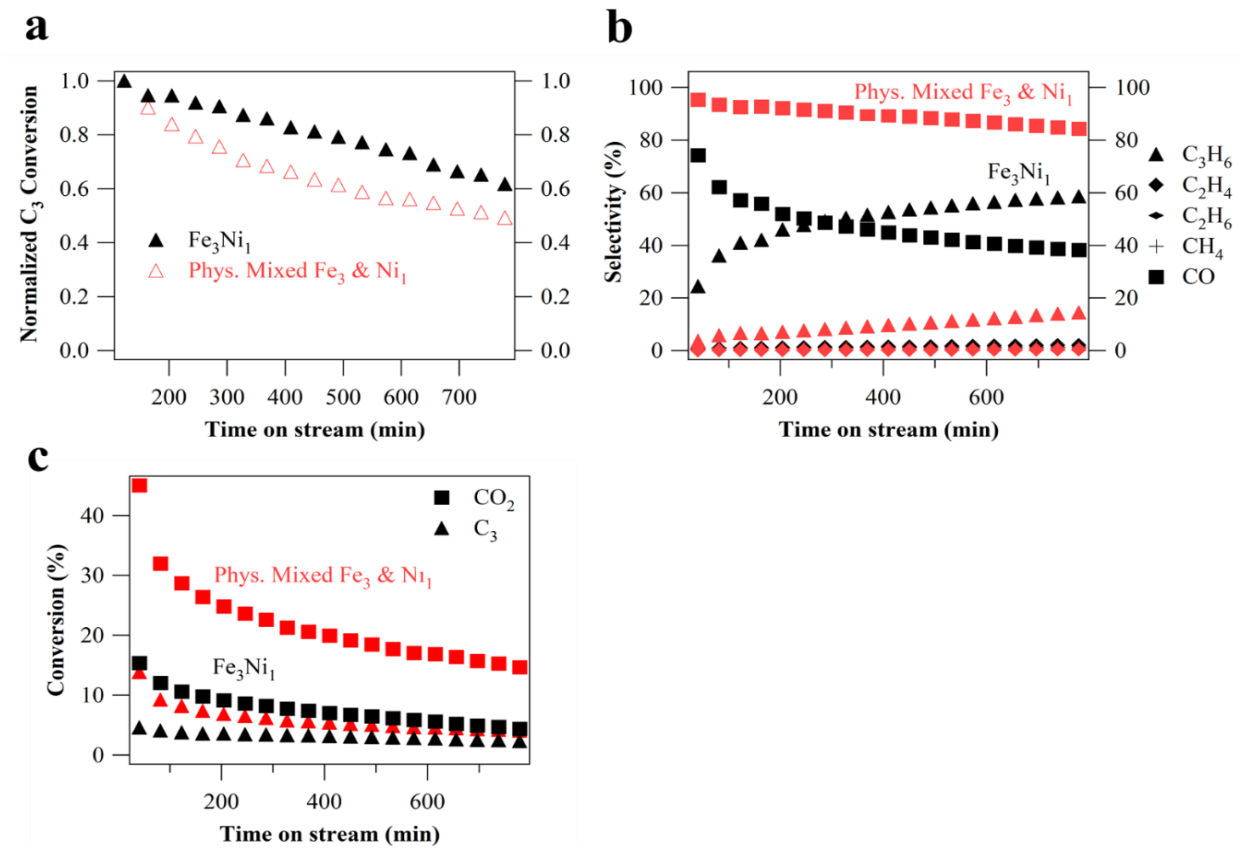


**Figure 4-12.** Bimetallic effect. Shown for $Fe_3Ni_1$; **(a)** conversion **(b)** selectivity and **(c)** stability. The physical mixture was made with an equivalent amount of metal as in the bimetallic experiment for accurate comparison.

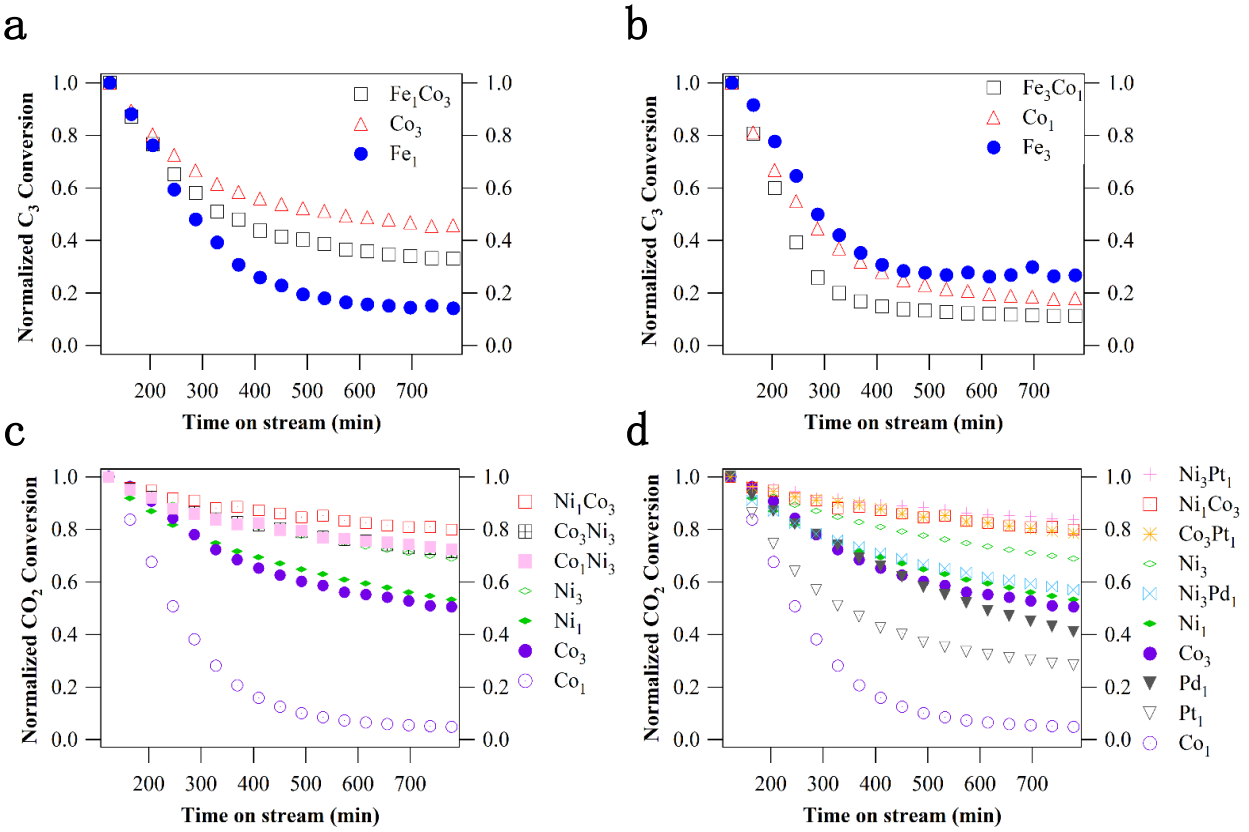


**Figure 4-13.** Stability profiles. Shown for **(a)** $Fe_1Co_3$ **(b)** $Fe_3Co_1$ **(c)** $Co_xNi_y$ and **(d)** $Ni_3Pt_1$, $Co_3Pt_1$, and $Ni_3Pd_1$ with respective monometallics.

As stated above, the previously examined (**Chapter 3:**) $Fe_3Ni_1$ catalyst was a promising system for the $CO_2$-ODHP reaction. To explore this bimetallic system further, three additional Fe-Ni catalysts were evaluated in the current Chapter to investigate the bimetallic effect on activity and selectivity. Doubling the catalyst metal loading while maintaining the 3:1 Fe to Ni ratio ($Fe_9Ni_3$), increased the conversion but negatively impacted the selectivity toward propylene (22.5% $S_{C_3H_6}$ at 3.4% $X_{C_3H_6}$). Setting an equal atomic concentration of Fe to Ni ($Fe_3Ni_3$) also increased the conversion, but at 5.0% $C_3H_8$ conversion the catalyst only exhibited 20.4% $C_3H_6$ selectivity. Finally, changing the atomic ratio from $Fe_3Ni_1$ to $Fe_1Ni_3$ also increased the catalyst activity but completely altered the selectivity pathway to favor the DRP (90.6% $S_{CO}$) even at a comparable propane conversion of 2.1%, see **Table 4-2**.

The $Fe_xCo_y$ bimetallic catalysts had low overall activity compared to the $Fe_xNi_y$ systems. The $Fe_3Co_1$ catalyst was inactive after 12 hours on stream. The steepest loss in activity for the $Fe_3Co_1$ catalyst occurred within the first 5 hours on stream; however, during that time the $C_3H_6$ selectivity was above 50%, see **Figure 4-1(g-h)**. The $Fe_1Co_3$ catalyst also experienced a loss in activity with time on stream (TOS) resulting in low steady-state conversions of $CO_2$ and $C_3H_8$ that corresponded to 1.5% and 0.9%, respectively. In addition, as TOS increased, the selectivity toward $C_1$, $C_2$, and $C_2^=$ products also increased over both the $Fe_3Co_1$ and $Fe_1Co_3$ catalysts.

While atomic percentages in most bimetallic catalysts influenced the conversion and selectivity ($Fe_xNi_y$ and to some extent the stability of the $Fe_xCo_y$ system), the $Co_xNi_y$ catalysts were not influenced. $Co_3Ni_1$, $Co_1Ni_3$, and $Co_3Ni_3$ were examined to investigate the effect of varying the atomic ratio of Co to Ni. All three $Co_xNi_y$ catalysts exhibited similar conversion, stability, and selectivity toward CO (average of 96.2).

### 4.4.4 In situ characterization of metal oxidation states

In situ XANES measurements were conducted to examine the oxidation states of the catalysts under reaction conditions, shown in **Figure 4-14**. $Ni_3Pt_1$ had previously been examined and it was determined that the catalyst under reaction conditions consisted of metallic Ni and Pt.[30] In the present study, in situ XANES results showed that $Ni_3Pd_1$ consisted of metallic Ni and Pd, see **Figure 4-15**. Therefore, both $Ni_3Pt_1$ and $Ni_3Pd_1$ were DRP catalysts that consisted of metallic phases under reaction conditions and showed improved stability compared to their respective precious metal monometallics.

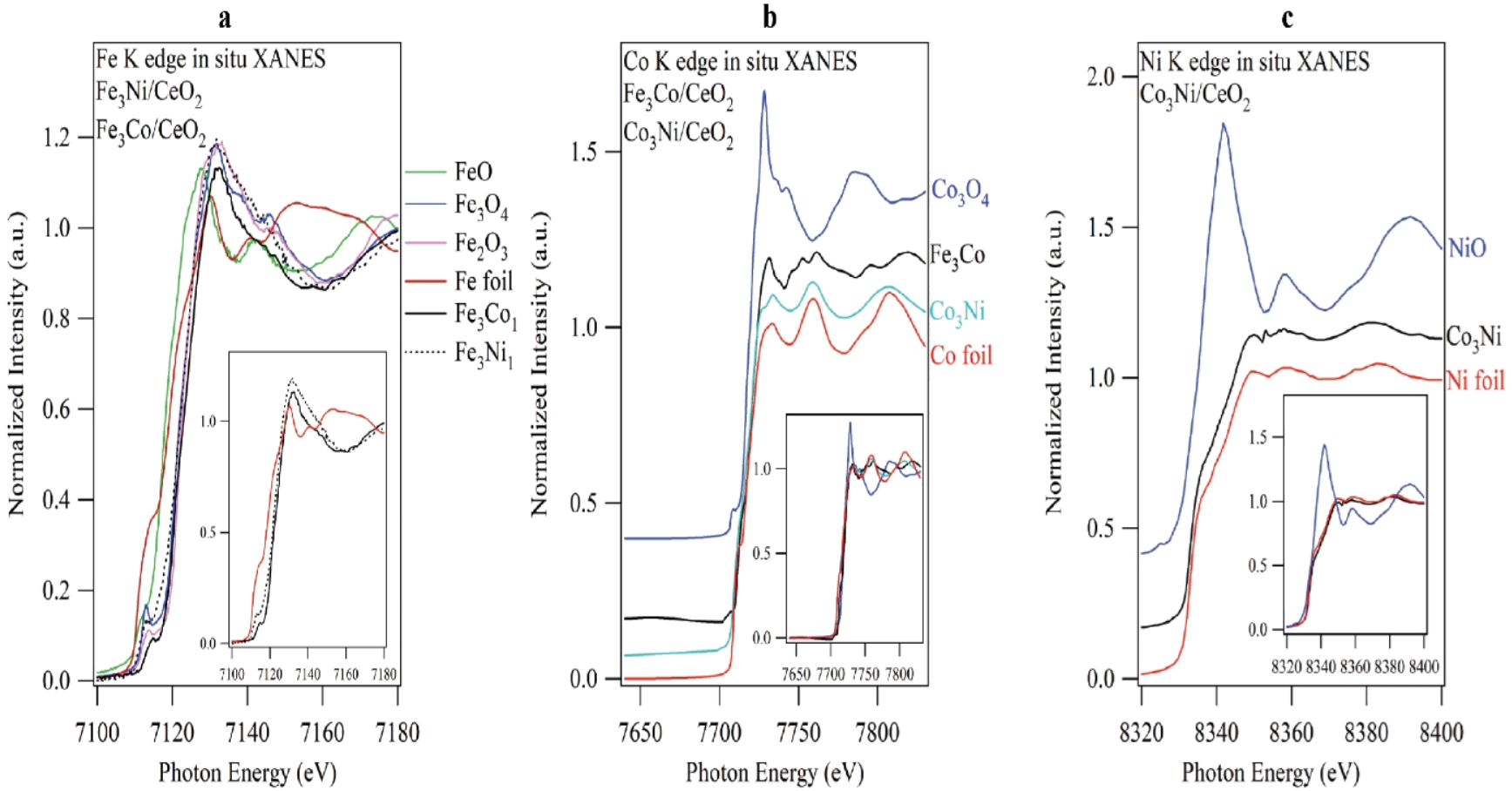


**Figure 4-14.** In situ XANES spectra with respective references. **(a)** Fe K edge of $Fe_3Co_1$ and $Fe_3Ni_1$[30], **(b)** Co K edge of $Co_3Ni_1$ and $Fe_3Co_1$, **(c)** Ni K edge of $Co_3Ni_1$.

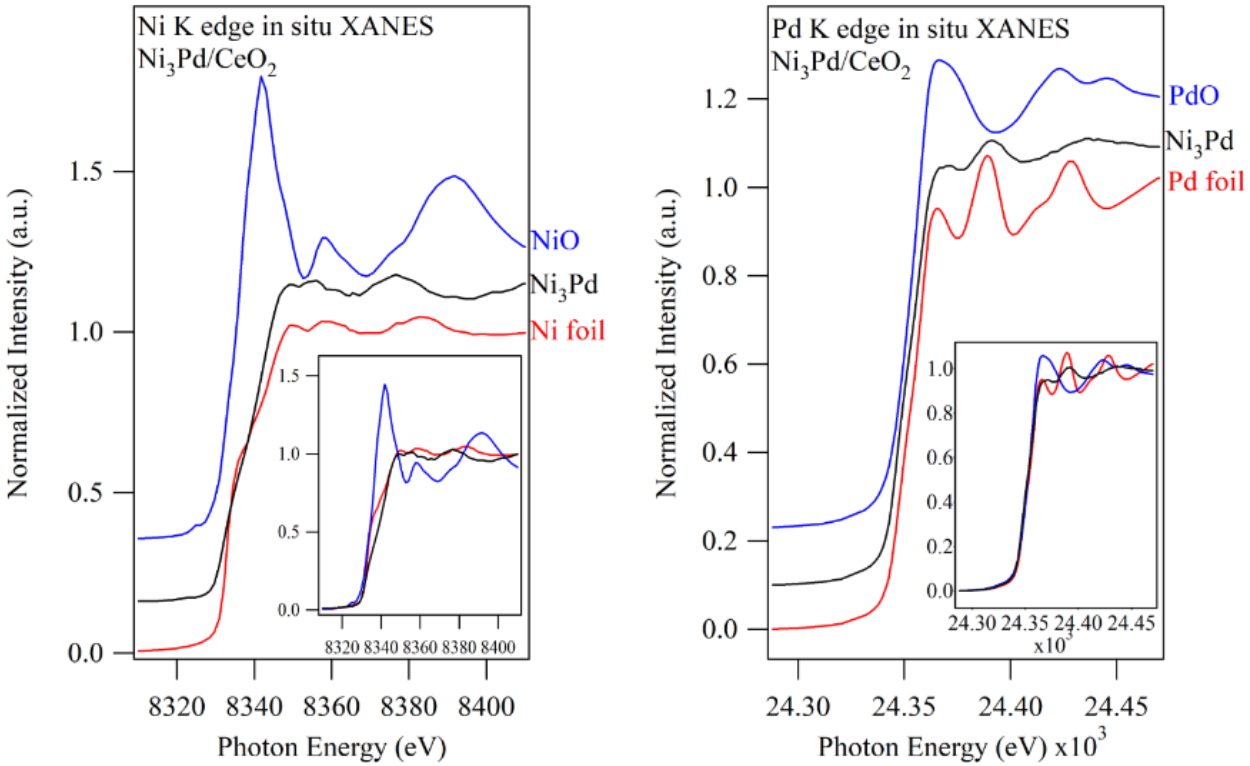


**Figure 4-15.** In situ XANES. Shown for **(a)** Ni K edge and **(b)** Pd K edge for $Ni_3Pd_1$ with references.

The $Fe_3Ni_1$ catalyst had also been previously determined to consist of metallic Ni and oxidized Fe under reaction conditions. This finding was incorporated into the DFT calculations of the previous study, and it was determined that the presence of oxidized Fe under reaction conditions was key to favor oxidative C-H bond cleavage via the $CO_2$-ODHP pathway. Thus, it was of interest in this study to investigate if the selectivity difference between the $CO_2$-ODHP $Fe_3Ni_1$ catalyst and the DRP $Fe_1Ni_3$ catalyst was attributed to different oxidation states. The in situ XANES results shown in **Figure 4-16** revealed that like $Fe_3Ni_1$, the DRP $Fe_1Ni_3$ catalyst also consisted of metallic Ni and oxidized Fe. Therefore, the selectivity differences among the various $Fe_xNi_y$ catalysts were not caused by changes in the bulk oxidation state. From the previous DFT calculations, it was also observed that in the presence of oxygen (from the dissociation of $CO_2$), Fe segregated to the surface due to a stronger Fe-O bond compared to Ni-O. However, on a surface that contained a greater amount of Ni than Fe, it is reasonable to believe that metallic Ni particles would be more pronounced. This essentially dampens the catalytic effect observed with oxidized Fe, therefore changing the active site and promoting activity in favor of the dry reforming reaction, similar to the work described for the reactions of $CO_2$ with ethane.[36]

The Fe-Co bimetallic catalysts also illustrated a preference to form propylene but have low performance due to deactivation. The in situ XANES results revealed that the $Fe_3Co_1$ catalyst consisted mainly of metallic Co and oxidized Fe, but the extent of Fe oxidation was less than that in the $Fe_3Ni_1$ catalyst (**Figure 4-14**), which may be the cause of the observed lower steady-state activity and stability. **Figure 4-14(b-c)** depicts the in situ XANES spectra of the DRP $Co_3Ni_1$ catalyst which demonstrated that under reaction conditions the catalyst consisted of metallic Ni and metallic Co; this is unlike the other non-precious systems, Fe-Ni and Fe-Co, which were

influenced by atomic concentration and contained an oxidized component in the catalysts. This comparison is consistent with the argument that unoxidized metals favor the DRP pathway.

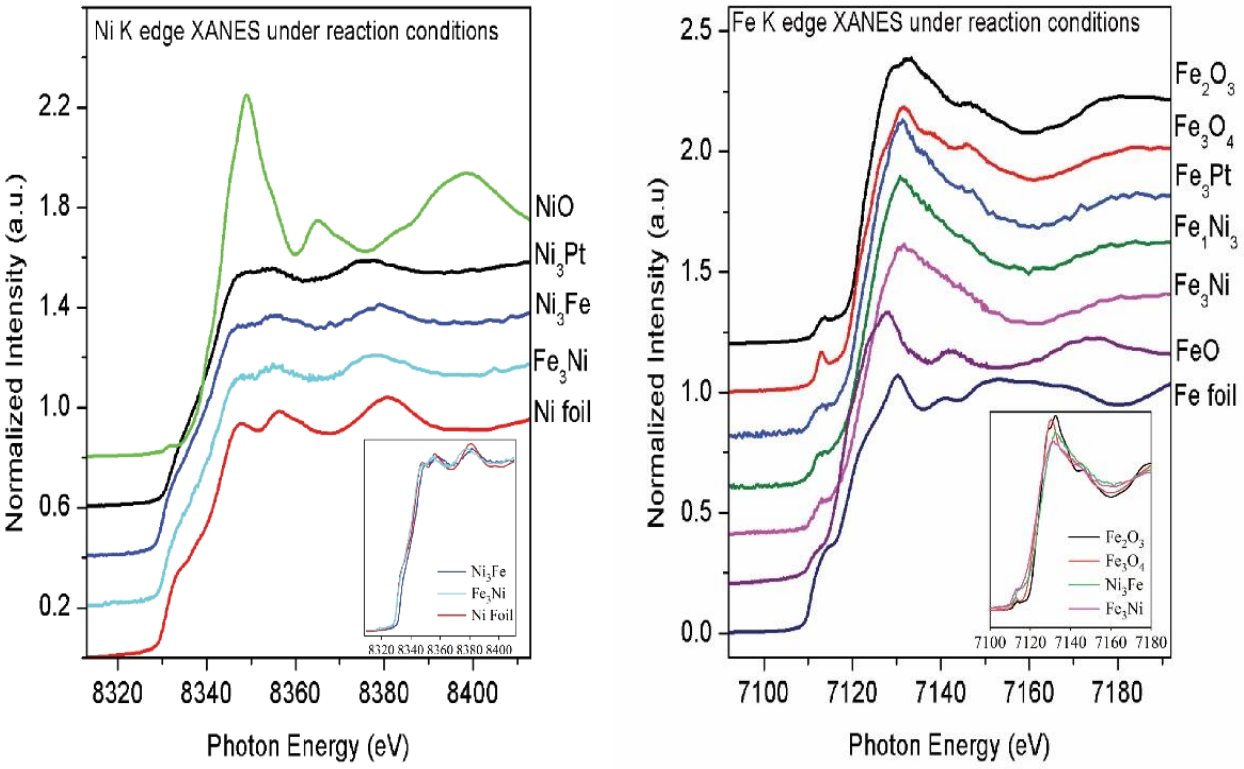


**Figure 4-16.** In situ XANES. Shown for **(a)** Ni K edge and **(b)** Fe K edge for $Fe_3Ni_1$ and $Fe_1Ni_3$ with references.

## 4.5 The role of oxide supports

The series of oxide supports included in this study were γ-$Al_2O_3$, $ZrO_2$, $SiO_2$, and $TiO_2$. These supports were selected to investigate the effects of oxide reducibility, surface defects, and strong metal-support interactions. $SiO_2$ provides an irreducible and relatively inert surface while γ-$Al_2O_3$ is an irreducible but reactive support due to the presence of surface hydroxyl groups. The $ZrO_2$ support is considered in the literature to be reducible or at least partially reducible. Additionally, the $ZrO_2$ support exhibits surface defects or kinks that can strongly influence catalyst activity and selectivity. The $TiO_2$ support, like $CeO_2$, is classified as an ionic reducible oxide with a formal valence of +4 but is prevalent in the literature to induce strong metal-support interactions (SSMI).[38]

Predominately, efforts for $CO_2$-ODHP have focused on chromium catalysts supported on $Al_2O_3$ and various types of $SiO_2$.[39] Studies performed for the $CO_2$-ODHP reaction at 873 K concluded that both the activity and propylene selectivity of $Cr/SiO_2$ would increase with increasing $CO_2$ partial pressure, whereas for the Cr/γ-$Al_2O_3$ catalyst activity would decrease with even a slight increase of $CO_2$ partial pressure.[40.,41,42] The variance in performance between these two supports was attributed to two possibilities: (1) the $CO_2$ molecule adsorbs more strongly on γ-$Al_2O_3$ (thereby reducing $C_3H_8$ adsorption) and or that (2) the acidity/basicity of the $CrO_x$/γ-$Al_2O_3$ catalyst is affected by the introduction of $CO_2$. Furthermore, the addition of Ni to the $CrO_x/SiO_2$ catalyst for $CO_2$-ODHP helps lower the activation energy for the dissociation of $CO_2$ due to the strong chemisorption of $CO_2$ on Ni, leading to the bending of the molecule that weakens the C=O bond to generate CO and activated atomic oxygen.[43] While the role of oxide supports for chromium-based $CO_2$-ODH chemistry has been examined, it was of interest to explore less toxic catalytic materials with longer lifecycles.

Non-chromium studies for $CO_2$-ODHP mainly investigate the use of $In_2O_3$ and $Ga_2O_3$. Among $In_2O_3$-$MO_x$ binary mixed oxide catalysts (M: Al, Zn, Zr, Ti, Fe, Mg, Si, and Ce), $In_2O_3$-$Al_2O_3$ was found to have the highest propylene formation with good stability due to high indium dispersion while the mixed metal oxide with Ce showed the lowest activity.[44] Unsupported $Ga_2O_3$ was tested for the $CO_2$-ODHP and was found to have high initial propylene selectivity (30%), but after 10 minutes the selectivity decreased to 7-8% due to deactivation from coke formation.[45] Among a series of $Ga_2O_3$ supported $TiO_2$, $ZrO_2$, γ-$Al_2O_3$, $SiO_2$, and MgO it was found that only over $TiO_2$ did the presence of $CO_2$ enhance the activity and selectivity due to its unique ability to promote the reverse water gas shift reaction.[45] While neither the activity nor selectivity of the $Ga_2O_3/ZrO_2$ catalyst was enhanced with $CO_2$, the stability did improve, and this was attributed to the ability to promote coke removal via the reverse Boudouard reaction.

Very few support effect studies with transition metal catalysts on metal oxides (apart from chromium) have been examined for the reactions of $CO_2$ and propane.[12] Even more limited are those that also examine the effect on the DRP pathway. Pradhan et al. investigated Ru supported on $CeO_2$ and $ZrO_2$ for the partial oxidation of propane with $CO_2$ in the temperature range of 473-823 K.[19] There was a clear need to expand the knowledge regarding the effect of oxide supports for the $CO_2$ + $C_3H_8$ chemistry, especially with bimetallic catalytic systems in order to develop highly active and selective catalysts for each pathway.

### 4.5.1 Catalytic evaluation of metal oxide supports on $Fe_3Ni_1$ and $Ni_3Pt_1$

**Table 4-3** summarizes the activity and selectivity of the $Fe_3Ni_1$ and $Ni_3Pt_1$ systems supported on γ-$Al_2O_3$, $SiO_2$, $TiO_2$, and $ZrO_2$ along with the corresponding CO chemisorption values. Conversion data following time on stream (TOS) are shown in **Figure 4-17** for both

bimetallic systems. For comparison, the results of the $Fe_3Ni_1$ and $Ni_3Pt_1$ systems supported on reducible $CeO_2$ from the study described in **Chapter 3** are also included in **Table 4-3**.[30]

**Table 4-3.** Support effects. Bimetallic catalyst flow reactor results for $CO_2$ + $C_3H_8$ reaction (10 mL/min each) at 823 K with Ar diluent (20 mL/min) and 100 mg of catalyst (40-60 mesh). Values are obtained by averaging data from hours 10-12. Selectivity and yield are on a $C_3H_8$ basis. Catalysts that are inactive at steady-state are not included. Catalysts are synthesized by atomic ratios corresponding to a 1.67 wt.% $Pt_1$ basis, thus the weight percent of $Fe_3$ and $Ni_3$ are 1.43 and 1.5, respectively. The nomenclature assigned by subscripts such as in $Fe_3Ni$ means that there are 3 atoms of Fe for every atom of Ni.

| Catalyst | CO uptake | Conversion (%) | | TOF ($site^{-1} \cdot min^{-1}$) | | Selectivity (%) | | | Yield (%) | |
|---|---|---|---|---|---|---|---|---|---|---|
| /Support | ($\mu mol \cdot g^{-1}$) | $CO_2$ | $C_3$ | $CO_2$ | $C_3$ | CO | $C_3H_6$ | $C_1$-$C_2$* | $C_3H_6$ | CO |
| **$Fe_3Ni$** | | | | | | | | | | |
| /$CeO_2$ | 31.9 | 4.1 | 2.8 | 5.7 | 3.4 | 40.4 | 58.0 | 1.6 | 1.6 | 1.1 |
| /$\gamma$-$Al_2O_3$ | 19.0 | 5.8 | 1.9 | 14.2 | 4.6 | 80.2 | 9.0 | 10.7 | 0.2 | 1.5 |
| /$ZrO_2$ | 74.5 | 1.0 | 0.8 | 0.62 | 0.47 | 33.8 | 43.7 | 22.5 | 0.3 | 0.3 |
| **$Ni_3Pt$** | | | | | | | | | | |
| /$CeO_2$ | 50.1 | 39.4 | 11.6 | 37.5 | 10.5 | 96.2 | 2.8 | 0.8 | 0.3 | 11.1 |
| d/$CeO_2$ | - | 7.8 | 2.2 | - | - | 87.8 | 11 | 1.2 | 0.2 | 2.0 |
| /$\gamma$-$Al_2O_3$ | 44.4 | 15.0 | 4.2 | 15.7 | 4.4 | 83.9 | 14.1 | 1.2 | 0.6 | 3.5 |
| /$ZrO_2$ | 58.4 | 25.0 | 7.2 | 19.8 | 5.5 | 92.6 | 5.8 | 1.6 | 0.4 | 6.7 |
| /$SiO_2$ | 59.0 | 18.7 | 4.7 | 14.9 | 3.6 | 95.5 | 3.7 | 0.7 | 0.2 | 4.5 |
| /$TiO_2$ | 40.9 | 1.1 | 0.9 | 1.3 | 0.98 | 31.2 | 62.3 | 3.5 | 0.6 | 0.3 |

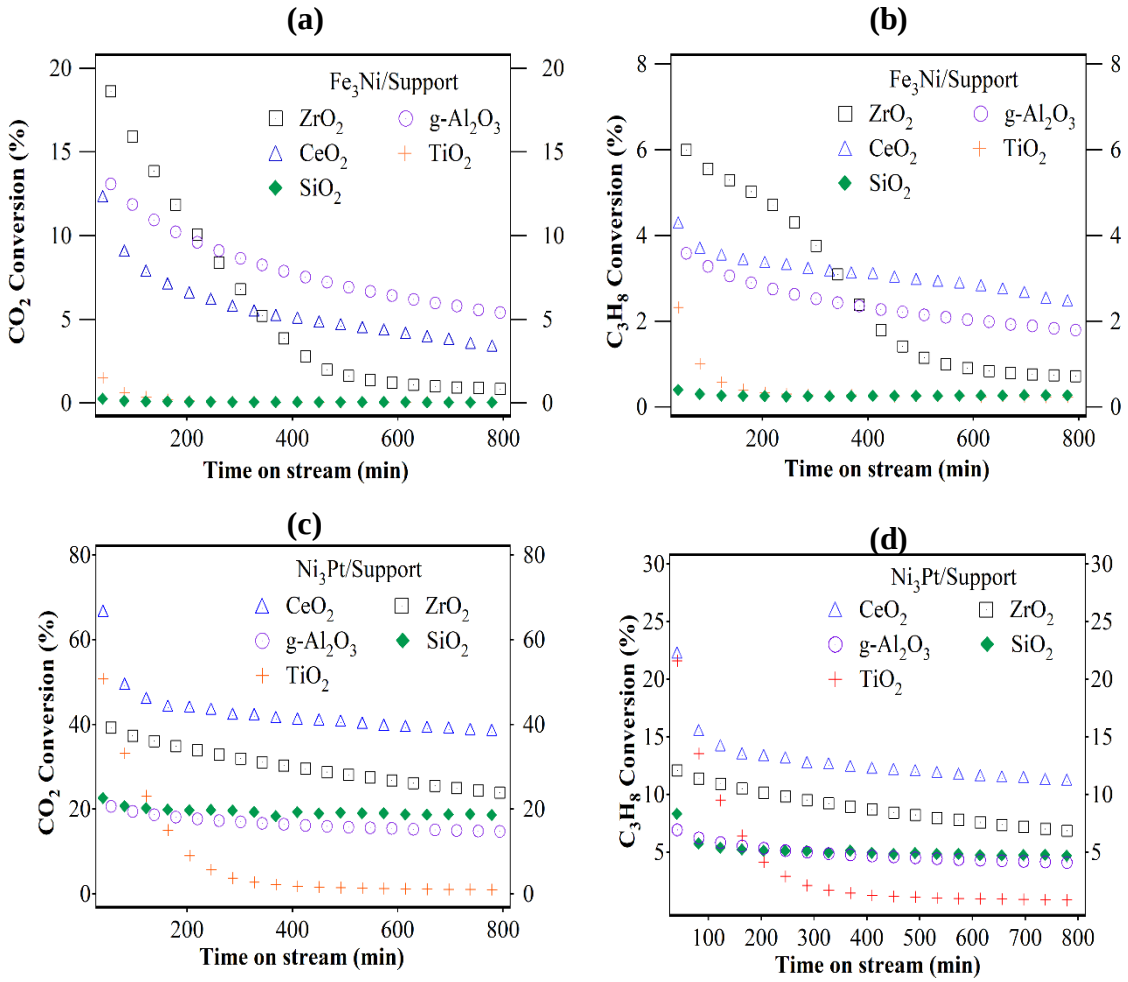


**Figure 4-17.** $CO_2$ and $C_3H_8$ conversion following time on stream for the $Fe_3Ni$ (**a** & **b**) and $Ni_3Pt$ (**c** & **d**) systems over various supports.

The detailed study between $Fe_3Ni_1$ and $Ni_3Pt_1$ supported on $CeO_2$ presented in **Chapter 3**: included both experiments and density functional theory (DFT) calculations. These calculations showed that there are higher barriers for the activation of propane on the $Fe_3Ni_1$ catalytic system compared to $Ni_3Pt_1$. Thus, the higher conversion over the $Ni_3Pt_1$ system on all the evaluated supports in this study compared to the $Fe_3Ni_1$ system was consistent with the DFT calculations performed in **Chapter 3.4.3**.

The selectivity profile of the $Fe_3Ni_1$ catalyst system varied extensively among the different evaluated supports within a $C_3H_8$ conversion range of 0.8-2.8%. The conversion of propane was not improved on any of the other examined supports compared to the activity when supported on $CeO_2$. The $Fe_3Ni_1/\gamma\text{-}Al_2O_3$ catalyst showed 1.9% $C_3H_8$ conversion, lower than the $C_3H_8$ conversion over the $Fe_3Ni_1/CeO_2$ catalyst. **Figure 4-18**, which illustrates the normalized $C_3H_8$ conversion following time on stream, showed that the $Fe_3Ni_1$ system is also more unstable on $\gamma\text{-}Al_2O_3$ than on $CeO_2$. Compared to the $CeO_2$ supported $Fe_3Ni_1$, the propylene selectivity on $\gamma\text{-}Al_2O_3$ decreased by 6.5 times, the same factor by which the cracking selectivity increased. Therefore, the selectivity profile of the $Fe_3Ni_1/\gamma\text{-}Al_2O_3$ catalyst favored the DRP reaction pathway with 80% CO selectivity, a two-fold increase compared to the $CO_2$-ODHP $Fe_3Ni_1/CeO_2$ catalyst. Thermogravimetric analysis (TGA) studies are used to measure the weight loss of a spent catalyst by subjecting the sample to a controlled temperature ramp treatment in an $O_2$ rich environment. The percent decrease in mass is attributed to an equivalent amount of coke that was on the spent catalyst after the $CO_2$ + $C_3H_8$ reaction at 823 K. TGA results, shown in **Figure 4-19,** illustrated that the $Fe_3Ni_1$ system on $\gamma\text{-}Al_2O_3$ support had a higher susceptibility to coke formation than when supported on $CeO_2$, with total weight loss values of 2.1% and 0.2%, respectively. The higher coke accumulation was a direct reflection of the increased cracking activity on the more acidic $\gamma\text{-}Al_2O_3$ support.

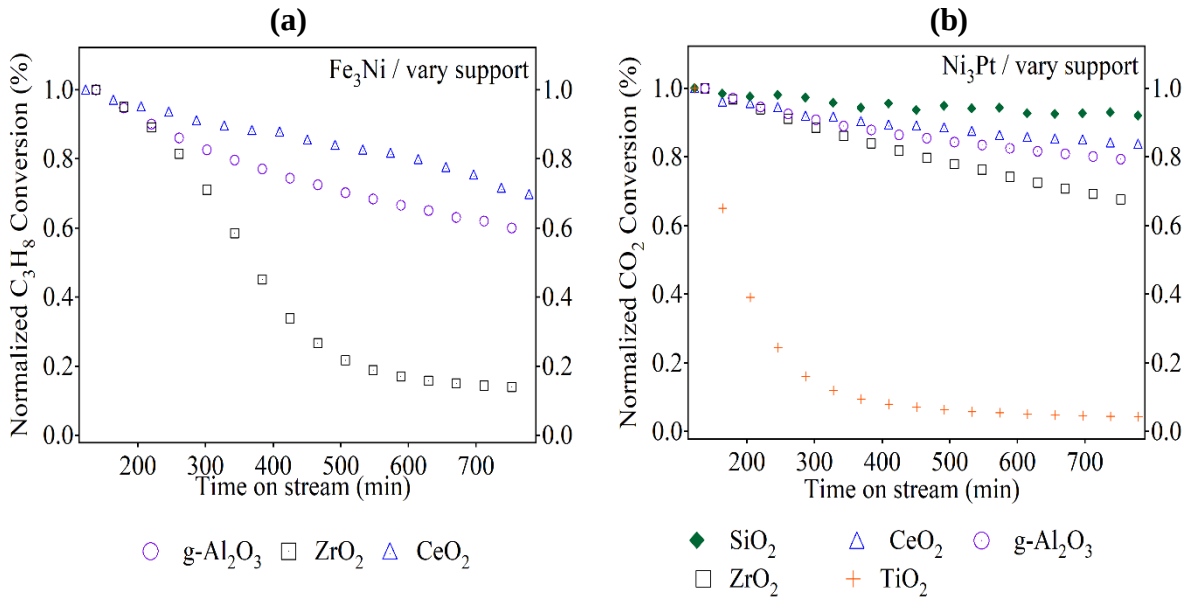


**Figure 4-18.** Normalized reactant conversion for the $Fe_3Ni$ (**a**) and $Ni_3Pt$ (**b**) systems over various supports to illustrate stability after the initial 123 minutes on stream.

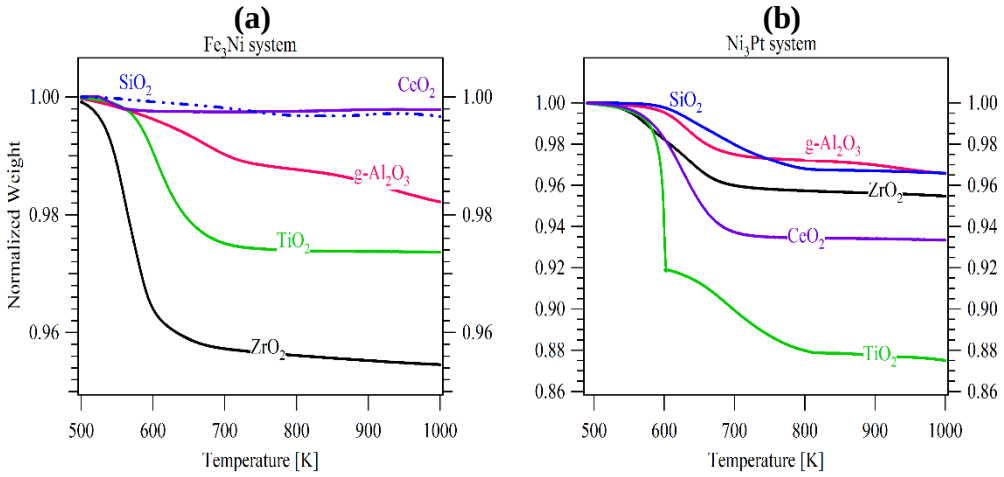


**Figure 4-19.** Normalized weight loss following temperature for the $Fe_3Ni$ (**a**) and $Ni_3Pt$ (**b**) systems on the evaluated supports and $CeO_2$.

Unlike the $Fe_3Ni_1$ system supported on $CeO_2$ and $\gamma$-$Al_2O_3$, the $Fe_3Ni_1/ZrO_2$ catalyst quickly lost activity within the first 500 minutes on stream, reducing the conversion at steady-state to only 1% for both reactants. Following selectivity with time on stream for the $Fe_3Ni/ZrO_2$ catalyst showed that the initial catalyst activity (15-220 minutes) favored reforming (above 50% CO selectivity), but with further deactivation the CO production decreased such that at steady-state the production of propylene ($S_{C_3H_6}$ 43.7%) and cracking products ($S_C$ 22.5%) was favored (**Figure 4-20**). TGA measurements showed that the $Fe_3Ni_1/ZrO_2$ catalyst lost 4.6% of its original mass, indicating that coking was a significant mode of deactivation for the $Fe_3Ni_1$ system on $ZrO_2$.

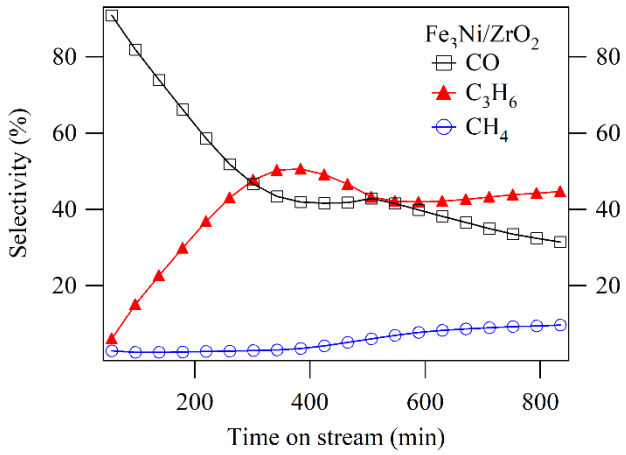


**Figure 4-20.** Selectivity following time on stream for the $Fe_3Ni/ZrO_2$ catalyst. The selectivity toward $C_2$ products is not shown.

The $Fe_3Ni_1$ system supported on $TiO_2$ showed low initial activity and fast deactivation. Despite the low conversion throughout time on stream over the $Fe_3Ni_1/TiO_2$ catalyst, the TGA measurement illustrated a 2.8% weight loss. Indicating that the $TiO_2$ support was the most susceptible to coke formation with the $Fe_3Ni_1$ catalytic system. Unlike the $Fe_3Ni_1/TiO_2$, the $Fe_3Ni_1/SiO_2$ catalyst was completely inactive even at early reaction times. When subjected to TGA

measurement, the spent $Fe_3Ni_1/SiO_2$ sample showed insignificant weight loss, corroborating with the observed inactivity.

Unlike the $Fe_3Ni_1$ system, the change in oxide support from $CeO_2$ to $\gamma$-$Al_2O_3$, $ZrO_2$, $TiO_2$, and $SiO_2$ did not alter the favored reaction pathway on the $Ni_3Pt_1$ catalytic system. While the evaluated oxide supports influenced the reactant conversion of the $Ni_3Pt_1$ system, the favored DRP reaction pathway remained the same with minimal selectivity differences. More than a twofold conversion decrease was observed over the $Ni_3Pt/\gamma$-$Al_2O_3$ catalyst compared to $Ni_3Pt_1/CeO_2$. The $Ni_3Pt/\gamma$-$Al_2O_3$ catalyst at 15% $CO_2$ and 4.2% $C_3H_8$ conversion, demonstrated 84% selectivity toward CO. The activity results of the diluted $Ni_3Pt/CeO_2$ catalyst from **Chapter 3**: are provided in **Table 4-3** to examine the selectivity profile at lower conversion, enabling a more accurate evaluation against the less active metal oxide supports.[30] At 7.8% and 2.2% $CO_2$ and $C_3H_8$ conversion, respectively, the d$Ni_3Pt/CeO_2$ exhibited 87.8% CO selectivity. Thus, the $Ni_3Pt_1$ system when supported on $\gamma$-$Al_2O_3$ was inherently less selective to CO than when supported on $CeO_2$. Additionally, the observed activity difference between $\gamma$-$Al_2O_3$ and $CeO_2$ was much more pronounced with the $Ni_3Pt_1$ system (62% difference) than with the $Fe_3Ni_1$ system (32% difference). This suggested that the $Ni_3Pt_1$ system may have had stronger interactions with the $\gamma$-$Al_2O_3$ support than the $Fe_3Ni_1$ system.

The $Ni_3Pt_1$ system on the partially reducible and defect-rich $ZrO_2$ support exhibited higher conversion than when on $\gamma$-$Al_2O_3$, with 25.0% $CO_2$ conversion and a CO selectivity of 92.6%. However, the $Ni_3Pt_1$ system was less stable on $ZrO_2$ than when supported on $CeO_2$, $\gamma$-$Al_2O_3$, and $SiO_2$ (**Figure 4-18**). Like the $Fe_3Ni_1$ system, $Ni_3Pt_1$ showed initial activity but substantial deactivation when supported on $TiO_2$ such that the steady-state activity reduced to roughly 1% for both $CO_2$ and $C_3H_8$. As shown in **Figure 4-19b**, the deactivation on the $TiO_2$ support was likely

due to excessive coke formation equivalent to a 12.5% weight loss in TGA measurements. Thus, for the $Ni_3Pt_1$ system, the $TiO_2$ support was the most susceptible to coke formation. The increased coke formation on both the $Fe_3Ni_1$ and $Ni_3Pt_1$ system when supported on $TiO_2$ may be an artifact of increased metal-support interactions, which in turn increased the barrier for products to desorb from the surface –leading to cracking reactions and thus excessive coke formation.

In contrast to $Fe_3Ni_1/SiO_2$, the $Ni_3Pt_1/SiO_2$ catalyst was active (18.7% $XCO_2$), selective to DRP ($S_{CO}$ 95.5%), and highly stable following time on stream. $CO_2$ activation may occur on the metal oxide support or the interfacial sites between the supported bimetallic and the support itself. The inactivity of the $Fe_3Ni_1$ system when supported on inert $SiO_2$ may be an indication that the Fe-Ni system was not capable of activating $CO_2$ at the rates required for the $CO_2 + C_3H_8$ reactions. The $Ni_3Pt_1$ system, however, showed modest but stable activity with $SiO_2$, indicating that the Ni-Pt bimetallic system was capable of both $CO_2$ and $C_3H_8$ alkane activation at appreciable rates that corresponded to turnover values of 14.9 and 3.6 site·min$^{-1}$, respectively. Lastly, while the conversion and susceptibility to coke of the $Ni_3Pt_1$ system on the two irreducible supports were similar, the $Ni_3Pt_1$ system was more stable on inert $SiO_2$.

## 4.6 Conclusions

The reduction of $CO_2$ by propane can proceed via the DRP or $CO_2$-ODHP pathways to produce synthesis gas or propylene, respectively, and both reactions may occur simultaneously at 823 K. The present work aimed to identify bimetallic combinations supported on $CeO_2$ that were active and selective for the reactions of $CO_2$+$C_3H_8$. $Pt_1$ and $Pd_1$ based bimetallic catalysts with $Fe_3$, $Co_3$, and $Ni_3$ as well as non-precious metal combinations with varying atomic composition have been evaluated in flow reactor studies. Furthermore, to explore the effect of other oxide supports

flow reactor studies were conducted over the two most promising catalytic systems representing each pathway supported on γ-$Al_2O_3$, $ZrO_2$, SiO2, and $TiO_2$.

Pt-based bimetallic catalysts outperformed Pd-based catalysts on both mass-based conversion and site-specific TOF values. Of the three transition metals examined with $Pt_1$ and $Pd_1$, $Ni_3$ outperformed $Fe_3$ and $Co_3$ in terms of $CO_2$ and propane conversions. Compared to monometallic $Pt_1$ and $Pd_1$, the bimetallics with $Ni_3$ and $Co_3$ were not only more active but also exhibited greater stability. The $Co_xNi_y$ catalysts, which are composed of metallic Co and Ni under reaction conditions, were also active and selective for the DRP pathway. In comparison, the $Fe_xNi_y$ catalysts exhibited selectivity toward both the $CO_2$-ODHP and DR pathways. The selectivity could be modified by changing the Ni content in the bimetallic composition, increasing the Ni atomic ratio above 1 altered the selectivity to favor the DRP pathway rather than $CO_2$-ODHP. Overall, a bimetallic catalyst library to determine inherent activity toward DRP or $CO_2$-ODHP was established and can be used toward future efforts to increase activity, stability, and selectivity.

Following the study on the effect of bimetallic interactions for the $CO_2$-ODHP and DRP reactions, the role of other oxide supports was evaluated. The $Ni_3Pt_1$ catalytic system exhibited higher conversion than the $Fe_3Ni_1$ system for all evaluated supports likely due to lower barriers for propane activation. Changing the metal oxide support of the $Fe_3Ni_1$ system influenced the selectivity profile and altered the preferred reaction pathway. Varying the support of the $Ni_3Pt_1$ system did not significantly affect selectivity, and therefore the preferred DRP reaction pathway remained the same over all of the evaluated supports. Among all the active supports for the $Fe_3Ni_1$ and $Ni_3Pt_1$ systems, $CeO_2$ was the most stable, active, and selective toward the $CO_2$-ODHP and DRP pathways, respectively. The $TiO_2$ support, while reducible like $CeO_2$, hindered the activity of both catalysts via excessive coke formation likely due to strong metal-support interactions. The

$Fe_3Ni_1$ system on irreducible $\gamma$-$Al_2O_3$ favored reforming while the inert $SiO_2$ was completely inactive. In addition, it was observed the inactivity of the $Fe_3Ni_1/SiO_2$ was likely due to the inability of the Fe-Ni system to promote $CO_2$ activation whereas the Ni-Pt catalytic system was capable of both $CO_2$ and $C_3H_8$ activation, allowing modest activity over the $Ni_3Pt_1/SiO_2$ system. On $Ni_3Pt_1$, the irreducible supports illustrated similar activity corresponding to a twofold conversion decrease compared to $CeO_2$. Thus, it has been identified that the unique interactions of the $Fe_3Ni_1$ and $Ni_3Pt_1$ catalytic systems with reducible $CeO_2$ were key to maintain selectivity to the desired products with good activity and selectivity. Future studies should be geared towards the controlled synthesis of $Fe_3Ni_1$ and $Ni_3Pt_1$ on $CeO_2$ and $CeO_2$-containing mixed oxides of high surface area to obtain enhanced performance and yield to desired products.

## 4.7 Acknowledgements

This work is supported by the U.S. Department of Energy (DOE) under contract number DE-SC0012704. The XAS measurements were performed at the 9-BM beamline of the Advanced Photon Source (APS) at the Argonne National Laboratory (DE-AC02-06CH11357). E.G acknowledges the U.S National Science Foundation Graduate Research Fellowship Program: DGE-16-44869 and the Gates Millennium Scholars Program. E.G would like to acknowledge Dr. Zhenhua Xie for performing CO chemisorption measurements for the catalysts in this chapter.

## 4.8 References


1. Pachauri RK, Meyer LA, eds. Climate Change 2014: Synthesis Report Contribution of Working Groups I, II and III to the Fifth Assessment Report of the Intergovernmental Panel on Climate Change. *Geneva, Switzerland*; 2014.

2. Centi G, Iaquaniello G, De Falco M, eds. $CO_2$: A Valuable Source of Carbon (1st edition). London: *Springer-Verlag London*; 2013. doi:10.1007/978-1-4471-5119-7

3. Dincer I, Acar C. Innovation in hydrogen production. *Int J Hydrogen Energy*. 2017;42:14843-14864.

4. Pakhare D, Spivey J. A review of dry ($CO_2$) reforming of methane over noble metal catalysts. *Chem Soc Rev*. 2014;43:7813-7837.

5. Tang P, Zhu Q, Wu Z, Ma D. Methane activation: the past and future. *Energy Environ Sci*. 2014;7:2580-2591.

6. Wang S, Zhu ZH. Catalytic Conversion of Alkanes to Olefins by Carbon Dioxide Oxidative Dehydrogenation *A Review*. *Energy and Fuels*. 2004;18:1126-1139.

7. Plotkin JS. The Propylene Gap: How Can It Be Filled? ACS News Industrial Chemistry & Engineering. https://www.acs.org/content/acs/en/pressroom/cutting-edge-chemistry/the-propylene-gap-how-can-it-be-filled.html. Published September 2015.

8. Zangeneh FT, Taeb A, Gholivand K, Sahebdelfar S. Thermodynamic Equilibrium Analysis of Propane Dehydrogenation with Carbon Dioxide and Side Reactions. *Chem Eng Commun*. 2016;203:557-565.

9. Ansari MB, Park S-E. Carbon dioxide utilization as a soft oxidant and promoter in catalysis. *Energy Environ Sci*. 2012;5:9419-9437.

10. Osaki T, Mori T. Kinetics of the reverse-Boudouard reaction over supported nickel catalysts. *React Kinet Catal Lett*. 2006;89:333-339.

11. Lim JY, McGregor J, Sederman AJ, Dennis JS. The role of the Boudouard and water-gas shift reactions in the methanation of CO or $CO_2$ over Ni/g-Al2O3 catalyst. *Chem Eng Sci*. 2016;152:754-766.

12. Atanga MA, Rezaei F, Jawad A, Fitch M, Rownaghi AA. Oxidative dehydrogenation of propane to propylene with carbon dioxide. *Appl Catal B Environ*. 2018;220:429-445.

13. Zhang F, Wu R, Yue Y, et al. Microporous and Mesoporous Materials Chromium oxide supported on ZSM-5 as a novel efficient catalyst for dehydrogenation of propane with $CO_2$. *Microporous Mesoporous Mater*. 2011;145:194-199.

14. Talati A, Haghighi M, Rahmani F. Oxidative dehydrogenation of ethane to ethylene by carbon dioxide over Cr/TiO2–ZrO2 nanocatalyst: Effect of active phase and support composition on catalytic properties and performance. *Adv Powder Technol*. 2016;27:1195-1206.

15. Takahara I, Chang W-C, Mimura N, Saito M. Promoting effects of $CO_2$ on dehydrogenation of propane over a SiO2 -supported Cr2O3 catalyst. *Catal Today*. 1998;45:55-59.

16. Baek J, Yun HJ, Yun D, Choi Y, Yi J. Preparation of Highly Dispersed Chromium Oxide Catalysts Supported on Mesoporous Silica for the Oxidative Dehydrogenation of Propane Using $CO_2$ : Insight into the Nature of Catalytically Active Chromium Sites. *ACS Catal*. 2012;2:1893-1903.

17. Asghari E, Haghighi M, Rahmani F. $CO_2$ Oxidative Dehydrogenation of Ethane to Ethylene over Cr/MCM-41 Nanocatalyst Synthesized via Hydrothermal/Impregnation Methods: Influence of Chromium Content on Catalytic Properties and Performance. *J Mol Catal A Chem.* 2016;418-419:115-124.

18. Solymosi F, Tolmacsov P, Zakar TS. Dry reforming of propane over supported Re catalyst. *J Catal*. 2005;233:51-59.

19. Pradhan S, Upham DC, Metiu H, McFarland EW. Partial Oxidation of Propane with $CO_2$ on Ru doped Catalysts. *Catal Sci Technol*. 2016;6:5483-5493.

20. Solymosi F, Tolmacsov P, Kedves K. $CO_2$ reforming of propane over supported Rh. *J Catal*. 2003;216:377-385.

21. Olafsen A, Daniel C, Schuurman Y, Råberg LB, Olsbye U, Mirodatos C. Light alkanes $CO_2$ reforming to synthesis gas over Ni based catalysts. *Catal Today*. 2006;115:179-185.

22. Siahvashi A, Adesina A a. Kinetic Study of Propane $CO_2$ Reforming over Bimetallic Mo−Ni/Al2O3 Catalyst. *Ind Eng Chem Res*. 2013;52:15377-15386.

23. Althenayan FM, Yei Foo S, Kennedy EM, Dlugogorski BZ, Adesina A a. Bimetallic Co-Ni/Al2O3 catalyst for propane dry reforming: Estimation of reaction metrics from longevity runs. *Chem Eng Sci*. 2010;65:66-73.

24. Kattel S, Liu P, Chen JG. Tuning Selectivity of $CO_2$ Hydrogenation Reactions at the Metal/Oxide Interface. *J Am Chem Soc*. 2017;139:9739-9754.

25. Bueno-López A, Krishna K, Makkee M. Oxygen exchange mechanism between isotopic $CO_2$ and Pt/CeO2. *Appl Catal A Gen*. 2008;342:144-149.

26. Trovarelli A. Catalytic Properties of Ceria and CeO2 -Containing Materials. *Catal Rev*. 1996;38:439-520.

27. Xie Z, Yan B, Lee JH, et al. Effects of oxide supports on the $CO_2$ reforming of ethane over Pt-Ni bimetallic catalysts. *Appl Catal B Environ*. 2019;245:376-388.

28. Cheng Z, Sherman BJ, Lo CS. Carbon dioxide activation and dissociation on ceria (110): A density functional theory study. *J Chem Phys*. 2013;138(014702). doi:10.1063/1.4773248

29. Lonergan WW, Vlachos DG, Chen JG. Correlating extent of Pt–Ni bond formation with low-temperature hydrogenation of benzene and 1,3-butadiene over supported Pt/Ni bimetallic catalysts. *J Catal*. 2010;271:239-250.

30. Gomez E, Kattel S, Yan B, Yao S, Liu P, Chen JG. Combining $CO_2$ reduction with propane oxidative dehydrogenation over bimetallic catalysts. *Nat Commun*. 2018:1-6. doi:10.1038/s41467-018-03793-w

31. Porosoff MD, Myint MNZ, Kattel S, et al. Identifying Different Types of Catalysts for $CO_2$ Reduction by Ethane through Dry Reforming and Oxidative Dehydrogenation. *Angew Chemie Int Ed*. 2015:15501-15505. doi:10.1002/anie.201508128

32. Myint M, Yan B, Wan J, Zhao S, Chen JG. Reforming and Oxidative Dehydrogenation of Ethane with $CO_2$ as a Soft Oxidant over Bimetallic Catalysts. *J Catal*. 2016;343:168-177.

33. Porosoff MD, Chen JG. Trends in the catalytic reduction of $CO_2$ by hydrogen over supported monometallic and bimetallic catalysts. *J Catal*. 2013;301:30-37.

34. Xie Z, Yan B, Kattel S, et al. Dry reforming of methane over $CeO_2$-supported Pt-Co catalysts with enhanced activity. *Appl Catal B Environ*. 2018;236:280-293.

35. Yan B, Yang X, Yao S, et al. Dry Reforming of Ethane and Butane with $CO_2$ over PtNi/CeO2 Bimetallic Catalysts. *ACS Catal*. 2016;6:7283-7292.

36. Yan B, Yao S, Kattel S, et al. Active sites for tandem reactions of $CO_2$ reduction and ethane dehydrogenation. *Proc Natl Acad Sci*. 2018:2-7. doi:10.1073/pnas.1806950115

37. Yu W, Porosoff MD, Chen JG. Review of Pt-Based Bimetallic Catalysis : From Model Surfaces to Supported Catalysts. *Chem Rev*. 2012; 112:5780-5817.

38. Van Santen R, Tranca I, Hensen EJM. Theory of surface chemistry and reactivity of reducible oxides. *Catal Today*. 2015;244:63-84. doi:10.1016/j.cattod.2014.07.009.

39. Wang S, Murata K, Hayakawa T, Hamakawa S, Suzuki K. Dehydrogenation of ethane with carbon dioxide over supported chromium oxide catalysts. *Appl Catal A Gen*. 2000;196:1-8. doi:10.1016/S0926-860X(99)00450-0.

40. Shishido T, Shimamura K, Teramura K, Tanaka T. Role of $CO_2$ in dehydrogenation of propane over Cr-based catalysts. *Catal Today*. 2012;185(1):151-156. doi:10.1016/j.cattod.2011.10.028.

41. Kocoń M, Michorczyk P, Ogonowski J. Effect of supports on catalytic activity of chromium oxide-based catalysts in the dehydrogenation of propane with $CO_2$. *Catal Letters*. 2005;101(1-2):53-57. doi:10.1007/s10562-004-3749-6.

42. Michorczyk P, Ze K, Niekurzak R, Ogonowski J. Dehydrogenation of propane with $CO_2$ – a new green process for propene and synthesis gas production. *Polish J Chem Techno.*2012;14(4):77-82.

43. Yun D, Baek J, Choi Y, Kim W, Lee HJ, Yi J. Promotional Effect of Ni on a CrOx Catalyst Supported on Silica in the Oxidative Dehydrogenation of Propane with $CO_2$. *ChemCatChem*. 2012;4(12):1952-1959. doi:10.1002/cctc.201200397.

44. Chen M, Xu J, Liu Y-M, Cao Y, He H-Y, Zhuang J-H. Supported indium oxide as novel efficient catalysts for dehydrogenation of propane with carbon dioxide. *Appl Catal A Gen*. 2010;377(1-2):35-41. doi:10.1016/j.apcata.2010.01.011.

45. Michorczyk P, Ogonowski J. Dehydrogenation of propane in the prescence of carbon dioxide over oxide-based catalysts. *React Kinet Catal Lett*. 2003;78(1):41-47.

46. Xu B, Zheng B, Hua W, Yue Y, Gao Z. Support effect in dehydrogenation of propane in the presence of $CO_2$ over supported gallium oxide catalysts. *J Catal*. 2006;239(2):470-477. doi:10.1016/j.jcat.2006.02.017.

# Chapter 5: Enhancing the tandem reactions of $CO_2$-assisted ethane dehydrogenation and aromatization

## 5.1 Abstract

A one-step process that can produce liquid aromatics from the reaction of $CO_2$ and ethane using phosphorous and Ga modified ZSM-5 has been evaluated. Aromatization of lower alkanes is of great interest since this can expand the raw materials used to produce benzene, toluene, and xylenes to include fractions of natural gas that are readily available and inexpensive. Flow reactor studies measuring both the $CO_2$-assisted oxidative dehydrogenation and direct dehydrogenation and aromatization of ethane over unmodified as well as Ga and phosphorous modified ZSM-5 catalysts were performed at 873 K and atmospheric pressure. The addition of phosphorous at an optimal loading improved the hydrothermal stability of Ga/ZSM-5, reduced coke formation on the catalyst surface, and allowed for the formation of more liquid aromatics through the $CO_2$-assisted oxidative dehydrogenation and aromatization reaction pathway compared to the direct dehydrogenation and aromatization reaction. With the aid of density functional theory (DFT) calculations, the mechanisms for the production of aromatics from ethane were identified. DFT also illustrated the effect of Ga modification on ethylene formation over ZSM-5 as well as the role of $CO_2$ on the aromatization of ethylene.

## 5.2 Introduction

Effective chemistries that reduce $CO_2$ while simultaneously producing valuable chemicals remains a challenge.[1,2,3] Utilizing light alkanes as $CO_2$ reduction feedstock is a promising route in

which abundant and underutilized reactants can produce valuable olefins or synthesis gas via the $CO_2$-oxidative dehydrogenation ($CO_2$-ODH) or dry reforming reactions (DR), respectively.[4,5,6] While both the $CO_2$-ODH and DR reactions of alkanes produce valuable molecules, the separation of gas phase products is challenging and requires additional energy. It is therefore highly desirable to develop a tandem reaction scheme in which the reaction of $CO_2$ and alkanes can produce liquid products. Aromatics (i.e., benzene, toluene, and xylene) are important liquid petrochemical intermediates produced via naphtha reforming, a process in which the feedstock constitutes 60-70% of the total manufacturing costs.[7,8] Expanding the library of raw materials used to produce aromatics is of significant interest, especially if using an abundant fraction of shale gas such as ethane. Literature suggests that the one of the limiting steps in ethane aromatization is the production of the olefin. Our previous work focused on the production of olefins from the $CO_2$-ODH of $C_2$[9,10,11], $C_3$[12], and $C_4$[13] with $CeO_2$ supported bimetallics under operating conditions applicable to aromatization. Combining $CO_2$ reduction with the tandem reactions of ethane dehydrogenation and aromatization can potentially produce valuable $C_6$-$C_7$ liquid products while consuming a greenhouse gas in a one-step process.

Typical DDA catalysts suffer from deactivation due to high carbon deposition rates, but in the proposed tandem $CO_2$-oxidative dehydrogenation and aromatization ($CO_2$-ODA) reaction, $CO_2$ can consume the coke via the reverse Boudouard reaction ($CO_2 + C \rightarrow 2CO$), enhancing stability. Also, $CO_2$ can promote the reverse water gas shift reaction (RWGS), consuming $H_2$ and thereby enhancing dehydrogenation activity. To account for the effect of $CO_2$ via the RWGS reaction, thermodynamic calculations evaluating both the DDAE and $CO_2$-ODAE reaction pathways were performed. **Figure 5-1** illustrates the equilibrium reactant conversions and product distributions as a function of temperature in the presence and absence of $CO_2$. The DDAE reaction

pathway occurred via direct dehydrogenation of ethane to ethylene and subsequent aromatization of ethylene to benzene with an initial feed of Ar/$C_2$ of 1:1, while the $CO_2$-ODAE pathway included the simultaneous occurrence of the RWGS reaction with an initial feed of $CO_2/C_2$ of 1:1.**Figure 5-1a** illustrates that the $CO_2$-ODAE pathway can obtain higher ethane equilibrium conversions at lower reaction temperatures, achieving up to 30% $C_2$ conversion below 700 K. The addition of $CO_2$ as a co-reactant can help overcome the thermodynamic limitations of the DDAE reaction by accepting $H_2$ formed during dehydrogenation and aromatization, shifting the reaction equilibrium toward the products, **Figure 5-1b-d**. Furthermore, the positive effect of $CO_2$ on both the $C_2$ equilibrium conversion and benzene mol% is also observed with increasing $CO_2/C_2$ ratios as shown in **Figure 5-2**.

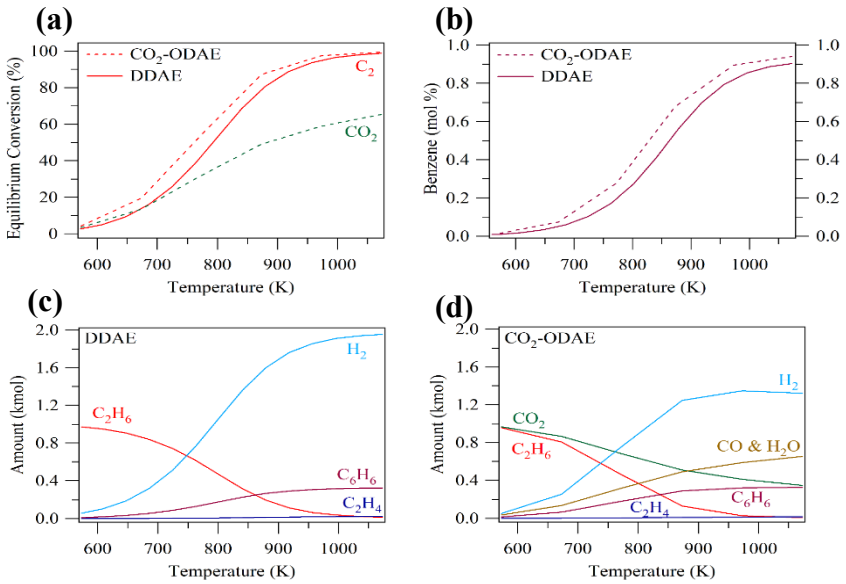


**Figure 5-1.** Thermodynamic analysis. Effect of temperature on the **(a)** equilibrium conversion of reactants and **(b)** mol% of benzene product for the DDAE and $CO_2$-ODAE reactions. Effect of temperature on the equilibrium composition for the **(c)** DDAE and **(d)** $CO_2$-ODAE reactions. DDAE was evaluated by direct dehydrogenation of ethane

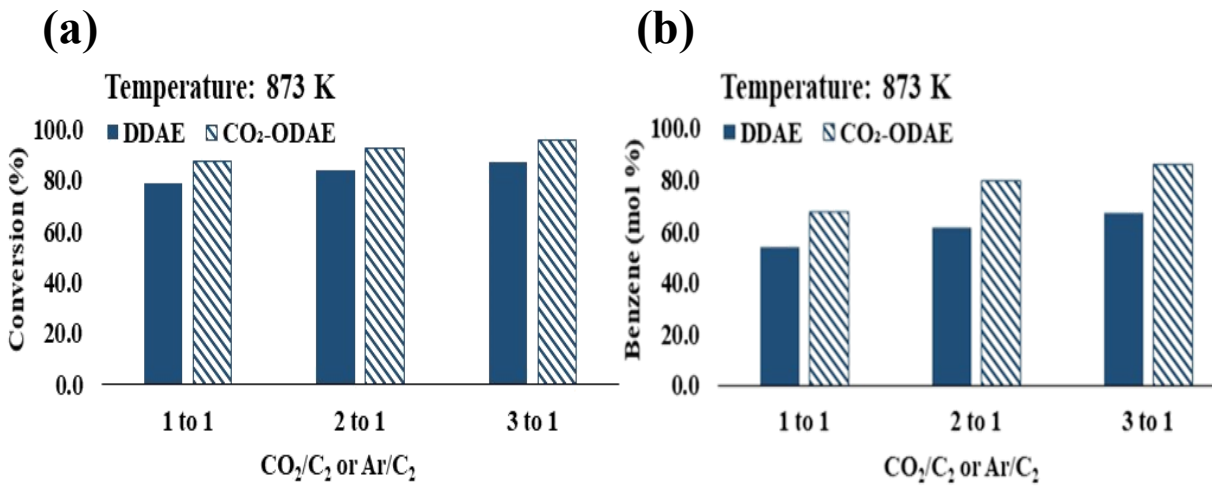


**Figure 5-2.** Thermodynamic analysis. Effect of the inlet feed ratio, $CO_2/C_2H_6$ or $CO_2/C_2H_6$, on the **(a)** equilibrium conversion of $C_2H_6$ and **(b)** benzene mol % for the DDAE and $CO_2$-ODAE reactions at 873 K and atmospheric pressure. DDAE was evaluated by direct dehydrogenation of ethane to ethylene and subsequent aromatization of ethylene to benzene, while $CO_2$-ODAE included the simultaneous occurrence of the RWGS reaction. Calculations were performed with the assistance of HSC Chemistry Outotec software v8.

The direct dehydrogenation and aromatization (DDA) of light alkanes typically occur over pentasil-type zeolites (ZSM-5) due to their unique micropores and acidic properties, see **ZSM-5 framework information**.[8] Ethane is the second-largest component in shale gas, but unlike propane and butane, intrinsically shows lower conversion and production of aromatics over unmodified ZSM-5 for the DDAE reaction.[14] Literature suggests that proton activation of ethane is very low, in contrast to higher alkanes, which can be activated by protons effectively leading to high conversions over ZSM-5 (≥57%).[15,16,17] The difference in activity between ethane and higher alkanes ( i.e., propane) for DDA reactions over ZSM-5 can be attributed to the ease at which the interaction between propane and proton can form a secondary carbenium ion, whereas the

interaction with ethane leads to only the primary carbenium ion. Thus, with ethane, the protolytic cleavage of a C-H bond is 30 times faster than the C-C bond scission despite the involvement of unstable primary carbenium ions. For higher alkanes, the protolytic C-C bond scission occurs faster than that of C-H bonds.[14], allowing for (1) decomposition to methane and ethylene by proton attack on the C-C bond and (2) activation via abstraction of hydride ions by carbenium ions.[17] Modification of ZSM-5 with metal cations, such as Zn and Ga, can increase the alkane conversion and selectivity to aromatics for the DDAE reaction.[15,16] For short chain hydrocarbons such as ethane, the Lewis acid site provided by the metal is critical for activation.[18,19] Typically, the involvement of Brønsted acid sties in alkane activation decreases as the number of carbons in the alkane decreases. Thus, the role of exchanged metals in the ZSM-5 framework have been reported to be the primary active sites for dehydrogenation and aid in the combinative desorption of $H_2$ from the surface. [20] Oligomerization and cyclization are then catalyzed by acid sites and selectivity is heavily influenced by the strength of the acid site.

Zn-ZSM-5 is especially active and selective for the aromatization of ethane and propane because Zn cations inhibit β-scission induced side reactions and can decrease the residence time of olefins within oligomerization/β-scission cycles.[21] In addition, Zn cations promote the recombination of H atoms therefore depleting surface hydrogen that would be available for reverse hydrogenation reactions. The implementation of Zn for the DDAE reaction is limited due to the likely evaporation of zinc cations during reaction, however, one study found that the incorporation of $Pd^{2+}$ cations to Zn-ZSM-5 can decrease the rate of Zn evaporation.[15] Ga for DDAE reactions with ZSM-5 has been reported to influence the strength of the acid sites on the zeolite, facilitate the $H_2$/ethylene desorption, and lower the activation energy for C-H bond scission.[20] Therefore, in

this study to increase ethane activation on ZSM-5, Ga was chosen as the metal modifier and used to compare the baseline activity of the DDAE and $CO_2$-ODAE reactions.

There are still two key challenges to overcome for the introduction of $CO_2$ to an aromatization scheme to be successful, the chosen catalytic metal must (1) activate both $CO_2$ and the alkane to be able to promote the $CO_2$-ODA pathway and (2) exhibit long-term stability under reaction conditions, indicating that the material must withstand the presence of water in order to benefit from the presence of $CO_2$. There are a few studies in the literature that illustrate that the presence of $CO_2$ promoted the dehydrogenation and subsequent aromatization of ethane using zeolite catalysts but with very short reaction times.[22,23] Nakagawa et al. illustrated that the presence of $CO_2$ promoted the dehydrogenation and aromatization of ethane over a $Ga_2O_3$ + HZSM-5 catalyst above 650$^o$C but with a reaction time of only 30 minutes.[23] For large scale catalytic reduction of $CO_2$ and production of aromatics, it is of interest to enhance the stability and liquid product yield of a $CO_2$-ODA catalyst. The modification of ZSM-5 with phosphorous has been shown to increase hydrothermal stability, tune the acid-base properties, and decrease coke formation. To date, the phosphorous modification technique has been applied to methanol-to-olefins[24], propylene to ethylene[25], as well as olefin and $C_5$+ cracking[26] chemistries but has not been explored for the $CO_2$-ODA reaction. In this study, we explore the phosphorous modification of Ga/ZSM-5 for the first time in literature, to enhance long term stability and yield to aromatics for the $CO_2$-assisted tandem reactions of dehydrogenation and aromatization of ethane.

## 5.3 Methods

### 5.3.1 Density functional theory calculations

DFT calculations were performed using the Vienna ab initio simulation package (VASP) with the ion cores represented by the projector augmented wave (PAW) potentials implemented in VASP[27,28,29]. The MFI-type zeolite was modeled by using a periodic unit cell with experimentally determined lattice constant of 20.02 Å×19.90 Å×13.38 Å. The exchange and correlation energies were treated with the generalized gradient approximation (GGA) with the Perdew−Burke−Ernzerh of (PBE) functional[30], and the DFT-D3 method[31,32] was used to consider the dispersion interaction of the zeolite system. The cutoff energy of the plane-wave basis was set to 400 eV. A Gamma-point mesh was applied for all calculations and the Gaussian smearing method with an electronic temperature of $k_B t$ = 0.02 eV was employed to achieve fast convergence. Structure optimizations were conducted using a damped molecular dynamics method until the forces on all atoms were less than 0.03 eV/Å.

Transition states were searched using the climbing image nudged elastic band (CI-NEB)[33] method. The minimum energy pathway was examined using 8~14 images, including the initial and final state, during the transition state search. Each transition state was confirmed to have a single imaginary vibrational frequency along the reaction coordinate. Zero-point energy, heat capacity, and entropy were computed with standard methods for adsorbates and gas phase molecules, and then used to convert the electronic energies into free energies at temperature of 783 K to correlate experiments. **Figure 5-3** and **Figure 5-4** illustrate the optimized structures of initial, transition, and final states obtained.

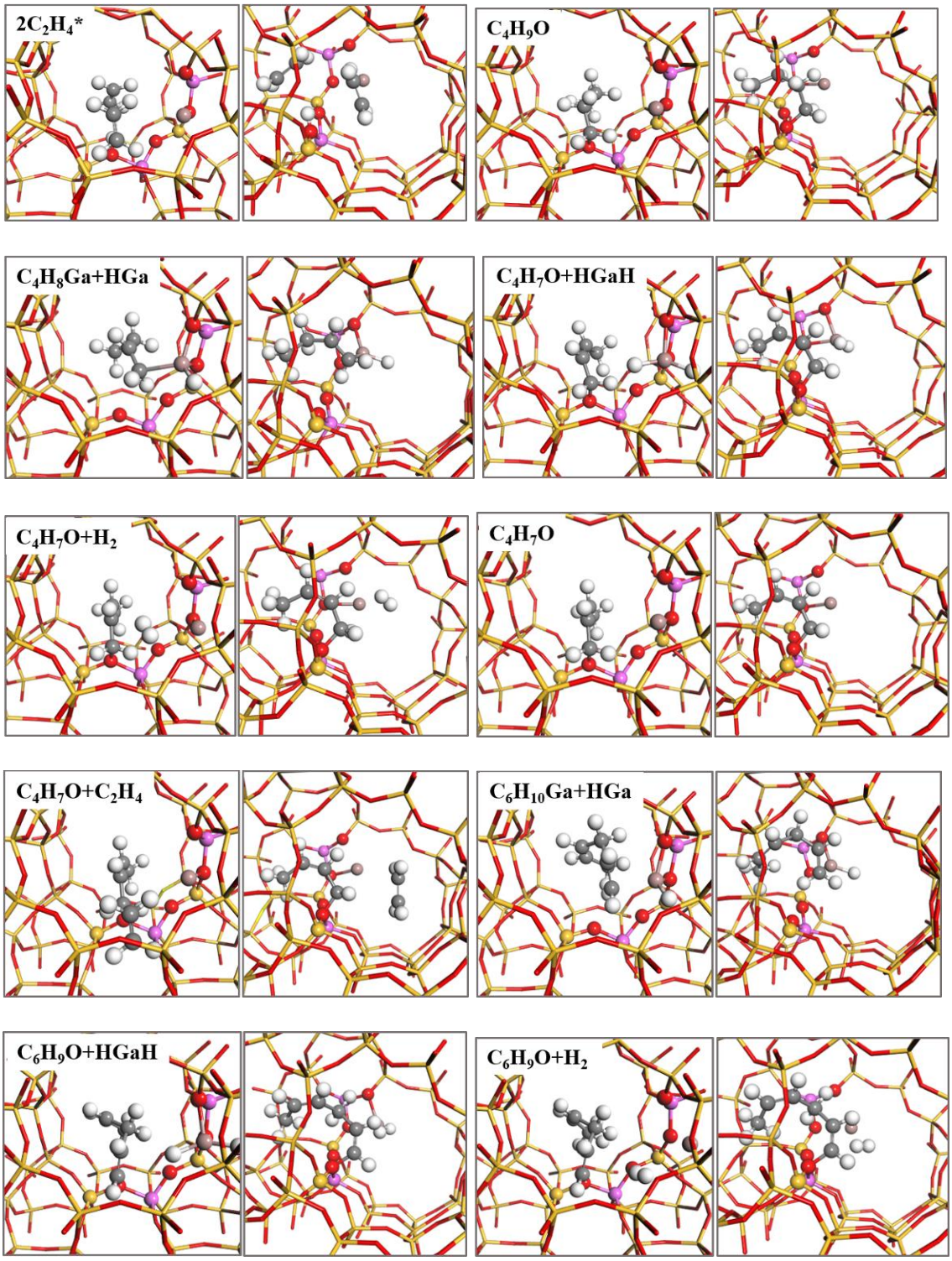
2C2H4*
C4H9O
C4H8Ga+HGa
C4H7O+HGaH
C4H7O+H2
C4H7O
C4H7O+C2H4
C6H10Ga+HGa
C6H9O+HGaH
C6H9O+H2

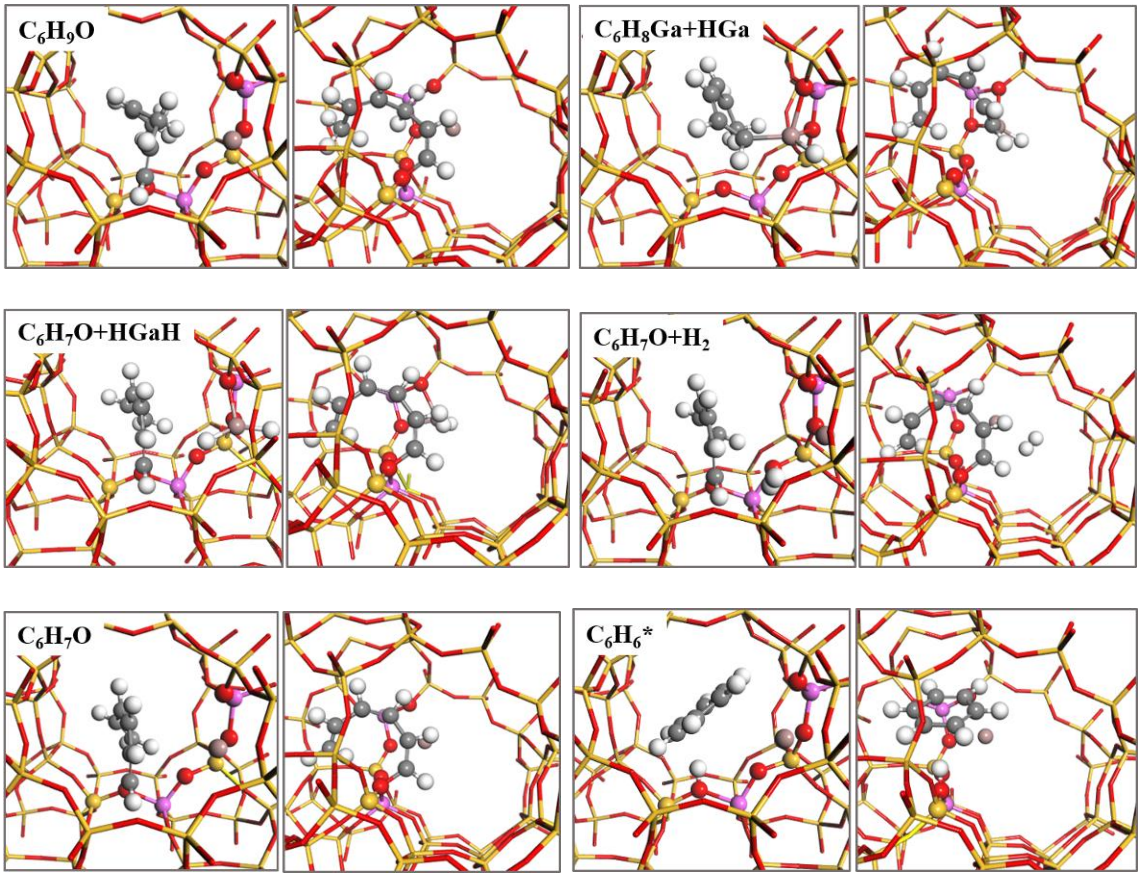


**Figure 5-3.** Optimized structures of reactant, intermediates, and product involved in ethylene transformation to benzene over Ga/ZSM-5. (Yellow: Si, Pink: Al, Brown: Ga, Red: O, Grey: C, White: H)

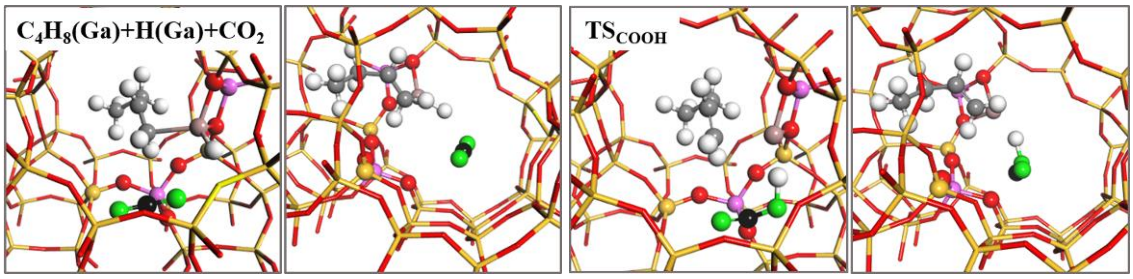

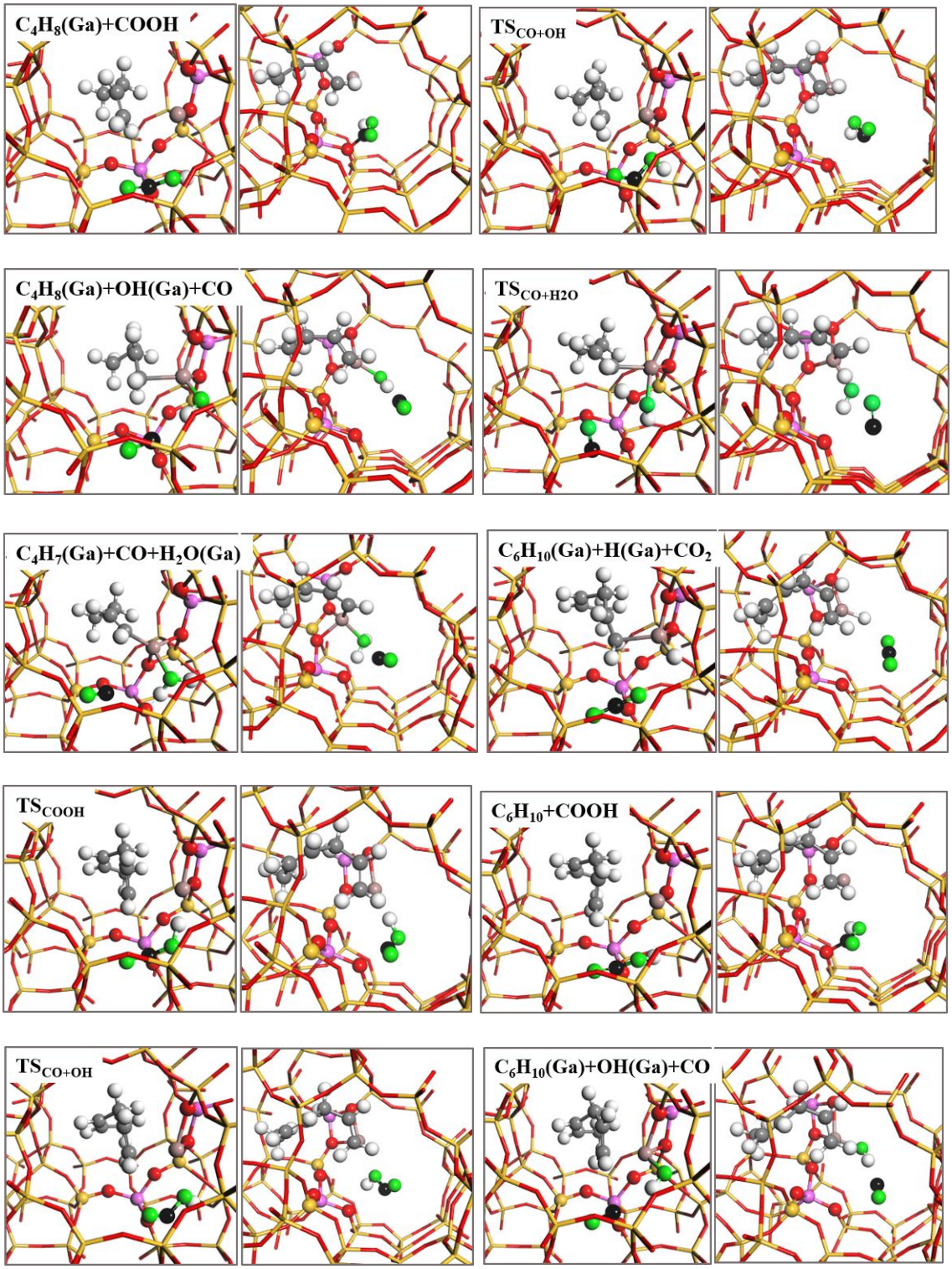
$C_4H_8$(Ga)+COOH
$TS_{CO+OH}$
$C_4H_8$(Ga)+OH(Ga)+CO
$TS_{CO+H2O}$
$C_4H_7$(Ga)+CO+$H_2O$(Ga)
$C_6H_{10}$(Ga)+H(Ga)+$CO_2$
$TS_{COOH}$
$C_6H_{10}$+COOH
$TS_{CO+OH}$
$C_6H_{10}$(Ga)+OH(Ga)+CO

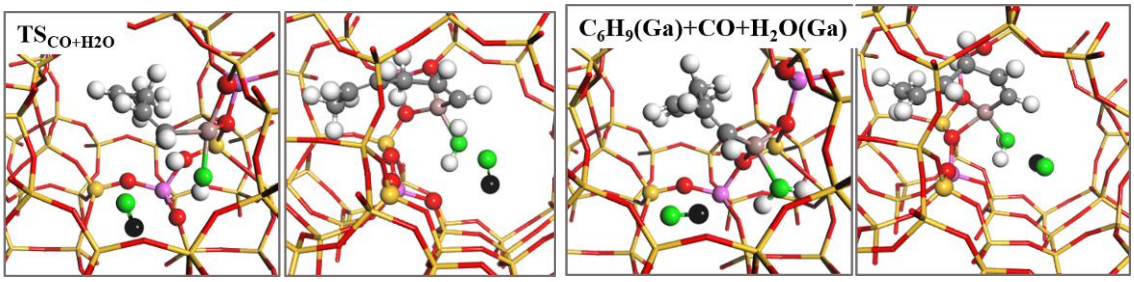


**Figure 5-4.** Optimized structures of initial, transition, and final states associated with the two $H_2$ formation steps involved in ethylene transformation to benzene over Ga/ZSM-5 in the presence of $CO_2$. (Yellow: Si, Pink: Al, Brown: Ga, Red: O, Grey: C, White: H, Green: O of $CO_2$; Black: C of $CO_2$)

### 5.3.2 Catalyst preparation and flow reactor studies

All catalysts were synthesized with proton exchanged ZSM-5 containing a Si/Al molar ratio of 30 (sourced from Riogen Catalysis for Chemicals and Energy). Phosphorous modification, ZSM-5P(X) was achieved via a slurry technique that was mixed at 40$^o$C for 12 hours. The calculated mixture of ethanol, water, and 85 wt.% $H_3PO_4$ was sonicated for 10 mins before combining with a paste of ZSM-5 (created with 5 ml of water). Calcination followed a program at 550$^o$C for 6 hours (5$^o$C/min ramp). Incorporation of 2 wt.% Ga to ZSM-5 was achieved via incipient wetness impregnation with $Ga(NO_3)_3$ salt (Sigma-Aldrich) onto ZSM-5 or ZSM-5P(X) followed by calcination at 290$^o$C for 2 hours (0.8$^o$C/min ramp). Flow reactor experiments were performed under atmospheric pressure utilizing a 4 mm quartz tube. All catalysts were pretreated with an activation period under Ar flow for 1 hour at 873 K (20mL/min, 9.6 $^o$C/min ramp) before contacting reaction gasses. Steady-state experiments were performed with 300 mg of 40-60 mesh catalyst particles. Apparent activation barrier reaction order experiments were conducted at slightly different reaction conditions to minimize the effects of heat and mass transport

### 5.3.3 ZSM-5 framework information

Single ZSM-5 crystals are parallelepiped-shaped and can have sizes that range from 100 nm to 100 μm. Within the crystal are three-dimensional microporous channel systems comprised of both straight and sinusoidal pores. The average pore size of the channels is 5.5 x 5.5 Å.[34] Channel intersections create cavities that are 6.36 Å in diameter. This prevents molecules that exceed the dimension of the channel from entering/exiting the zeolite, but larger molecules can form in the cavities, making ZSM-5 an effective molecular sieve. All zeolite frameworks consist of silica and alumina tetrahedra linked by shared oxygen atoms. The acid character of zeolites is attributed to the negatively charged $AlO_4^-$ tetrahedra within the zeolite lattice which is neutralized by a counter-cation. If the counter-cations are protons, then strong Brønsted acid sites are formed. If more aluminum is incorporated into the framework then more acid sites are created, increasing the density of Brønsted acid sites. Since the overall acidity of a zeolite depends on the density (i.e. concentration) and strength of Brønsted acid sites acidity decreases with increasing Si/Al molar ratio. Lewis acid sites are usually related to the extra-framework aluminum species that are formed by aluminum that has been extracted from the lattice or metal ions that were exchanged in the place of protons. It is believed that extra-framework trivalent Al species reduce the concentration while simultaneously increasing the strength of Brønsted acid sites and thus there is a combined effect between Brønsted and Lewis acid sites.[35]

## 5.4 Results

### 5.4.1 Catalytic evaluation

Flow reactor studies measuring both $CO_2$-ODAE and DDAE activity over unmodified as well as Ga and phosphorous modified catalysts are summarized in **Table 5-1**. All catalysts were synthesized with proton exchanged ZSM-5 containing a Si/Al molar ratio of 30 (Riogen), for additional details see **Methods**. Results for conversions following time on stream for selected catalysts are available in **Figure 5-5** and selectivity profiles are depicted in **Figure 5-6** and **Figure 5-7**.

#### 5.4.1.a $CO_2$-ODAE and DDAE activity over ZSM-5 and Ga modified ZSM-5

Under DDAE reaction conditions the unmodified ZSM-5 catalyst initially exhibited $C_2$ conversion of roughly 7%, but after 10 hours on stream, the activity decreased to less than 2% with 26.7% liquid aromatic selectivity. The activity profile was similar in the presence of $CO_2$, except for the formation of CO, which altered the selectivity profile to be 24.9% toward liquid aromatics and 5.6% toward CO. When ZSM-5 was modified with 2 wt.% Ga via an incipient wetness technique and exposed to DDAE conditions the conversion increased roughly by a factor of 10 (17.1% $C_2$ conversion) with increased selectivity to liquids (42.6%) and enhanced stability. In the presence of $CO_2$, neither the $C_2$ conversion nor the selectivity toward liquids was enhanced compared to the DDAE reaction over Ga/ZSM-5. However, the formation of water and CO provided direct evidence of $CO_2$ activation, resulting in $CO_2$ conversion corresponding to 10.2%. The selectivity toward liquid aromatics was similar with and without $CO_2$ (41.8 vs. 42.6 %), but the formation of methane with $CO_2$ is almost 2x that compared to the reaction in the absence of $CO_2$. In addition, the conversion profile following time on stream (TOS) indicated that the reaction with $CO_2$ was slightly less stable. As observed, the introduction of $CO_2$ in the feed altered the

dehydrogenation pathway in a mildly oxidative manner by consuming $H_2$, consequently producing water. Studies have shown that zeolite catalysts are highly sensitive to the presence of water under reaction conditions. Thus, to improve zeolite tolerance to water and allow the benefits of co-feeding $CO_2$ to enhance performance, it was of interest to examine a series of phosphorous modified Ga/ZSM-5P(X) catalysts.

**Table 5-1.** Catalyst flow reactor results. Shown for activity in the presence and absence of $CO_2$ (3 and 0 ml/min, respectively) performed with a total flow rate 10ml/min at 873 K with Ar diluent (4 and 7 ml/min, respectively), 300 mg of catalyst (40-60 mesh). Values are obtained by averaging the data from hours 9-10 on stream. Selectivity and yield are on a $C_2H_6$ basis (including carbonaceous species only). For catalysts containing modifiers, the Ga and phosphorous loading are 2 wt.% and 0.8 wt.%, respectively and the Si/Al molar ratio for all catalysts is 30.

| | | Conversion % | | T.O.F mol reactant · mol metal$^{-1}$ · hr$^{-1}$ | | Selectivity % | | | | | Yield % | |
|---|---|---|---|---|---|---|---|---|---|---|---|---|
| Catalyst | Treatment | $C_2H_6$ | $CO_2$ | $C_2H_6$ | $CO_2$ | Liq. | Ethylene | Methane | CO | $C_3$ & $C_4$ | Liq. | CO |
| ZSM-5 | $C_2CO_2$ | 1.4 | 0.8 | — | — | 24.9 | 18.9 | 49.6 | 5.6 | 1.0 | 0.35 | 0.08 |
| | $C_2Ar$ | 1.5 | — | — | — | 26.7 | 24.3 | 45.8 | 0 | 3.1 | 0.39 | 0.00 |
| Ga/ZSM-5 | $C_2CO_2$ | 14.6 | 10.2 | 12.48 | 8.74 | 41.8 | 34.4 | 11.9 | 9.5 | 2.4 | 6.1 | 1.4 |
| | $C_2Ar$ | 17.1 | — | 14.62 | — | 42.6 | 48.3 | 6.3 | 0 | 2.7 | 7.3 | 0.0 |
| Ga/ZSM-5P(X) | | | | | | | | | | | | |
| (0.8) | $C_2CO_2$ | 24.6 | 18.6 | 21.03 | 15.94 | 55.5 | 31.7 | 2.7 | 7.7 | 2.3 | 13.7 | 1.9 |
| | $C_2Ar$ | 23.3 | — | 19.88 | — | 49.8 | 45.7 | 1.5 | 0 | 3.0 | 11.6 | 0.0 |
| (0.4) | $C_2CO_2$ | 19.2 | 15.5 | 16.4 | 13.2 | 59.7 | 24.3 | 3.7 | 10.5 | 1.8 | 11.5 | 2.0 |
| (0.2) | $C_2CO_2$ | 15.5 | 11.6 | 13.3 | 9.9 | 50.6 | 34.3 | 2.6 | 10.4 | 2.2 | 7.9 | 1.6 |
| (1.62) | $C_2CO_2$ | 9.8 | 6.4 | 8.3 | 5.5 | 47.0 | 37.6 | 2.6 | 10.6 | 2.2 | 4.6 | 1.0 |
| ZSM-5 P(0.8) | $C_2CO_2$ | 2.7 | 6.4 | — | — | 21.2 | 23.9 | 46.7 | 7.1 | 1.1 | 0.58 | 0.18 |
| | $C_2Ar$ | 0.52 | — | — | — | 20.7 | 31.5 | 43.7 | 0.0 | 4.1 | 0.11 | 0.00 |

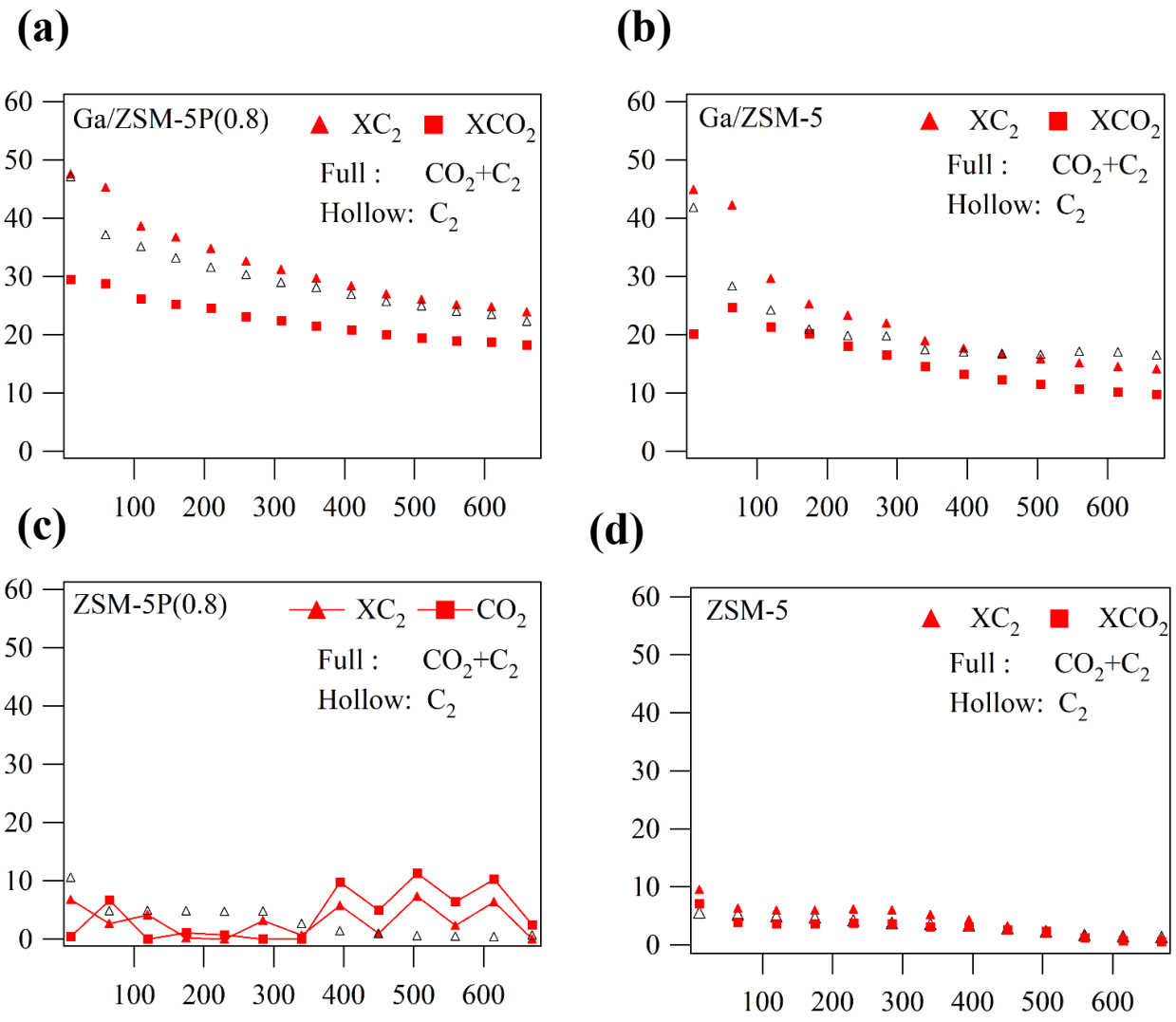


**Figure 5-5.** Conversion vs. time on stream. Shown for **(a)** Ga/ZSM-5P(0.8) **(b)** Ga/ZSM-5 **(c)** ZSM-5P(0.8) **(d)** ZSM-5 for reactions of $C_2$+$CO_2$ with Ar (full symbols) and $C_2$+Ar (hollow symbols) at 873 K and atmospheric pressure.

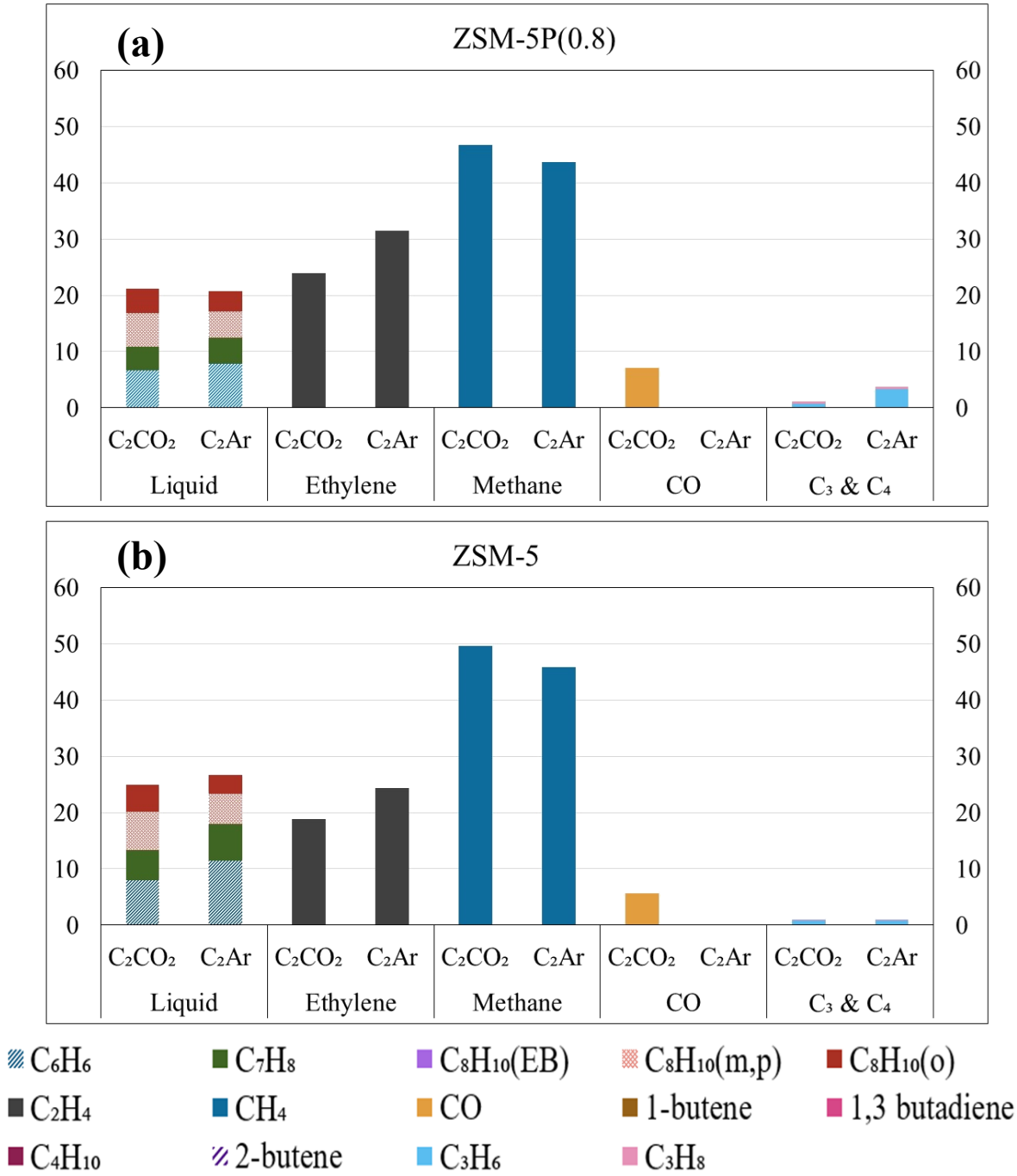


**Figure 5-6.** Selectivity profiles. ZSM-5 (Si/Al 30 molar) modified with **(a)** 0.8 wt.% and **(b)** 0 wt.% phosphorous.

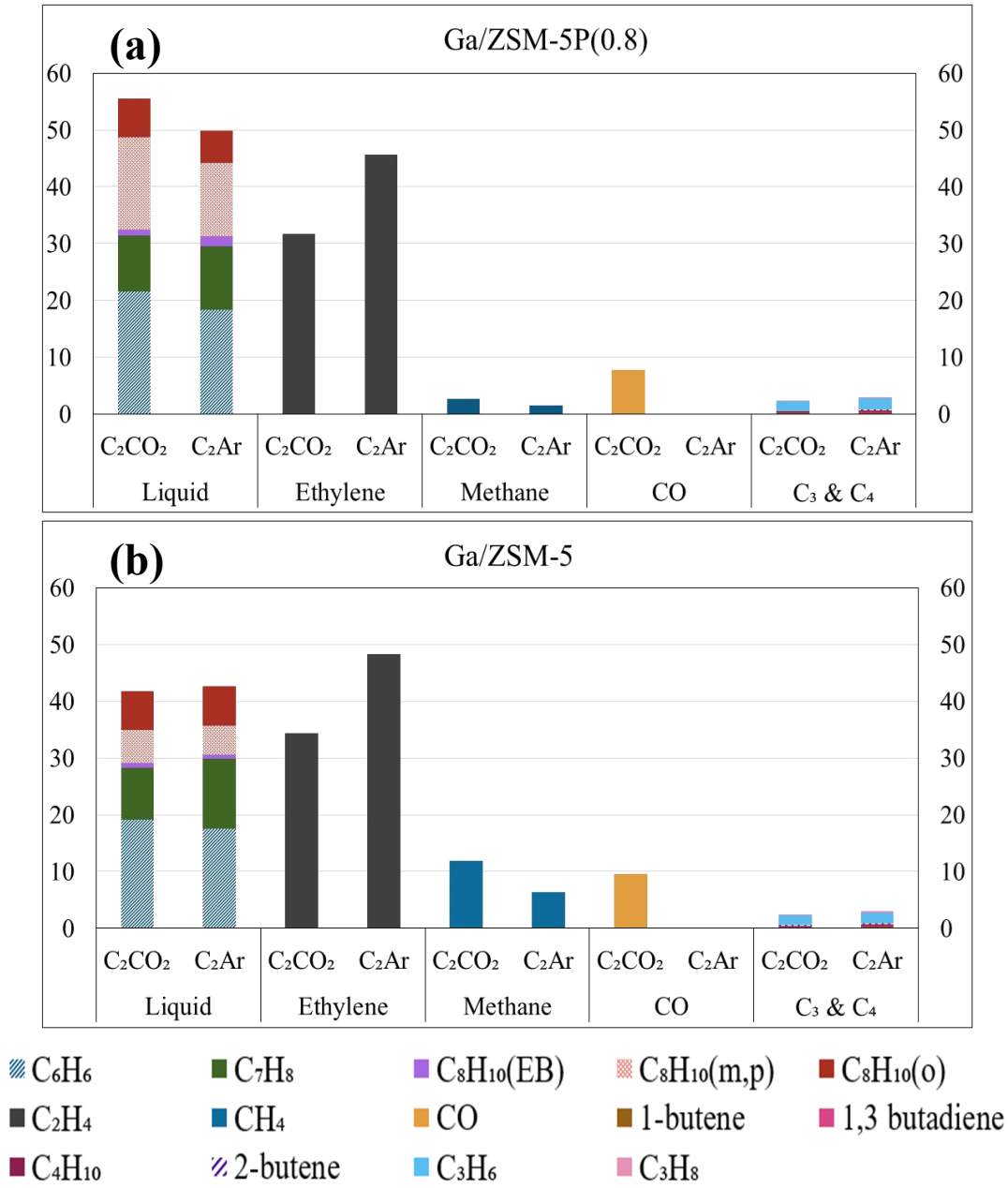


**Figure 5-7.** Selectivity profiles. 2 wt.% Ga on ZSM-5 (Si/Al 30 molar) modified with **(a)** 0.8 wt.% and **(b)** 0 wt.% phosphorous.

### 5.4.1.b $CO_2$-ODAE activity over phosphorous modified Ga/ZSM-5P(X) catalysts

To determine an optimal loading a series of catalysts were modified with 0.2, 0.4, 0.8, and 1.62 wt.% phosphorous and evaluated for the $CO_2$-ODAE reaction. The values are listed in **Table 5-1**. Overall, the addition of phosphorous positively influenced the yield toward liquid aromatics (**Figure 5-9a**), improved stability (**Figure 5-9b**), and decreased the production of methane (**Figure 5-8**). Positive effects on the liquid aromatic yields were present with the addition of 0.2 wt.% phosphorous but the stability was not enhanced until modified with 0.4 wt.% phosphorous. The $CO_2$ and $C_2$ conversions continued to increase with similar selectivity profiles until a phosphorous loading of 0.8 wt.%, **Figure 5-10**. Increasing the loading to 1.62 wt.% negatively impacted $CO_2$ and $C_2$ conversion to values (6.4 and 9.8%, respectively) below that of the unmodified Ga/ZSM-5 catalyst. Improved stability was still observed for the 1.62 wt.% catalyst, but this effect may also be attributed to the low formation of aromatic products. Thus, the 0.8 wt.% phosphorous modified Ga/ZSM-5P(0.8) catalyst had the highest yield of liquid aromatics with improved stability compared to the unmodified Ga/ZSM-5 catalyst for the $CO_2$-ODAE reaction.

To further examine the effect of phosphorous on stability for the Ga/ZSM-5 catalytic system, thermogravimetric analysis (TGA) studies were performed on $CO_2$-ODAE spent samples and results are shown in **Figure 5-11**. TGA studies examine the weight loss of a sample as a function of time and temperature under oxidizing conditions with either $O_2$ or $CO_2$ as the oxidant. In $O_2$-TGA studies, the spent Ga/ZSM-5 showed a weight loss of 9.7%, reflecting the amount of coke that burned off from the sample, while the spent Ga/ZSM-5P(0.8) catalyst lost 6.2%. Therefore, modifying the Ga/ZSM-5 catalyst with phosphorus helped lessen coke formation under reaction conditions apart from improving aromatic selectivity.

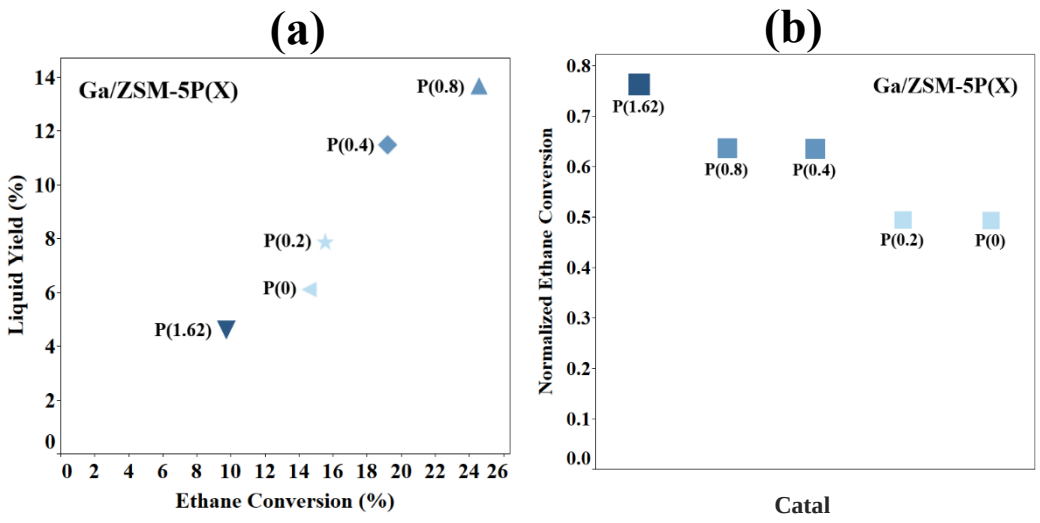


**Figure 5-9.** Impact of phosphorous wt.%. The influence of P(X) on the $CO_2$-ODAE reaction over 2 wt.% Ga on ZSM-5 (Si/Al 30 molar) modified with 0, 0.2, 0.4, 0.8, and 1.62 wt.% phosphorous. **(a)** Liquid yield vs $C_2$ conversion and **(b)** normalized $C_2$ conversion. The tone of color from light to dark and size of symbol from small to large signifies increasing stability.

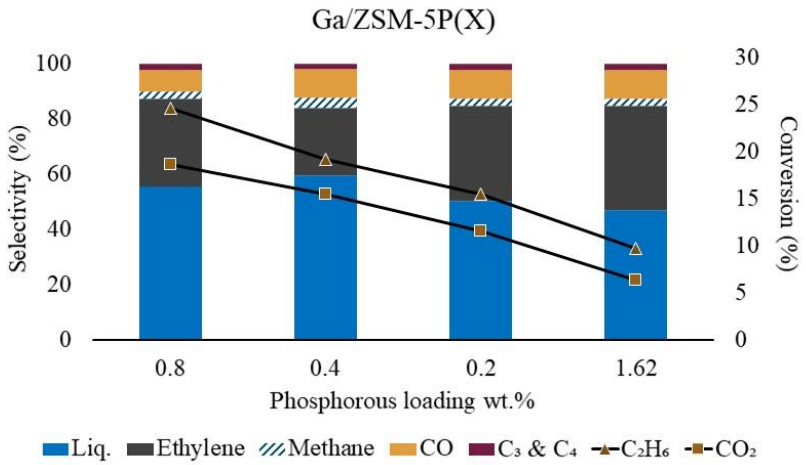


**Figure 5-8.** Activity of phosphorous catalysts. The activity of 2 wt.% Ga on ZSM-5 (Si/Al 30 molar) modified with 0.2, 0.4, 0.8, and 1.62 wt.% phosphorous for the CO2-ODAE reaction. The axis for selectivity is located on the left, while the axis for conversion is on the right. Data are presented in the order of highest to lowest conversion from left to right.

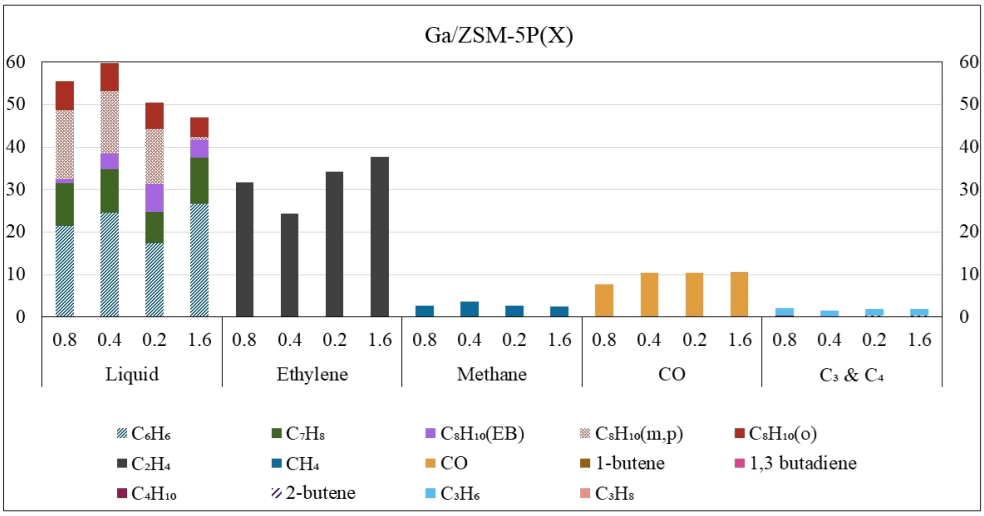


**Figure 5-10.** Selectivity profiles. 2 wt.% Ga on ZSM-5 (Si/Al 30 molar) modified with 0.2, 0.4, 0.8, and 1.6 wt.% phosphorous, listed in order of highest liquid yield.

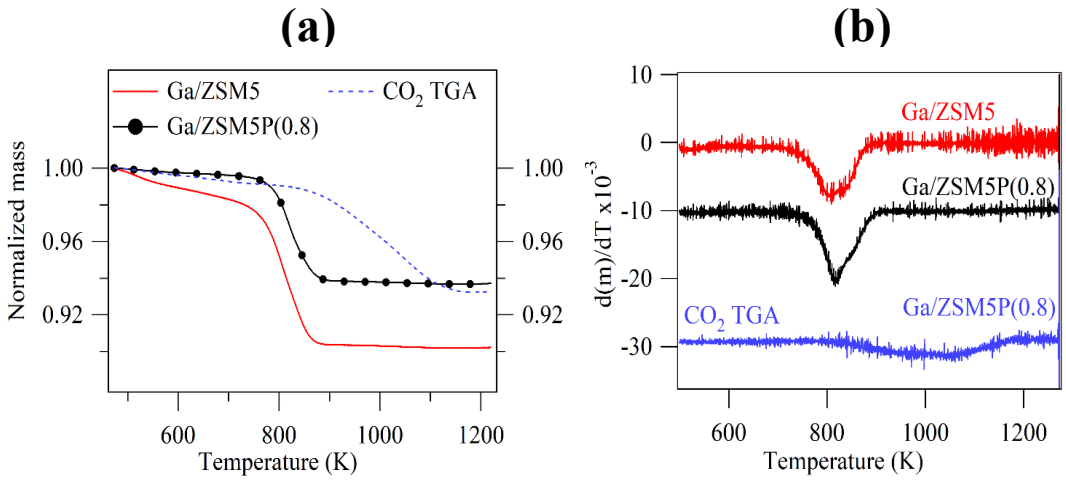


**Figure 5-11.** Thermogravimetric analysis. TGA analysis results for $CO_2$-ODAE spent Ga/ZSM-5 with 0 and 0.8 wt.% phosphorous obtained with $O_2$ as the oxidant (unless labeled with $CO_2$). **(a)** Normalized mass loss vs. temperature and **(b)** first derivative of mass loss as a function of temperature.

Increasing the consumption of $CO_2$ per mol of product in a given process is highly desirable to help off-set anthropogenic emissions. One possible technique to increase the consumption of $CO_2$ in a process is to consider using the molecule's oxidizing ability for the removal of coke formation not only during the reaction where it is limited by many competitive kinetic steps, but also in a catalyst regeneration cycle. Therefore, a $CO_2$-TGA profile was obtained for Ga/ZSM-5P(0.8) to determine the conditions that would be required for a regeneration cycle. The weight loss of the Ga/ZSM-5P(0.8) with $CO_2$ as the oxidant remained the same as when $O_2$ was used as the oxidant. However, the final temperature at which all the coke in the sample was removed increased from 800 K to 1090 K as seen in **Figure 5-11**. Thus, for effective coke removal with $CO_2$ as the oxidant during a regeneration cycle the temperature would need to be increased beyond that of the investigated reaction temperature of 873 K.

### 5.4.1.c $CO_2$-ODAE and DDAE activity comparison between Ga/ZSM-5 and Ga/ZSM-5P(0.8)

The observed improvement with phosphorous modified catalysts in the above section was evaluated using the $CO_2$-ODAE reaction, but it was also of interest to evaluate the activity of the highest performing phosphorous modified catalyst, Ga/ZSM-5P(0.8) for the DDAE reaction. The effect of $CO_2$ for the unmodified and 0.8 wt.% phosphorous modified Ga/ZSM-5 catalysts is shown in **Figure 5-12**. Unlike the unmodified Ga/ZSM-5 catalyst, the Ga/ZSM-5P(0.8) catalyst showed an improvement in liquid aromatic selectivity (55.5 %) in the presence of $CO_2$, resulting in a higher yield. Therefore, the incorporation of phosphorous at an optimal loading allowed for the formation of more liquid aromatics through the $CO_2$-ODAE reaction compared to the DDAE reaction with considerable $CO_2$ consumption and slightly increased $C_2$ turn-over per mol of Ga metal (19.9 vs. 21.03 mol reactant·mol $Ga^{-1}$·$hr^{-1}$, respectively)

.

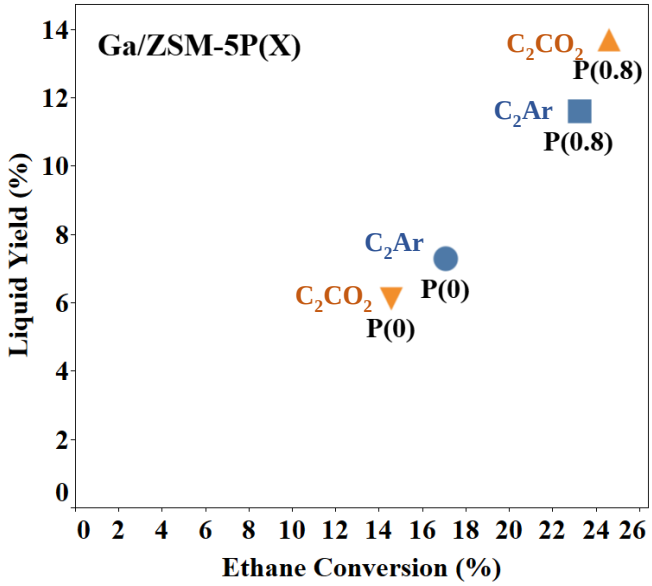


**Figure 5-12.** Effect of $CO_2$. The influence of $CO_2$ on ethane conversion and liquid aromatic yield. 2 wt.% Ga on ZSM-5 (Si/Al 30 molar) modified with phosphorous 0 and 0.8 wt.%. Upward and downward triangles represent the $CO_2$-ODAE reaction while the square and circle represent DDAE

### 5.4.1.d Kinetic studies over Ga/ZSM-5P(0.8)

Further understanding of the promising $CO_2$-ODAE Ga/ZSM-5P(0.8) catalyst was obtained through kinetic measurements. Kinetic measurements were performed under slightly different reaction conditions to minimize the effects of heat and mass transport. The apparent activation energies were derived by measuring production rates in the temperature range of 530-660 K, and the results are depicted in **Figure 5-13**. The activation barrier to produce liquid aromatics from ethane was measured as 121 kJ·mol$^{-1}$, similarly, the barrier for the production of ethylene was 124 kJ·mol$^{-1}$. The similar apparent activation barrier values may signify that the formation of ethylene was the most challenging step in the $CO_2$-ODAE reaction. While the subsequent formation of liquids was still an uphill energy requirement, aromatization proceeded in a more facile nature

compared to ethylene production via dehydrogenation. The barrier value for $CO_2$ activation, 163 $kJ \cdot mol^{-1}$, was much greater than for the transformation of ethane to ethylene and aromatics. In a previous $CO_2$-assisted oxidative dehydrogenation study performed over readily reducible $CeO_2$ support (no aromatic production), $CO_2$ was activated by the support and interfacial sites between the supported bimetallic system ($Fe_3Ni_1$) and $CeO_2$, resulting in a $CO_2$ activation barrier of 115 $kJ \cdot mol^{-1}$. In the present study, the use of ZSM-5 was critical for the production of aromatics but this support likely did not facilitate $CO_2$ activation. Therefore, effective metal sites (i.e., Ga) capable of $CO_2$ activation were essential for the $CO_2$-ODAE reaction to proceed over ZSM-5-based catalysts.

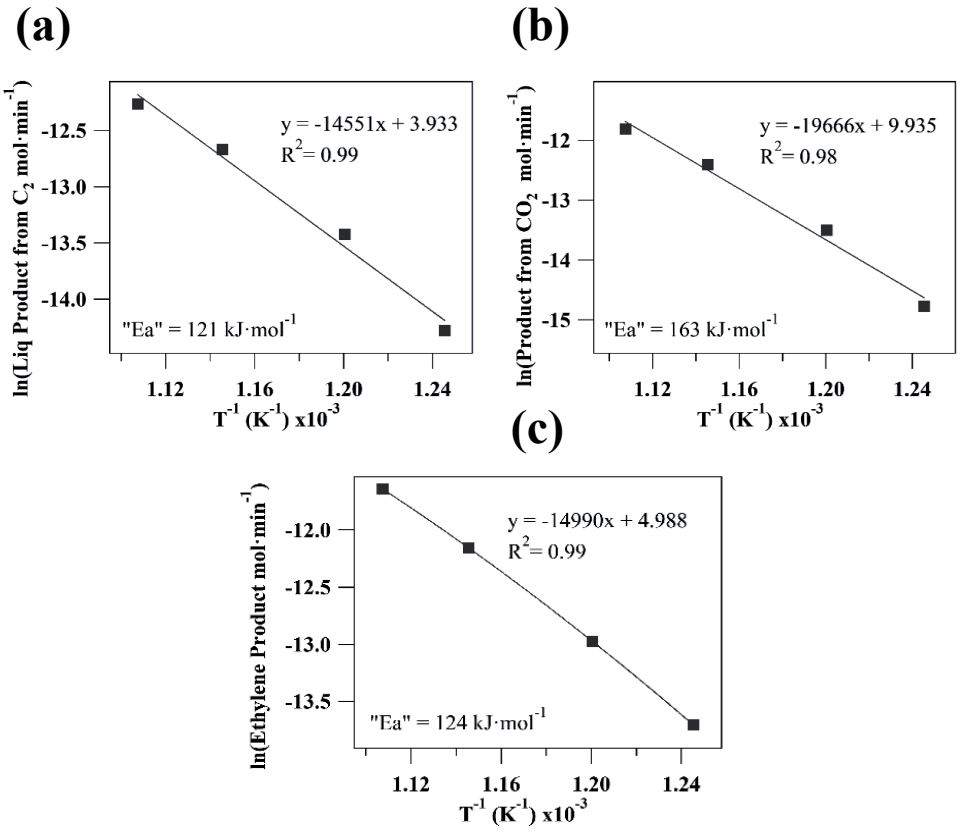


**Figure 5-13.** Apparent activation energies. Effect of varying temperature over a diluted Ga/ZSM-5P(0.8). Apparent activation energy **(a)** liquid aromatic product formation from $C_2$ **(b)** product formation from $CO_2$ and **(c)** ethylene formation from $C_2$.

The influence of the reactant vol.% on the production of aromatics and $CO_2$ activation was examined by gradually increasing one reactant while maintaining the other constant (30 vol%). The total flow rate remained the same by varying the Ar diluent accordingly. **Figure 5-14a** shows that as the vol.% of $CO_2$ increased the rate of aromatic formation decreased linearly. **Figure 5-15**a also showed that $CO_2$ has a negative effect on the production of ethylene. However, the effective

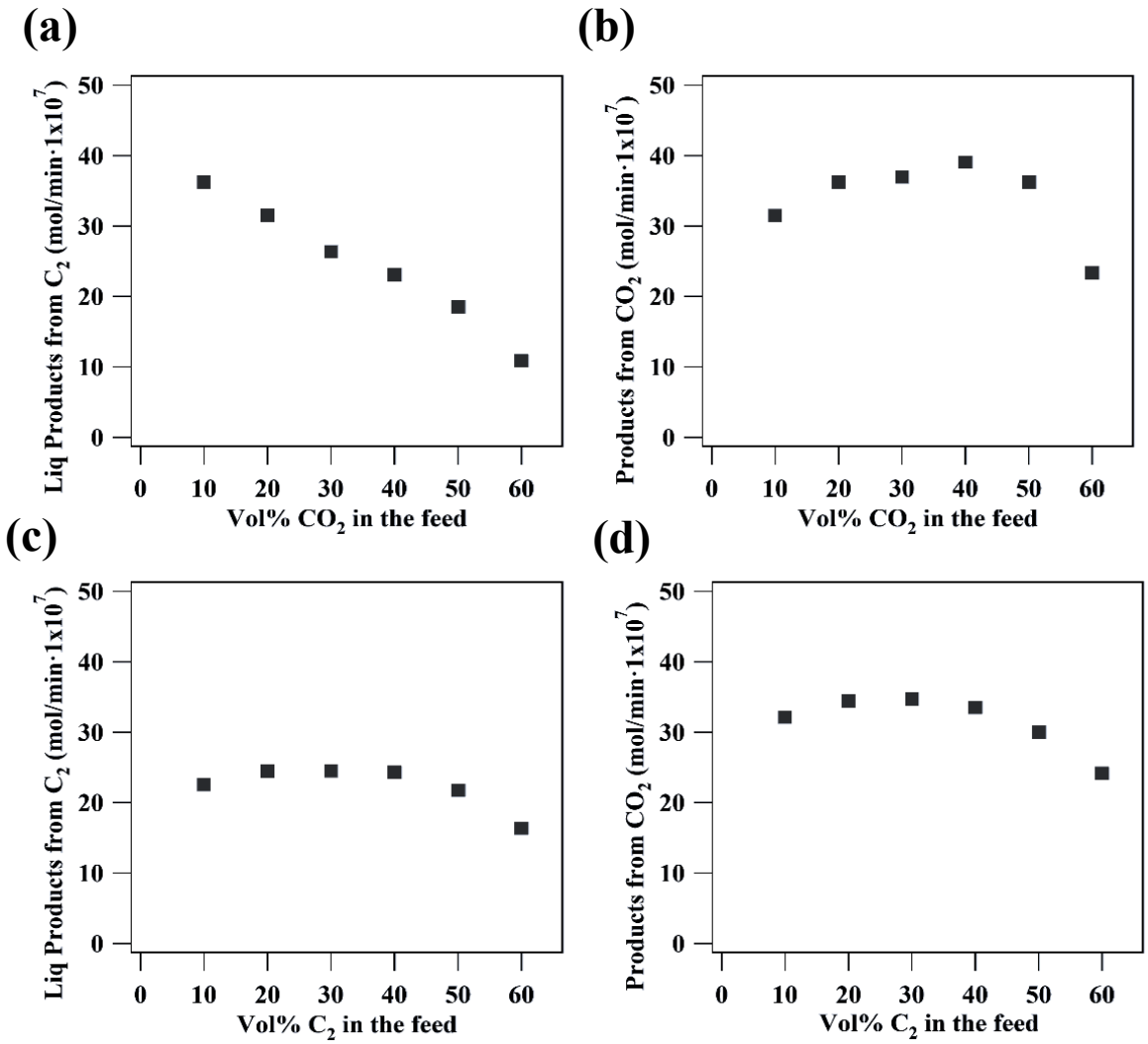


**Figure 5-14.** Effect of the vol.% of reactant$_{A/B}$. Influence of varying the vol.% of reactant$_{A/B}$ in the feed on the products from reactant$_{A/B}$ over diluted Ga/ZSM-5P(0.8). **(a)** Liquid product formation vs. $CO_2$ vol.% **(b)** products from $CO_2$ vs. $CO_2$ vol.% **(c) l**iquid product formation vs. $C_2$ vol.% and **(d)** products from $CO_2$ vs. $C_2$ vol%.

transformation of $CO_2$ to CO, **Figure 5-14b**, was positively influenced until a $CO_2/C_2$ ratio of 1.7, after which the rate also began to decline. Increasing the ethane vol.% in the feed had a linearly positive effect on ethylene production and a minimal effect on both the liquid aromatic and CO production until a $C_2/CO_2$ feed ratio of 1.7, then after all three production rates began to decline. These trends were indicative of competitive adsorption of reactants where one type of active site was capable of both $CO_2$ and $C_2H_6$ transformation to products.

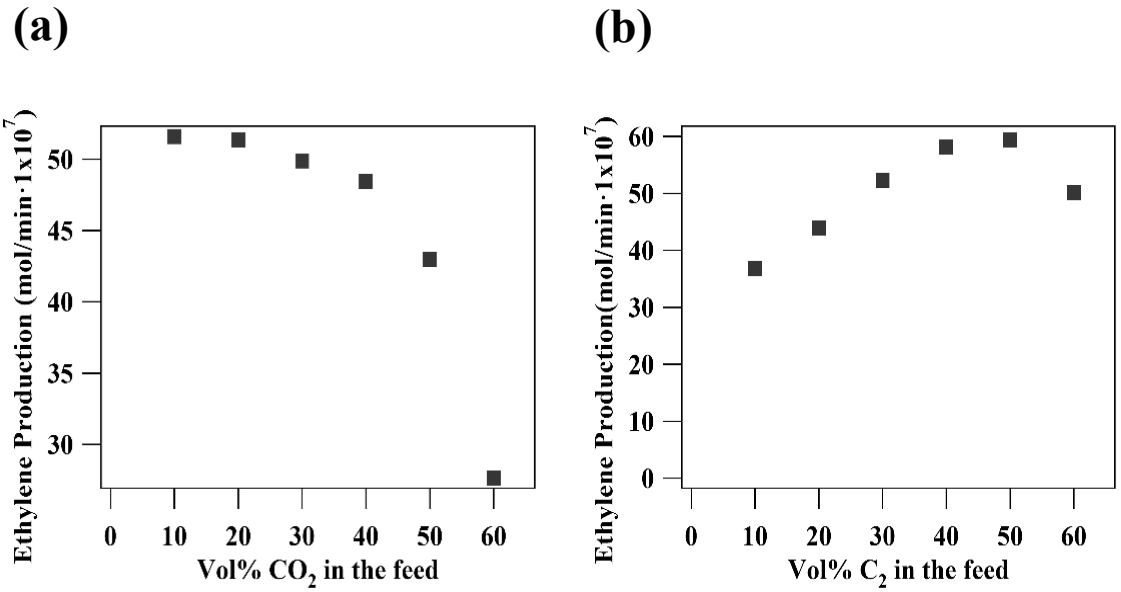


**Figure 5-15.** Effect of the vol.% of reactant$_{A/B}$. Influence of varying the vol.% of reactant$_{A/B}$ in the feed on the production of ethylene over diluted Ga/ZSM-5P(0.8). **(a)** Ethylene product formation vs. $CO_2$ vol.% and **(b)** ethylene product formation vs. $C_2$ vol.%.

### 5.4.1.e $CO_2$-ODAE reaction performed with carbon-13 labeled $CO_2$ and carbon-12 labeled ethane

Isotope experiments with carbon-13 labeled $CO_2$ were performed with carbon-12 ethane over Ga/ZSM-5P(0.8) to gain mechanistic understanding regarding the carbon that can potentially form aromatics (i.e., benzene). The catalyst underwent normal activation in Ar before the

introduction of reaction gasses, beginning with carbon-12 $CO_2$ and carbon-12 $C_2H_6$. The reaction was held on stream for 54 minutes before collecting 4 data sets (collected during TOS 55-85 mins) of m/z values 1 to 100. After data collection for carbon-12 labeled $CO_2$, the gas was switched to feed carbon-13 labeled $CO_2$ and was allowed to stabilize for 14 mins before collecting another 4 data sets (collected during TOS 100-130 mins). The formation of benzene was tracked with m/z values of 72-78, the range of fragments possible if carbon-12 labeled $CO_2$ or carbon-13 labeled $CO_2$ was involved in the molecule's formation and the result is shown in **Figure 5-16**. The intensity of 72-78 m/z did not change with the change of different carbon-labeled $CO_2$, indicating that aromatics were solely formed via the $C_2H_6$ molecule. On the other hand, **Figure 5-17** shows m/z masses 44 and 45 ($CO_2$) as well as 28 and 29 (CO), which underwent changes in intensity that corresponded to the switch to isotope-labeled $CO_2$ and illustrated the formation of some carbon-13 labeled CO.

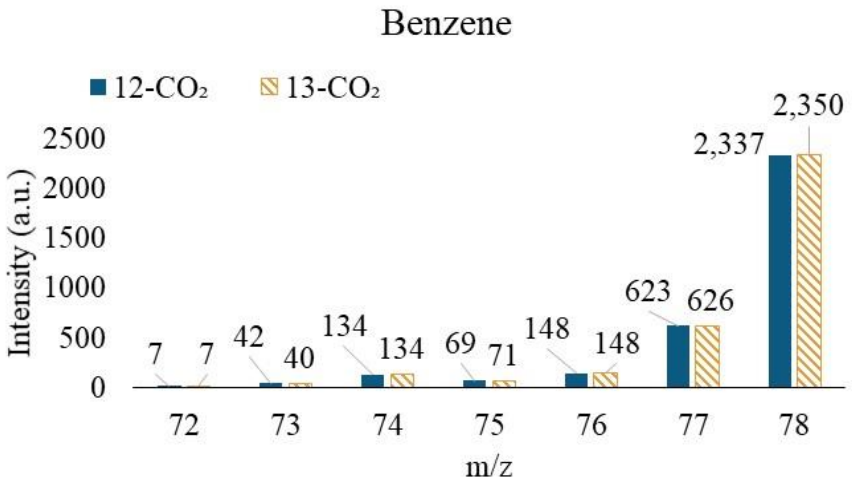


**Figure 5-16.** Isotope experiment. Tracking product benzene with m/z values 72-78 to include a range of fragments that are possible with carbon 12-labeled and carbon 13-labeled $CO_2$. Activation period with Ar followed by reaction gasses first with carbon 12-labeled $CO_2$ (allowed to stabilize for 54 mins before scans) followed by carbon 13-labeled $CO_2$. Values displayed are the average of data collected at reaction times 55-85 min and 100-130 min with 12-$CO_2$ and 13-$CO_2$, respectively

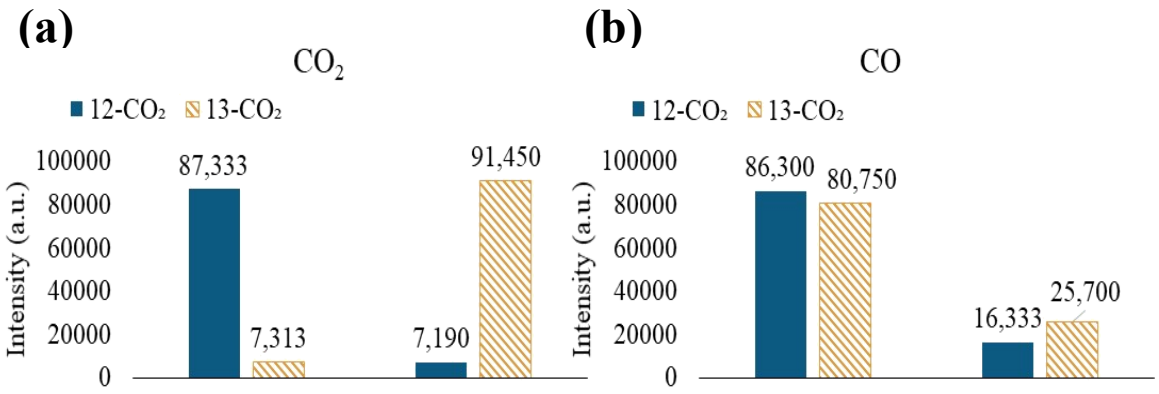


**Figure 5-17.** Isotope experiment. **(a)** m/z 44 and 45 for tracking reactant $CO_2$ and **(b)** m/z 28 and 29 for tracking product CO which can originate from both 12/13-$CO_2$ and 12-$C_2H_6$. Activation period with Ar followed by reaction gasses first with carbon 12-labeled $CO_2$ (allowed to stabilize for 54 mins before scans) followed by carbon 13-labeled $CO_2$. Values displayed are the average of data collected at reaction times 55-85 min and 100-130 min with 12-$CO_2$ and 13-$CO_2$, respectively.

### 5.4.1.f Increasing $CO_2$ consumption per mol of aromatic product via dual catalyst beds

While the Ga/ZSM-5P(0.8) catalyst effectively performed the $CO_2$-ODAE reaction, a consecutive dual catalyst bed reaction scheme was proposed to further enhance $CO_2$ conversion and increase the production of liquid aromatics. In the consecutive dual catalyst bed arrangement, reaction gasses first contacted a $CO_2$-ODH catalyst to increase the local concentration of ethylene before passing over the second bed which contained a $CO_2$-ODAE catalyst capable of aromatization. $Fe_3Ni_1/CeO_2$ was previously examined for the $CO_2$-ODH reaction of ethane, propane, and butane and showed promising olefin selectivity. Thus, in this study the dual catalyst bed experiments were performed by allowing reaction gases to contact a bed consisting of 150 mg of $Fe_3Ni/CeO_2$ particles before reaching the second bed containing 150 mg of Ga/ZSM-5P(0.8) catalyst particles, the results are shown in **Figure 5-18**. The production of liquid aromatics over

the consecutive dual bed was 1.4 times higher than the single Ga/ZSM-5P(0.8) bed. In addition, the conversions of $C_2$ and $CO_2$ were improved by factors of 1.6 and 2.6, respectively. The consecutive dual catalyst bed illustrated the positive effect of increasing the local concentration of ethylene in the feed for a $CO_2$-ODAE catalyst. Rather than co-feeding ethylene outsourced from other energy-intensive processes (cracking or direct dehydrogenation), the dual bed scheme allowed for direct alkane conversion, in a one-step process, to liquid aromatics with increased $CO_2$ consumption. In addition, this would facilitate downstream separation requirements compared to the isolated $CO_2$-ODH process.

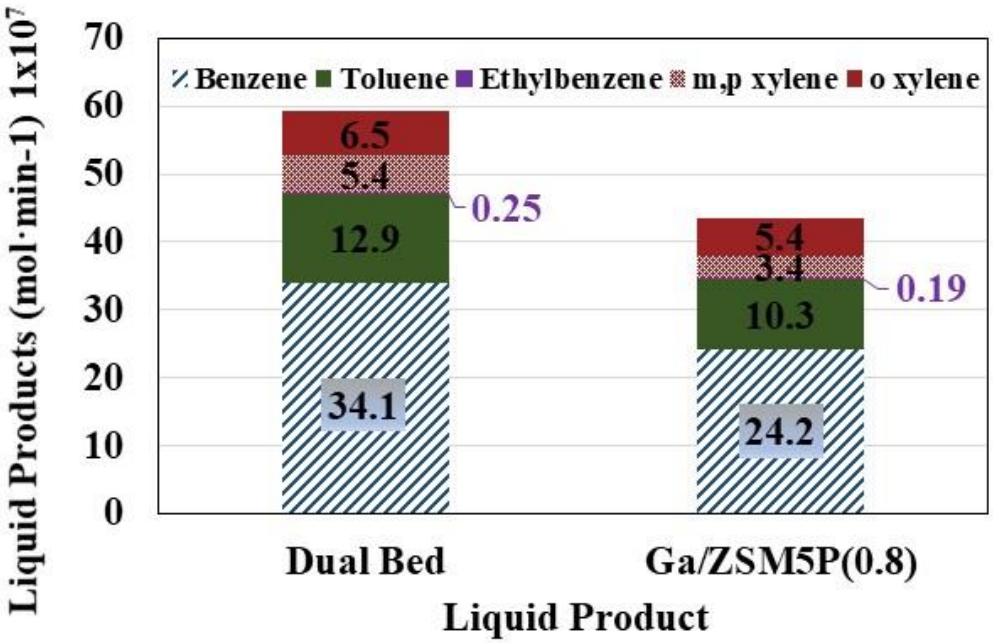


**Figure 5-18.** Consecutive dual catalyst bed experiment. Reaction gases first contact a bed consisting of 150 mg of $Fe_3Ni/CeO_2$ particles (40-60 mesh) before contacting a second catalyst bed containing 150 mg of 40-60 mesh Ga/ZSM5P(0.8).

### 5.4.2 Reaction pathways and DFT calculations

#### 5.4.2.a DDE activity over ZSM-5 and Ga modified ZSM-5

Density functional theory (DFT) calculations were performed to gain insight on the possible reaction mechanisms of direct ethane dehydrogenation to ethylene over ZSM-5 and Ga/ZSM-5, with a focus on identifying the intrinsic role of Ga. The active site structures of ZSM-5 and Ga/ZSM-5 employed in the present DFT calculations are illustrated in **Figure 5-19 (a) and (b)**. Both structures included two Al substitutions with Si at framework positions T12 and T2. For Ga/ZSM-5, the active site was composed of a Brønsted-Lewis (B-L) acid site pair, similar to the work of Schreiber *et al.* for propane dehydrogenation.[36]

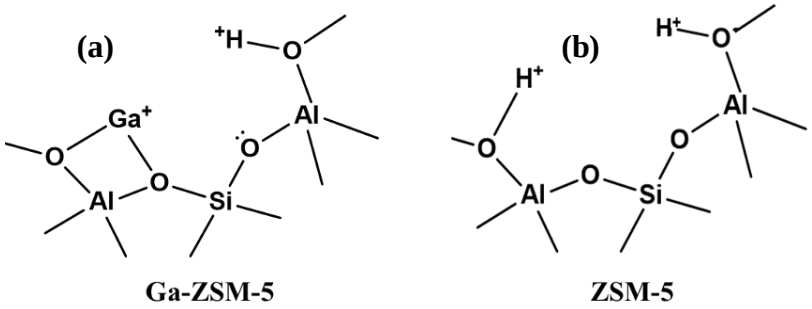


**Figure 5-19.** The active site structures of Ga/ZSM-5 and ZSM-5 employed in DFT calculations.

The energy diagrams for ethylene formation from the DDE reaction over ZSM-5 and Ga/ZSM-5 are shown in **Figure 5-20** and the corresponding mechanisms are illustrated in **Figure 5-21**. Over ZSM-5, ethane dehydrogenation to an ethoxide ($C_2H_5O$) species was catalyzed by a Brønsted acid site and was uphill in energy with a considerable activation barrier of 2.48 eV. Accompanying the formation of the ethoxide species was the formation of $H_2$ molecules inside the ZSM-5 pore. The subsequent dehydrogenation of $C_2H_5O$ to form $C_2H_4$ and the simultaneous regeneration of the B acid site was facile, with a barrier of 0.62 eV.

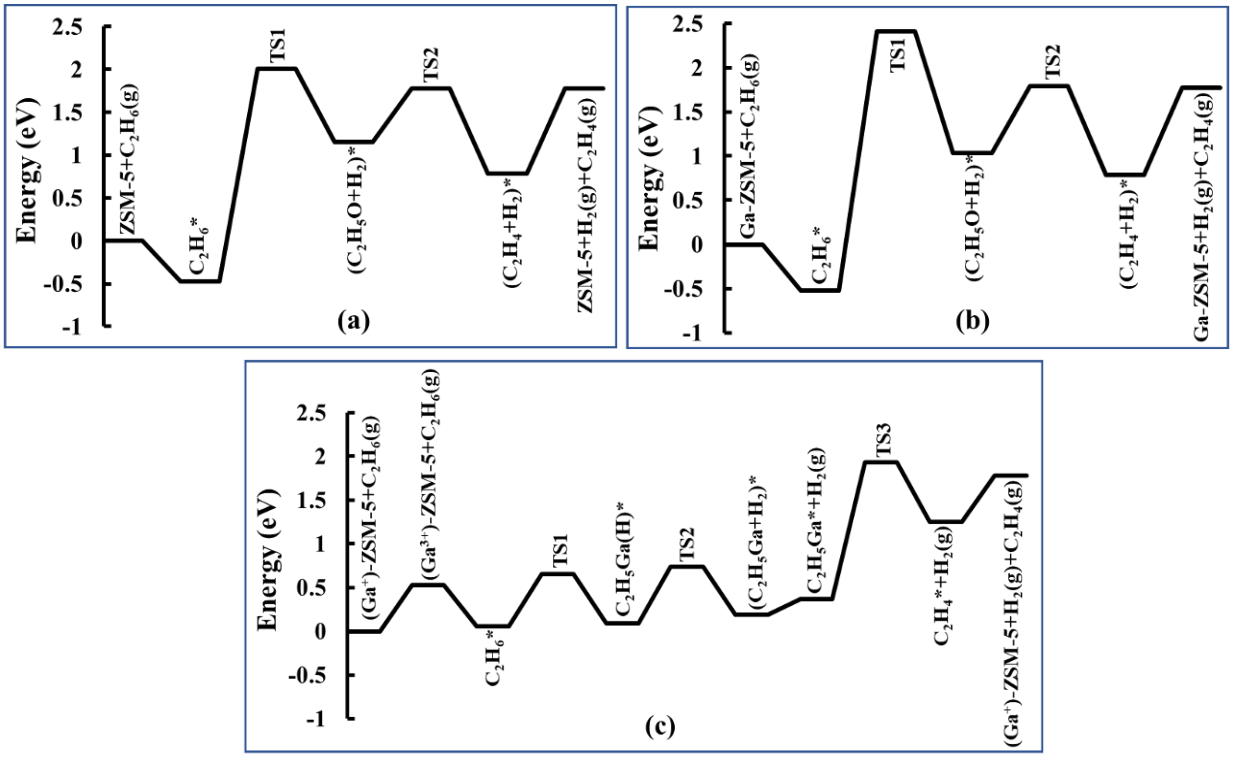


**Figure 5-20.** Energy diagrams of ethane dehydrogenation to ethylene over **(a)** ZSM-5 and **(b)**, **(c)** Ga/ZSM-5.

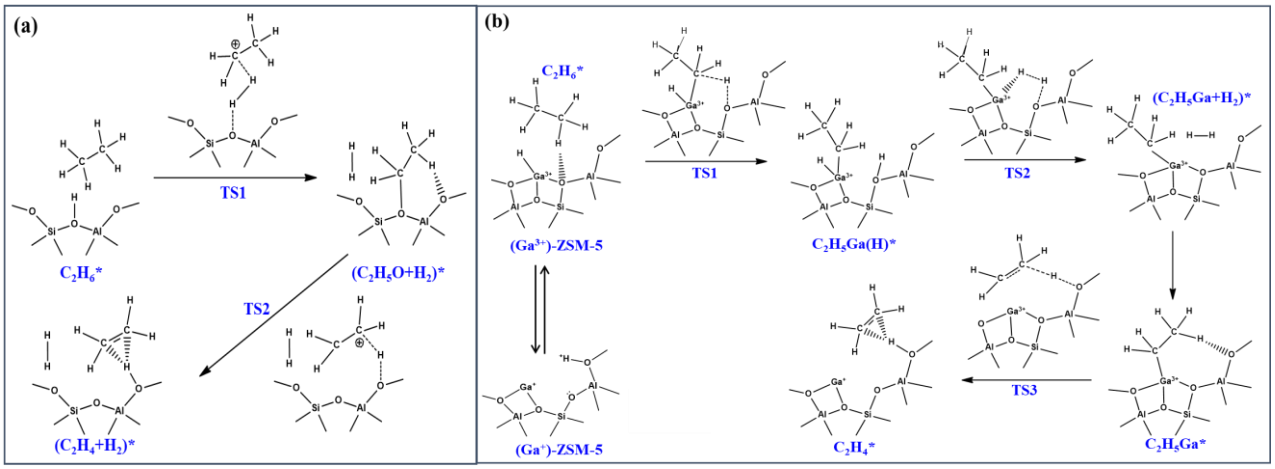


**Figure 5-21.** Mechanistic illustration of ethane deprotonation to ethylene over **(a)** ZSM-5 (B acid site catalysis) and **(b)** Ga/ZSM-5 (B-L acid site cooperative catalysis).

Two distinct mechanisms were examined for the DDE reaction over Ga/ZSM-5, the first pathway occurred via a B acid site and the second via a B-L acid site. The dehydrogenation mechanism via the interaction of the B acid site was similar to the pathway observed over unmodified ZSM-5, where ethane dehydrogenation to $C_2H_5O$ was rate determining with a high barrier of 2.94 eV. In this mechanism, the $Ga^+$ species bound above the O-Al-O bridge did not participate in the catalytic process, and therefore the addition of Ga did not influence performance. Catalytic conversion of light alkanes to olefins via a Ga/ZSM-5 Lewis acid site was highly unlikely due to insurmountable energy barriers[36,37], indicating that the $Ga^+$ species itself was not sufficient to catalyze ethane dehydrogenation. While Lewis acid sites cannot catalyze reactions, there was a synergistic effect when the Lewis acid site paired with a Brønsted acid site, creating a B-L acid site pair. For instance, the B acid site transferred a proton to the $Ga^+$ site to form a $(GaH)^{2+}$ species, thereby altering the oxidation state of Ga to 3+ and increasing the Lewis acid strength. This proton transfer process was calculated to be 0.53 eV and endothermic, inferring that the B-L acid site model was the lowest energy state of Ga/ZSM-5. Once the $Ga^{3+}$ species was generated, ethane dehydrogenation to ethylene was facilitated and proceeded much faster (barrier of 0.60 eV). Consequently, the rate of $H_2$ formation was also increased (barrier of 0.65 eV).

Thus, for the addition of Ga to promote ethane transformation to ethylene, the reaction mechanism must have occurred via cooperative B-L acid sites and not just via B acid sites. The B-L acid site was bifunctional in nature. The B acid site protonated the $Ga^+$ to form a $(GaH)^{2+}$ active species, which then, together with the basic framework oxygen, heterolytically activated one of the C-H bonds of ethane with a low barrier. Thereout, a $C_2H_5Ga$ intermediate was produced and further dehydrogenated to $C_2H_4$, completing the regeneration of the B-L acid site. The second dehydrogenation step was rate-limiting, with a barrier of 1.56 eV. Overall, the increased ethane

conversion over Ga/ZSM-5 compared to unmodified ZSM-5 in flow reactor experiments were attributed to the synergistic catalysis induced by the B-L acid sites.

### 5.4.2.b The role of $CO_2$ in the dehydrogenation and aromatization of ethane

The flow reactor results in this study illustrated that in the presence of $CO_2$ neither the $C_2$ conversion nor the selectivity towards aromatics was enhanced over Ga/ZSM-5 after 10 hours on stream. The incorporation of phosphorus significantly increased the yield to aromatics and improved the stability, indicating that $CO_2$ was assisting the tandem reactions of ethane dehydrogenation and aromatization. To gain insight into the intrinsic role of $CO_2$ on a molecular level, we performed comprehensive DFT calculations to investigate the possible mechanisms of ethane dehydrogenation to ethylene coupled with ethylene transformation to benzene. In these calculations, benzene was used as the model aromatic since flow reactor studied showed it is the dominate liquid product.

Four possible mechanisms for ethane dehydrogenation to ethylene over Ga/ZSM-5 in the presence of $CO_2$ were examined. By calculating the minimum energy pathways, we identified that the most energetically favorable mechanism required that ethane first dehydrogenate to $C_2H_5Ga$ and $H_2$ over the B-L acid sites. Then, $CO_2$ reacted with the produced $H_2$ to form CO and $H_2O$ via RWGS and the $C_2H_5Ga$ further dehydrogenated to $C_2H_4$, regenerating the acid site. The energy diagram of this mechanism is shown in **Figure 5-22** and the other examined mechanisms are provided in **Figure 5-23**. Comparing the energetics between **Figure 5-20c** and **Figure 5-22** illustrated that the transformation of ethane to ethylene in the presence of $CO_2$ was anticipated to be lower compared to the reaction in the absence of $CO_2$ over Ga/ZSM-5. This may be attributed to high barriers for $CO_2$ hydrogenation to CO and $H_2O$, indicating that $CO_2$ was not capable of consuming $H_2$ at an appreciable rate to adequately shift the equilibrium toward the production of

olefin over Ga/ZSM-5. Despite the low rates of $CO_2$ hydrogenation, the amount of $H_2O$ that was produced had the potential to influence the reaction mechanism since the DFT calculations showed that $H_2O$ molecules can adsorb strongly on the $Ga^+$ site, with a binding energy of 1.65 eV. Due to the interaction of $H_2O$ with the active site, dehydrogenation of the formed $C_2H_5Ga$ to $C_2H_4$ needed to surmount a higher barrier compared to the case without $CO_2$ (2.12 *vs.* 1.56 eV). Literature has shown that in the presence of steam (over 400°C), the Si-O-Al framework will gradually hydrolyze and Al will be expelled. A zeolite that is susceptible to dealumination inherently exhibits lower hydrothermal stability and activity under reaction conditions that produce water. Previous studies have demonstrated that phosphorous modification can improve the hydrothermal stability and resistance to coke on ZSM-5 catalysts, this will be further described in detail in the Discussion section.[38,39]

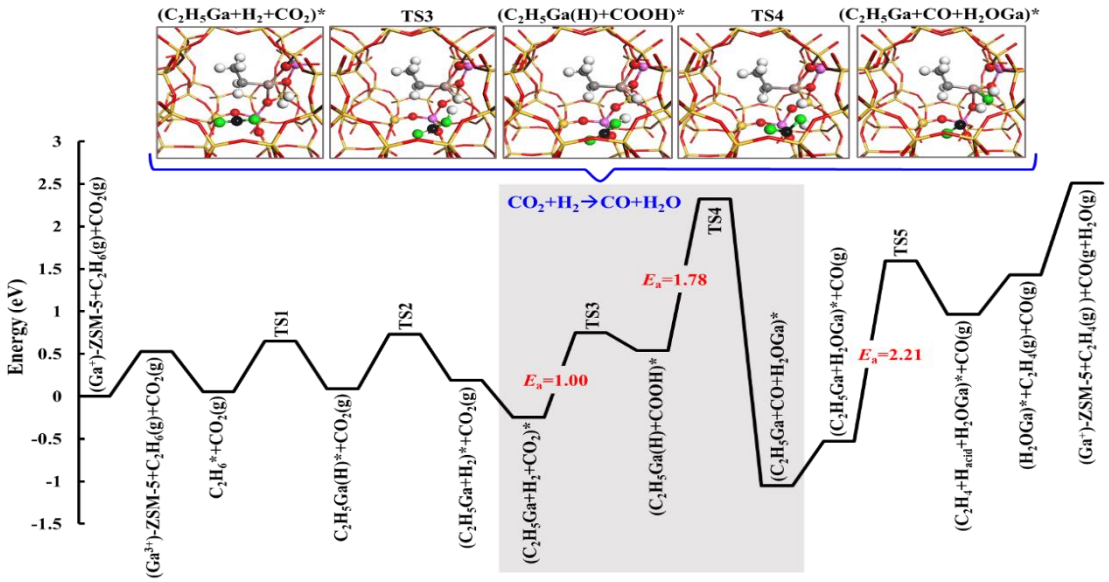


**Figure 5-22.** Energy diagram of ethane dehydrogenation to ethylene over Ga/ZSM-5 in the presence of $CO_2$. Structures of states involved in $CO_2$ conversion to CO and $H_2O$ within the path were included (Yellow: Si, Pink: Al, Brown: Ga, Red: O, Grey: C, White: H, Green: O of $CO_2$; Black: C of $CO_2$).

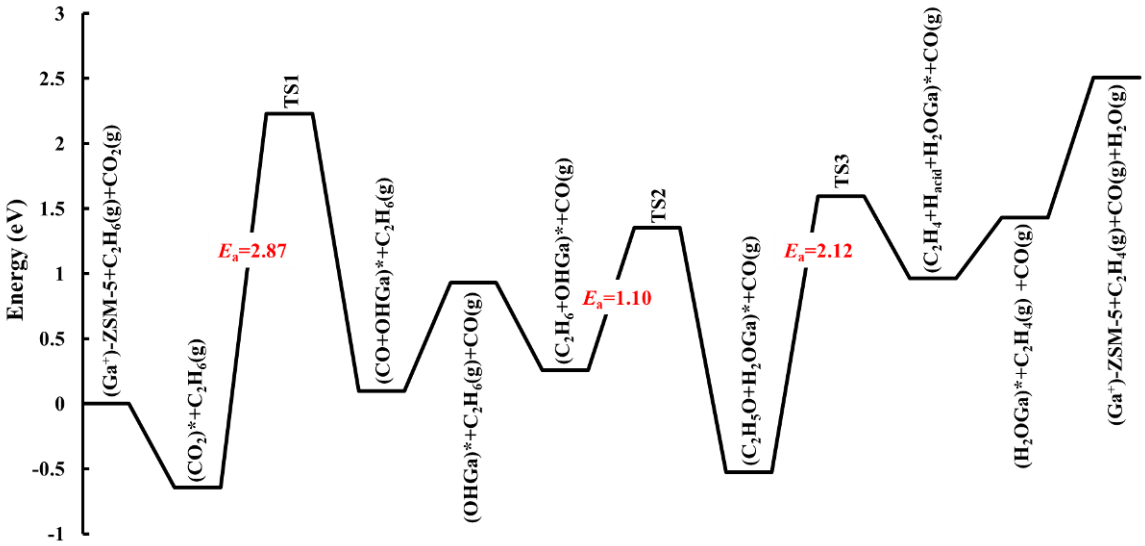


**(a)** $CO_2$ first reacts with the B acid site to form CO and OH-Ga, then the adsorbed $C_2H_6$ reacts with OH-Ga to produce $H_2O$-Ga and $C_2H_5O$, and finally, the $C_2H_5O$ dehydrogenates to $C_2H_4$ and regenerate the B acid site.

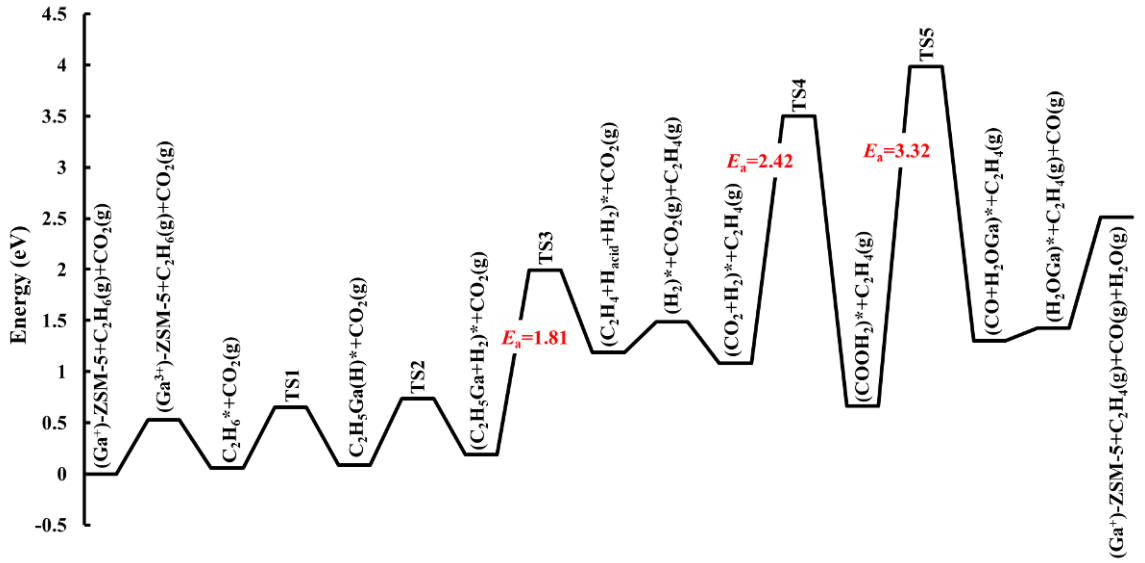


**(b)** Adsorbed $C_2H_6$ first dehydrogenates to $C_2H_4$ and $H_2$ via the B-L acid site cooperative catalysis, and then the adsorbed $CO_2$ reacts with the produced $H_2$ to form CO and $H_2O$ via RWGS ($C_2H_4$ desorbs from the B acid site prior to $CO_2$ reaction).

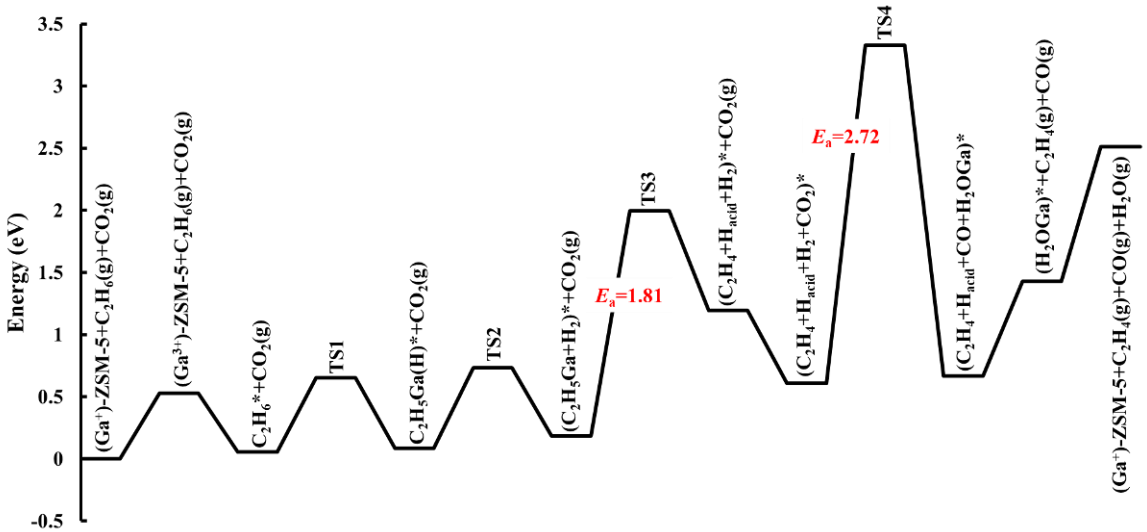


**(c)** Adsorbed $C_2H_6$ first dehydrogenates to $C_2H_4$ and $H_2$ via the B-L acid site cooperative catalysis, and then the adsorbed $CO_2$ reacts with the produced $H_2$ to form CO and $H_2O$ via RWGS ($C_2H_4$ remains adsorbed at the B acid site during $CO_2$ reaction).

**Figure 5-23.** Reaction mechanisms examined for ethane conversion to ethylene over Ga/ZSM-5 at the presence of $CO_2$.

Further calculations were conducted to explore the effect of $CO_2$ on ethylene conversion to benzene over Ga/ZSM-5. The diagram based on reaction energies is shown in **Figure 5-24**, and the free energy diagram calculated at 873 K is provided in **Figure 5-25**. These two figures demonstrated that $H_2$ formation was substantially uphill in energy and may determine the overall rate for benzene formation over Ga/ZSM-5. The introduction of $CO_2$ to the feed may facilitate the reaction since the produced -H from dehydrogenation can directly be consumed via RWGS. To verify this assumption, barrier calculations were conducted on the two $H_2$ formation steps (P1; $C_4H_8Ga+HGa \rightarrow C_4H_7O+HGaH \rightarrow C_4H_7O+H_2$ and P2; $C_6H_{10}Ga+Hga \rightarrow C_6H_9O+HGaH \rightarrow C_6H_9O+H_2$) with the highest uphill energy requirement of the reaction pathway. The effect of $CO_2$ on the mechanism and kinetics for these two $H_2$ formation steps was also investigated. As shown in the insets of **Figure 5-24**, the formation of $H_2$ must overcome large barriers at both selected P1

and P2 steps, with barrier values of 2.97 and 2.86 eV, respectively. However, in the presence of $CO_2$, the produced -H directly hydrogenated $CO_2$ to COOH which then dissociated to CO and OH. The -OH bound at the $Ga^+$ site then takes the other H from $C_4H_8$ or $C_6H_{10}$ to produce $H_2O$ on the site. Thus, in the presence of $CO_2$, the reaction mechanism was altered and the formation of molecular $H_2$ was hindered, and most importantly, the P1 and P2 barriers were significantly reduced.

These DFT results demonstrated a promoting effect of $CO_2$ on the production of aromatics over Ga/ZSM-5. However, flow reactor experiments over Ga/ZSM-5 illustrated that the presence of $CO_2$ did not increase the selectivity to aromatics. This difference can likely be attributed to the instability of the ZSM-5 framework in the presence of water under reaction conditions due to the strong adsorption of $H_2O$ on Ga sites. As demonstrated by flow reactor studies, modifying the Ga/ZSM-5 catalyst with phosphorous enhanced the production of aromatics and limited coke formation in the presence of $CO_2$, indicating that the role of phosphorous was likely to improve the hydrothermal stability of the ZSM-5 framework.

Overall, the DFT calculations in this study identified that the B-L acid site was responsible for the increased activity of the Ga modified ZSM-5 compared to the unmodified catalyst. DFT calculations also provided insight on the role of $CO_2$ for the dehydrogenation of ethane to ethylene over Ga/ZSM-5. High barriers for $CO_2$ hydrogenation and high $H_2O$ binding energy on Ga sites hindered the production of ethylene compared to the reaction in the absence of $CO_2$. However, $CO_2$ had a positive effect on the subsequent aromatization of ethylene by decreasing the energy barriers of the two most energetically demanding $H_2$ formation steps by consuming $H_2$ via the RWGS.

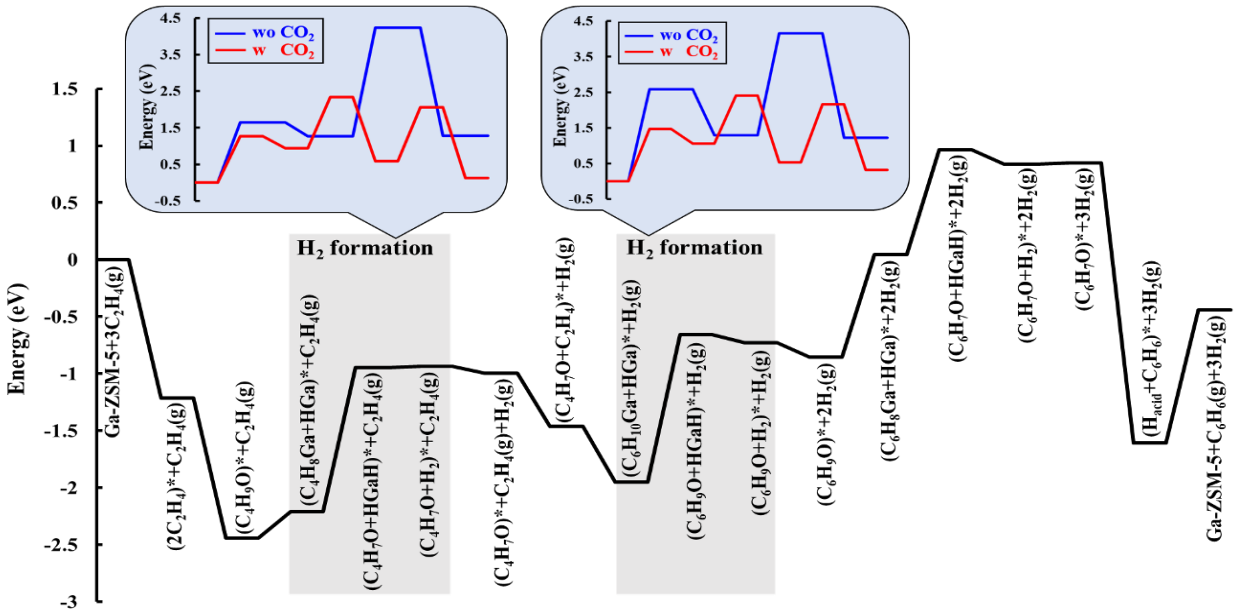


**Figure 5-24.** Reaction energy diagram of ethylene transformation to benzene over Ga/ZSM-5 (Barrier calculations for two $H_2$ formation steps are included in boxed figures for the cases in the absence and presence of $CO_2$).

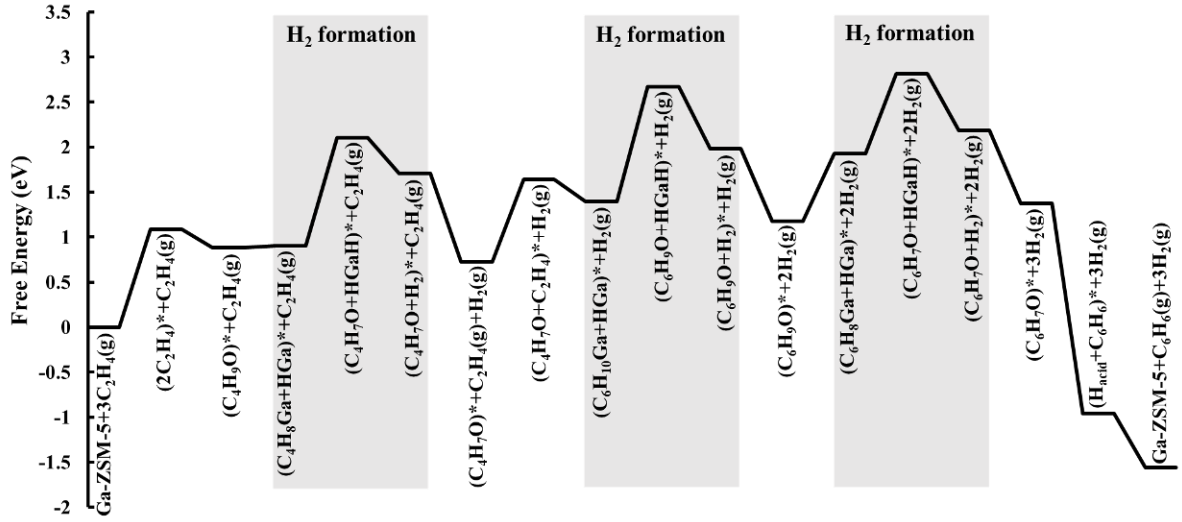


**Figure 5-25.** Reaction free energy diagram of ethylene transformation to benzene over Ga/ZSM-5 calculated at 873 K.

## 5.5 Discussion

In this study Ga/ZSM-5 was used as a baseline indicator because of the reported ability of Ga to increase the activity of ZSM-5 for the DDAE pathway. As anticipated, Ga effectively increased the $C_2$ conversion and selectivity to aromatics for the DDAE reaction pathway compared to unmodified ZSM-5. The Ga/ZSM-5 catalyst also improved the $C_2$ conversion and aromatic selectivity compared to the ZSM-5 blank for the $CO_2$-ODAE pathway, but compared to the results under DDAE conditions, the presence of $CO_2$ did not promote a significant improvement in the production of aromatics. This is contrary to the thermodynamic calculations and expectations of $CO_2$ as a mild oxidant.

One critical change upon the introduction of $CO_2$ to the dehydrogenation/aromatization pathway is the formation of water. The presence of water under reaction conditions has been shown to be problematic for zeolites as it causes dealumination and therefore a change in the zeolitic framework. Several studies have shown that phosphorous prevents structural changes of the zeolite by stabilizing lattice aluminum ions in the tetrahedrally coordinated framework, but exactly how or the specific type of effective phosphorous species that is capable of these functions is not well understood.[34,35,40,19] Xue et al. demonstrated that phosphorous interacts with exposed silanol nests that are formed by the dealumination process and creates new hydrothermally stable acid sites when exposed to water molecules under reaction conditions. Indicating that the role of phosphorous is to fill the zeolitic position that was left exposed due to dealumination by coupling with the expelled aluminum species. Thus, the insertion of the phosphorous into the zeolitic framework stabilizes and protects against the reoccurrence of dealumination. Lercher et al. proposed that during phosphorous modification with phosphoric acid the oxygen of the strongly acidic bridging OH groups of ZSM-5 are replaced by two much less acidic OH from $PO_4H_2$-.

Altogether, the modification of ZSM-5 with phosphorous decreases Brønsted acidity, converts strong Brønsted acid sites into weak Brønsted acid sites thereby increasing the density of the weak Brønsted acid sites in the catalyst. This change in the overall acidity of the catalyst as a result of creating a reinforced water-tolerant framework can also help reduce coke formation since there are a reduced number of highly acidic sites on which cracking is favorable.

In the present study, the incorporation of phosphorous on Ga/ZSM-5 with a loading as low as 0.2 wt.% improved $C_2$ conversion and aromatic selectivity of the $CO_2$-ODAE reaction. As the loading of phosphorous increased, the liquid aromatic yield and stability continued to improve. Contrary to the trend with Ga/ZSM-5, the activity of Ga/ZSM-5P(0.8) under $CO_2$-ODAE reaction conditions showed higher liquid aromatic yield compared to the results when exposed to DDAE conditions. This indicated that phosphorous helped stabilize the catalyst in the presence of water that was formed by the RWGS and allowed the benefits of co-feeding $CO_2$ to enhance the selectivity toward aromatics. In addition, the Ga/ZSM-5P(X) catalysts showed decreased selectivity to methane compared to Ga/ZSM-5, but the selectivity to CO remained similar. This may be indicative that phosphorous decreased cracking reactions (reduced amount of methane and coke) and over-oxidation compared to Ga/ZSM-5. In $CO_2$-oxidative dehydrogenation, over-oxidation can contribute to the formation of CO while still providing a net reduction in $CO_2$ as opposed to other oxidative techniques which produce additional $CO_2$. The inhibition of cracking reactions that form methane and coke was further supported by the TGA experiments performed over Ga/ZSM-5 and Ga/ZSM-5P(0.8) which illustrated that the phosphorous modified catalyst contained less coke.

Further understanding of the Ga/ZSM-5P(0.8) catalyst was obtained via reaction order-type and activation barrier experiments. The trends obtained via the reaction order-type experiments

illustrated that $CO_2$ and $C_2$ may be competing for the same type of active site, and that increasing one reactant over the other (especially $CO_2$) decreases the production of aromatics. The activation barrier value corresponding to the formation of ethylene was only slightly higher than the barrier to produce aromatics, suggesting that the formation of ethylene was the most difficult step in the $CO_2$-ODAE process. Therefore, to further increase the production of aromatics and consumption of $CO_2$ per mol of product, a consecutive dual bed reaction scheme was proposed. In this arrangement the local concentration of ethylene over the Ga/ZSM-5P(0.8) bed was increased by using a $CO_2$-ODH catalyst in a preceding bed instead of out-sourcing the olefin via energy and $CO_2$ intensive process such as direct dehydrogenation or cracking.

Finally, to gain understanding regarding the type of carbon that forms aromatics under $CO_2$-ODAE reaction conditions, carbon 13-labeled $CO_2$ experiments were performed with Ga/ZSM-5P(0.8). Early studies of the DDAE reaction believed that aromatics were produced via a stitching-type mechanism with carbon from methane. Since $CO_2$ hydrogenation to methane is possible under high temperatures that are rich in $H_2$, it was decided to identify via isotope experiments that only carbon from ethane can form liquid aromatic products.

DFT calculations identified that the high-activity of ethane dehydrogenation to ethylene over Ga modified ZSM-5 was due to the synergetic catalysis induced by a B-L acid site pair. In the presence of $CO_2$, ethylene production was impaired due to the increased barrier caused by $H_2O$ co-adsorption at the active site. Additionally, increased barriers on $CO_2$ hydrogenation were observed both via DFT calculations and flow reactor experiments. With respect to ethylene transformation to benzene, $H_2$ formation steps had considerable barriers and may limit the overall reaction rate. Upon the introduction of $CO_2$, the mechanism was altered due to the direct participation of $CO_2$ and its conversion to CO and $H_2O$ via RWGS. Most importantly, $CO_2$

involvement in the reaction promoted benzene formation by reducing kinetic barriers. The DFT results helped confirm that the role of phosphorus on Ga/ZSM-5 was to improve hydrothermal stability and suppress coke formation. Furthermore, DFT also provided the understanding that water intolerance inhibited the production of aromatics for the $CO_2$-ODAE reaction over Ga/ZSM-5. The insight gained by DFT not only offered a standpoint on the synergetic catalysis of the B-L acid sites of ZSM-5 but can also help guide the strategy of designing highly active $CO_2$-assisted ODAE catalysts by introducing efficient metal sites capable of enhancing $CO_2$ activation.

## 5.6 Conclusions

In summary, the tandem reactions of $CO_2$-assisted ethane dehydrogenation and aromatization have the potential to produce liquid products of higher value from inexpensive and abundant shale gas while mitigating a greenhouse gas. We report for the first time the impact of phosphorous modification on Ga/ZSM-5 catalysts for the $CO_2$-ODHE reaction, and have identified Ga/ZSM-5P(0.8) as a promising $CO_2$-ODAE catalyst with greater activity and stability than Ga/ZSM-5. The incorporation of phosphorous at a loading of 0.8 wt.% improved the hydrothermal stability of Ga/ZSM-5, reduced coke formation, and allowed for the formation of more liquid aromatics via the $CO_2$-ODAE reaction pathway compared to DDAE. The role of $CO_2$ in the $CO_2$-ODAE reaction was to help aid in the formation of ethylene and consequently enhance aromatic formation via the consumption of $H_2$. Carbon 13-labeled $CO_2$ experiments confirmed that aromatics do not contain carbon sourced from $CO_2$.

Lastly, $CO_2$ consumption and aromatic production was further increased by the use of a consecutive dual bed reaction scheme with a $CO_2$-ODH catalyst preceding Ga/ZSM-5P(0.8). DFT calculations provided fundamental insight into the mechanisms for ethane transformation to aromatics and elucidated the important role of $CO_2$ in promoting the selectivity towards aromatics.

Future efforts should be geared toward enhancing aromatics yield through the design of hydrothermal stable zeolite-based materials with bimetallic active centers that are capable of activating $CO_2$.

## 5.7 Acknowledgements

E.G. acknowledges the U.S. National Science Foundation Graduate Research Fellowship Program: dge-16-44869 and the Gates Millennium Scholars Foundation. The computational work was financially supported by the National Key Research and Development Program of China (No. 2016YFB0600902) and the National Natural Science Foundation of China (No. 21872012). E.G. would like to acknowledge Dr. Xiaowa Nie for providing the DFT calculations and for the discussions and revisions during the writing of this chapter.

## 5.8 References


**1.** Centi G, Iaquaniello G, De Falco M, eds. $CO_2$*: A Valuable Source of Carbon*. 1st ed. London: Springer-Verlag London; 2013. doi:10.1007/978-1-4471-5119-7

2. Aresta M, Dibenedetto A, Quaranta E. *Reaction Mechanisms in Carbon Dioxide Conversion*. 1st ed. Berlin: Springer-Verlag; 2016. doi:10.1007/978-3-662-46831-9

3. Aresta M, Dibenedetto A, Quaranta E. State of the art and perspectives in catalytic processes for $CO_2$ conversion into chemicals and fuels: The distinctive contribution of chemical catalysis and biotechnology. *J Catal*. 2016. doi:10.1016/j.jcat.2016.04.003

4. Ansari MB, Park S-E. Carbon dioxide utilization as a soft oxidant and promoter in catalysis. *Energy Environ Sci*. 2012;5(11):9419-9437. doi:10.1039/$C_2$ee22409g

5. Mukherjee D, Park SE, Reddy BM. $CO_2$ as a soft oxidant for oxidative dehydrogenation reaction: An eco benign process for industry. *J* $CO_2$ *Util*. 2016;16:301-312. doi:10.1016/j.jcou.2016.08.005

6. Kawi S, Kathiraser Y. $CO_2$ as an oxidant for high-temperature reactions. *Front Energy Res*. 2015;3:1-13. doi:10.3389/fenrg.2015.00013

7. Rahimpour MR, Jafari M, Iranshahi D. Progress in catalytic naphtha reforming process: A review. *Appl Energy*. 2013;109:79-93. doi:10.1016/j.apenergy.2013.03.080

8. Hagen A, Roessner F. Ethane to Aromatic Hydrocarbons : Past , Present , Future. *Catal Rev*. 2007;42(4):403-437. doi:10.1081/CR-100101952

9. Porosoff MD, Myint MNZ, Kattel S, et al. Identifying Different Types of Catalysts for $CO_2$ Reduction by Ethane through Dry Reforming and Oxidative Dehydrogenation. *Angew Chemie - Int Ed*. 2015;54:15501-15505. doi:10.1002/anie.201508128

10. Yan B, Yao S, Kattel S, et al. Active sites for tandem reactions of $CO_2$ reduction and ethane dehydrogenation. *Proc Natl Acad Sci*. 2018:2-7. doi:10.1073/pnas.1806950115

11. Yao S, Yan B, Jiang Z, et al. Combining $CO_2$ Reduction with Ethane Oxidative Dehydrogenation by Oxygen-Modification of Molybdenum Carbide. *ACS Catal*. 2018;8(6):5374-5381. doi:10.1021/acscatal.8b00541

12. Gomez E, Kattel S, Yan B, Yao S, Liu P, Chen JG. Combining $CO_2$ reduction with propane oxidative dehydrogenation over bimetallic catalysts. *Nat Commun*. 2018:1-6. doi:10.1038/s41467-018-03793-w

13. Li X, Yan B, Yao S, Kattel S, Chen JG, Wang T. Oxidative dehydrogenation and dry reforming of n-butane with $CO_2$over NiFe bimetallic catalysts. *Appl Catal B Environ*. 2018;231(February):213-223. doi:10.1016/j.apcatb.2018.02.063

14. Guisnet M, Gnep NS, Aittaleb D, Doyemet YJ. Aromatization of $C_2$-C4 alkanes on H-ZSM-5 -reaction mechanisms. *Appl Catal A, Gen*. 1992;87(2):255-270. doi:10.1016/0926-860X(92)80060-P

15. Ono Y, Nakatani H, Kitagawa H, Suzuki E. *The Role of Metal Cations in the Transformation of Lower Alkanes into Aromatic Hydrocarbons*. Vol 44.; 1989. doi:10.1016/S0167-2991(09)61303-3

16. Saito H, Terunuma R, Kojima K, et al. Non-oxidative Ethane Dehydroaromatization on Co / H-ZSM-5 Catalyst Copyright © The Chemical Society of Japan Electronic Supporting Information for Chemistry Letters. 2017;8553:4-6.

17. Sendoda Y, Ono Y. Transformation of Propane into Aromatic over ZSM-5 Zeolites. *J Catal*. 1986;101:12-18. doi:10.1627/jpi1958.30.77

18. Mehdad A, Lobo RF. Ethane and ethylene aromatization on zinc-containing zeolites. *Catal Sci Technol*. 2017;7:3562-3572. doi:10.1039/C7CY00890B

19. Kaliaguine S, Nagy JB, Gabelicaz Z. Chemically modified ZSM-5 zeolites: Structure and catalytic properties. *Stud Surf Sci Catal*. 1988;35:381-429. doi:10.1016/S0167-2991(09)60490-0

20. Samanta A, Bai X, Robinson B, Chen H, Hu J. Conversion of Light Alkane to Value-Added Chemicals over ZSM-5/Metal Promoted Catalysts. *Ind Eng Chem Res*. 2017;56(39):11006-11012. doi:10.1021/acs.iecr.7b02095

21. Biscardi J a., Iglesia E. Reaction Pathways and Rate-Determining Steps in Reactions of Alkanes on H-ZSM5 and Zn/H-ZSM5 Catalysts. *J Catal*. 1999;182:117-128. doi:10.1006/jcat.1998.2312

22. Roessner F, Klepel O, Hagen A. A new route to syngas- combined conversion of carbon dioxide and ethane on zeolites. *Stud Surf Sci Catal*. 1997;107:517-524.

23. Nakagawa K, Kajita C, Ide Y, Okamura M, Kato S, Kasuya H. Promoting effect of carbon dioxide on the dehydrogenation and aromatization of ethane over gallium-loaded catalysts. *Catal Letters*. 2000;64:215-221. doi:10.1023/A:1019047306179

24. Chaouki J, Nerlov J, Cenni R, Patience GS, Kaarsholm M, Joensen F. Phosphorous modified ZSM-5: Deactivation and product distribution for MTO. *Chem Eng Sci*. 2007;62(18-20):5527-5532. doi:10.1016/j.ces.2006.12.076

25. Jun J, Kim T, Hong S Il, Kim J, Jhung SH, Kim C. Selective and stable production of ethylene from propylene over surface modified ZSM-5 zeolites. *Catal Today*. 2018;303:86-92. doi:10.1016/j.cattod.2017.10.004

26. Lee J, Hong UG, Hwang S, Youn MH, Song IK. Catalytic cracking of C5 raffinate to light olefins over lanthanum-containing phosphorous-modified porous ZSM-5: Effect of lanthanum content. *Fuel Process Technol*. 2013;109:189-195. doi:10.1016/j.fuproc.2012.10.017

27. Kresse G, Joubert D. From ultrasoft pseudopotentials to the projector augmented-wave method. *PhysRev B*. 1999;59(3):1758-1775.

28. Kresse G, Furthmüller J. Efficiency of ab-initio total energy calculations for metals and semiconductors using a plane-wave basis set. *Comput Mater Sci*. 1996;6:15-50. doi:10.1016/0927-0256(96)00008-0

29. Blöchl PE. Projector augmented-wave method. *Phys Rev B*. 1994;50(24):17953-17979. doi:10.1103/PhysRevB.50.17953

30. Perdew JP, Burke K, Ernzerhof M. Generalized Gradient Approximation Made Simple. *Phys Rev Lett*. 1997;78(7):3865.

31. Grimme S. Accurate description of van der Waals complexes by density functional theory including empirical corrections. *J Comput Chem*. 2004;25(12):1463-1473.

32. Grimme S, Antony J, Schwabe T, Mück-Lichtenfeld C. Density functional theory with dispersion corrections for supramolecular structures, aggregates, and complexes of (bio)organic molecules. *Org Biomol Chem*. 2007;5:741-758. doi:https://doi.org/10.1007/s00393-018-0552-0

33. Henkelman G, Uberuaga BP, Jónsson H. A climbing image nudged elastic band method for finding saddle points and minimum energy paths. *J Chem Phys*. 2000;113(22):9901-9904.

34. Van Der Bij HE, Weckhuysen BM. Phosphorus promotion and poisoning in zeolite-based materials: synthesis, characterisation and catalysis. *Chem Soc Rev*. 2015;44(20):7406-7428. doi:10.1039/c5cs00109a

35. Rahimi N, Karimzadeh R. Catalytic cracking of hydrocarbons over modified ZSM-5 zeolites to produce light olefins: A review. *Appl Catal A Gen*. 2011;398:1-17. doi:10.1016/j.apcata.2011.03.009

36. Schreiber MW, Plaisance CP, Baumgärtl M, et al. Lewis-Brønsted Acid Pairs in Ga/H-ZSM-5 to Catalyze Dehydrogenation of Light Alkanes. *J Am Chem Soc*. 2018;140(14):4849-4859. doi:10.1021/jacs.7b12901

37. Pidko EA, Kazansky VB, Hensen EJM, van Santen RA. A comprehensive density functional theory study of ethane dehydrogenation over reduced extra-framework gallium species in ZSM-5 zeolite. *J Catal*. 2006;240(1):73-84.

38. Chu Y, Gao X, Zhang X, Xu G, Li G, Zheng A. Identifying the effective phosphorous species over modified P-ZSM-5 zeolite: A theoretical study. *Phys Chem Chem Phys*. 2018;20(17):11702-11712. doi:10.1039/c8cp00946e

39. Huang Y, Dong X, Li M, Yu Y. A density functional theory study on ethylene formation and conversion over P modified ZSM-5. *Catal Sci Technol*. 2015;5(2):1093-1105. doi:10.1039/c4cy01205d

40. Blasco T, Corma A, Martínez-Triguero J. Hydrothermal stabilization of ZSM-5 catalytic-cracking additives by phosphorus addition. *J Catal*. 2006;237(2):267-277. doi:10.1016/j.jcat.2005.11.011

# Chapter 6: Conclusions and future directions of $CO_2$ reduction with light alkanes

## 6.1 Conclusions on the $CO_2$-ODH and DR reaction pathways

Among one of the most challenging scientific issues of our time is to effectively convert the very stable $CO_2$ molecule into value-added products. High atmospheric concentrations of $CO_2$ contribute to ocean acidification and other detrimental effects on the climate that impact human health.[1,2] The need to reduce $CO_2$ emissions is evident, and the International Panel on Climate Change (IPCC) stated that climate stabilization (no more than a 2$^o$C rise from pre-industrial levels) would require rigorous combinations of mitigation, utilization, and even negative emission technologies.[3,4,5] Many of the storage and sequestration technologies under development today still require a price tag on $CO_2$ to be economically viable.[6] Since the Chen group specializes in heterogenous thermocatalysis with bimetallic systems[7,8] among other interests, the work presented in this dissertation entertains the leading question:

***What if we wanted to effectively utilize $CO_2$ to help close the carbon cycle, but with a chemical process that would be economically incentivizing in today's market?***

The reverse water gas shift reaction (RWGS) is one of the most common catalytic $CO_2$ reduction reactions. However, the feasibility of RWGS depends on large scale $CO_2$-free renewable hydrogen sources, which are still under development.[9] Another viable option is to utilize light hydrocarbons, such as ethane or propane, as feedstock for $CO_2$ reduction. Unlike $CH_4$, these light alkanes contain C-C bond(s) that could advantageously be preserved and used to build high-value olefins. Particularly, in **Chapter 3: and Chapter 4:** it was of interest to use propane due to its increasing

abundance, competitive pricing, and highly marketable respective olefin. Propylene is a highly important petrochemical building block that is used in the production of polypropylene, propylene oxide, and acrylonitrile. In recent years, the cracking of lighter feeds has caused a significant gap in propylene production.[10] As the demand for propylene continues to rise globally, the industry sector has turned to investigate "on-purpose" propylene technologies. As discussed in **Chapter 1**:**,** utilizing $CO_2$ as a soft oxidant has several advantages compared to conventional direct propane dehydrogenation or even $O_2$ assisted oxidative dehydrogenation. Thus, $CO_2$ reduction by propane is a viable chemical process that is economically incentivizing since it has the potential to fill the propylene gap while consuming a greenhouse gas.

At temperatures above 823 K, the $CO_2$ + alkane chemistry can proceed via two distinct reaction pathways simultaneously. As discussed, the $CO_2$ oxidative dehydrogenation of alkanes ($CO_2$-ODH) can produce olefins, while the dry reforming reaction (DR) can produce synthesis gas (CO and $H_2$) in a favorable ratio for downstream Fischer Tropsch reactions. Until recently, there has been little understanding regarding the identification of bimetallic catalytic systems that either selectively cleave the C-H bonds to produce olefins or effectively break all the C-C and C-H bonds to produce dry reforming products. Recent studies using a combined approach of flow reactor experiments, in situ characterization, and density functional theory calculations (discussed in **Chapter 1**:) have demonstrated the feasibility to determine why a catalyst is either inherently active for $CO_2$-ODH or DR. In **Chapter 3**:, $Fe_3Ni_1$, $Fe_3Pt_1$, and $Ni_3Pt_1$ supported on $CeO_2$ were evaluated for the reduction of $CO_2$ with propane at atmospheric pressure and 823 K. Results showed that $Fe_3Ni_1/CeO_2$ favored the production of propylene via the $CO_2$-ODHP reaction pathway whereas the $Ni_3Pt_1/CeO_2$ catalyst favored DRP. In situ X-ray absorption near edge and extended X-ray absorption fine structure spectroscopy identified that the $Fe_3Ni_1/CeO_2$ catalyst

consisted of metallic Ni and oxidized Fe while the DRP $Ni_3Pt_1$ catalysts consisted of metallic Ni and Pt. To account for the potential FeO–Ni interfacial active sites based on the in situ experimental observation of oxidized Fe in the $Fe_3Ni_1$ catalyst, DFT calculations were performed to investigate the pathways for the oxidative C–H and C–C bond cleavage of propane on the FeO/Ni(111) interface. The calculations showed that the oxygenated species prefer to adsorb at the interfacial sites while $*C_xH_y$ species most favorably adsorb on Ni(111) sites. Additionally, the energy diagram of the $FeO_x$/Ni interface identified that the first steps in oxidative C–C and C–H bond cleavage pathways were competitive. The subsequent step to form the non-oxygenated intermediate from propane was downhill in energy along the oxidative C–H bond cleavage pathway; in contrast, the subsequent steps were uphill in energy along the oxidative C–C bond cleavage pathway and would form an oxygenated intermediate from propane. This indicated that over the $FeO_x$/Ni(111) interface it was more energetically favorable for the stable adsorbed *O to remain on the surface, facilitating the selective C-H bond scission. In contrast, over the Pt-ter-$Ni_3Pt$(111) surface the pathway for C-C bond cleavage was energetically favorable and the adsorbed oxygen species would react with $C_xH_y$ fragments to form oxygenated intermediates from propane.

To build upon and expand the library of bimetallic catalysts for $CO_2$-ODHP or DRP, **Chapter 4**: identified bimetallic combinations of Pt and Pd catalysts with Fe, Co, and Ni as well as non-precious metal combinations with varying atomic composition that were active and selective for the reactions of $CO_2$ + $C_3H_8$. Results showed that Pt-based bimetallic catalysts outperformed Pd-based catalysts and that combinations with Ni exhibited higher activity and stability than the Fe and Co counterparts. Apart from $Ni_3Pt_1/CeO_2$, non-precious $Co_xNi_y/CeO_2$ catalysts were also identified to be active and selective for the DRP pathway. Additionally, results

showed that the selectivity of $Fe_xNi_y$ could be modified by changing the Ni content in the bimetallic composition. An atomic ratio of Ni above 1 (i.e., $Fe_3Ni_1$ to $Fe_1Ni_3$ or $Fe_3Ni_3$) altered the selectivity to favor the DRP pathway. The simultaneous investigation of ethane over $Fe_xNi_y$ by the Chen group (summarized in **Chapter 1**:) revealed that the change of reaction pathway is the result of distinct active sites that form under reaction conditions. When a large amount of Fe was present ($Fe_3Ni_1/CeO_2$), the preferential oxidation of Fe resulted in a Ni decorated-$FeO_x$ interface active site that favored the $CO_2$-ODH reaction pathway. In contrast, in the presence of a large amount of Ni on the surface with a low amount of Fe the resulting $FeO_x$ species was between the Ni metal particles and the $CeO_2$ support. Therefore, the Ni-$CeO_x$ interface was identified as the active site for the DRE reaction over the $Fe_1Ni_3/CeO_2$ catalyst.

In addition to the $Fe_xNi_y$ catalysts, **Chapter 4**: also examined $Fe_xCo_y$ catalysts which illustrated a preference to form propylene but have low performance due to deactivation. The findings in **Chapter 3**: regarding oxidation states suggested that identifying the active phase of metals under reaction conditions is key for future efforts geared toward the design of more active and selective catalytic materials for both reaction pathways and prompted further in situ XANES studies in **Chapter 4:** on $Fe_xCo_y$, FexNiy, and $Co_xNi_y$ catalysts. The in situ XANES results revealed that the $Fe_3Co_1$ catalyst consisted of metallic Co and oxidized Fe, but the extent of Fe oxidation was less than that in the $Fe_3Ni_1$ catalyst, leading to lower $CO_2$-ODHP activity and stability. Unlike the other non-precious systems (Fe-Ni and Fe-Co) which were influenced by atomic concentration and contained an oxidized component, the spectra of $Co_3Ni_1$ demonstrated that under reaction conditions the catalyst consisted of metallic Ni and Co. These findings suggested that unoxidized metals favor the DRP pathway.

Furthermore, support effect studies of $Fe_3Ni_1$ and $Ni_3Pt_1$ on γ-$Al_2O_3$, $ZrO_2$, $SiO_2$, and $TiO_2$ illustrated that varying the metal oxide support of the $Fe_3Ni_1$ system influenced the selectivity profile and can alter the preferred reaction pathway. Varying the support of the $Ni_3Pt_1$ system did not significantly affect selectivity, and therefore the preferred DRP reaction pathway remained the same over all the evaluated supports. The $Ni_3Pt_1$ catalytic system exhibited higher conversion than the $Fe_3Ni_1$ system for all evaluated supports likely due to lower barriers for propane activation. Overall, a bimetallic catalyst library for the reactions of $CO_2$-ODHP and DRP was established using a combined experimental and theoretical approach to determine inherent activity and can be used as a benchmark for future efforts geared to increase activity, stability, and selectivity.

## 6.2 Future directions

Future efforts for the $CO_2$-ODH of light alkanes should focus on the design of catalysts that can achieve high yields of olefins through the conversion of large amounts of $CO_2$ but with small volumes of alkanes. The combined experimental and theoretical efforts discussed in **Chapter 1**: can be used to identify descriptors (i.e., oxidation state, oxygenated intermediates, oxygen binding energy) that indicate how the selectivity and activity of a $CO_2$-ODH catalyst relate to the mechanism of the reaction. Addressing the dependence of olefin selectivity to the forms and properties of the intermediates participating in the reaction can clarify the distinct functions, and potentially the type of active sites, necessary for a promising $CO_2$-ODH catalyst. In situ characterization techniques can identify active sites under reaction conditions. The determination and subsequent controlled synthesis of active sites are among the key steps necessary to help create a path toward large-scale commercialization.

The selection of metals and support will influence the mechanism of oxidative dehydrogenation due to differences in the mode of $CO_2$ and alkane activation. New bimetallic

combinations with rare-earth metal oxides, including $CeO_2$, and or metal-modified carbides are promising bifunctional materials that warrant further investigation. Previous literature has identified redox and lattice oxygen as important factors for $CO_2$ activation, but the correlation between oxygen storage capacity/mobility and olefin yields is not well understood. Further examining oxide support effects of $CO_2$-ODH catalysts will enable rational manipulation of activity and selectivity, offering the opportunity to produce olefins more efficiently. Thus, synthesis geared toward producing high surface area oxide supports while maintaining high availability of active facets[11] is of interest.

The $CO_2$-ODH reactions will ultimately produce a mixture of olefin, water, CO, and unreacted feed (i.e., $CO_2$/alkane). The separation of gas phase products will be another challenge encountered before scale-up, requiring creative solutions in the form of process design (i.e., reactors, separators) or reactive separation. To achieve a more significant impact on reducing anthropogenic $CO_2$ emissions, chemistries that can receive the unseparated products of the $CO_2$-ODH reaction as a starting feed are highly desirable. For instance, oxidative $CO_2$ coupling with olefins to produce acrylic acids and acrylate is attractive as it would replace two high-energy steps (1) olefin to acrolein and (2) acrolein to acrylate with one step.[5] Equally ambitious is the development of a heterogeneous catalytic process for the hydroformylation of ethylene.[12] One-pot synthesis of oxygenates from $CO_2$ and light alkanes[13] using a single or consecutive catalyst bed arrangement is highly attractive as it facilitates the gas separations of the $CO_2$ + alkane reaction pathways and produces value-added oxygenates such as propanol.[14] However, heterogeneous hydroformylation chemistries typically result in poorer performance than homogeneous counterparts due to a lack of fundamental mechanistic understanding using heterogeneous catalysts. Other challenges include a

temperature-pressure mismatch since ethylene hydrogenation requires high temperatures, but the desired products are favorable at low temperature – requiring increased pressure for operation.

Another potential chemistry, but with increased similarity to the operating conditions of $CO_2$-ODH, is the tandem reactions of $CO_2$-assisted oxidative dehydrogenation and aromatization of light alkanes ($CO_2$-ODAE), discussed in **Chapter 5**:. In this process, alkanes are transformed directly into aromatics without the need for expensive naphtha while increasing the consumption of $CO_2$ per mol of value-added product and facilitating downstream separation because of the production of liquid aromatics (i.e., benzene, toluene, xylene). Studies in **Chapter 5** evaluate ZSM-5 as well as Ga and phosphorus modified ZSM-5 with a Si/Al 30 molar ratio. Unmodified ZSM-5 shows very low activity for the $CO_2$-ODAE reaction and the direct dehydrogenation and aromatization reaction (DDAE) due to low activation of reactants at Brønsted acid sites. Modification with Ga increases the activity and yield to aromatics for both reactions, and DFT calculations suggest the reaction proceeds on synergistic Brønsted -Lewis acid sites. The addition of phosphorous at an optimal loading of 0.8 wt.% improved the hydrothermal stability of Ga/ZSM-5, reduced coke formation on the catalyst surface, and allowed the formation of more liquid aromatics through the $CO_2$-ODAE reaction pathway compared to the DDAE reaction. DFT calculations showed that high barriers for $CO_2$ hydrogenation and high $H_2O$ binding energy on Ga sites hinder the production of ethylene in the presence of $CO_2$. However, $CO_2$ has an overall positive effect on the subsequent aromatization of ethylene by decreasing the energy barriers of the two most energetically demanding $H_2$ formation steps by consuming $H_2$ via the RWGS.

Future efforts on the tandem reactions of $CO_2$-assisted dehydrogenation and aromatization should focus on enhancing aromatics yield through the design of hydrothermal stable zeolite-based materials. As suggested by DFT calculations, decreasing the high barrier for $CO_2$ hydrogenation

and or binding strength of $H_2O$ on active sites may provide promising results, and this potentially may be achieved by developing Ga-based bimetallic zeolitic catalysts. Preliminary experimental efforts using bimetallic $Ga_3Fe_1$, $Ga_3Ni_1$, $Ga_3Co_1$, and $Ga_{10.5}Pt_1$ on ZSM-5P(0.8) for the $CO_2$-ODAE reaction are shown in **Figure 6-1** The catalysts were synthesized with 2 wt.% Ga and 0.53 wt.% of transition metal Fe, Co, Ni or Pt. The main trends that were identified over monometallic Ga/ZSM-5P(0.8) in **Chapter 5:.** were also observed with the selected bimetallics. For instance, the $CO_2$-ODAE reaction over phosphorous modified $Ga_{10.5}Pt_1$/ZSM-5P(0.8) had higher $C_2H_6$ conversion and liquid aromatic yield than the counterpart without phosphorous. Additionally, the bimetallic catalysts show better performance over the $CO_2$-ODAE reaction than over the DDAE reaction as shown with the example of $Ga_3Fe_1$/ZSM-5P(0.8) in **Figure 6-1**. However, the conversion of $C_2H_6$ and yield to aromatics over all the examined bimetallics was less than the observed activity of monometallic Ga/ZSM-5P(0.8).

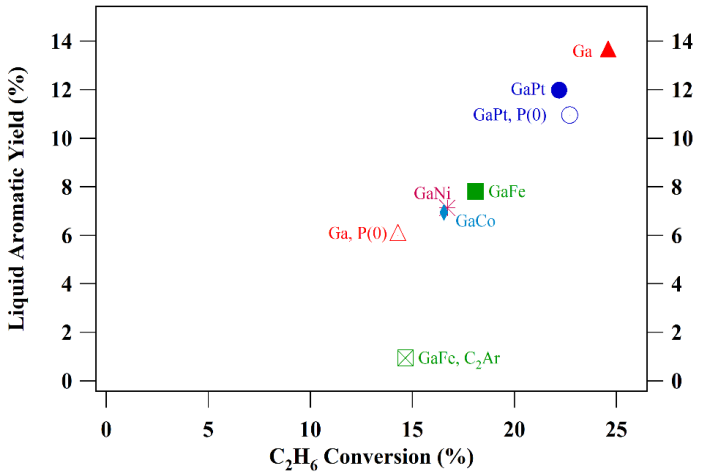


**Figure 6-1.** Bimetallic effect. Bimetallic $Ga_3Fe_1$, $Ga_3Co_1$, $Ga_3Ni_1$, and $Ga_{10.5}Pt_1$ were evaluated for the $CO_2$-ODAE reaction unless otherwise noted with $C_2Ar$. Catalysts were synthesized with 0.8 wt.% phosphorus modified ZSM-5 (Si/Al 30 molar) unless otherwise noted as P(0). Catalysts with phosphorous have full symbols, those without are hollow with a center dot. Reaction with $C_2Ar$ is symbolized with a hollow and x-crossed square

Additionally, the activity of the Ga-based bimetallic catalysts composed of Fe, Co, and Ni was similar. The similar activity profiles may be attributed to the intrinsic performance of these metals or due to the lack of bimetallic bonds with Ga. Future work on the controlled synthesis of Ga-based bimetallic catalysts and subsequent evaluation for the $CO_2$-ODAE reaction with in situ characterization may help determine if interactions between Ga and transition metal are present and whether or not the bimetallics show increased performance compared to the Ga monometallic. In addition, the promising catalytic systems identified for the $CO_2$-ODA of ethane should be extended to propane and butane due to the large mechanistic differences in aromatization between ethane and higher alkanes.

## 6.3 Closing remarks

The tandem $CO_2$ reduction and light alkane transformation reactions over specialized bifunctional catalysts have the potential to produce olefins, synthesis gas, or aromatics by efficiently utilizing the $C_2$-$C_4$ components in shale gas while reducing a greenhouse gas. Several challenges remain including catalyst development, optimal synthesis techniques, and downstream separations before large scale implementation. Effective catalyst design platforms that include a combined approach of experimental and theoretical techniques can expedite the development of selective and stable materials while also providing the critical mechanistic and kinetic understanding required for commercialization.

## 6.4 References


1. Goddard PB, Yin J, Griffies SM, Zhang S. An extreme event of sea-level rise along the Northeast coast of North America in 2009–2010. *Nat Commun*. 2015;6:6346-6354. doi:10.1038/ncomms7346

2. Clarkson MO, Wood RA, Lenton TM, et al. Ocean acidification and the Permo-Triassic mass extinction. *Science (80- )*. 2015;348(6231):229-233.

3. The Royal Society. *Geoengineering the Climate: Science, Governance and Uncertainty*.; 2009. doi:10.1007/s10098-010-0287-3

4. Core Writing Team, Pachauri RK, Meyer LA, eds. *Climate Change 2014: Synthesis Report*. Geneva, Switzerland; 2014.

5. Aresta M, Dibenedetto A, Quaranta E. State of the art and perspectives in catalytic processes for CO2 conversion into chemicals and fuels: The distinctive contribution of chemical catalysis and biotechnology. *J Catal*. 2016. doi:10.1016/j.jcat.2016.04.003

6. Wilcox J. *Carbon Capture*. Springer; 2012. doi:10.1007/978-1-4614-2215-0

7. Yu W, Porosoff MD, Chen JG. Review of Pt-based bimetallic catalysis: From model surfaces to supported catalysts. *Chem Rev*. 2012;112:5780-5817. doi:10.1021/cr300096b

8. Porosoff MD, Yu W, Chen JG. Challenges and opportunities in correlating bimetallic model surfaces and supported catalysts. *J Catal*. 2013;308:2-10. doi:10.1016/j.jcat.2013.05.009

9. Gandia LM, Arzamendi G, Dieguez PM. *Renewable Hydrogen Energy: An Overview*. 1st ed. (Gandía LM, Arzamendi G, Diéguez PM, eds.). Amsterdam: Elsevier Science; 2013. doi:10.1016/B978-0-444-56352-1.00001-5

10. Plotkin JS. The Propylene Gap: How Can It Be Filled? ACS News Industrial Chemistry & Engineering. https://www.acs.org/content/acs/en/pressroom/cutting-edge-chemistry/the-propylene-gap-how-can-it-be-filled.html. Published September 2015.

11. Cheng Z, Sherman BJ, Lo CS. Carbon dioxide activation and dissociation on ceria ( 110 ): A density functional theory study. *J Chem Phys*. 2013;138(014702). doi:10.1063/1.4773248

12. Kainulainen TA, Niemela MK, Krause AOI. Rh/C catalysts in ethene hydroformylation : the effect of different supports and pretreatments. *J Mol Catal A Chem*. 1999;140:173-184.

13. Ahlers SJ, Pohl M-M, Holena M, Linke D, Kondratenko E V. Direct propanol synthesis from CO2, $C_2$H4, and H2 over Cs–Au/TiO2 rutile: effect of promoter loading, temperature and feed composition. *Catal Sci Technol*. 2015;6:2171-2180. doi:10.1039/c5cy01425e

14. Navidi N, Thybaut JW, Marin GB. Experimental investigation of ethylene hydroformylation to propanal on Rh and Co based catalysts. *Appl Catal A Gen*. 2014;469:357-366. doi:10.1016/j.apcata.2013.10.019